HAEMOZOIN FORMATION, EFFECTS OF CHLOROQUINE ON IRON DISTRIBUTION IN PLASMODIUM FALCIPARUM AND THE CORRELATION OF THERMORDYNAMIC AND STRUCTURAL FACTORS WITH 4-AMINOQUINOLINE ACTIVITY

By

Tebogo E. Mabotha

MSc. (University of Cape Town)

Thesis presented to the

UNIVERSITY OF CAPE TOWN

for the degree of

DOCTOR OF PHILOSOPHY

Department of Chemistry

February 2007

HAEMOZOIN FORMATION, EFFECTS OF CHLOROQUINE ON IRON DISTRIBUTION IN PLASMODIUM FALCIPARUM AND THE CORRELATION OF THERMORDYNAMIC AND STRUCTURAL FACTORS WITH 4-AMINOQUINOLINE ACTIVITY

I, Tebogo E. Mabotha hereby declare that the above thesis is my own unaided work, both in concept and execution apart from the acknowledged cited references and normal guidance from my supervisors. No part of the above thesis has been submitted in the past, or is being, or is to be submitted for a degree at this University or at any other University. I grant the University of Cape Town free licence to produce the thesis in whole or in part, for the purpose of research. I present this thesis in partial fulfilment of the requirements for the degree of Doctor of Philosophy in the Department of Chemistry.

Signed by candidate

Date: .....19/02/2007.....

ABSTRACT

An interfacial method was developed in order to investigate the role lipids might play in haemozoin biosynthesis. Infrared and X-ray diffraction measurements demonstrated that β-haematin, a synthetic counterpart of haemozoin, forms efficiently at pentanol/water, octanol/water and lipid/water interfaces, but to lesser extent at a toluene/water interface under physiological conditions of pH and temperature and does not form at all in the absence of the interface. These interfaces resemble the surfaces of lipid structures known to be present in the food vacuole of the malaria parasite, providing an environment that promotes β-haematin formation. Crystals observed in SEM micrographs indicate a biomineralisation-like process which involves crystal nucleation followed by growth. β-haematin forms efficiently under acidic conditions at pH values relevant to the food vacuole (pH 4.8 — 5.5) but does not form at higher pH (pH ≥ 6). Based on likely pK_a values, this suggests that β-haematin formation is optimal when one Fe(III)PPIX propionate group is deprotonated and the other is protonated. A kinetic study conducted in the presence of lipids showed that the reaction follows a first-order rate law with a rate constant, ***k***, of 0.199 ± 0.032 min^{-1} for MMG/water interface and 0.049 ± 0.019 min^{-1} in a mixture of equal amounts of MMG, MOG, DMG, DOG, TOG and CHL at 37°C and pH 4.8. These findings demonstrate that β-haematin in this system under physiologically relevant conditions occurs at a rate sufficient to account for haemozoin formation *in vivo*. The formation of haemozoin therefore does not appear to require an enzyme but only a suitable lipid environment for β-haematin to self assemble.

The distribution of iron in the *Plasmodium falciparum* parasite treated with chloroquine was investigated using electron spectroscopic imaging (ESI) and transmission electron microscopy (TEM) and indicated that this drug has no effect on the development of merozoites into the ring-stage. Furthermore, it does not have observable effects on the ring-stage but it does affect the parasite development from ring to trophozoite. Merozoite and ring stages of the parasite do not contain a significant amount of elemental iron. A reduction in the amount and size of the

haemozoin crystals was observed in the trophozoite-stage. Some of the crystals appeared to have a halo or fuzzy edge, which might indicate the presence of Fe(III)PPIX precipitate. Furthermore, the parasites also contained a significant amount of iron in the parasite cytosol. The parasites treated with a high concentration of chloroquine contained large numbers of transport vesicles inside the parasite cytosol with the same apparent concentration of iron as the red blood cell cytoplasm. The results demonstrate that chloroquine exclusively target the trophozoite stage of the parasite causing a drastic redistribution of iron in the parasite.

The nature of the interaction between chloroquine (**CQ**) and CQ-analogues (compounds **1**, **2**, **4** and **5**) and Fe(III)PPIX in solution was studied using spectroscopic and computational methods. Thermodynamic data obtained in 40% (v/v) aqueous DMSO containing 0.02 M HEPES buffer (pH 7.5) shows a strong thermodynamic compensation effect with a slope (α) of 1.0 ± 0.02 and intercept, $T\Delta S_0$, of 31.2 ± 0.60 kJmol^{-1}, indicating a large loss of flexibility and high degree of desolvation upon complex formation. This indicates that hydrophobicity may play a major role and supports the hypothesis that the complexes form through π-π stacking. The complexes formed between Fe(III)PPIX and both **CQ** and compound **1** are strongly driven by entropy, while compound **2** is mainly enthalpy driven, with those formed with compounds **4** and **5** being entirely enthalpy driven. This suggests that complexes of **CQ**, compound **1** and to a lesser extent compound **2** are far more flexible than those of compounds **4** and **5**. There is a significant correlation between ^{1}H T_1 data with the thermodynamic data suggesting that weak β-haematin inhibitors (compound **3**) and non β-haematin inhibitors (compounds **4** and **5**) form tighter complexes while strong β-haematin inhibitors (**CQ** and compounds **1** and **2**) form more flexible complexes. ^{1}H T_1 data shows that the quinoline nucleus in **CQ** and compounds **1**, **2** and **3** lies further away on average from the porphyrin nucleus than compounds **4** and **5**. Furthermore, the IC_{50} of the 4-aminoquinolines for β-haematin inhibition correlates significantly with the ^{1}H T_1 data, with stronger correlations observed with **H2** and **H3**. A significant correlation between the IC_{50} of the 4-

aminoquinolines and ΔS suggest that the activity of the 4-aminoquinolines is not related to strength but to the flexibility of the complexes.

Attempts were made to obtain the conformations of such complexes from molecular dynamics and simulated annealing (MD/SA) calculations using distant constraints obtained from ^1H T_1 values using Solomon-Bloembergen equation. However, a poor correlation between the experimental ^1H T_1 data and the data obtained from the computed model structures was observed. This was traced to a fundamental statistical weighing problem in the computation of distance constraints in a flexible complex such as this. This has been acknowledged in previous studies which purport to provide definitive structures.

PUBLICATIONS AND CONFERENCE PROCEEDINGS

Parts of this thesis have been published:

- Egan, T. J.; Chen, J. Y-J.; de Villiers, K. A.; Mabotha, T. E.; Naidoo, K. J.; Ncokazi, K. K.; Langford, S. J.; McNaughton, D.; Pandiancherri, S.; Wood, B. R. Haemozoin (β-haematin) biomineralization occurs by sefl-assembly near the lipid/water interface. *FEBS Lett.* **2006**, *580*, 5105-5120

Parts of this thesis have been presented at the following conferences:

2006: 37th International Conference on Coordination Chemistry to be held at the CTICC, Cape Town on 13-18 August 2006.
Poster: Mechanism of Haemozoin Formation in *Plasmodium Falciparum.*

2005: 2nd COST B22 Congress on "Drug Discovery and Development for Parasitic Diseases" held at the University of Siena, Department of Chemistry, Siena, Italy on 29 Sept-1 Oct 2005.
Poster: The Effect of Haemoglobin Catabolism on the Action of Quinoline Antimalarial.

2005: 12th South African Chemical Institute Conference in Inorganic Chemistry 2005 held at the University of KwaZulu-Natal on 10-13 April 2005.
Poster: The Role of Haemoglobin Catabolism on the Activity of Antimalarial Quinolines.

2004: 37th National Convention of the South African Chemical Institute held at CSIR, Pretoria on 4-9 July 2004.
Poster: Determination of Antimalarial Drug-Haem Complex Structures in Solution by NMR Spectroscopy and Molecular Modelling.

ACKNOWLEGDEMENTS

I would like to convey my sincere gratitude to the following people:

- My supervisors, Professor Timothy J. Egan and Dr. Heinrich C. Hoppe for their guidance, excellent advice, encouragement, enthusiasm and great supervision during the course of this study. I would also like to thank you for your excellent expertise and your commitment to me and to this project.
- Professor Helder Marques from the University of the Witwatersrand for his valuable input and for teaching me how to use HyperChem for my molecular dynamics studies.
- Mr Mohammed Jaffer for his help in collecting the ESI/TEM images.
- Mr Pete Roberts for collecting the ^{1}H (T_1) NMR spectra.
- Professor Donatella Taramelli as well as members of the Istituto di Microbiologia, Universiti di Milano in Milan for their help and friendliness during my stay in Milan.
- Members of the Bioinorganic Chemistry group, Katherine and Kanyile for their support and encouragement during the course of this work and my dear friends Phili, Lesego, Malefa and Molalase for being such wonderful friends. A big thanks to Shane for proof reading my thesis. Special thanks to Lebo and Mbuso for their wonderful friendship throughout the years. I would also like to thank the members of the Division of Pharmacology for their help and for teaching me how to culture malaria parasites, especially Sumaya for keeping the TC in a good working order.
- My parents and siblings, Pheladi, Sello and Chuene and extended family members for their valuable support and encouragement through out my study and my stay in Cape Town.
- The National Research Foundation and GOOT for financial support and the Department of Chemistry.

TABLE OF CONTENTS

CHAPTER 1.

LITERATURE REVIEW AND INTRODUCTION

LITERATURE REVIEW AND INTRODUCTION

1.1. INTRODUCTION

1.1.1. History of Malaria

Malaria is one of the oldest diseases known to humankind having been clinically described as long ago as the fourth century B. C. by Hippocrates and as mentioned in early writings in Egypt, India and China [1]. The disease, also known as "marsh fever", was thought to be associated with marshes by Italians and the word "malaria" is in fact derived from the Italian for "bad air". The cause of the disease was only discovered in 1880 by Charles Laveran, who observed moving bodies from the fresh blood of a patient suspected of having malaria which he identified as the malaria parasite [2].

In 1897 Sir Ronald Ross discovered that the disease was transmitted by mosquitoes, and he also established the life cycle of the parasite [2]. Great advances have been made since then to understand the nature of the parasite and to discover treatments for this disease.

1.1.2. Malaria Today

Malaria is a protozoan parasitic disease that occurs in man. About 300 — 500 million cases are reported annually, with approximately 1.5 — 3 million deaths occurring each year [3]. The disease exists mainly in the tropical areas, namely Africa, Asia, and Latin America (**Fig. 1.1**) [4]. About 90% of these cases occur in Sub-Saharan Africa, and the disease affects mostly children under five years of age [2]. The disease has spread due to an increase in vector resistance to insecticides and mainly due to resistance to antimalarial drugs. There is therefore, a need to prepare new antimalarial drugs to combat this disease.

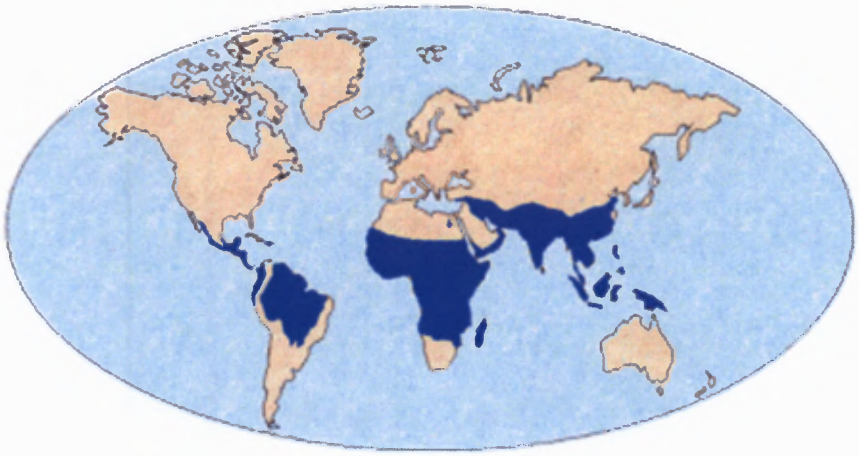

FIGURE 1.1. Global distribution of malaria [4].

1.2. BIOLOGY OF PLASMODIUM FALCIPARUM

1.2.1. The Life Cycle of *Plasmodium falciparum*

Malaria is caused by parasites belonging to the genus *Plasmodium* and four species infect humans, namely *Plasmodium falciparum*, *Plasmodium ovale*, *Plasmodium malariae* and *Plasmodium vivax* [1]. Most deaths in humans are caused by *Plasmodium falciparum*, however, significant morbidity is also associated with *Plasmodium vivax*. The life cycle of *Plasmodium falciparum* is divided into three stages, the vector (mosquito), liver and blood stages (host) (**Fig. 1.2**) [5, 6]. The parasite develops sexually in the gut of a female mosquito of the genus *Anopheles*, but only 60 species are able to transmit the disease. During its blood meal, a small amount of saliva containing sporozoites enters the bloodstream. The sporozoites then travel rapidly through the blood into the liver and invade the liver cells where they remain for 5 — 10 days [7]. In the liver cells they undergo asexual reproduction to form tissue schizonts, which divide to form thousands of merozoites. This stage of the infection is called the liver stage and does not account for the symptoms of the disease. The merozoites then rapture out of the liver cells and invade red blood cells.

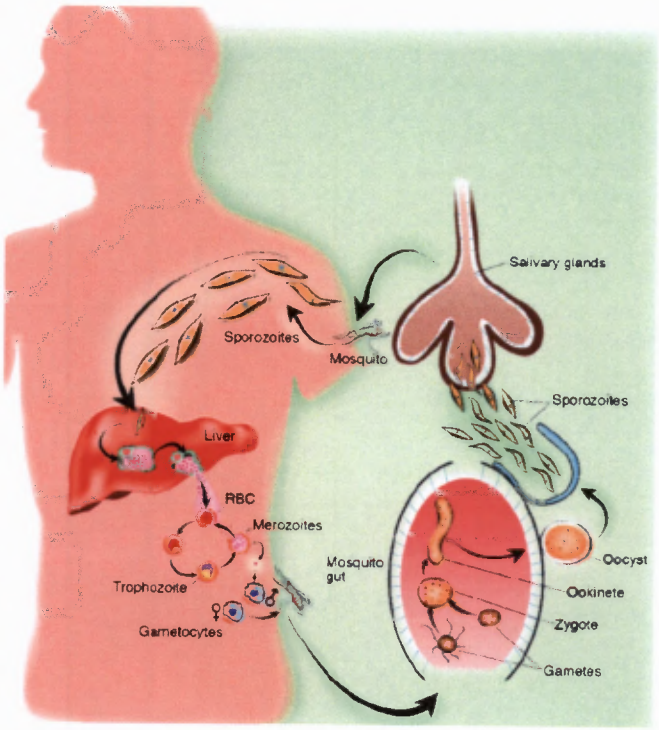

FIGURE 1.2. The life cycle of *Plasmodium falciparum* in the human host and mosquito vector [5]. Reproduced with permission from the authors.

In the red blood cell, the merozoites develop into ring forms, which then mature into trophozoites. This stage of the parasite is associated with haemoglobin degradation. The trophozoites develop further to form schizonts, which mature, divide and then lyse the red blood cell to release more merozoites. These merozoites then invade further red blood cells to begin a new erythrocytic cycle. Each erythrocytic cycle lasts for 48 hours in the case of *Plasmodium falciparum* [7]. The continuous invasion of red blood cells is associated with symptoms of malaria such as fevers, chills and anaemia and can lead to death if left untreated [8]. A small percentage of merozoites develop into sexual forms called gametocytes, which can be taken up by a mosquito when it feeds on an infected person. In the gut, the gametocytes reproduce sexually to form zygotes, which develop into oocysts and then into sporozoites. The sporozoites then travel to the salivary glands, where they remain until they are injected into the next host during a blood feed by a mosquito [5]. The parasite is thus transmitted from person to person.

1.2.2. Ingestion and Degradation of Haemoglobin in *Plasmodium falciparum*

The parasite resides in the human red blood cell (RBC) during the pathogenic part of its life cycle. During this stage of the life cycle, the parasite, mainly in the trophozoite and early shizont stage, ingests large amounts of haemoglobin (Hb) via a cytostome and transport vesicles (**Fig. 1.3**) [9, 10]. Interestingly, the parasite utilises only a small fraction of the amino acids derived from haemoglobin [11] and it has been suggested that the large amount of Hb is ingested in order for the parasite to prevent premature haemolysis of the infected red blood cell [12] or to make space for the growing parasite [13]. These stages of the parasite are also the most metabolically active.

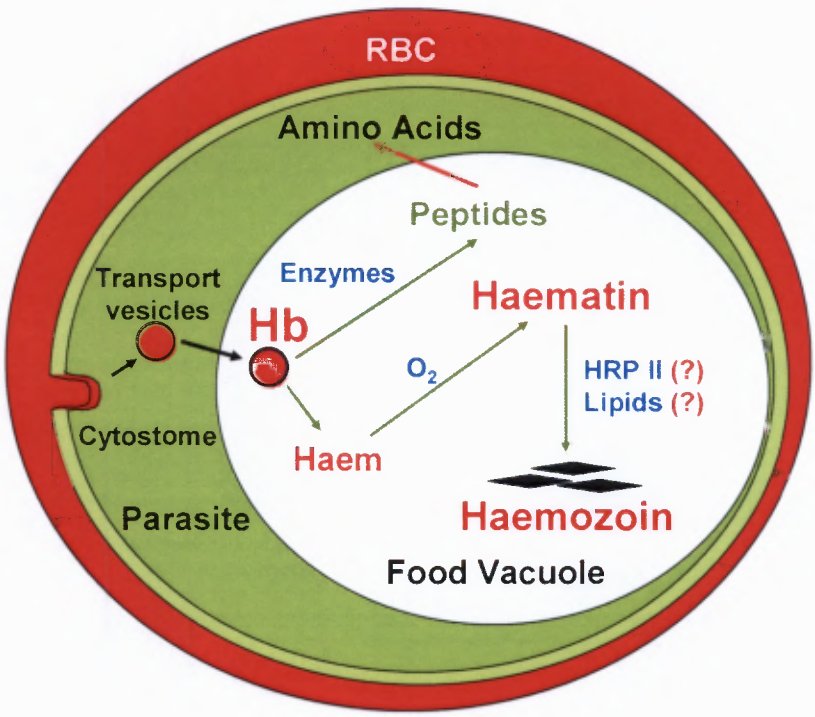

FIGURE 1.3. Schematic representation of ingestion and degradation of haemoglobin in malaria parasite [10]. Reproduced with permission from the authors.

The ingested Hb is transported into an acidic compartment in the parasite called the food vacuole [14]. The actual pH of the food vacuole has been a matter of debate with reported pH values ranging between 4.3 and 5.5 [15-18]. Geary *et al.* [15, 17] used methylamine or chloroquine as probes to measure the pH of the chloroquine

sensitive strain and an estimate of 4.3 — 4.7 was reported. Values of between 5 and 5.5 [16, 18] have also been reported using fluorescein. Ginsburg *et al.* [19] monitored the pH in chloroquine resistance parasites using a weak base acridine orange and Roepe and co-workers [20-22] have subsequently claimed a pH value of 5.6 in chloroquine sensitive parasites from single-cell measurements using acridine orange. However, two independent studies have shown that fluorescence from acridine orange monomer is quenched in the food vacuole and that the observed fluorescence is in fact localised in the parasite cytosol [23, 24]. Hayward *et al.* [14] have recently reported pH values of 4.89 and 4.7 measured with dextran-linked fluorescein and Oregon Green, respectively in the early trophozoite-stage (16 — 22 hours post invasion). However, the values diverged significantly in mature trophozoites (32 — 38 hours post invasion) to pH of 4.5 and 5.5 measured with fluorescein and Oregon Green, respectively [14]. Nevertheless, the estimated pH converged in the range of 4.5 — 4.9 in both the chloroquine-sensitive and chloroquine-resistant strains at lower dye concentrations. A study conducted by Kuhn *et al.* [24A] confirmed the similarity of the vacuolar pH in both the chloroquine-sensitive and chloroquine-resistant strains estimatated to be 5.18 ± 0.05 using pHluorin (pH sensitive green fluorescent protein) The discrepancies between the different studies highlight the limitations of these methods making it difficult to verify the actual pH of the food vacuole in late trophozoites, as Hayward *et al.* [14] have argued that the pH of the food vacuole is not tightly controlled in the late trophozoite stage.

Upon entering the food vacuole, 60 — 80% of Hb is degraded by enzymes into peptides [25, 26] and finally hydrolysed into amino acid in the parasite cytosol [10], some of which the parasite uses as a food source for growth and maturation. Several enzymes are thought to be involved in the process of Hb hydrolysis, namely cysteine proteases (falcipain 1, 2 and 3) [27], aspartic proteases (plasmepsins I, II and IV and histo-aspartic protease) [28] and metalloproteases (falcilysin) [29]. Studies [30, 31] have suggested that degradation of Hb is an ordered process which involves cleavage of the Hb tetramer by plasmepsin I followed by digestion of the denatured

substrate by plasmepsin II and falcipain. Other enzymes including aminopeptidases have been implicated in the cleavage of globin fragments into amino acids [31A]. Hydrolysis of Hb is inhibited by cysteine and aspartic protease inhibitors [27, 32]. These inhibitors are now under study as potential antimalarials. During Hb degradation, haem (Fe(II)PPIX) is released and oxidised to toxic ferriprotoporphyrin IX (Fe(III)PPIX). In an acidic aqueous environment it is likely that this will be ligated by a water molecule to form haematin (H_2O-Fe(III)PPIX) (**Fig 1.4**) [29]. Free Fe(III)PPIX in the parasite is believed to disrupt membranes, inhibit enzymatic processes and initiate oxidative damage [25, 32]. The parasite therefore has to avoid accumulation of Fe(III)PPIX, which could interfere with its survival.

FIGURE 1.4. Structure of a single molecule of aqua-ferriprotoporphyrin IX (H_2O-Fe(III)PPIX) . The hydrogen atoms on water and propionic acid groups are represented in white (the rest are omitted for clarity), the iron centre is represented in green, the nitrogen atoms are represented in blue and the carbon atoms in cyan.

The study of Fe(III)PPIX in aqueous solutions is problematic as it forms aggregates. The speciation and structure of Fe(III)PPIX in aqueous solution has not been fully understood, but a previous hypothesis suggested that it forms a μ-oxo dimer based on spectrophotometric studies by Brown *et al.* [33]. The μ-oxo dimer forms when two H_2O-Fe(III)PPIX molecules bridge together through one of the oxygen atoms derived from the OH group and elimination of H_2O to form a Fe-O-Fe bond with a 180° angle between the two Fe(III)-O bonds. A recent study by de Villiers *et al.* [34] has confirmed using spectrophotometric and diffusion measurements that Fe(III)PPIX dimerises in aqueous solution and does not form higher aggregates as suggested by Brown *et al.* [33]. However, they have unequivocally demonstrated by UV-visible,

NMR and magnetic measurements that the dimer is not a μ-oxo dimer. They proposed that the species exists as a dimer where the axial ligands (H_2O/OH^-) are directed outwards and the unligated faces of the porphyrin interact via non-covalent π-π interactions.

1.2.3. Fe(III)PPIX Detoxification in *Plasmodium falciparum*

There has been a debate over the years as to how the malaria parasite disposes Fe(III)PPIX. Fe(III)PPIX is known to be highly toxic to microorganisms [35] and likely also to *Plasmodium falciparum*. It has been shown that high concentrations of Fe(III)PPIX cause haemolysis of RBC membranes [36-38] and parasite swelling [39]. The parasite therefore needs a mechanism of disposing Fe(III)PPIX to avoid cell damage. It has been proposed over the years that Fe(III)PPIX is removed by conversion to haemozoin or malaria pigment, which is a black crystalline material observed in the food vacuole of the parasitised erythrocyte (**Figure 1.5**) [40-42]. The pigment is ingested by macrophages when mature parasitised red blood cells rapture [43], and finally enters the tissues [43, 44], accumulating in the liver and spleen of the host as the parasitemia increases.

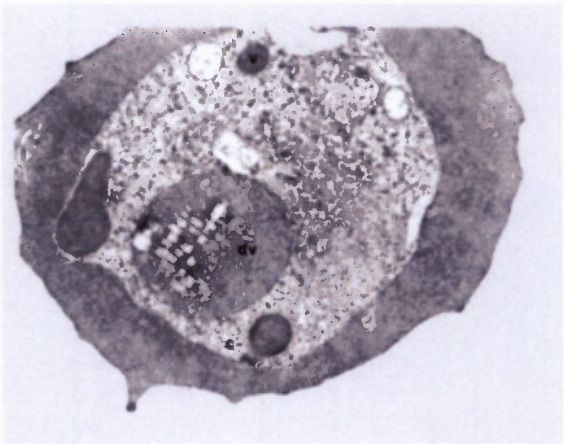

FIGURE 1.5. Transmission electron micrograph of *Plasmodium falciparum* trophozoite. **c**, cystome; **v**, transport vesicle; **dv**, digestive vacuole (food vacuole) [42]. Reproduced with permission from the authors.

The pigment has also been identified in other *Plasmodium* species (**Fig 1.6**) [45]. The crystals generally have a regular shape and are cuboidal with different sizes, with the exception of the avian parasite *P. gallinaceum*.

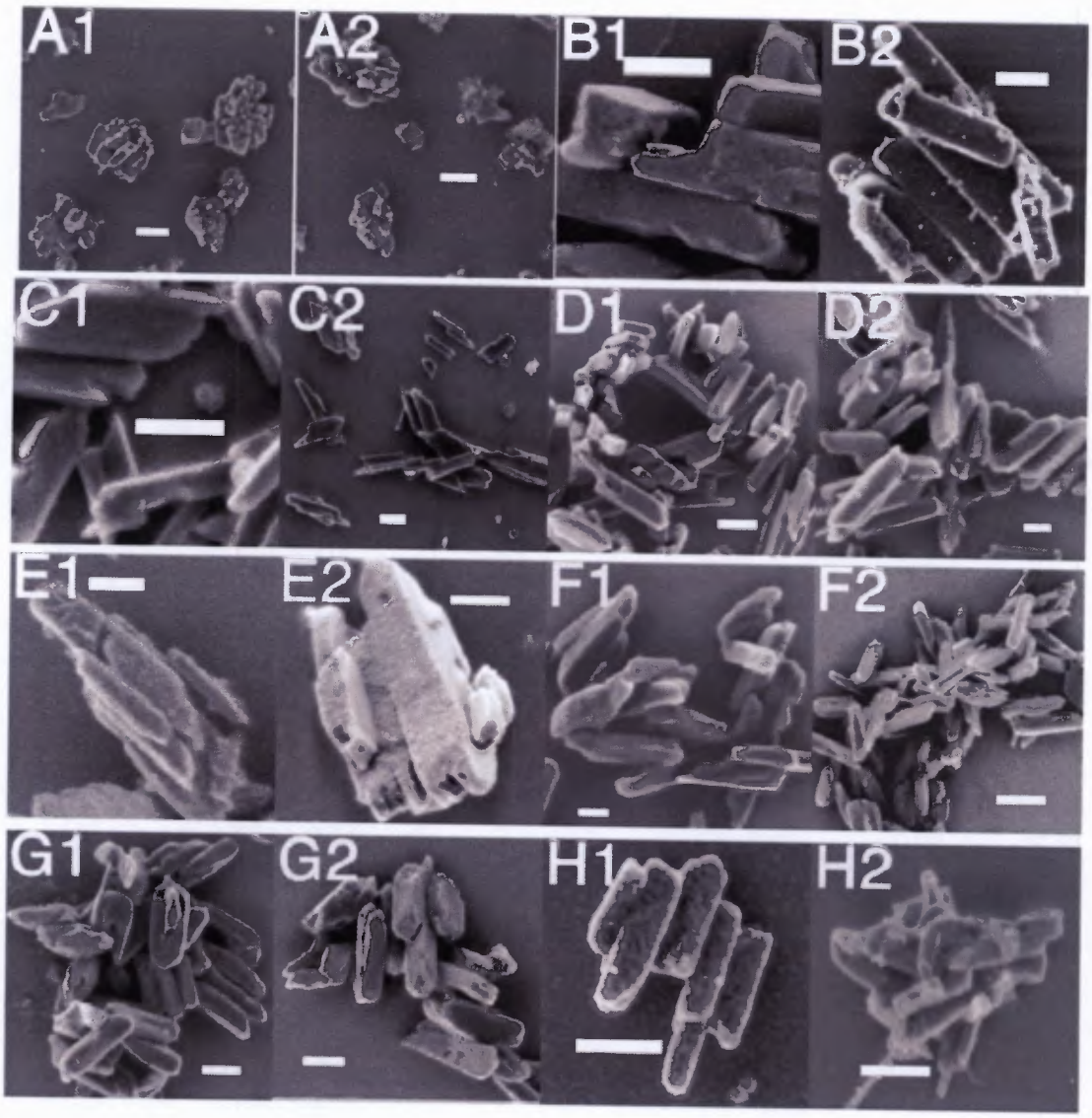

FIGURE 1.6. Electron micrographs showing haemozoin from different species of *Plasmodium*. (**A**) *P. gallinaceum*, (**B**) *P. falciparum* , (**C**) *P. vivax*, (**D**) *P. ovale*, (**E**) *P. malariae*, (**F**) *P. brasilianum*, (**G**) *P. knowlesi* and (**H**) *P. yoelii* [45]. *P. gallinaceum* parasites infect birds. *P. brasilianum* and *P. knowlesi* are parasites that infect monkeys. *P. yoelii* infect mice. The bar size is 200 nm. Reproduced with permission from the authors.

More recently, a study done by Ginsberg *et al.* suggested that only 30% of Fe(III)PPIX is converted to haemozoin, and that the remaining Fe(III)PPIX escapes from the food vacuole into the parasite cytosol and is degraded by glutathione (GSH) [26]. Another study by Loria *et al.* has also claimed that only one third of Fe(III)PPIX is converted to haemozoin and suggested that the remainder is degraded within the food vacuole by H_2O_2 generated from oxidation of Fe(II)PPIX to Fe(III)PPIX [25]. However, Egan *et al.* have subsequently shown from Mössbauer spectroscopy, electron spectroscopic imaging (ESI) and chemical analysis of the iron content in the parasite that at least 95% of the iron is converted into haemozoin [46]. Elemental analysis performed by colorimetric assay using ferrozine performed on isolated parasitised RBCs, trophozoites, food vacuoles and haemozoin showed that 92 ± 6% of the parasite iron is in the food vacuole and 88 ± 9% of this iron is in the form of haemozoin (**Fig 1.7** (**a**)).

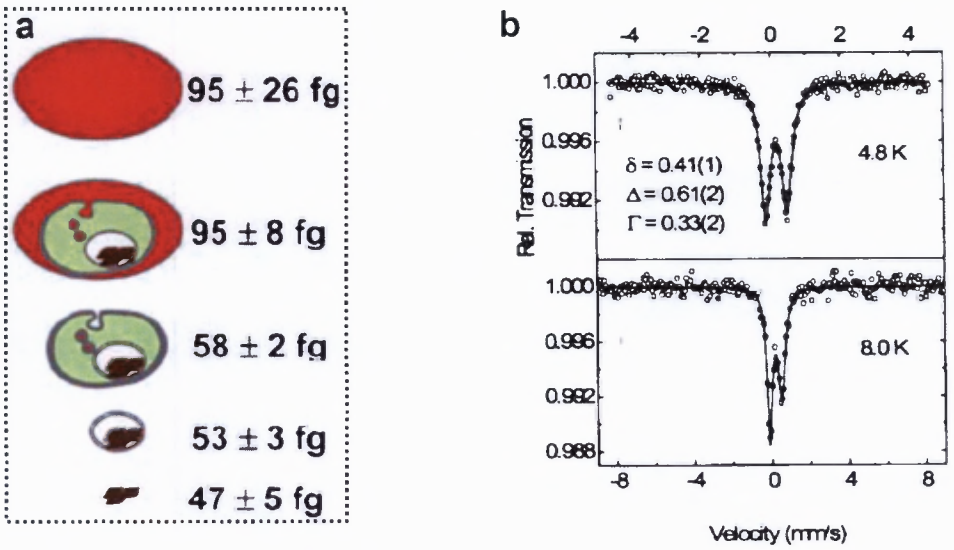

FIGURE 1.7. (**a**) Iron content within (top to bottom) unparasitised red blood cells, parasitised red blood cells, isolated trophozoites, food vacuoles and haemozoin. (**b**) Mössbauer spectra of freeze-dried trophozoites [46, 47]. The spectrum is characteristic of haemozoin. Reproduced with permission from the authors.

^{57}Fe Mössbauer spectroscopy of freeze-dried trophozoites demonstrated that the only detectable iron species is in the form of haemozoin (**Fig 1.7** (**b**)) and given the size of the baseline scatter, places an upper limit on non-haemozoin Fe of 5%. These findings are consistent with ESI images (**Fig 1.8**) showing the distribution of elemental iron in the trophozoites. Both the transmission electron microscopy (TEM) and ESI pictures show clearly that the iron distribution in the parasite corresponds exactly with haemozoin. It is virtually certain from these findings that Fe(III)PPIX in *Plasmodium falciparum* is almost entirely incorporated into haemozoin.

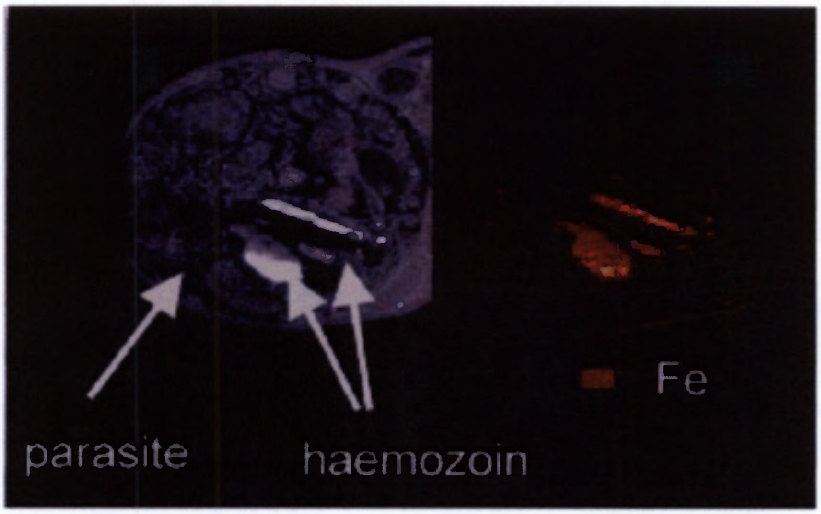

FIGURE 1.8. TEM image (left) of a parasite occupying a red blood cell and the distribution of elemental iron from ESI (right) [46]. Reproduced with permission from the authors.

Haemozoin has also been identified in other blood-feeding organisms such as *Rhodnius prolixus* [48, 49], *Schistosoma mansoni* [50] and *Haemoproteus columba.* [51]. *Rhodnius prolixus* is a blood-sucking insect (**Fig 1.9** (**a**)) that is a vector of the parasite *Trypanosoma cruzi*, which causes Chagas' disease affecting the heart and the nervous system [48]. TEM studies have shown that the insect digests haemoglobin and forms haemozoin in the midgut as shown by large electron-dense granules that are similar to haemozoin granules found in *Plasmodium falciparum* [48, 49]. The worm *Schistosoma mansoni* (**Fig 1.9** (**b**)) is the main causative agent of schistosomiasis (bilharzia) in humans and ranks second in number of infections after

malaria [52] in the list of human parasitic diseases. The worm ingests and digests haemoglobin in the gut for maturation and development [53, 54], thus producing Fe(III)PPIX in the process. The toxic Fe(III)PPIX is then converted to a dark-brown material called schistosoma pigment [49, 50, 52] (**Fig 1.9** (**c**)) followed by elimination through regurgitation.

FIGURE 1.9. (**a**) *Rhodnius prolixus* [55], (**b**) *Schistosoma mansoni* [56], (**c**) bright field microscopic image of *Schistosoma mansoni* showing haemozoin crystals [52] and (**d**) *Helisoma trivolvis* [57]. Reproduced with permission from the authors.

Haemoproteus columbae infects birds, especially pigeons, and is transmitted by flies. The gametocytes of *Haemoproteus columbae* digest haemoglobin and dispose of the toxic Fe(III)PPIX by forming haemozoin [51]. Haemozoin has recently also been found in the gut of *Echinostoma trivolvis* radiae a parasite found in *Helisoma trivolvis* snails (**Fig 1.9** (**d**)) [58]. It is estimated that about 50 million people are infected, with the majority of cases being brought about by consumption of uncooked or undercooked fish or shellfish and morbidity is manifested by diarrhea, anorexia and anaemia [59]. The rediae feeds on the hemolymph and digestive gland tissues of the snail and forms a black pigment while inside the snail host.

Scanning electron microscopy (SEM) micrographs of haemozoin from these different species is shown in **Fig 1.10**. The crystals of *S. mansoni* and *R. prolixus* (**Fig 1.10** (**b**) and **Fig 1.10** (**c**)) [60] are spherical and composed of irregularly shaped crystalline units compared to haemozoin crystals from *Plasmodium falciparum* (**Fig 1.10** (**a**)) [51] which are large and cuboidal in shape. The pigment from *H. columbae* [45] has a smaller rougher cuboidal appearance with slightly irregular shape (**Fig 1.10** (**d**)) and the pigment of *E. trivolis* [58] has irregular ovoid crystals with a diameter of approximately 200 — 300 nm (**Fig 1.10** (**e**)) Although these crystals share the same molecular structure as haemozoin and share the same unit cell as that of *Plasmodium falciparum* [60], their external morphology is different. This may be indicative of the different environment from which crystallisation take places which results in different organisation of the crystals.

The findings show that some blood-feeding organisms other than *Plasmodium* dispose toxic Fe(III)PPIX by converting it to a less toxic crystalline material. However this is not universally the case, as it has been shown that species such as *Anopheles*, *Entamoeba histolytica* [61]and *Boophilus microplus* [62] do not produce haemozoin. Therefore it appears that formation of haemozoin is dependent on the chemical environment including the pH. Formation of haemozoin requires that one of the propionate groups be deprotonated which would allow coordination with the Fe (III) centre with the remaining protonated propionate forming hydrogen bonds between the haemozoin dimers in the crystal [63]. Therefore, the species that form haemozoin digest haemoglobin in an acidic environment which allows haemozoin formation to occur.

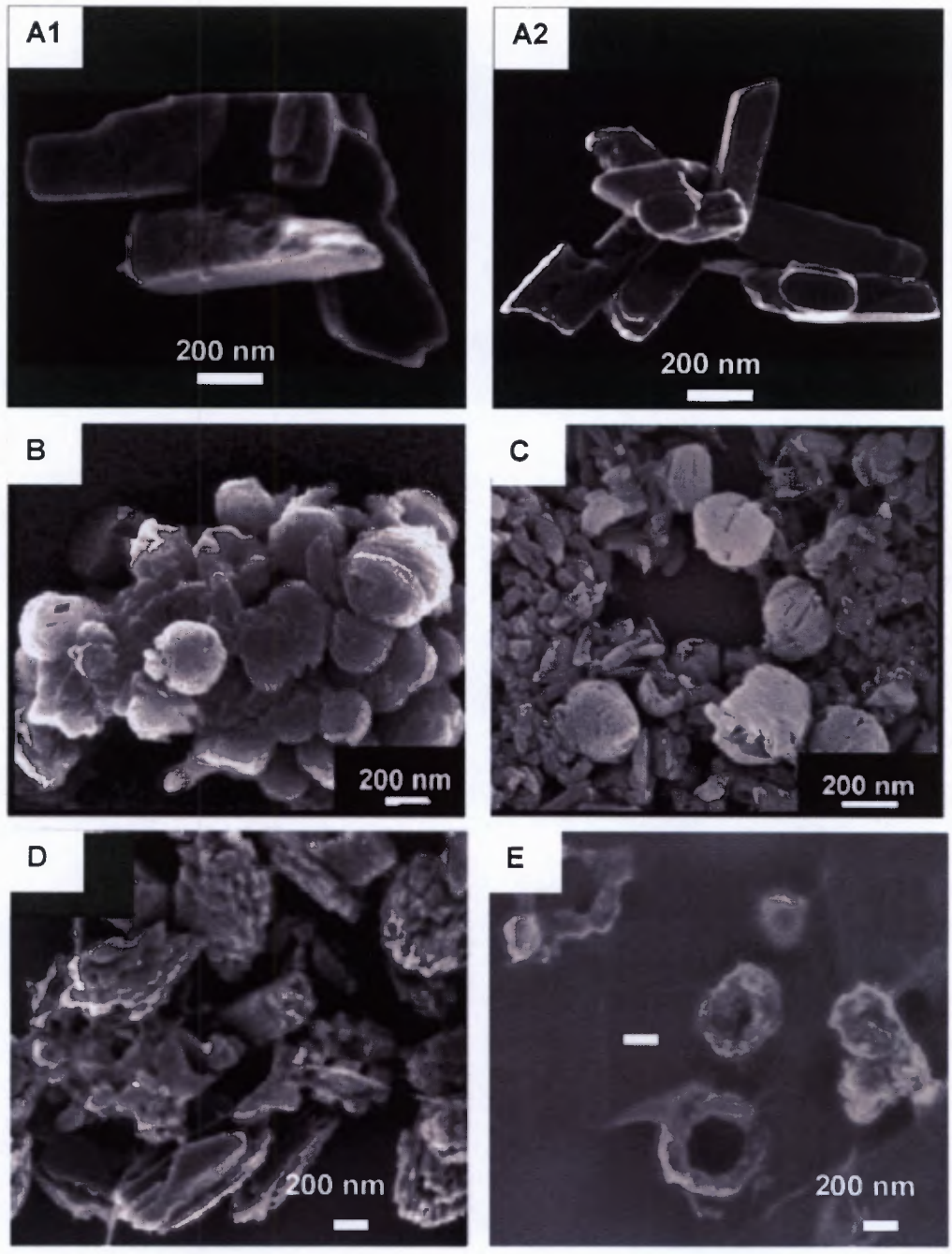

FIGURE 1.10. Scanning electron micrographs of haemozoin from (**a**) *P. falciparum* [51], (**b**) *S. mansoni* [60], (**c**) *R. prolixus* [60], (**d**) *H. columbae* [45] and (**e**) *E. trivolis* [58]. Reproduced with permission from the authors.

1.3. CHEMICAL COMPOSITION AND MOLECULAR STRUCTURE OF HAEMOZOIN

Haemozoin, also known as malaria pigment, was discovered centuries ago where it was observed in organs of malaria patients as it is responsible for organ discolouration in people who die of malaria [8]. Initially the pigment was thought to be melanin but later Brown demonstrated that it is not melanin, but rather a product of haem (Fe(II)PPIX) released during haemoglobin degradation [64]. Ghosh and Sinton [65] later showed that the pigment contains non-ionisable Fe and that solubilised haemozoin has the same elemental composition as that of haematin [66]. The first preparation of β-haematin was obtained by Hamsik [67] who showed that this preparation was identical to haemozoin extracts. Ashong *et al.* [40] suggested in their studies that haemozoin is a crystalline protein complex and that the protein component is related to haemoglobin [68, 69]. The pigment was characterised biochemically and was shown to contain 65% protein, 16% Ferriprotoporphyrin IX, 6% carbohydrate and traces amounts of nucleic acid and lipids [41].

Fitch and Kanjananggulpan [70] later demonstrated that the pigment can be freed of protein, contains haem only and confirmed that it is similar to β-haematin based on solubility studies. This investigation showed that both these substances are insoluble in ethanol, sodium bicarbonate and chloroform and also have the same electronic absorption spectrum. Slater *et al.* [63] were the first to provide evidence of the chemical nature of haemozoin using a combination of Fourier transform infrared spectroscopy (FTIR), elemental analysis, extended X-ray absorption fine structure spectroscopy (EXAFS) and X-ray diffraction (XRD). They suggested that haemozoin has an iron-carboxylate bond between two Fe(III)PPIX units and came to the conclusion that the structure is polymeric. The infrared spectrum of haemozoin crude extracts is virtually identical to that of synthetic β-haematin (**Fig 1.11**). The 1663 and 1209 cm^{-1} peaks arise from the iron-carboxylate linkage between the Fe(III)PPIX subunits arising from stretching of the localised C=O and C-O bonds, respectively

[63]. Adams *et al.* further provided evidence using Mössbauer spectroscopy [71] that these two species are chemically identical.

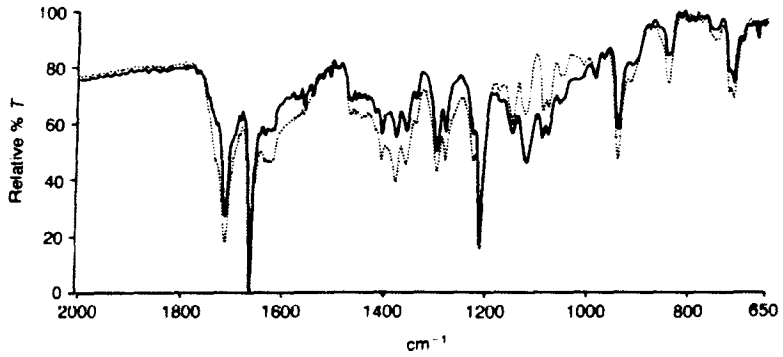

FIGURE 1.11. Comparison of the infrared spectra of haemozoin (—) and β-haematin (...) [63]. Reproduced with permission from the authors.

The identical structural and chemical properties of haemozoin and β-haematin was conclusively verified by Bohle [72] from the X-ray powder diffraction patterns. The diffraction patterns of both β-haematin prepared in dry methanol and haemozoin in lyophilised parasites are identical (**Fig 1.12**) which unequivocally demonstrates that both haemozoin and β-haematin crystallise with the same unit cell and are identical on the atomic level [72].

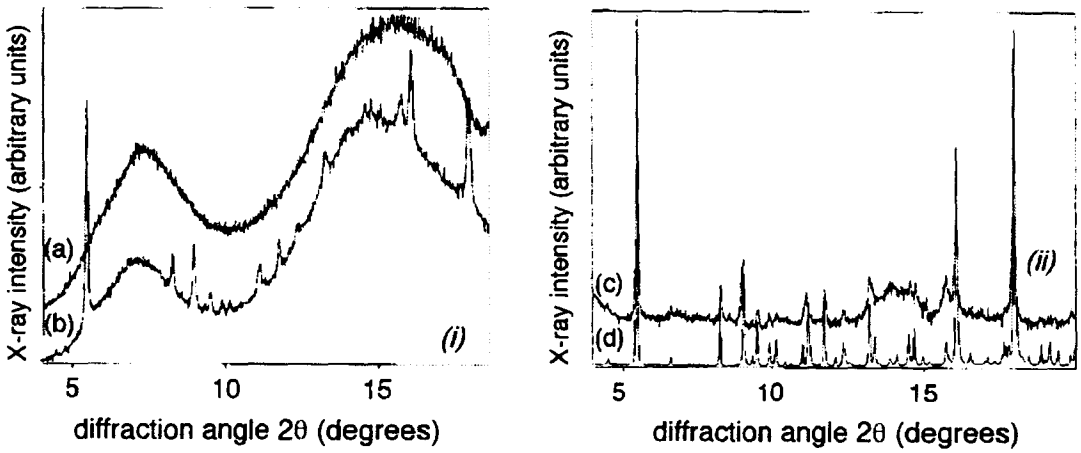

FIGURE 1.12. X-ray powder diffraction patterns of (**a**) lyophilised uninfected red blood cells, (**b**) lyophilised *Plasmodium falciparum* infected red blood cells, (**c**) difference between (**a**) and (**b**), and (**d**) β-haematin [72]. Reproduced with permission from the authors.

Finally in 2000, Pagola *et al.* showed using high-resolution synchrotron radiation, that β-haematin is a crystalline dimer, where the propionate side chain of one Fe(III)PPIX coordinates to the Fe(III) centre of the next unit in a cyclic dimer and the crystal is formed through hydrogen bonding between the remaining propionic acid group of each Fe(III)PPIX (**Fig. 1.13**) [73].

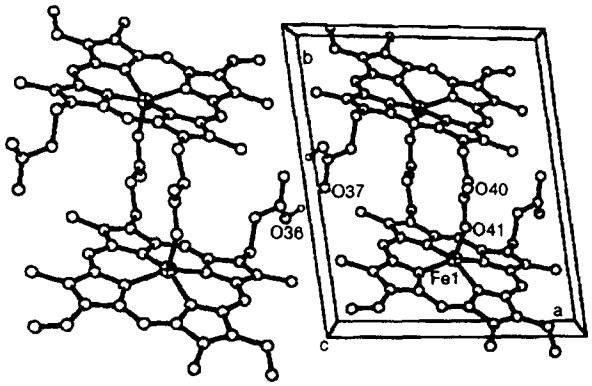

FIGURE 1.13. Unit cell structure of β-haematin [73]. Reproduced with permission from the authors.

1.4. MECHANISM OF HAEMOZOIN/β-HAEMATIN FORMATION

As stated above, it is now well established that at least 95% of toxic Fe(III)PPIX is disposed by conversion to haemozoin or malaria pigment in *Plasmodium falciparum* (**Section 1.2.3**). The mechanism of haemozoin formation is however not well understood. Slater and Cerami proposed that haemozoin formation is catalysed by a haem polymerase enzyme [74], as haemozoin was believed to be a polymer at the time. But this was later questioned by Dorn *et al.* who observed that heat-treatement of isolates of the parasite made little difference to the rate of reaction [75]. They suggested that haemozoin forms autocatalytically as haem is liberated and that the catalytic agent is haemozoin itself as haemozoin itself was found to promote β-haematin formation. This observation is in fact consistent with a crystal growth process, but cannot explain how haemozoin formation is initiated. Thus several hypotheses have since been proposed to explain the formation of haemozoin in

Plasmodium falciparum and these include the involvement of lipids and proteins. Studies done to date to understand haemozoin formation in the parasite have been performed on β-haematin formation, which is a synthetic counterpart of haemozoin [63]. The formation of β-haematin can be conducted under non-biological conditions in organic acids [63] or non-aqueous solutions [76] or under more biologically realistic conditions, for example in the presence of parasite membrane (lysates) [77], lipids [78-81] or histidine-rich proteins (HRPs) [82, 83].

1.4.1. β-Haematin Formation under Non-Biological Conditions

β-haematin can be formed under non-biological conditions in organic solvents [76], acetic acid [63, 84] and benzoic acid [85]. Bohle *et al.* [76] have synthesised β-haematin in dry methanol at room temperature over 16 hours. The process involves the abstraction of HCl from haemin (Cl-Fe(II)PPIX) with the base 2,6-lutidine. Another method of synthesising β-haematin involves heating haematin in 4.5 M acetic acetic at 70°C overnight [63]. The product obtained from these methods was analysed mainly by X-ray powder diffraction, infrared spectroscopy and solubilisation. Egan *et al.* [84, 85] have reported a simplified method which does not involve extensive washings, centrifugation or long incubation time. The method involves dissolution of haematin in NaOH and neutralisation with HCl followed by incubation in either 4.5 M acetate buffer or 0.05 M benzoic acid at 60°C. The rate of formation is however faster in benzoic acid compared to acetate buffer. The reaction reaches completion within 2 hours at 60°C in 0.05 M benzoic acid and 1 hour in 4.5 M acetate buffer [84, 85], which is 90 times more concentrated. Furthermore, they have demonstrated that the reaction is complete within 2 hours at 37°C and 8 days at 6°C in 4.5 M acetate buffer in the absence of any parasitic material [84]. Acetate or benzoate was originally hypothesised to catalyse the reaction through its ability to solubilise Fe(III)PPIX through formation of a weak complex under these acidic conditions, followed by spontaneous formation of β-haematin as acetic acid was found to solubilise Fe(III)PPIX. On the basis of this proposal, it was suggested that haemozoin formation does not require an enzyme but may in fact be spontaneous. Later it was suggested

by Fitch [78] that lipids may play such a solubilisation role *in vivo*. However, benzoic acid shows no evidence of such solubilisation and so it was recently proposed that the carboxylic acid may act by disrupting hydrogen bonding and π-π stacking (in the case of benzoic acid) in haematin, thus facilitating β-haematin formation (**Fig 1.14**).

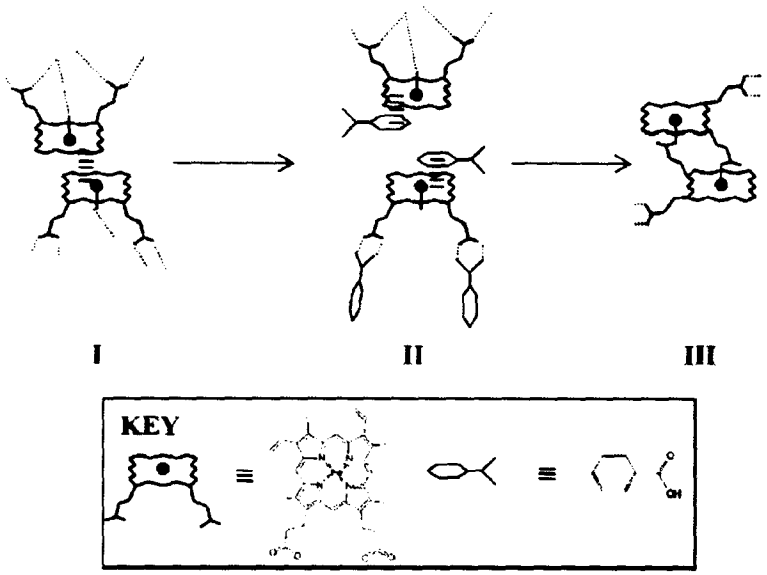

FIGURE 1.14. Proposed mechanism of β-haematin formation in aqueous benzoic acid. Amorphous haematin (**I**) forms hydrogen bonds (...) with other haematin molecules and water molecules and it can also form π-π stacking interactions (≡). Benzoic acid can disrupt these interactions by interacting with haematin (**II**). This will then allow the rearrangement of haematin molecules to form β-haematin (**III**) [85]. Reproduced with permission from the authors.

These studies have not been without controversy. Pandey and Tekwani [86] have suggested that the product formed in acetate is not β-haematin but a Fe(III)PPIX-acetate complex. However, Egan *et al.* [87] showed no evidence of Fe(III)PPIX-acetate complex even in 11.4 M acetate solution. The reaction also proceeds in a mixture of 0.1 M glutamate and 0.4 M glycine at pH 4.5 (91 hours at 65°C) [84]. Adams *et al.* conducted kinetic studies of β-haematin formation using Mössbauer spectroscopy [88] in 4.5 M acetate. The kinetics of β-haematin formation were followed by measuring the relative amounts of both haematin and β-haematin as indicated by the intensity of the Mössbauer lines at various times between 0 and 60

minutes. The samples were filtered and washed with water and dried. The results indicated a pseudo-zero-order kinetic process. Egan *et al.* [89] have subsequently monitored the process by measuring the absorbance of the C-O stretching frequency of the coordinated propionate group by infrared spectroscopy. They demonstrated that the process follows sigmoidal kinetics and not the zero-order kinetics as suggested previously. The sigmoidal kinetics are indicative of a process that involves nucleation and growth. The reaction kinetics were fitted to the Avrami equation, which is characteristic of a process involving nucleation and crystal growth. This study suggests that β-haematin formation under these conditions proceeds *via* rapid precipitation of amorphous haematin followed by dissolution and re-precipitation to crystalline β-haematin through nucleation and crystal growth. Kinetic studies have also been performed in 0.05 M benzoic acid and they were monitored by differential solubilisation of haematin, but not β-haematin in 5% aqueous pyridine to form a Fe(III)PPIX-pyridine complex [85]. This study confirmed that the kinetics are sigmoidal, fitting to the Avrami model. The authors have thus proposed that haemozoin formation is a form of bio-mineralisation process.

1.4.2. β-Haematin Formation in the presence of Histidine-Rich Proteins (HRPs)

Sullivan *et al.* originally suggested that histidine-rich proteins (HRPs) are responsible for β-haematin formation *in vivo* [82]. They identified two HRPs, HRP II and HRP III in *Plasmodium falciparum* and have demonstrated that these proteins can promote β-haematin formation. HRP II contains 51 repeats of the sequence Ala-His-His while HRP III has 28 repeats of the Ala-His-His sequence. *In vitro*, β-haematin formation assays with HRP II and other haem binding proteins such as bovine serum albumin and lysozyme or the homopeptides polyhistidine, polylysine and polyasparagine showed that only HRP II promoted the formation of β-haematin and the others did not. Recent studies have shown that the HRP II-Fe(III)PPIX complex has peroxidative activity, thus suggesting that HRP II may act as a protective template against oxidative effects of toxic Fe(III)PPIX [90]. Several researchers have suggested that HRP may act mainly as a bionucleation template for haemozoin formation, thus behaving as a growth surface.

The role of HRP as a nucleation template was investigated by Ziegler *et al.* [91] who synthesised a model dendrimer template peptide based on the repeat motif of HRP II from *Plasmodium falciparum* with the sequence Ala-His-His-Ala-His-His-Ala-Ala-Asp. This dendrimer template is capable of binding Fe(III)PPIX and other porphyrins such as Zn(II)PPIX and PPIX. Binding of the metal free PPIX seems to suggest that the HRPs associate with the porphyrin moiety through π-π stacking and do not coordinate to the metal ion through a histidine residue. This proposal was further supported when they demonstrated that Fe(III)PPIX can also bind to metal free phthalocyanine and metallophthalocyanines. However, this supposition is contradicted by Choi *et al* [92] and Lynn *et al.* [93] who have suggested that HRP II is association with the metal. Ziegler *et al.* suggested, based on the dendrimer findings, that the formation of haemozoin is a biomineralisation process. This proposal was supported by Egan *et al.* [89] who studied the formation of β-haematin in acetate solution as mentioned above. Other studies conducted independently have also demonstrated that HRP II initiates haemozoin formation in *Plasmodium falciparum* [83, 92, 93]. Chloroquine has been shown to disrupt the formation of HRP II-Fe(III)PPIX complex thus indicating that chloroquine may act by inhibiting Fe(III)PPIX detoxification by binding to HRP II [94].

Pandey *et al.* [95] have suggested that haemozoin formation is a two-step process involving both HRP II and lipids. The rate of haemozoin formation in HRP II and lipid alone is too slow. They suggested that HRPs may facilitate haemozoin formation by binding a large number of Fe(III)PPIX molecules and linking the molecules together to form a dimers, while the lipids then promote the linking of the dimers through hydrogen bonding of the propionate groups. It is still uncertain at present what role, if any, the HRPs play in haemozoin formation in *Plasmodium falciparum*. Indeed, a *P. falciparum* clone lacking both HRP II and HRP III has been shown to form haemozoin normally [61], which calls into question the role of HRP in haemozoin formation. Furthermore, *P. vivax* and the mouse malarial parasites *P. berghei* and *P. yoelii* which all lack HRP II and HRP III also form haemozoin. Consequently, the support for this model has decreased recently.

1.4.3. β-Haematin Formation in the presence of Lipids

The involvement of lipids as catalysts of haemozoin formation has been proposed as the main route [78-81]. Bendrat *et al.* [79] suggested that the reaction is promoted by lipids as shown by the activity of the acetonitrile extract of *P. falciparum* promotes rapid formation of β-haematin. Extensive analysis of the acetonitrile extract revealed the presence of several methyl esters of oleic, palmitic and stearic acids [79]. A comparative study by Dorn *et al.* [75] confirmed that β-haematin can form in the presence of pre-formed haemozoin/β-haematin as well as acetonitrile extracts of trophozoites and several phospholipids. Studies conducted by Fitch *et al.* [78] have shown that chloroform lipid extracts of *Plasmodium berghei* also promote β-haematin formation. Studies of individual unsaturated fatty acids including oleic, arachidonic, linoleic and palmitoleic acids as well as 1-monoglycerol and di-oleoylglycerol are able to promote β-haematin formation with 1-monoleoylglycerol showing greater activity. Tri-oleoylglycerol, cholesterol, di-oleoylphosphotidylethanolamine, stearic acid and palmitic acid were reportedly inactive [78]. Linoleic acid or its derivative were suggested to be the main promoter of β-haematin formation since malaria parasites are enriched with linoleic acids [96].

Recently, compelling evidence has begun to mount, indicating that haemozoin formation is a lipid driven process. Fluorescence images using Nile Red labelling of red blood cells infected with *Plasmodium falciparum* have shown an association of neutral lipid bodies with the food vacuole [97] (**Fig 1.15**). Lipid analysis of these lipid bodies has revealed that they compose of di- and triacylglycerols [97]. Furthermore, Pisciotta *et al.* [98] have recently identified lipid nanospheres composed of mono-acylglycerols as well as smaller amounts of di-acylglycerols together with some polar lipids which surround the haemozoin crystals in *Plasmodium falciparum*. They have suggested that the lipid nanosphere inside the food vacuole provide a non-polar environment for efficient haemozoin crystallisation and protects Fe(III)PPIX from peroxide degradation.

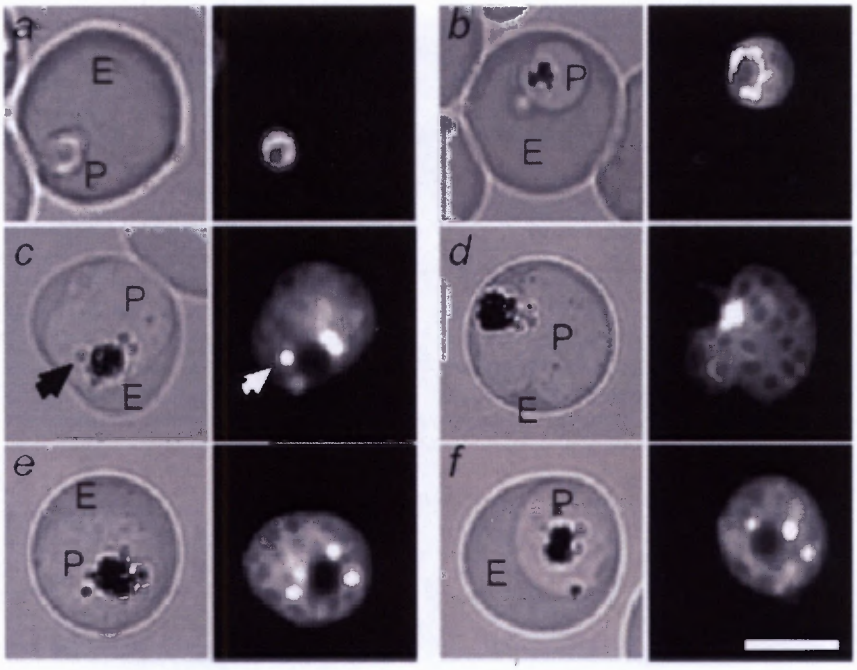

FIGURE 1.15. Nile Red labelling of *P. falciparum* infected red blood cells. Bright field (left) and fluorescence images (right) of red blood cells infected with (**a**) ring, (**b**) young trophozoite and (**c** — **f**) mature trophozoite and schizoint-stage parasites. P denotes parasite and E denotes the red blood cell. The white and black arrows indicate the fluorescence spots showing the lipid bodies. The 3D7 strain was maintained in culture in the presence of Nile Red at a final concentration of 1 μg/ml. The images were collected with an epifluorescence microscope using a rhodamine filter set. The scale bar is 5 μm [97]. Reproduced with permission from the authors.

TEM micrographs of sucrose-purified haemozoin (SPHz) isolated from *Plasmodium falciparum* (**Fig 1.16** (**a**) and **Fig 1.16** (**b**)) shows a lipid nanosphere surrounding a cluster of haemozoin crystals. The SPHz crystals fixed with Malachite Green (**Fig 1.16** (**c**) — (**e**)) exhibit a film-like material around the haemozoin in contrast with samples first processed with ethanol or SDS subsequently with and without Melachite Green (**Fig 1.16** (**f**) and **Fig 1.16** (**g**)), respectively). Processing of samples using either ethanol or SDS therefore removes any evidence of lipid nanospheres associated with haemozoin [98], explaining why they have never previously been observed.

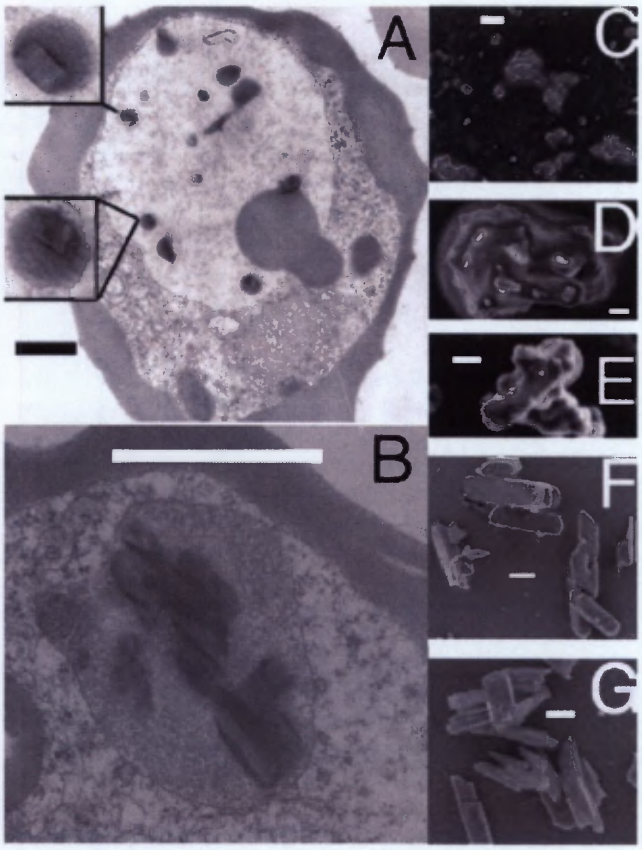

FIGURE 1.16. TEM of (**a**) early trophozoite stage and (**b**) mature trophozoite showing haemozoin crystals surrounded by lipid nanospheres. The insert in (**a**) shows the lack of bilayer membrane at the periphery of the lipid nanosphere. (**c** — **e**) SEM of SPHz fixed in the presence of Malachite Green showing a film-like material around haemozoin. (**f**) SEM of customarily processed haemozoin. (**g**) SEM of customarily processed haemozoin in the presence of Malachite Green. (**f**) and (**g**) shows no evidence of lipid nanospheres. Scale bar = 1 μm (**a** and **b**) and 100 nm (**c** — **g**) [98]. Reproduced with permission from the authors.

Gel electrophoresis (**Fig 1.17** (**a**)) demonstrated that SPHz contains almost no detectable proteins. This observation was confirmed by western blot which shows that this fraction contains no significant amount of histidine-rich protein, chloroquine resistance transporter (CRT) or aldose, all known parasite proteins (**Fig 1.17** (**b**)). Significant amounts of monoacylglycerols were observed from thin layer chromatography (TLC) analysis (**Fig 1.17** (**c**)) in both enriched food vacuoles and SPHz, with lesser amounts of di- and tri-acyglycerols in SPHz compared to

trophozoites and enriched food vacuoles. Analysis of these lipids by ESI-MS (electrospray ionisation mass spectrometry) reveals that they contain mainly palmitic and stearic acid esters. The palmitic derivative was found to be most active in β-haematin formation *in vitro*.

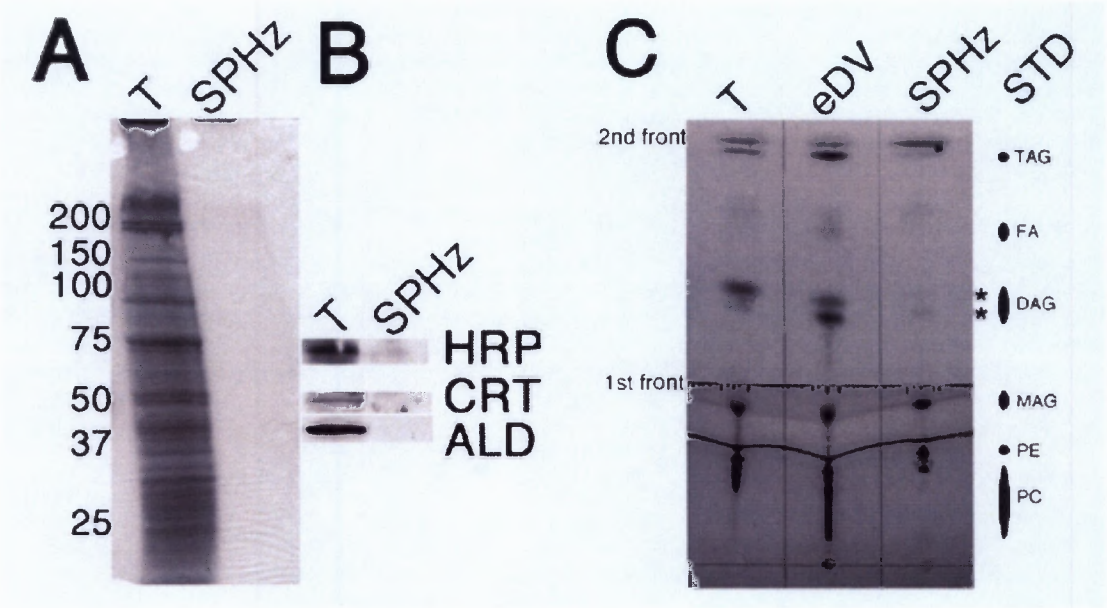

FIGURE 1.17. Gel electrophoresis of (**a**) saponin-purified trophozoites (T) and SPHz stained by Coomassie Brilliant Blue. (**b**) Western-blot analysis of the food vacuole membrane protein PfCRT, cytosolic Pfaldolase (ALD) and PfHRP II with molecular masses of 48, 40 and 30 kDa, respectively. PfHRP II runs as a dimer at 60 kDa. (**c**) TLC of saponin-purified trophozoites (T), enriched digestive vacuoles (eDV) and SPHz. Lipid standards (STD) are: PC, phosphotidylcholine; PE, phosphotidylethanolamine; MAG, monoacyglycerol; DAG, diacyglycerol; FA, non-esterified fatty acid; TAG, triacylglycerol [98]. Reproduced with permission from the authors.

Oliveira *et .al.* [60] have also shown that haemozoin formation in *S. mansoni* and *R. prolixus* is associated with lipid droplets and perimicrovillar membranes, respectively (**Fig 1.18**). These studies indicate that lipids play an important role in haemozoin formation in general.

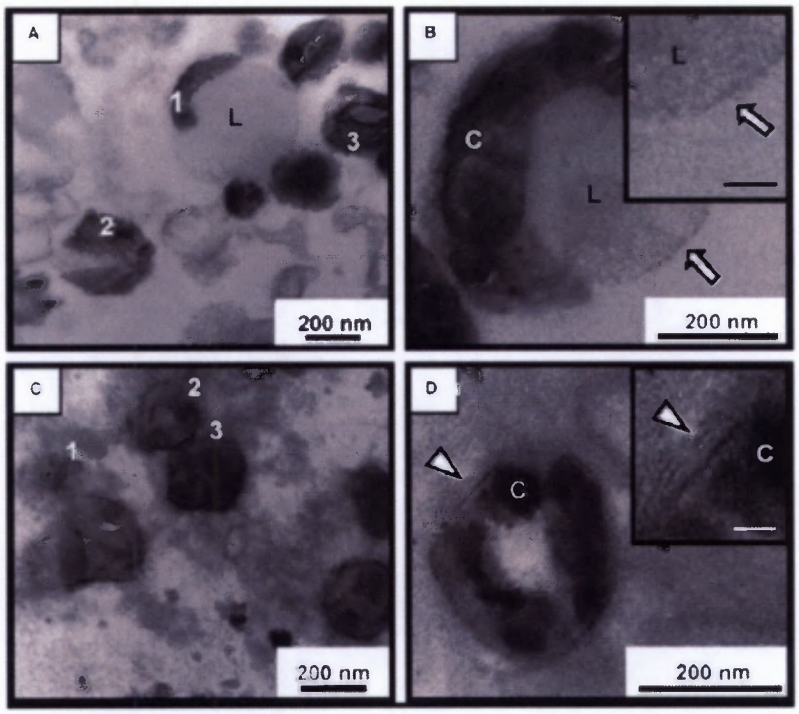

FIGURE 1.18. Transmission electron micrographs of haemozoin crystals observed in the luminal gut contents of (**a**, **b**) *S. mansoni* and (**c**, **d**) *R. prolixus*. (**a**) and (**c**) show crystalline assembly at different stages of formation: (1) initial, (2) intermediate and (3) final in the gut of *S. mansoni* and *R. prolixus*, respectively. C denotes haemozoin crystal and L denotes lipid droplet-like particle. Arrows in (**b**) indicate the absence of phospholipid double membrane in a lipid droplet-like particle. The arrowheads in (**d**) indicate the presence of a phospholipid double membrane in perimicrovilar membranes. The inserts in (**b**) and (**d**) have a scale bar of 25 nm [60]. Reproduced with permission from the authors.

1.5. MECHANISM OF ACTION OF QUINOLINE ANTIMALARIALS

Drugs used today target different stages of the malaria life cycle, namely gametocytes, the liver stage and the asexual blood stage. It is the asexual blood stage that is associated with symptoms of malaria such as fevers, chills and anaemia. This section will only deal with quinoline antimalarials that target the blood stage.

Quinoline antimalarial drugs have been used in the treatment of malaria for centuries. They are ultimately derived from quinine, which was discovered in 1630 by Peruvian Indians [1]. The drug occurs naturally in the bark of the cinchona tree. Legend claims that the name "cinchona" comes from the Countess of Cinchon who was cured of fever by using the bark of the cinchona tree. The bark was distributed throughout Europe by Catholic Jesuits in 1640, and hence gained the name 'Jesuit's bark' [99]. Quinine was isolated in 1820 from a crude mixture extracted from the bark of the cinchona tree by Pelletier and Caventou and its structure was elucidated in 1908 [1]. The high demand for quinine during the World War I led to the development and production of synthetic quinolines. This led to the synthesis of various antimalarial drugs such as chloroquine, amodiaquine and primaquine by 1944 [100]. Chloroquine turned out to be the most effective and was subsequently used for over 50 years as a drug of choice for treatment of malaria and as a prophylactic. Several hypotheses have been proposed to explain the mechanism of action of these drugs. The proposed mechanisms can be divided into two categories, those positing action outside the food vacuole (extravacuolar) and those inside the food vacuole (intravacuolar). Extravacuolar mechanisms include binding of the drug to DNA, thus inhibiting DNA and RNA synthesis [101]. The major drawback with this hypothesis is that the concentration of chloroquine required is much higher than the IC_{50} with no known mechanism of accumulation in the nucleus [9]. The second hypothesis involves inhibition of protein synthesis [102], however, little evidence is available to support this study [103-105]. Lastly, a study done by Königk *et al.* showed that chloroquine and mefloquine inhibit polyamine metabolism [106], however, the study failed to explain why chloroquine is only active in the blood stage and not in the other stages where the enzyme is present [9]. It is now believed that the activity of chloroquine and other related drugs is more likely to occur inside the food vacuole than outside.

The drugs are weak bases and therefore are expected to accumulate inside the acidic food vacuole through pH trapping [107]. Once inside the food vacuole the drug is protonated both at the quinoline nitrogen and the amino group in the side chain, thus resulting in an increase in drug concentration in the food vacuole because these charged species cannot diffuse back across the vacuolar membrane [108, 109]. Morphological changes such as swelling of the food vacuole [110, 111] and pigment clumping [112, 113] upon drug treatment have been observed. Measurements of radioactivity of isolated food vacuoles treated with [^{3}H] chloroquine [114] further support the idea that the food vacuole is the site of drug action. Hypotheses of intravacuolar drug action include increased vacuolar pH as a result of drug accumulation due to the ability of the drug to act as a weak base [107], inhibition of vacuolar lipase enzymes [115, 116], inhibition of vacuolar proteases [117] and inhibition of haemozoin formation as a result of drug interaction with Fe(III)PPIX. Studies have indicated an increase in pH upon exposure of parasites to chloroquine, however the pH changes by only 0.25 units [16] and furthermore, the theory fails to explain why other weak bases are not active as antimalarials [118]. Inhibition of lipase enzyme and vacuolar proteases require drug concentrations higher than those likely to occur in the food vacuole [9], which could be due to the fact that these enzymes have optimal activity at a pH of 8 [118A].

Consequently, it is now widely accepted that 4-aminoquinoline antimalarials act by inhibiting haemozoin formation and this mechanism will be explored further as it forms the basis on which the present study is based. In this regard, two main hypotheses have been postulated regarding the primary mode of action of quinoline antimalarials: interaction of the drug with Fe(III)PPIX in solution and inhibition of haemozoin growth by attachment to the growing crystal. These hypotheses will be discussed further.

1.5.1. Interaction of Fe(III)PPIX with 4-Aminoquinoline Antimalarials

Studies conducted by Cohen *et al.* [119] showed for the first time that chloroquine forms a complex with Fe(III)PPIX. The studies were based on the change in UV-visible spectrum of CQ at 343 and 329 nm upon complexation with Fe(III)PPIX. This study led to the proposal that Fe(III)PPIX is in fact the target of quinoline antimalarials [120]. Fitch *et al.* [121] suggested that the accumulation of CQ-Fe(III)PPIX inside the parasite may account for its activity against *Plasmodium falciparum*. Macomber *et al.* [112] then proposed that accumulation of CQ in the parasite is due to binding of the drug with Fe(III)PPIX and is required for antimalarial activity. In support of this, Moreau *et al.* [122] later showed that 4-aminoquinolines are localised in the digestive food vacuole of *P. berghei* parasites. This proposal led to investigations of binding affinity and mode of interaction or association of Fe(III)PPIX with quinoline antimalarials. There is substantial evidence that shows that the drug interacts directly with Fe(III)PPIX to inhibit haemozoin formation [123-125], thus preventing its incorporation into haemozoin [126, 127]. These studies provide strong evidence that Fe(III)PPIX may be the target of these drugs. An interesting analogy is provided by Oliveira *et al.* [49] who have shown recently that CQ inhibits haemozoin formation in *R. prolixus* and results in the build up of Fe(III)PPIX in the haemolymph of the insect, which further resulted in increased lipid peroxidation. This provides a model of what may occur in the malaria parasite and thus supports the proposal that Fe(III)PPIX is the target of 4-aminoquinoline antimalarials.

1.5.1.1. Association of 4-Aminoquinolines with Fe(III)PPIX

A number of studies have since been conducted using spectroscopic techniques such as UV-visible, NMR and Mössbauer spectroscopy to study the association of Fe(III)PPIX with quinoline antimalarials [71, 118, 128-136]. The first studies were done using NMR in aqueous solution and showed that the binding occurs through π-π interactions between the quinoline ring of the antimalarial drugs and the porphyrin macrocycle [128, 129, 134, 135]. Most of these studies are qualitative indicating that the interactions between Fe(III)PPIX and quinoline antimalarials do occur. Little work was done on measuring the association constants of these complexes before 1997.

The lack of information on association constants of complexes formed between Fe(III)PPIX and quinolines could be ascribed to the fact that Fe(III)PPIX aggregates in aqueous solutions, thus the results obtained from these studies were difficult to interpret. Fitch and co-workers [120] were the first to conduct such studies for Fe(III)PPIX -CQ interaction using equilibrium dialysis in aqueous medium. Studies have been conducted more recently to measure the strength of association of a range of quinoline antimalarials with Fe(III)PPIX in order to understand the thermodynamics of interactions [123, 137-140] and to gain insight into the strength of these complexes. Dorn *et al.* [123] reported association constants in aqueous solution at pH 6.5 using isothermal titration calorimetry (ITC) for a range of quinoline antimalarials (**Table 1.1**).

TABLE 1.1. Values of association constants between quinoline antimalarials and Fe(III)PPIX

Compound	log *K* (Egan *et al.*)	log *K* (Dorn *et al.*)
Chloroquine	5.52 ± 0.03 (1:1)[a]	5.60 ± 0.20 (1:4)[c]
Amodiaquine	5.39 ± 0.04 (1:1)[a]	4.97 ± 0.10 (1: 4)[c]
Quinacrine	—	5.70 ± 0.04 (1: 4)[c]
Pyronaridine	—	5.48 ± 0.03 (1:7)[c]
Quinine	4.10 ± 0.02 (1:1)[a]	4.32 ± 0.04 (1:5)[c]
Quinidine	5.02 ± 0.03 (1:1)[b]	—
9-epiquinine	4.04 ± 0.03 (1:1)[a]	—
Mefloquine	3.90 ± 0.08 (1:1)[a]	4.08 ± 0.10 (1:3)[d]
Halofantrine	5.29 ± 0.01 (1:1)[b]	4.66 ± 0.07 (1:1)[e]
Ro 48-6910	—	5.79 ± 0.10 (1:19)[c]

[a]Association constants obtained by spectrophotometric titrations in 40% aqueous DMSO at pH 7.5, 25°C [137]. [b]Association constants obtained by spectrophotometric titrations in 40% aqueous DMSO at pH 7.5, 25°C, 30% acetonitrile was included to increase the solubility of the drug [87]. [c]Association constants obtained in aqueous buffer at pH 6.5, 37°C by isothermal calorimetric titration [123]. [d]Association constant was obtained in pure water at pH 6.5 [123]. [e]Association constant was obtained in 80% aqueous ethanol [123]. Stoichiometric values (drug:Fe(III)PPIX) are shown in brackets.

The values obtained by Dorn *et al.* [123] are at least three orders of magnitude smaller than those obtained by Chou *et al.* [120] for chloroquine and exhibit different stoichiometries, which emphasises not only the difficulty of investigating these types of interactions in aqueous medium but also the effects of different methods used to monitor the interactions. Dorn's results were interpreted on an assumption that Fe(III)PPIX exists exclusively as a μ-oxo dimer under these conditions. Efforts have since been made to conduct such experiments using strictly monomeric Fe(III)PPIX. Egan *et al.* [137] have investigated the association constants using spectrophotometric titrations in 40% aqueous DMSO (pH 7.5) in which Fe(III)PPIX exists strictly as a monomer (**Table 1.1**). Egan *et al.* [125, 141] and Vippagunta *et al.* [142] have also conducted similar investigations on a variety of CQ analogues in 40% aqueous DMSO and aqueous medium, respectively.

Despite the difficulties mentioned above, comparison of the association constants obtained by Dorn *et al.* and Egan *et al.* (**Table 1.1**) show a good correlation. The surprising observation is that 9-epiquinine forms a complex with a similar strength to that of quinine, in spite of the fact that 9-epiquinine has been shown not to inhibit β-haematin formation [84]. Therefore, detailed structures of these complexes are required in order to study structural factors that are involved in inhibitory activity. The stoichiometry of the complexes seems to vary between different studies. Chou *et al.* reported stoichiometric values of 1:4 of drug to Fe(III)PPIX for chloroquine. This value is similar to that reported by Moreau *et al.* [129] and Dorn *et al.* [123] and it was proposed that one chloroquine molecule is sandwiched between two Fe(III)PPIX μ-oxo dimers. Higher stoichiometric ratios of 1:7 and 1:19 have also been reported for pyronaridine and the bisquinoline Ro 48-6910, respectively (**Table 1.1**). This suggests that Fe(III)PPIX exists as a mixture of monomers, dimers and higher aggregates in aqueous solution in the presence of these drugs. 1:1 stoichiometric ratios were obtained by Egan *et al.* in 40% aqueous DMSO (**Table 1.1**). These studies indicate the importance of solvent and pH on stoichiometry of the complexes which is related to the nature of the Fe(III)PPIX species present under different experimental conditions.

Enthalpies and entropies of association have also been reported in both aqueous medium and 40% aqueous DMSO to gain insight into the nature of the complexes under both sets of conditions [87, 123, 137, 139]. Despite the similarities in association constants in both these systems, their entropies and enthalpies are different. However, a strong thermodynamic compensation effect in both (**Fig 1.19**) is observed and is remarkably similar. These plots were used to obtain an indication of the degree of desolvation and loss of flexibility in these systems. The slopes (α) and intercepts ($T\Delta S_0$) of both plots for the data obtained in 40% aqueous DMSO (**Fig 1.19** (**a**)) and aqueous solution (**Fig 1.19** (**b**)) are identical within experimental error (α = 1.1 ± 0.1 and α = 1.0 ± 0.1 and $T\Delta S_0$ = 29 ±2 kJ mol^{-1} and $T\Delta S_0$ = 29 ± 5 kJ mol^{-1}, respectively).

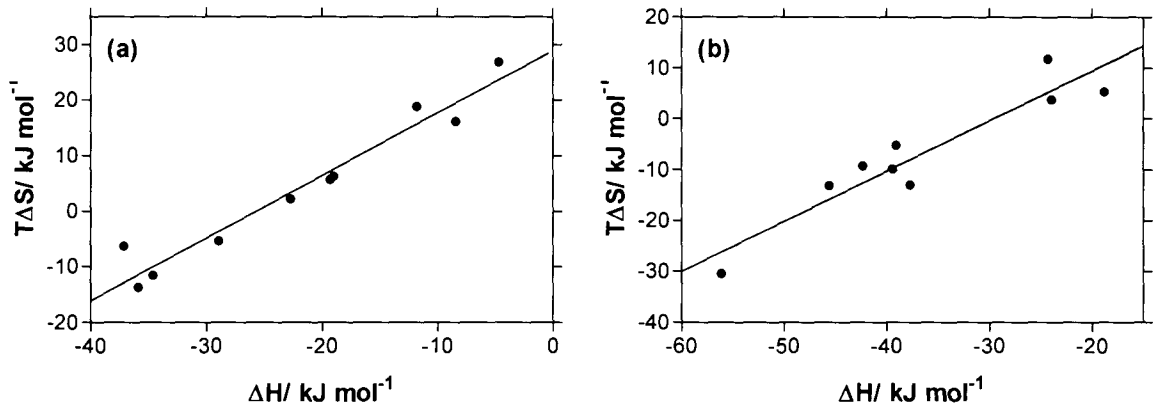

FIGURE 1.19. Thermodynamic compensation plots for the association of quinoline antimalarials with Fe(III)PPIX in (**a**) 40% aqueous DMSO, pH 7.5 (0.02 M HEPES), 25°C [87, 137, 139] and (**b**) aqueous solution, pH 6.5 (0.25 M phosphate), 37°C [123]. Reproduced with permission from the authors.

Based on the hypothesis of Inoue and Wada [143], the large value of α indicates a large loss of flexibility and the high value of $T\Delta S_0$ indicates a high degree of desolvation upon complexation. The similarity of the thermodynamic compensation plots indicates that the interactions between Fe(III)PPIX and quinoline antimalarials are similar in both aqueous solution and 40% aqueous DMSO. The large degree of desolvation indicates that the water plays a major role in these types of interactions,

possibly in locking the conformers of the complexes. A study conducted by Egan *et al.* [139] confirmed the role of the solvent, showing that the strength of the complexes increased greatly with increasing solvent polarity. Weaker free energies of associations were observed in mixed aqueous solutions than in pure organic solvents, which was interpreted as being indicative of stronger electrostatic interactions in purely non-aqueous solutions.

1.5.1.2. Structures of Complexes formed between Fe(III)PPIX and 4-Aminoquinolines

Crystal structures of complexes formed between Fe(III)PPIX and 4-aminoquinolines are not yet available. Knowledge of structures of these complexes has therefore been obtained from NMR and computational studies. The first attempt to elucidate structures of these complexes was made by Moreau *et al.* [128, 129] using ^{1}H NMR. The investigations were carried out by monitoring the shifts in ^{1}H NMR spectra of chloroquine (CQ) and quinine (QN) upon complexation with either Fe(III)PPIX or uroporphyrin I due to paramagnetic effects of the Fe(III) centre and porphyrin ring currents respectively. The experiments were carried out by titrating the quinoline solutions with Fe(III)PPIX or uroporphyrin I (0 — 5% and 0 — 1.6% respectively). Structures of these complexes were then proposed based on mathematical calculations using a porphyrin ring current model developed by Abraham *et al.* [144]. The model strongly suggested a cofacial arrangement, commonly referred to as a π-π interaction, where a molecule of the drug is stacked between the Fe(III)PPIX μ-oxo dimers, with the quinoline nucleus situated above the porphyrin ring and not towards the periphery as observed in the interactions of porphyrins and various aromatic compounds carried out in organic solvents [145, 146]. The chlorine atom of CQ and the methoxy group of QN as well as their side chains were proposed to be orientated away from the porphyrin core (**Fig 1.20**). The model did not show any evidence of coordination between the Fe centre and the quinoline nitrogen as the metal free uropophyrin I also forms complexes with CQ and QN with association strength similar to that of the complexes formed with Fe(III)PPIX. Furthermore, the protons on or

adjacent to the quinoline nitrogens did not experience large shifts, thus confirming the lack of coordination between the quinoline nitrogen and the Fe centre.

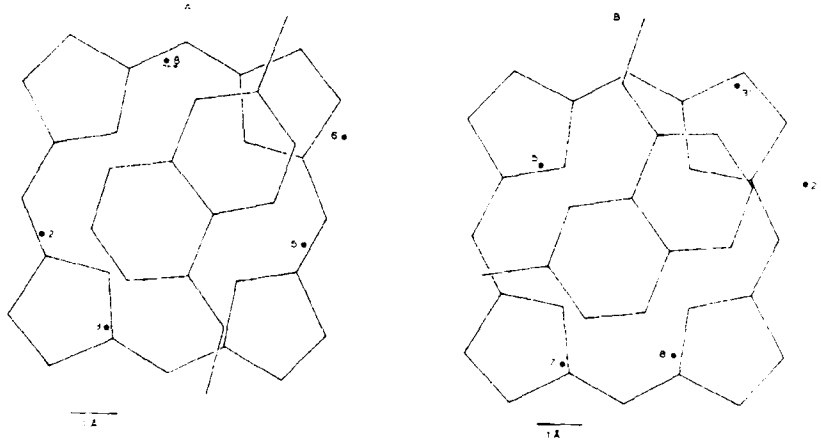

FIGURE 1.20. Predicted structural models of the complexes formed with (**a**) chloroquine and (**b**) quinine and the porphyrin core of uroporphyrin I [129]. Reproduced with permission from the authors.

Constantinidis and Satterlee [134, 135] undertook similar studies using ^{13}C NMR to determine the interactions of CQ and QN with both uroporphyrin I and urohemin I in aqueous solutions. The structures obtained from these studies also indicated a cofacial arrangement of the quinoline rings and the porphyrin rings, with additional coordination between the Fe(III) centre of urohaemin I and the hydroxyl group at 9-position of QN [135]. This coordination is however absent in CQ complexes [134]. Studies done by Marques *et al.* [138] seem to support coordination of the 9-hydroxy group to the metallophorphyrin as observed from a blue shift in the charge transfer band of the haem-octapeptide *N*-acetylmicroperoxidase-8 (NAcMP8) titrated with quinine or 9-epiquinine. However, subsequent studies conducted by Egan *et al.* [137] showed similar changes in the spectrum of Fe(III)PPIX titrated with CQ which lacks a hydroxyl group in 40% aqueous DMSO. Further studies are therefore necessary to investigate whether the hydroxyl group in quinoline methanols such as QN coordinate to the Fe(III) centre.

Computational studies of these complexes have been performed using molecular mechanics and molecular dynamics techniques [138, 147, 148] and docking [149]. Marques *et al.* [138] performed molecular dynamics and simulated annealing (MD/SA) calculations in vacuo to model the interactions between quinine, 9-epiquinine and CQ with NAcMP8 (**Fig 1.21**) instead of Fe(III)PPIX. NAcMP8, unlike Fe(III)PPIX remains monomeric in aqueous solution at moderate ionic strength and concentrations, thus making titration studies much easier to interpret. Quenched dynamics and simulated annealing (QD/SA) techniques were then used to identify the flexible portions of model complex structures. The complex structures showed that coordination of the 9-hydroxyl group for both QN and 9-epiquinine to the Fe centre is possible as indicated by Constantinidis and Satterlee [135], with the quinoline rings parallel to the porphyrin ring. The benzene ring of the quinoline nucleus was found to lie over the meso carbons of the porphyrin, while the pryridine ring lies over the pyrrole β-carbons. The quinuclidine ring was found to orientate upwards and away from the porphyrin ring. The complex structures of quinine and 9-epiquinine were similar, which would seem to suggest that the drugs should have similar abilities to inhibit β-haematin formation.

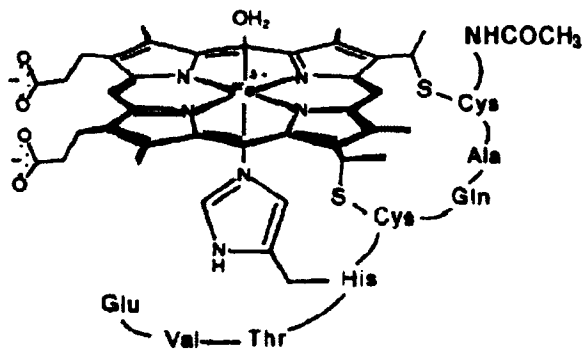

FIGURE 1.21. The chemical structure of haem-octapeptide N-acetylmicroproxidase-8 [138]. Reproduced with permission from the authors.

These results are inconsistent with the fact that 9-epiquinine does not in fact inhibit β-haematin formation [84] or indeed bind to Fe(III)PPIX in benzene [118] in contrast to QN. The CQ complex structures also indicated cofacial interactions with the quinoline

and the porphyrin rings parallel to each other, and the side chain of the quinoline orientated away from the porphyrin. The weakness of this study is that the calculations were performed in the absence of solvent, which has been experimentally shown to play a critical role in the interactions as described above [139]. Further studies of the complexes between Fe(III)PPIX with amodiaquine, chloroquine and tebuquine performed by O'Neill *et al.* [109] also indicated cofacial interactions with hydrogen bonding between the negatively charged propionate groups of the porphyrin and the positively charged protonated terminal amino groups of the drugs.

Leed *et al.* have recently studied the structures of these complexes in aqueous solution using NMR and molecular mechanics [147, 148]. The ^{1}H-Fe(III) distances between the putative Fe(III)PPIX μ-oxo dimer and antimalarial drug were obtained from NMR T_1 measurements obtained by inversion recovery methods using the Solomon-Bloembergen equation. These distances were then used as distance constraints in molecular dynamics calculations to deduce complex structures. Both studies support previous work that indicates Fe(III)PPIX interacts with 4-aminoquinoline antimalarial drugs through π-π interactions of one face of a putative μ-oxo dimer with the drug. The structures suggest that the quinoline ring lies over the porphyrin with the quinoline nitrogen orientated towards the periphery of the porphyrin, while the 4-amino group is located closer to the Fe(III) centre (**Fig 1.22**). Furthermore, the side chain was shown to orientate towards the porphyrin rim, suggesting strong interactions with the Fe(III)PPIX molecule. According to this model, the aliphatic side chains orient themselves into a conformation that maximises the van der Waals interactions with the porphyrin ring thus suggesting that changing the side chain by lengthening or shortening it will alter the stability of the complexes. The structures also indicate that the complexes are dynamic and that the quinoline ring is significantly tilted in most cases. The proposed structures do not include coordination of the 9-hydroxyl group for either quinine or quinidine to the Fe(III) centre. Hydrogen bonding between the propionate group and the protonated terminal amino groups of the drugs are also not present. However, in some respects these proposed structures

do not seem to accord with experimental evidence. Most notable, De *et al.* [150] have shown that CQ analogues with varying length of side chain show equal activity against CQ resistant strains, thus suggesting that interactions of the side chain with Fe(III)PPIX are not critical in complex formation. This has largely been confirmed by studies on the association constants of short-chain analogues with Fe(III)PPIX [125].

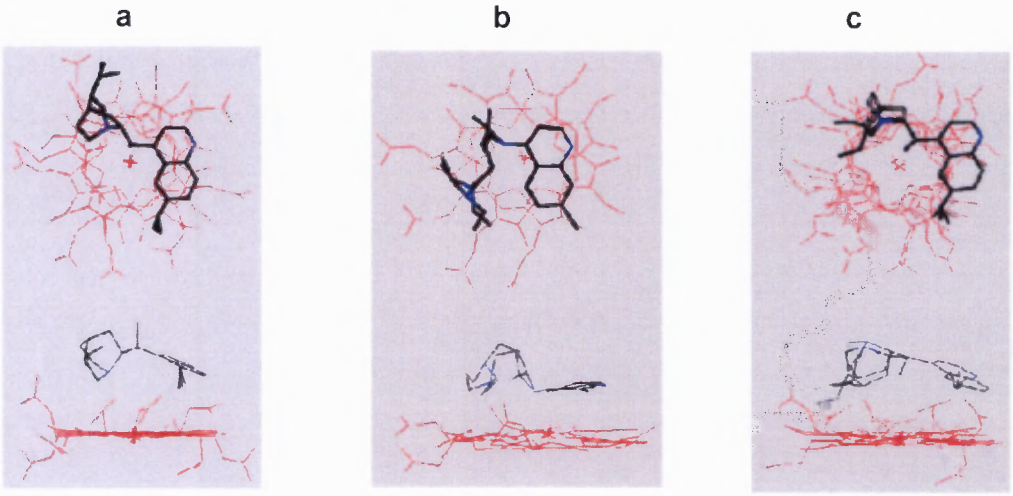

FIGURE 1.22. Axial (top) and side (bottom) views of superimposed lowest-energy structures of the complexes between the Fe(III)PPIX μ-*oxo*-dimer and the diprotic forms of (**a**) quinine, (**b**) chloroquine and (**c**) quinidine. Nitrogen atoms are shown in blue and Fe(III)PPIX is shown in red. All protons and the second Fe(III)PPIX of the μ-*oxo*-dimer have been omitted for clarity [147]. Reproduced with permission from the authors.

Roepe and co-workers [151] also performed solid-state NMR measurements on the CQ-Fe(III)PPIX aggregate formed in an aqueous solution. They observed chemical shifts in both ^{13}C and ^{15}N spectra, which suggested coordination of the quinoline N to the Fe(III) centre. Dascombe *et al.* [152] have provided support for this using ESI-MS. However, ESI-MS experiments led them to conclude that Fe(III)PPIX does not exists as a μ-oxo dimer in solution, but rather as a haematin monomer. In addition, computational work on the interaction of the bis-quinoline metaquine with Fe(III)PPIX showed that the drug hydrogen-bonds to the axial hydroxyl group of haematin in some of the structures obtained from docking interactions.

Quantum mechanical studies have also been attempted to gain insight into these interactions [142, 149, 152, 153]. Vippagunta *et al.* [142] performed *ab initio* calculations to describe the electrostatic potential surface of the quinoline compounds and the putative Fe(III)PPIX μ-oxo dimer in order to understand the structural aspects of the quinioline-Fe(III)PPIX μ-oxo dimer complexes and to understand the lack of interactions between Fe(III)PPIX μ-oxo dimer with CQ and some CQ-analogues. The three-dimensional electrostatic potential surfaces of CQ and CQ analogues with chlorine at the 7-position were identical. The presence of the chlorine atom at 7-position is critical as shown by a decrease in electrostatic potential surface when this atom is replaced with a hydrogen atom. Furthermore, the 6-chloro analogue showed a substantial gap in electrostatic potential surface at the N1-C8 edge of the quinoline ring, a region which appears to be critical for binding with Fe(III)PPIX. The electrostatic potential of the Fe(III)PPIX μ-oxo dimer indicates an electron rich region around the porphyrin ring and an electron deficient region around the Fe(III) core. These observations therefore suggest that the interactions are driven by attractive electrostatic interactions between the quinoline ring and the porphyrin ring of the Fe(III)PPIX μ-oxo dimer. This study has been supported by Portela *et al.* [149] using molecular docking and density functional theory [153]. They propose that the electron rich quinoline ring containing the N and C8 atoms interacts with the electron poor region of the Fe(III) core, while the electron poor region containing the 4-amino group interacts with the electron rich region of the porphyrin ring. The conclusions arrived at from these studies are that the β-inhibitory inhibitory activities of the quinoline antimalarials are based mainly on electronic effects rather than steric effects. One flaw with these models is that studies were performed using neutral quinolines which are likely to exist in much smaller fractions under the acidic conditions encountered in the food vacuole.

1.5.1.3. Structure Activity Relationships of 4-Aminoquinolines

It is still not possible as yet to deduce the general structural features of compounds that are required for interaction with Fe(III)PPIX and haemozoin inhibition due to limited evidence available so far. However, there is compelling evidence as discussed above that CQ binds to Fe(III)PPIX in the food vacuole to prevent haemozoin formation and that the interactions are mostly due to electronic and hydrophobic effects *via* π-π interactions. Attempts have been made to establish structural features of 4-aminoquinoline antimalarials that contribute to their ability to associate with Fe(III)PPIX, to inhibit β-haematin formation and to inhibit parasite growth using empirical structure activity studies. Complex formation between Fe(III)PPIX and aminoquinolines seems to depend on the quinoline nucleus required for π-π interactions with the porphyrin ring. Both 2- and 4-aminoquinolines have the ability to form strong complexes with Fe(III)PPIX, while quinoline itself and 3-, 5-, 6- and 8-aminoquinoline form only very weak complexes [125]. This is believed to occur either as a result of increased electron density in the pryridine ring, resulting in enhanced π-π interactions with the positively charged metal centre of the porphyrin ring as discussed above, or as a result of cation-π interactions resulting from protonation of the quinoline. Attachment of the chlorine (Cl) atom at the 7-position of the quinoline ring or the alkyl side chain on the 2- or 4-aminoquinoline nucleus has little effect on the strength of interaction [125, 142]. However, moving the Cl atom from the 7-position to the 6-position of the 4-aminoquinoline nucleus results in no association [142]. On the other hand, the group at the 7-position is required for β-haematin inhibitory activity. Replacement of the Cl atom at the 7-position with Br, I, NO_2 or CF_3 groups results in compounds able to inhibit β-haematin formation fairly strongly, however, introduction of F, NH_2, OCH_3 or OH groups at this position results in a decrease or abolition of activity [125, 142, 154]. A basic amino group at the terminal position of the side chain was shown to be essential for *in vitro* antimalarial activity [125, 142]. The basic nature of the terminal amino group is expected to increase drug accumulation in the food vacuole through pH trapping [107].

Egan *et al.* [125] have thus proposed a number of structural features of the aminoquinoline to better understand the relationship between the structure of these compounds and their ability associate with Fe(III)PPIX and to inhibit haemozoin formation based on these observations (**Fig 1.23**). Quantitative structure activity relationship (QSAR) studies have shown that there is a direct correlation between in vitro antimalarial activity normalised for pH trapping and β-haematin inhibition [125]. Vippagunta *et al.* [142] and Hawley *et al.* [155] have also shown that there is a significant correlation between inhibition of β-haematin formation and inhibition of parasite growth, thus providing further evidence that 4-aminoquinoline antimalarials act by inhibiting haemozoin formation in the parasite

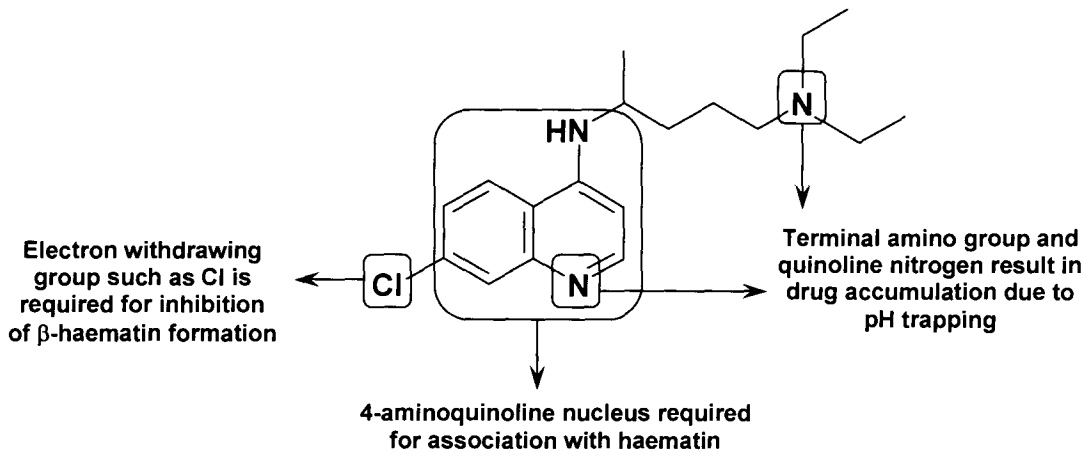

FIGURE 1.23. Proposed structure-activity relationship for CQ [125]. Reproduced with permission from the authors.

1.5.2. Interaction of 4-Aminoquinoline Drugs with Haemozoin

Several studies have proposed that the drugs may interact with haemozoin itself, thus preventing its further growth. Studies by Sullivan *et al.* [126] have provided direct evidence using autoradiographic electron micrographs that show that chloroquine is associated with haemozoin in the food vacuole (**Fig 1.24** (**a**)). Their findings seemed to suggest that a quinoline-Fe(III)PPIX complex incorporates into the growing haemozoin, thus terminating (capping) crystal extension. A model shown in **Fig 1.24** (**b**) was proposed to explain how the drug would inhibit haemozoin formation. At the time, haemozoin was believed to be a polymer. The authors

suggested that the quinoline drugs first bind to Fe(III)PPIX and then the drug-Fe(III)PPIX complex attaches itself to the elongation site of haemozoin polymer thus terminating chain extension which would result in accumulation of toxic Fe(III)PPIX in the food vacuole. The proposal can readily be reinterpreted in terms of inhibition of crystal growth. This study thus suggests that haemozoin itself might be the target.

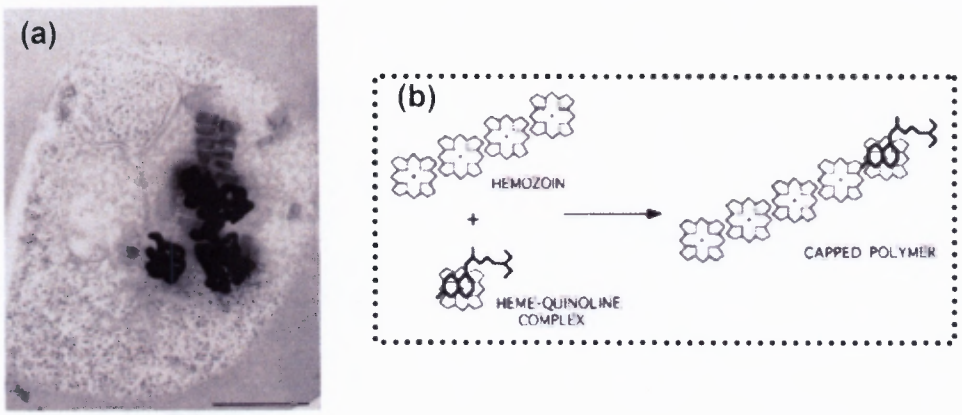

FIGURE 1.24. (**a**) Transmission electron micrograph of *Plasmodium falciparum* (HB3) treated with [^{3}H] chloroquine, showing [^{3}H] chloroquine (black patches) located over the haemozoin crystals situated in the food vacuole (Bar = 0.5 μm). (**b**) Proposed model of inhibition of haemozoin formation by quinoline antimalarials [126]. Reproduced with permission from the authors.

Pagola *et al.* [73] proposed that the drug interacts with the fastest growing face of the crystal, thus inhibiting haemozoin formation. This proposal came about when they observed that crystal structure of haemozoin is a dimer with hydrogen bonding between the dimers [73], and not a polymer as suggested before by Slater *et al.* [74]. Leiserowitz and co-workers [156] further investigated this proposal using computer models (**Fig 1.25**). They were able to model the morphology of the crystal and identify the fastest growing face based on the structure reported by Pagola *et al.* [73] (**Fig 1.25** (**a**)). The computed crystal appears to be similar in both shape and form to the crystal from *Plasmodium falciparum* (**Fig 1.25** (**b**)). Manual docking of chloroquine with the fastest growing corrugated face (**Fig 1.25** (**c**)) shows that the drug can intercalate between the iron porphyrin groups, covering the surface and

thus retarding crystal growth. **Fig 1.25** (**d**) shows the chloroquine functional groups that form strong interactions with haemozoin (interacting with the vinyl, methyl and ionised propionate groups of the porphyrin molecules) and are proposed to be essential for inhibition of haemozoin formation. One possible drawback with the model is that the quinoline nitrogen of the drug has to be unprotonated, which is unlikely under acidic conditions of the food vacuole. On the other, it may be possible in that the porphyrin groups interacting with the drug suppress the pK_a of the quinoline nitrogen as the drug approaches the crystal surface. Furthermore, the model does account for the different groups of the quinoline drug that are essential for inhibition of haemozoin formation (Section 1.5.1). Currently, the question of whether drugs inhibit haemozoin formation via interactions in solution, with the crystal surface of haemozoin or both remains unanswered.

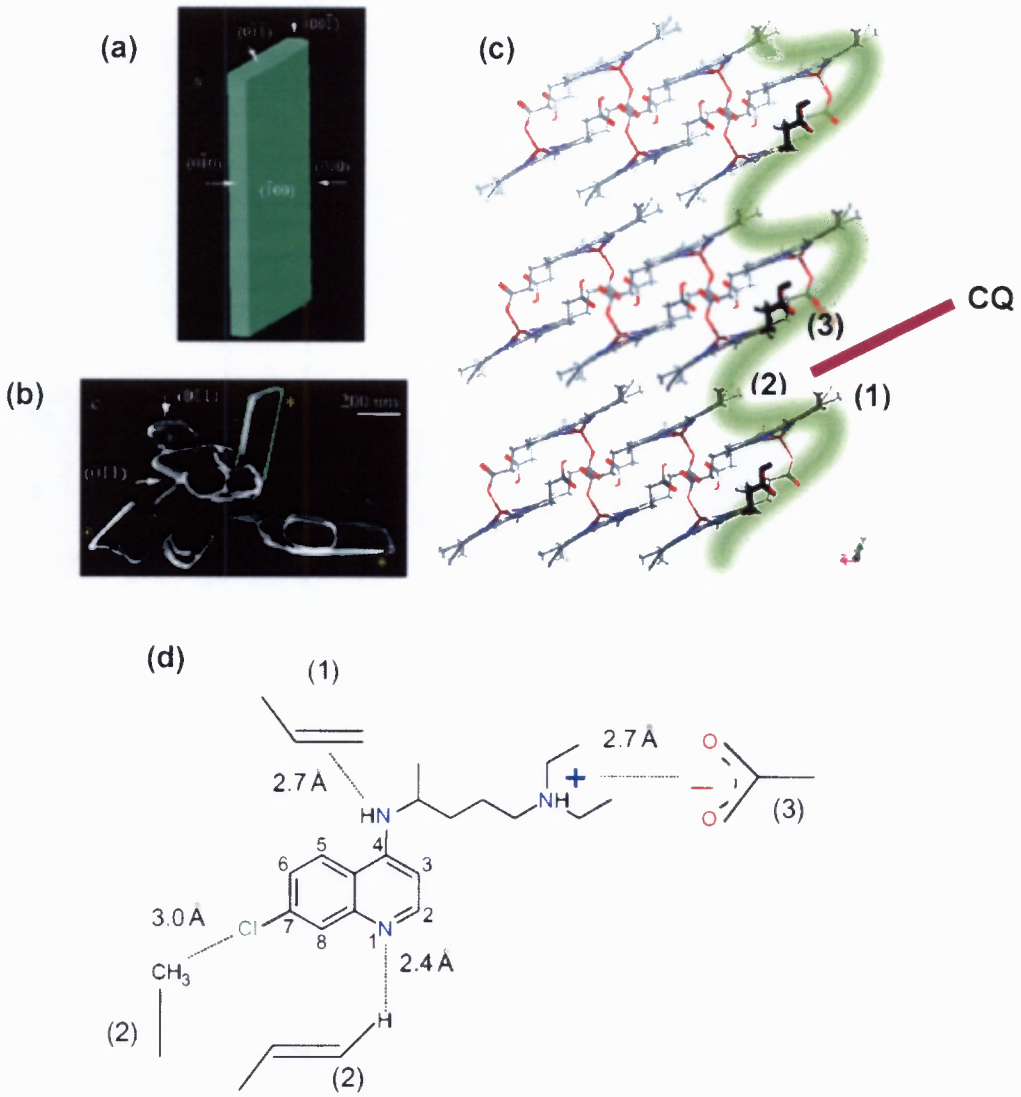

FIGURE 1.25. (**a**) Morphology of the computed crystal structure of haemozoin [156], (**b**) haemozoin crystals from *Plasmodium falciparum* [51], (**c**) Schematic representation of the corrugated surface (green) of the crystal into which CQ intercalates, interacting with three porphyrin groups (numbers 1 to 3) [156] and (**d**) proposed interactions between CQ and haemozoin. The 4-amino group interacts with the vinyl group of porphyrin (1), the Cl of the quinoline ring interacts with the methyl group of porphyrin (2), the quinoline N atom interacts with the vinyl group of porphyrin (2) and the positively charged terminal amino group interacts with the negatively charged propionate group, forming a salt bridge with porphyrin (3) [156]. Reproduced with permission from the authors.

1.6. DRUG RESISTANCE MECHANISMS

Drug resistance is not a focus of this work. Nonetheless, it is an issue of major importance in any discussion of quinoline antimalarials. Consequently, a short overview of the topic is given here. Several reviews cover this topic in more detail [157-160].

Resistance to CQ is attributed mainly to a decrease in drug accumulation in the parasitised red cell, probably arising from decreased accumulation in the food vacuole [161-163]. The mechanism that causes a decrease in CQ accumulation is however not clear. Several hypotheses have been proposed. Earlier research suggested that chloroquine resistance was associated with an increased drug efflux from the food vacuole [161]. Subsequent studies by Bray *et al.* [164] and Martiney *et al.* [165] could not distinguish between the efflux rates of CQ sensitive and resistant strains. It has also been proposed that CQ resistance is associated with reduced drug accumulation [166] and not drug efflux, or that resistance of malaria parasites to CQ might be related to the pH of the food vacuole [107]. As stated earlier, CQ is a diprotic weak base that accumulates in the food vacuole through pH trapping. Therefore a slight change in pH would affect its accumulation in the food vacuole.

Studies performed by Geary *et al.* [15] and Ginsburg and Stein [167] have reported that reduction of CQ accumulation results from an increase in pH in the food vacuole. These observations were further supported by Bray *et al.* [168]. Studies performed by Roepe and co-workers [21, 22] however, have claimed that CQ resistant parasites have a more acidic food vacuole than CQ sensitive parasites using acridine orange. Acridine orange is a weak base predicted to accumulate in the acidic food vacuole through pH trapping and measurements of the pH rely on the fluorescence intensity arising from the acridine orange. They suggested that a more acidic pH in CQ resistant parasites would accelerate the rate of Fe(III)PPIX aggregation and thus reduce its concentration, which would result in decreased availability to interact with CQ [169]. However, other studies indicate that the quantity of Fe(III)PPIX receptor is

unchanged in CQ resistant parasites [108, 166, 170], but that its apparent affinity for chloroquine is reduced. Two independent studies have later shown that fluorescence from acridine orange monomer is quenched in the food vacuole and that the observed fluorescence is in fact localised in the parasite cytosol [23, 24]. Roepe and co-workers [20] have subsequently repeated their studies using a dextran-tagged pH probe. These studies further seemed to confirm that CQ resistant lines exhibit a more acidic pH than CQ sensitive lines. However, other studies have failed to support these observations and they have concluded that the pH of the digestive food vacuole does not play any role in CQ resistance [14, 16].

Other researchers have argued that CQ resistance results from an impaired Na^+/H^+ exchanger (NHE) [166, 171]. It was suggested that CQ is transported into the parasite by NHE leading to accumulation in the parasite food vacuole. This theory is based on the ability of amiloride, an inhibitor of Na^+/H^+ exchange, to inhibit CQ uptake. This hypothesis was challenged by Bray *et al* [108, 172] who showed that the reduction of CQ uptake is due to the fact that amiloride and its derivatives compete with CQ for Fe(III)PPIX. This hypothesis has since been discarded as the mechanism of quinoline drug resistance. Bray *et al.* [108] have proposed that CQ resistance is associated with access of chloroquine to Fe(III)PPIX. These studies have shown that there is a decrease in CQ accumulation in the absence of Fe(III)PPIX and that drug accumulates due to its association with Fe(III)PPIX and not only due to pH trapping. This association is reduced in resistant parasites. However, verapamil and related compounds which are able to reverse CQ resistance, increase the apparent affinity of CQ for Fe(III)PPIX in CQ resistant parasites [173], presumably by restoring access of the drug to Fe(III)PPIX.

Genetic studies originally led to the hypothesis that CQ resistance is similar to multi-drug resistance (MDR) in mammalian cancer cells. *mdr* genes which encode P-glycoproteins (Pgp) are involved in membrane transport and are inhibited by verapamil [173]. Early studies investigated the role of the *pfmdr1* gene located on chromosome 5 of *P. falciparum* that encodes P-glycoprotein 1 (Pgh1) [174].

Overexpression or amplification of the *pfmdr1* gene was proposed to be the cause of CQ resistance, allowing CQ to be pumped from the parasite food vacuole [175]. Specific alleles were suggested to be involved in CQ resistance from isolates of *Plasmodium falciparum* [176]. In particular, point mutations at position 86 were linked to CQ resistance in a number of isolates [176, 177]. A genetic cross study of CQ-resistant (Dd2) and CQ-sensitive (HB3) clones of *Plasmodium falciparum* however showed no link between CQ resistance and *pfmdr1* or their amplification, indicating that these genes are not associated with CQ resistance [178]. A polymorphic gene denoted *cg2* located on chromosome 7 was later proposed to be responsible for CQ resistance [179, 180]. Subsequently, it has been shown that the gene *pfcrt*, located close to the *cg2* and not *cg2* is a convincing candidate [181]. Evidence from transfection studies [179, 181, 182] strongly suggests that CQ resistance in *Plasmodium falciparum* is linked mainly to mutations of *pfcrt* exchanging lysine for threonine at position 76 (K76T). *pfcrt* encodes a 424 amino acid protein, PfCRT (*Plasmodiun falciparum* Chloroquine Resistance Transporter) located in the vacuolar membrane and is believed to be either a channel or a transporter [181, 183]. Other studies have shown that K76T mutation is accompanied by other specific mutations in the same protein in different geographical regions [184]. It is now widely accepted that resistance in *Plasmodium falciparum* to CQ is caused primarily by mutations in the *pfcrt* gene and that CQ resistant parasites accumulate less CQ than sensitive parasites. The mechanisms by which mutated *pfcrt* results in CQ resistance are still a subject of intense investigation. However, several hypotheses have been proposed to understand how these mutations result in CQ resistance in malaria parasites and these include changes in vacuolar pH and changes in CQ flux [181]. Reeves *et al.* [185] have suggested that mutations of *pfcrt* modulate the pH of the parasite food vacuole thus affecting CQ availability. However, this proposal has been strongly challenged by a number of studies [14]. The second model suggests that CQ resistance is associated with an energy-dependent CQ efflux system [186]. The most recent theory suggests a 'charged drug leak' hypothesis [159, 187]. The K76T mutations are associated with a loss of a basic positively charged residue in the transmembrane region, thus providing a route for the protonated CQ to passively

leak from the food vacuole down an electrochemical gradient [159, 187, 188]. This would result in a decrease in the overall concentration of CQ in the food vacuole and hence a decrease in CQ sensitivity. The model suggests that *pfcrt* is directly involved in moving CQ out of the food vacuole [189]. Furthermore, the model is inconsistent with the efflux or active carrier models which are energy dependent.

Mutations in *pfcrt* have been shown to be involved in the mechanism of CQ resistance reversal induced by verapamil [181, 190]. These observations suggest that verapamil competes with protonated CQ for binding to *pfcrt*, thus enhancing accumulation of CQ in CQ resistant isolates [189]. A combination of CQ and two or three of the CQ resistance reversers has been shown to result in pharmacological activities against CQ resistant parasites similar to those effective against CQ sensitive parasites [191]. Many of these agents have similar structural features to that of CQ, such as a hydrophobic heterocyclic ring system and an alkyl side chain with a terminal amine [192]. These agents can therefore bind to *pfcrt* because of their lipophilic character, thus blocking the passage of CQ.

Irrespective of the mechanism of CQ resistance, it is important to note that quinolines such as amodiaquine and quanacrine [188, 193, 194] and CQ analogues with shortened and elongated side chains [150, 195, 196] show enhanced activity relative to CQ against CQ resistant strains. A significant correlation between the hydrophobicity of a range of quinolines and their relative activities against CQ resistant parasites has been observed [193, 197], suggesting that more lipophillic quinolines tend to avoid leakage from the food vacuole compared to their hydrophilic counterparts. Biot *et al.* [198] and Chibale *et al.* [199] have shown that the introduction of a ferrocene group on the side chain also enhances activity against the CQ resistant parasites. These observations are of considerate importance, as they demonstrate that resistance does not arise from changes in the drug target. Thus haemozoin inhibition remains an important target for new antimalarials.

1.7. AIMS AND OBJECTIVES

The aims of the study were to gain a mechanistic understanding of the process of β-haematin formation relevant to its biogenesis *in vivo*, to determine the effects of chloroquine treatment on iron distribution in the malaria parasite and to gain a deeper understanding of the relationship between the structure of Fe(III)PPIX-quinoline complexes and their ability to inhibit β-haematin formation.

Specific objectives were:

a) To develop an experimental model of the lipid/water interface in order to investigate the feasibility of haemozoin biosynthesis at such interfaces and to attempt to elucidate the rate and mechanism of the process in such an environment.
b) To observe the effects of chloroquine (CQ) on iron distribution in *Plasmodium falciparum* using transmission electron microscopy (TEM) with electron spectroscopic imaging (ESI).
c) To use spectroscopic and computational methods to investigate structural characteristics of the complexes formed between 4-aminoquinoline antimalarials with Fe(III)PPIX in solution in order to gain further insight into how these compounds inhibit haemozoin formation and to attempt to arrive at structural models of these complexes which can be related to their activity.

CHAPTER 2.

THE FORMATION OF β-HAEMATIN AT THE LIPID/WATER INTERFACE

THE FORMATION OF β-HAEMATIN AT THE LIPID/WATER INTERFACE

2.1. INTRODUCTION

As described in Chapter 1, there is now strong evidence that haemozoin formation is a lipid driven process, probably involving neutral lipids. However, while these studies have provided evidence that haemozoin formation occurs at lipid interfaces in *Plasmodium falciparum* [97, 98] and other haemozoin forming organisms [60], it is very challenging to observe this process directly *in vivo* either inside the lipid droplets from *S. mansoni* or nanospheres from *P. falciparum*. Furthermore, the rates of formation reported in model systems using lipids are too slow to account for its formation *in vivo*. In addition, these studies have not been able to provide a mechanistic rationale for haemozoin formation. A simple interface system to model these interfaces in order to determine how haemozoin biosynthesis could occur at such lipid/water interfaces *in vivo* might provide a way to obtain considerable insight into the process. Octanol/water biphasic systems are used extensively in the field of medicinal chemistry to model partitioning of drugs between aqueous and lipid environments, suggesting that such a system may be useful in studying haemozoin formation. A computational study by Benjanim [200] has recently provided evidence that octanol molecules are strongly aligned at the aqueous interface resembling half the surface of a lipid membrane, in that the OH groups of the octanol form hydrogen bonds with the water molecules while the alkyl chains are aligned in a parallel arrangement resulting in a region that is less polar than that of both bulk liquids. A preliminary study suggested that pentanol/water systems can be directly filtered through cellulose membrane filters as opposed to octanol. In this chapter an investigation of β-haematin formation in octanol/water, pentanol/water and lipid/water systems is described

2.2. MATERIALS

The materials used in the study are listed in **Table 2.1**. They were of AR or other high purity grade and were used without purification.

TABLE 2.1. A list of materials obtained from commercial suppliers

Materials	Commercial Supplier
CHEMICALS	
Ferriprotoporphyrin IX hydroxide (Haematin)	Sigma-Aldrich
Sodium hydroxide (NaOH)	Saarchem
Citric acid	Saarchem
Sodium bicarbonate ($NaHCO_3$)	BDH
N-2-morpholino-N-2-ethanesulfonic acid (MES)	Sigma-Aldrich
N-2-hydroxyethylpiperizine-N'-2-ethanesulfonic acid (HEPES)	Sigma-Aldrich
Sodium perchlorate ($NaClO_4$)	Merck
Tris (hydroxymethyl) aminomethane (Tris)	Merck
Sodium dodecyl sulphate (SDS)	BDH
SOLVENTS	
1-Octanol	BDH
1-Pentanol	BDH
Toluene	Saarchem
Chloroform	KIMIX
Methanol	Saarchem
Acetone	Saarchem
Dimethyl sulphoxide (DMSO)	BDH
Pyridine	BDH
Perchloric acid ($HClO_4$)	BDH
Hydrochloric acid (HCl)	ORION

TABLE 2.1. A list of materials obtained from commercial suppliers (*continues*)

LIPIDS	
rac 1-Monomyristoylglycerol (**MMG**)	Sigma-Aldrich
rac 1-Monooleoylglycerol (**MOG**)	Sigma-Aldrich
1,3-Dimyristoylglycerol (**DMG**)	Sigma-Aldrich
1,3-Dioleoylglycerol (**DOG**)	Sigma-Aldrich
Trioleoylglycerol (**TOG**)	Sigma-Aldrich
1,2-Dioleoyl-glycero-3-phosphoethanolamine (**DOPE**)	Sigma-Aldrich
1,2-Dimyristoyl-glycero-3-phosphocholine (**DMPC**)	Sigma-Aldrich
1,2-Dioleoyl-glycero-3-phosphocholine (**DOPC**)	Sigma-Aldrich
1,2-Dipalmitoyl-glycero-3-phosphocholine (**DPPC**)	Sigma-Aldrich
n-octyl-β-D-glucopyranoside (**OGP**)	Sigma-Aldrich
Cholesterol (**CHL**)	Sigma-Aldrich

2.3. SAMPLE PREPARATION

2.3.1. Preparation of 0.1M NaOH Stock Solutions

The sodium hydroxide (NaOH) solution was prepared by weighing 3.997 g of NaOH pellets. The pellets were dissolved in 1000 ml of distilled water to make up a concentration of 0.1 M NaOH solution.

2.3.2. Preparation of Haematin Solution

Haematin solution was prepared by firstly dissolving 0.005 g of haematin in 0.6 ml of 0.1 M NaOH solution in a 2 ml eppendorf tube. A volume of 0.9 ml of acetone was added to the pre-dissolved haematin solution and vortexed. This solution was used for characterisation purposes. For quantification studies, 0.001 g of haematin was predissolved in 0.1 M NaOH and the solution was made up to volume with either 1:9 (v/v) acetone/methanol or chloroform/methanol. The solutions were prepared fresh for every experiment as haematin degrades over time.

2.3.3. Preparation of 0.05 M Citrate Buffer Stock Solution

10.507 g of citric acid was dissolved in 750 ml of distilled water. The pH was adjusted to 4.8 with a highly concentrated NaOH solution. The solution was made up to 1000 ml with distilled water.

2.3.4. Preparation of 0.05 M MES Buffer Stock Solution

2.44 g of MES was dissolved in 200 ml of distilled water. The pH was adjusted to 4.8 with a concentrated NaOH solution. The solution was made up to 250 ml with distilled water.

2.3.5. Preparation of 0.1 M $NaHCO_3$ Stock Solutions

The sodium bicarbonate solution ($NaHCO_3$) was prepared by dissolving 0.8401 g in 50 ml of distilled water. The pH of the solution (9.1 and 10.2) was adjusted using a highly concentrated solution of NaOH. The volume of each solution was made up to 100 ml with distilled water.

2.3.6. Preparation of 0.02 M Tris Buffer containing DNase1 and Proteinase K

0.1211 g of Tris buffer was dissolved in 50 ml of distilled water. DNase1 (0.0013 g) was added to the 50 ml Tris buffer solution. Proteinase K (0.0250 g) was added to the haemozoin suspension as outlined in the experimental section (Section 2.4.3).

2.3.7. Preparation of 0.025 M Tris Buffer containing 2.5% SDS at pH 7.8

The Tris buffer was prepared by dissolving 0.1514 g of Tris buffer in 50 ml of distilled water to which 0.0125 g of SDS was added. The pH was adjusted to 7.8 with NaOH.

2.3.8. Preparation of 0.2 M HEPES Buffer (pH 7.5)

A stock solution of HEPES buffer was prepared by dissolving 4.776 g of HEPES in 80 ml of distilled water. The pH of the solution was adjusted to 7.5 with a highly concentrated solution of NaOH. The solution was made up to 100 ml with distilled water.

2.3.9. Preparation of 5% Pyridine in 0.02 M HEPES (pH 7.5) and 50% Acetone

The pyridine solution was prepared by mixing 5 ml of pyridine with 10 ml of 0.02 M HEPES buffer at pH 7.5 and 50 ml acetone. The solution was made up to 100 ml with distilled water. The solution was used either to wash off the unreacted haematin from the product or to quantify unreacted haematin where appropriate.

2.4. EXPERIMENTAL PROCEDURES

2.4.1. Preparation of β-Haematin at the Pentanol/Water Interface

The reaction was carried out in a glass vessel with an internal diameter of 5 cm. 50 ml of 0.05 M citrate buffer was dispensed into the glass vessel and 10 ml of pentanol was added on top of the citrate buffer to form two layers. The mixture was pre-heated at 37°C in a thermostatted water bath. 1 ml solution of haematin (3.33×10^{-3} g/ml) prepared as in Section 2.3.3 was added drop-wise with a 1 ml syringe on top of the pre-incubated mixture. The haematin solution settled at the interface between the two layers. The reaction mixture was incubated for 30 minutes at 37°C in the water bath. The mixture was agitated at the end to allow the product to drop from the interface. The product was then collected by filtration using a 0.22 μm cellulose nitrate disc. The unreacted haematin was washed off with 5% pyridine solution (Section 2.3.9). A fraction of the wet product was analysed by infrared spectroscopy (IR) as a nujol mull on NaCl plates. The remaining material was dried in a desiccator in the presence of silica gel and phosphorus pentoxide for 48 hours. The dried product was analysed and characterised by IR (KBr), XRD, solubilisation studies and SEM.

2.4.2. Solubility Studies of β-Haematin obtained at the Pentanol/Water Interface

A suspension of 5×10^{-4} g of the dried product obtained as described in Section 2.4.1 was made up in 50 ml of bicarbonate buffer (pH 9.1 and 10.2) or DMSO. The absorbance of the solubilised haematin was measured at 387 or 402 nm in bicarbonate buffer or DMSO, respectively [63].

2.4.3. Isolation of Haemozoin from *Plasmodium falciparum*

Haemozoin was isolated from the parasite using a modified method of Yamada and Sherman [201]. A chloroquine (CQ) sensitive strain of *Plasmodium falciparum* (D10) was kept in continuous culture as outlined in Chapter 3. The parasite culture was continuously harvested in the trophozoite stage and stored at -80°C. The frozen parasitised red blood cell (pRBC) pellet was thawed in a 37°C water bath. A 50 ml volume of distilled water was added to the thawed pellet and sonicated for 30 minutes. The sample was then centrifuged at 2000 rpm (revolutions per minute) for 5 minutes at room temperature and the supernatant was discarded. The pellet was resuspended in 0.02 M Tris buffer containing DNase1 (Section 2.3.6) and incubated at 37°C for 10 minutes. 0.025 g of proteinase K was added to the suspension and incubated for 30 minutes at 37°C. The solution was then centrifuged for 30 minutes at 2000 rpm and the supernatant was discarded. The resulting pellet was resuspended in a 0.025 M Tris buffer containing 2.5% SDS at pH 7.8 (Section 2.3.7) and left overnight at room temperature. The sample was then centrifuged at room temperature for 30 minutes and the supernatant was removed by suction. The haemozoin pellet was washed twice with distilled water and the final pellet was freeze-dried for 48 hours to obtain dry pure haemozoin. The material was analysed by IR (nujol mull) and SEM and these results were compared with that of the product formed at the pentanol/water interface (Section 2.4.1).

2.4.4. The Effect of Conditions on β-Haematin Formation at the Interface

2.4.4.1. The Effect of Aqueous Buffer Composition on β-Haematin Formation

The effect of buffer composition was investigated using a 0.05 M citrate buffer or MES buffer at pH 4.8 using pentanol as the organic layer. The reaction was carried out as outlined in Section 2.4.1. The filtered wet product was analysed by nujol mull IR.

2.4.4.2. The Effect of the Interface on β-Haematin Formation

The effect of the interface on the formation of β-Haematin was investigated by carrying out the reaction in either the organic solvent alone or the citrate buffer alone. 10 ml of pentanol was dispensed into a reaction vessel and pre-incubated at 37°C (Section 2.4.1). A 0.005 g sample of solid haematin was added to the pentanol and incubated for 30 minutes at 37°C. The product was filtered and analysed by IR without washing. For the aqueous buffer experiment, 50 ml of citrate buffer at pH 4.8 was also incubated at 37°C in a thermostated water bath. 1 ml of a 3.33×10^{-3} g/ml solution of haematin (Section 2.3.2) was added drop-wise to the reaction vessel with a syringe and was incubated for 30 minutes at 37°C. The product was again filtered and the buffer was washed off with distilled water. The product was analysed by nujol mull IR.

2.4.4.3. The Effect of the Organic Solvent on β-Haematin Formation

The effect of the organic solvent on the formation of β-haematin was investigated using octanol and toluene instead of pentanol as the organic layers. The experiments were carried out as outlined in Section 2.4.1 using each solvent in the presence of 0.05 M citrate buffer at pH 4.8. The product was collected from the aqueous layer after agitation at the end of the reaction. The unreacted haematin was washed off with 5% pyridine solution and quantified by measuring the absorbance at 405 nm. The remaining product was analysed by nujol mull IR, SEM and XRD.

2.4.4.4. The Effect of Medium in which Haematin is Dissolved on β-Haematin Formation

The effect of dissolving haematin in NaOH was investigated by dissolving 0.005 g of haemin in pure methanol instead of 0.1 M NaOH. The solution was added to the pentanol/water interface and incubated for 30 minutes. The unreacted haemin was washed off with 5% pyridine solution and 50% acetone/water mixture and was analysed by nujol mull IR.

2.4.4.5. The Effect of Ionic Strength on β-Haematin Formation

0.05 M citrate buffer containing 0.154 M of $NaClO_4$ was used as buffer to determine the effect of ionic strength on the formation of β-haematin at the interface. The reaction was carried out at the pentanol/water interface and the product was treated and analysed as described in Section 2.4.4.4.

2.4.5. The Role of Lipids in the Formation of β-Haematin at the Interface

The role of lipids (**Table 2.1** and **Fig 2.1**) in the formation of β-haematin was investigated by replacing the pentanol with a layer of lipid solution dissolved as described below.

2.4.5.1. β-Haematin Formation at the Lipid/water (MMG/water) Interface

0.0025 g of *rac* 1-monomyristoylglycerol (**MMG**) was dissolved in 5 ml of 1:9 (v/v) acetone/methanol (0.0005 g/ml) and 1 ml of the lipid solution was layered on top of 50 ml of 0.05 M citrate buffer (Section 2.4.1). Haematin solution was prepared by dissolving 0.001 g of haematin in 0.6 ml of 0.1 M NaOH and a volume of 0.9 ml of 1:9 (v/v) acetone/methanol was added to make up the solution to 1.5 ml volume. 0.5 ml solution of haematin was added to the interface of the lipid/aqueous system and incubated for 30 minutes. The product was collected by centrifugation and unreacted haematin was removed using 5% pyridine followed by characterisation by nujol mull IR, SEM and XRD.

2.4.5.2. Kinetic Study of β-Haematin Formation at the MMG/water Interface

β-haematin was prepared as in Section 2.4.5.1 over different time intervals. The reaction was however, carried out in glass vials with an internal diameter of 1.1 cm in triplicate. 1.8 ml of buffer was added to the reaction vial followed by 0.2 ml of 5.0 x 10^{-4} g/ml of lipid. 0.1 ml of 6.66 x 10^{-4} g/ml of haematin solution was added to the interface with a syringe. The reaction systems were incubated at 37°C for 0, 5, 15, 30, 45 and 60 minutes. The percent β-haematin formed at each time point was obtained by adding 1 ml of 5% (v/v) pyridine (50% acetone and 0.02 M HEPES buffer at pH 7.5) to the pellet collected after centrifugation. This is a modification of the

assay developed recently by Egan *et al.* [202]. 5% (v/v) aqueous pyridine forms a complex with haematin but not with β-haematin. The pellet was shaken and the unreacted haematin was allowed to dissolve. The solution was centrifuged for 5 minutes to allow β-haematin to settle. 0.02 ml of the supernatant was mixed with 1.98 ml of 5% pyridine and the absorbance was read at 405 nm. The absorbance was used to quantify the amount of unreacted haematin. These results were used to obtain the percent of β-haematin formed.

2.4.5.3. The Effect of Lipid Mass on the Rate of β-Haematin Formation

A concentrated solution of lipid was prepared by dissolving 0.0125 g of MMG in 1 ml of 1:9 (v/v) of acetone/methanol. The solution was serially diluted to make up solutions with different concentrations (0.2, 1.0, 5.0 and 25.0 x 10^{-4} g/ml solutions, respectively). In each case, the volume of solution added to the surface of the citrate buffer was identical, so that only the mass of lipid varied. The formation of β-haematin in the presence of each of the lipid masses was monitored and the amount of β-haematin formed in each case was obtained as described in Section 2.4.5.2 above. The percentage β-haematin formed was obtained as a function of mass of lipid present at the interface.

Monoglycerides

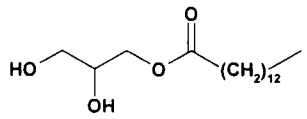

MMG

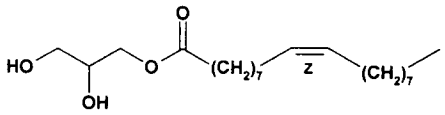

MOG

Diglycerides

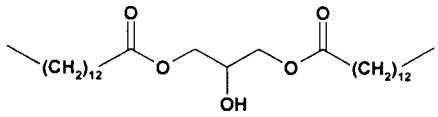

DMG

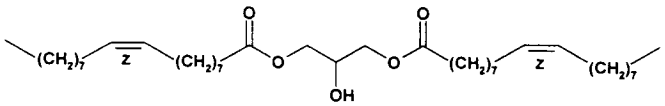

DOG

Triglycerides

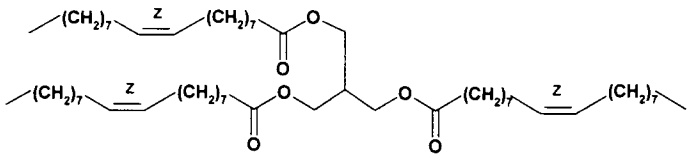

TOG

Phosphoglycerides

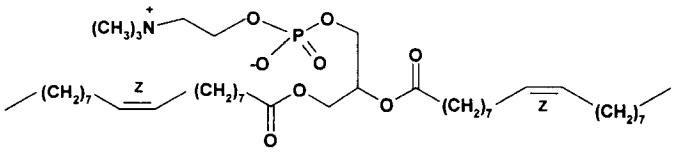

DOPC

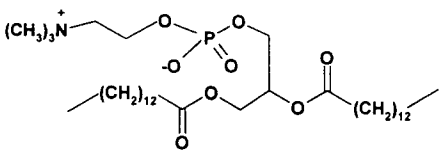

DPPC

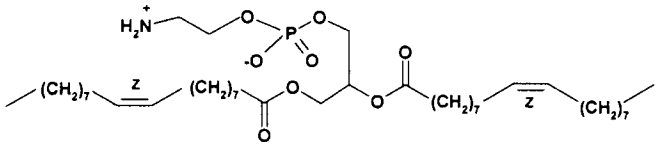

DOPE

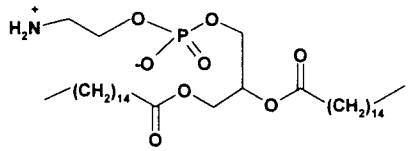

DMPC

Others

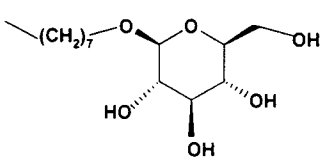

OGP

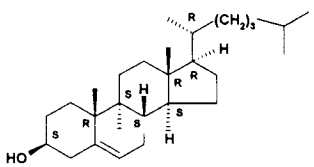

CHL

FIGURE 2.1. Chemical structures of the lipids used in the study

2.4.5.4. The Effect of pH on β-Haematin Formation

0.05 M stock solutions of citrate buffer at different pHs (3.0, 4.8, 5.5, 6.0 and 6.5) were prepared (Section 2.3.3). Each reaction was carried out at the MMG/water interface out as described in Section 2.4.5.2. The fraction of β-haematin formed in these systems was obtained using 5% pyridine as described above.

2.4.5.5. The Effect of Temperature on β-Haematin Formation

The formation of β-haematin was monitored at 20, 30, 37 and 40°C to determine the effect of temperature on β-haematin formation at the MMG/water interface. The reactions were carried out as in Section 2.4.5.2.

2.4.5.6. The Formation of β-Haematin in the Presence of other Lipids

A number of lipids (**Fig 2.1**) were used to investigate the formation of β-haematin. The lipids were prepared as outlined in Section 2.4.5.1 using either 10% acetone/methanol or 10% chloroform/methanol. The haematin solution was dissolved in 0.1 M NaOH and was made up to the correct volume in either 10% acetone/methanol or 10% chloroform/methanol, respectively depending on the type of lipid used. The reactions were then performed as outline in Section 2.4.5.1. The unreacted haematin was quantified using 5% pyridine (Section 2.4.5.2).

2.4.5.7. The Efficiency of Mixed Lipids in Promoting the Formation of β-Haematin at the Interface

The efficiency of the mixed lipids was further investigated by mixing the neutral lipids together. 1 ml of 5.0×10^{-4} g/ml of each lipid was mixed together and 0.2 ml of this solution (8.33×10^{-5} g/ml) was added to the reaction vial. The amount of β-haematin formed using this mixture was obtained.

2.5. RESULTS

2.5.1. Characterisation of β-Haematin Formed at the Pentanol/Water Interface

The product formed using the interface method was analysed using both chemical and instrumental methods to confirm that the product formed is indeed β-haematin, and for comparison with haemozoin. This was done using FTIR spectroscopy, XRD, solubilisation studies and SEM. The IR spectra were collected on a Perkin Elmer Spectrum One spectrometer. XRD patterns were recorded using a Philips PW3710 mpd controlled goniometer connected to a PW3830 X-ray generator with 2θ values in the range 5 to 30° with Cu Kα radiation (λ=1.542 Å). The samples were finely ground into powder to avoid preferred orientation effects and were carefully packed onto a glass sample holder for analysis. Solubilisation studies and spectroscopic measurements were obtained using a Varian Cary 100 UV-visble spectrophotometer fitted to a thermostated cell holder. SEM was carried out on a LEO S440 scanning electron microscope. Finely ground samples were sprinkled onto aluminium stubs pre-coated with carbon and glue mixture and further coated with gold-palladium. These methods have been employed extensively in the literature for characterisation and quantification of haemozoin and β-haematin formed using a number of different methods. These methods are therefore used routinely to monitor the formation of β-haematin. Characterisation was performed on the product obtained at the pentanol/water (citrate buffer, pH 4.8) interface incubated for 30 minutes at 37°C, unless otherwise specified. Freeze-dried haemozoin obtained from harvested malaria parasites was also analysed for comparison purposes. The key bands in the spectrum on wet material obtained as a nujol mull are identical to those obtained on dry material using KBr. Nujol mull was used as the product obtained does not require drying, making it easier to monitor the reaction. Therefore, nujol mull was used throughout the study to save time. Further characterisation was done on material dried for 48 hours in a desiccator in the presence of silica gel and phosphorus pentoxide.

2.5.1.1. FTIR Spectroscopy

Fig 2.2 (**a**) shows the infrared spectra of haematin, β-haematin formed at the pentanol/water interface and haemozoin isolated from *Plasmodium falciparum*. The region between 1550 and 1320 cm^{-1} has been removed for clarity, because it is dominated by two strong nujol peaks as shown in **Fig 2.2** (**b**). The dotted lines (**Fig 2.2** (**a**)) indicate characteristic peak positions of the Fe-COO^- group in β-haematin. The 1663 and 1209 cm^{-1} peaks arise from the iron-carboxylate linkage (**Fig 2.2** (**c**)) between the haematin subunits as a result of stretching of the C=O and C-O bonds, respectively [63].

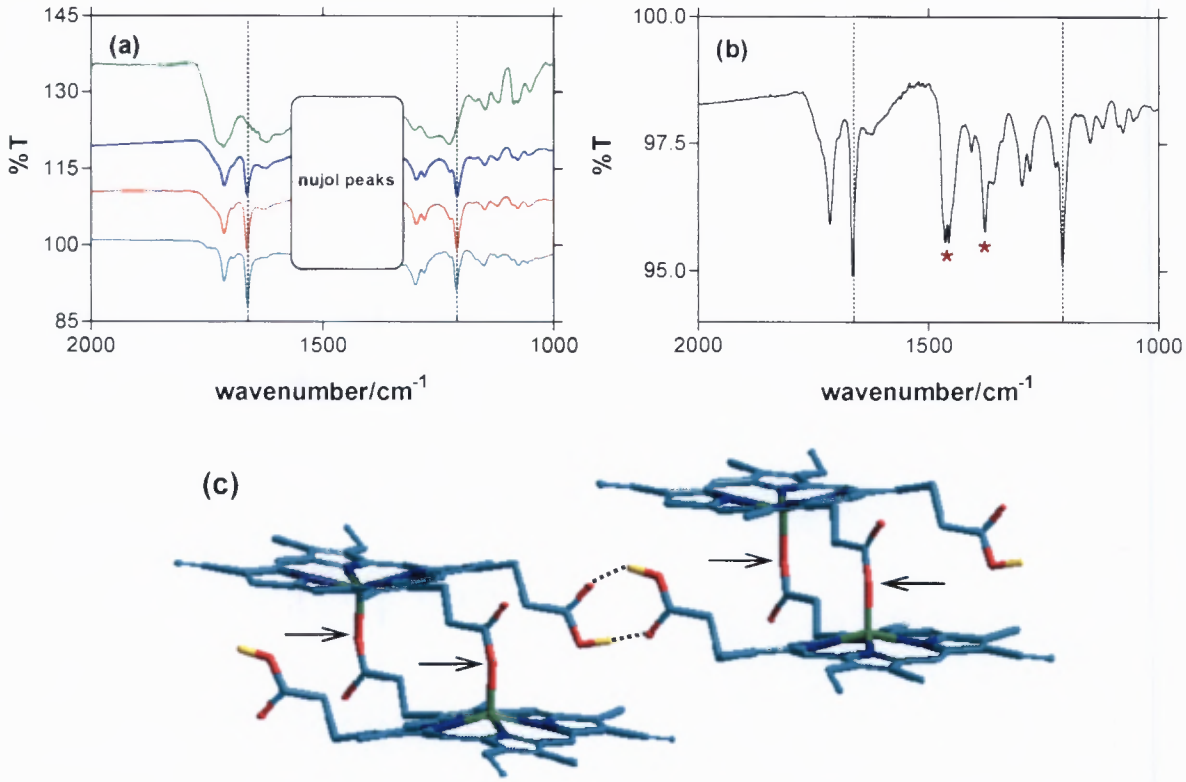

FIGURE 2.2. (**a**) Infrared spectra of (—) haematin in citrate buffer, (—) β-haematin prepared at the pentanol/water (pH 4.8) interface incubated for 5 minutes, (—) 30 minutes at 37°C and (—) haemozoin harvested from freeze-dried D10 strain *Plasmodium falciparum*. (**b**) Infrared spectrum of β-haematin prepared at the pentanol/water (pH 4.8) interface incubated for 30 minutes showing the nujol peaks (red asterisks). The characteristic peaks at 1663 and 1209 cm^{-1} are marked with vertical dotted lines. (**c**) Schematic representation of haemozoin showing iron-carboxylate linkages (black arrows) and hydrogen bonding (black dotted lines).

These peaks are absent in the spectrum of haematin. The appearance of these peaks has been used in a number of studies to monitor the formation of β-haematin. They have, therefore been used as fingerprints for the identification of β-haematin and are also characteristic of haemozoin isolated from *Plasmodium falciparum* (**Fig 2.2** (**a**)). The peak at 1714 cm^{-1} arises from the remaining protonated carboxylic acid groups which form intermolecular hydrogen bonds between the β-haematin dimers in the crystal (**Fig 2.2** (**c**)). The peaks for β-haematin and haemozoin are sharper compared to that of haematin. This has been attributed to a reduction of intermolecular hydrogen bonding in β-haematin or haemozoin compared to haematin [63]. These spectra confirm that the product formed at the interface is identical to haemozoin obtained from the parasite.

2.5.1.2. X-ray Powder Diffraction (XRD)

Intensities and scattering angles of diffracted X-rays can be used to determine crystal structures of substances or they can be used as fingerprints for identifying substances. XRD was used to confirm the identity of the product formed in this study. **Fig 2.3** (**a**) shows an XRD pattern of haematin, diffraction patterns of β-haematin prepared at the pentanol/water interface in 5 minutes and 30 minutes, respectively. The patterns were measured from 2θ values of 5 to 30° with Cu Kα radiation (λ=1.542 Å). The diffraction pattern of haematin gives broad humps which show that the material is non-crystalline or consists of extremely small nanocrystals. This material is clearly different from the product obtained in the study as observed from the differences in the diffraction patterns. The position of the observed diffraction lines of the product were compared to that predicted from the structure of β-haematin reported by Pagola *et al.* (**Fig 2.3** (**b**)) [73]. The diffraction lines occur at the same positions confirming that the two materials are structurally and chemically identical at the atomic level. The patterns are also identical to that of β-haematin prepared by Bohle *et al.* in dry methanol [76] and of haemozoin obtained from lyophilised parasitized red blood cells [72]. The patterns obtained in the present study have broader peaks which are less intense compared to those of Pagola *et al.* This could

be due to the fact that Pagola *et al.* used a synchrotron X-ray source, while our product was analysed using a conventional source. The synchrotron source has a resolution much higher than that of a conventional radiation source.

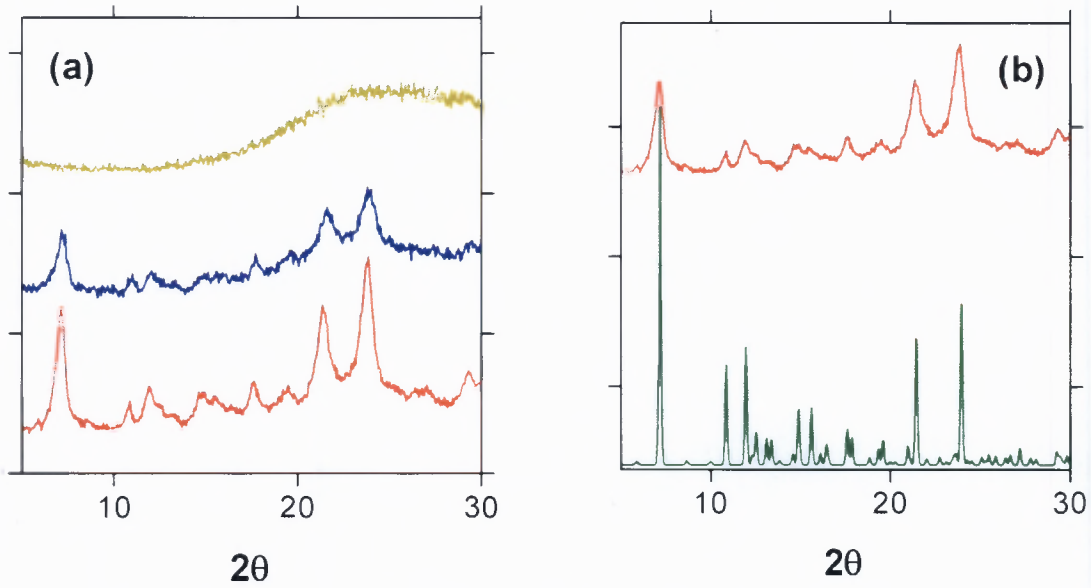

FIGURE 2.3. (**a**) X-ray diffraction patterns of (—) haematin obtained from citrate buffer, β-haematin prepared at the pentanol/water (pH 4.8) interface incubated for (—) 5 minutes and (—) 30 minutes at 37°C and (**b**) positions of β-haematin diffraction lines calculated from the structure of Pagola *et al.* (—) [73], compared with the XRD pattern of the product obtained after 30 minutes of incubation (—). The data were collected with Cu Kα radiation, λ = 1.542 Å. (—) Reprodued with permission from the authors.

The d-spacings of the major peaks were calculated for both β-haematin prepared in this study and that obtained from Pagola *et al.* (**Table 2.2**). The 2θ values were corrected for a systematic error of -0.2° caused by the instrument before calculating the value of the d-spacings. The values are in good agreement with each other. These results confirm that these two substances are identical in composition and structure, and that the product formed in this study is indeed β-haematin.

TABLE 2.2. Comparison of d-spacings of β-haematin prepared at the pentanol/water interface and from Pagola *et al.* [73]

β-haematin prepared at the interface		**β-haematin from Pagola *et al.***	
2θ	**d (Å)**	**2θ**	**d (Å)**
7.325	11.980	7.375	11.991
11.125	7.953	11.075	7.989
12.275	7.210	12.175	7.274
15.125	5.857	15.125	5.859
17.925	4.947	17.825	4.977
19.725	4.499	19.825	4.472
21.675	4.100	21.650	4.105
24.125	3.688	24.150	3.685
29.575	3.020	29.525	3.026

2.5.1.3. Solubilisation Studies

Solubilisation experiments were carried out to investigate the physical properties of the product formed. These were conducted in 0.1 M $NaHCO_3$ (pH 9.1 and pH 10.2) and pure DMSO (**Fig 2.4** (**a**) — (**c**)). The solubilisation profiles are almost identical to those reported for haemozoin by Slater (**Fig 2.4** (**d**)) [63]. Haematin is known to solubilise readily in weakly basic bicarbonate buffers and solvents such as pyridine and DMSO. Haemozoin on the other hand is known to be insoluble in these solvents. The insolubility of haemozoin is an indication of coordination of carboxylate of one porphyrin with the Fe centre of the other porphyrin (**Fig 2.2** (**c**)).

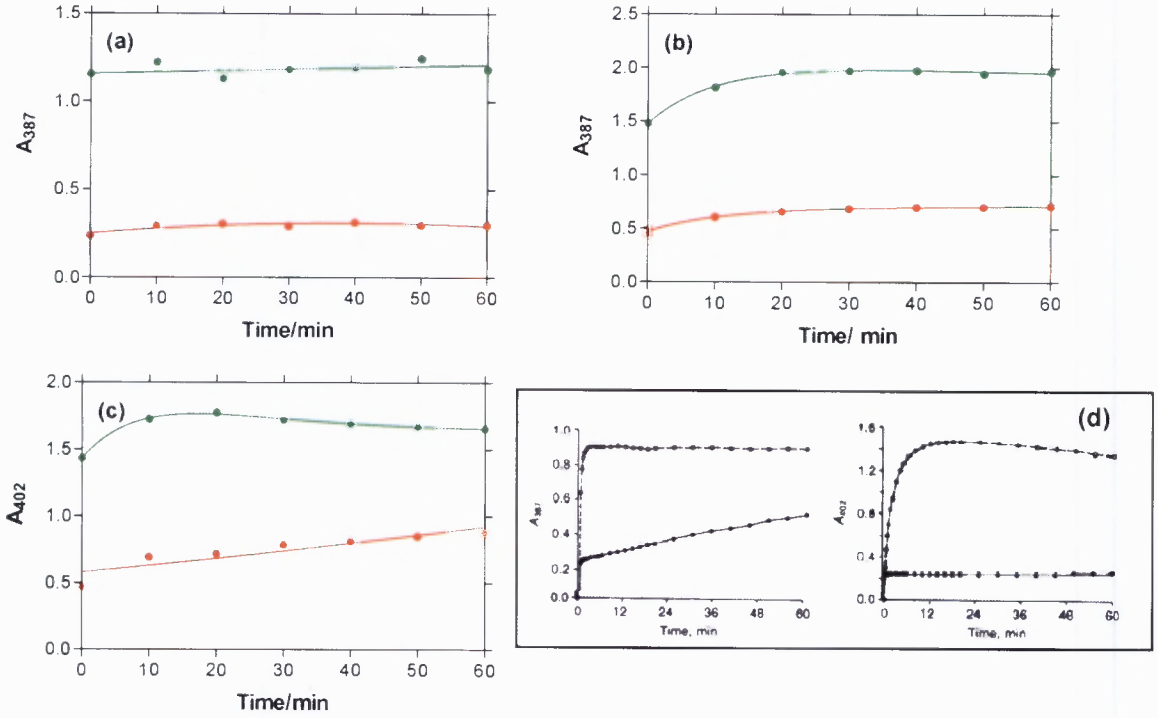

FIGURE 2.4. Solubilisation studies of equal amounts of (•) haematin and (•) β-haematin prepared at the pentanol/water (pH 4.8) interface incubated for 30 minutes at 37°C in: 0.1 M bicarbonate buffer (**a**) pH 9.1, (**b**) pH 10.2 and (**c**) dimethyl sulphoxide (DMSO). A suspension of 0.5 mg of material in 50 ml volume was made up and the absorbance of the solubilised haematin was measured at 387 or 402 nm in bicabonate buffer or DMSO, respectively. (**d**) Solubility studies of haematin (top plot) and haemozoin (bottom plot) in: 0.1 M bicarbonate buffer at pH 10.2 (left graph) and DMSO (right graph), respectively [63]. The data for (**a**), (**b**) and (**c**) represent a single representative experiment. (**d**) Reproduced with permission from the authors.

2.5.1.4. Scanning Electron Microscopy (SEM)

Scanning electron microscopy was used to examine the crystal morphology or the appearance of crystalline material prepared using the interface method. **Fig 2.5** shows scanning electron micrographs (SEM) of β-haematin prepared in this study and of haemozoin harvested from malaria parasites. The SEM of haematin appears to have relatively featureless surface (**Fig 2.5** (**a**)) with no clear sign of crystalline material present. This is consistent with this material being either amorphous or non-crystalline. After 5 minutes of incubation at the pentanol/aqueous interface, crystals

appear that are long and needle-like (**Fig 2.5** (**b**)). After 30 minutes of incubation the entire surface now consists of big crystals (**Fig 2.5** (**c**)). The crystals in **Fig 2.5** (**b**) and **Fig 2.5** (**c**) are similar to those of haemozoin (**Fig 2.5** (**d**)) in size and shape and are totally different in appearance to haematin. These observations further confirm that the material produced at the interface is very similar to haemozoin formed in malaria parasite.

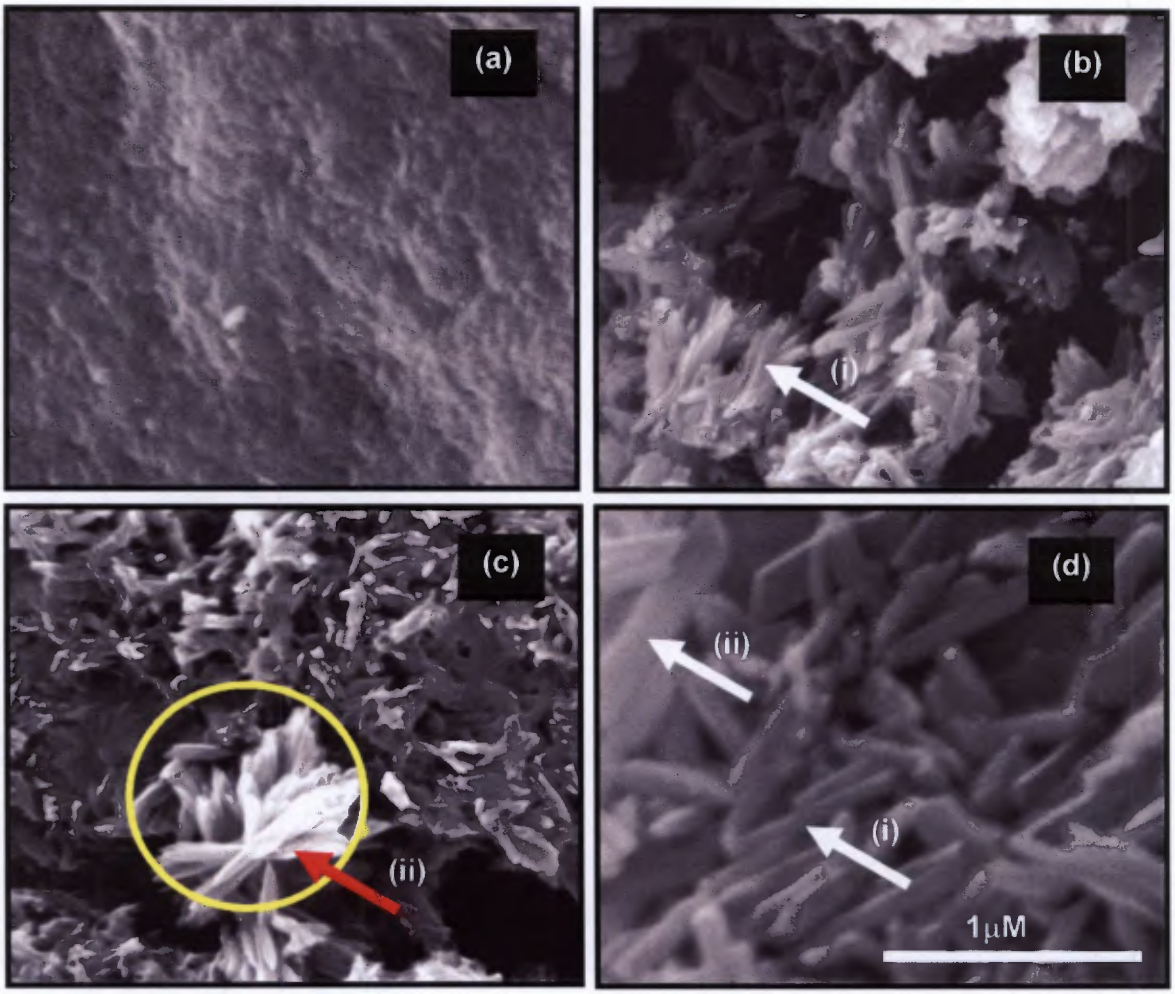

FIGURE 2.5. Scanning electron micrographs of (**a**) haematin, (**b**) β-haematin prepared at the pentanol/water (pH 4.8) interface incubated for 5 minutes, (**c**) 30 minutes at 37°C and (**d**) haemozoin harvested from freeze-dried D10 strain *Plasmodium falciparum*. The arrows point to crystals that are (i) small and (ii) large. The yellow circle indicates crystals that appear to have grown from a common site of nucleation. The large white line shows the scale which is the same in each panel.

2.5.2. The Effect of Conditions on β-Haematin Formation at the Interface

Various conditions were investigated to determine their role, if any, in the formation of β-haematin using the interfacial method. These include, buffer composition, the presence of the interface itself, identity of the organic solvent, the effect of medium in which haematin is dissolved and ionic strength. These conditions were investigated using the pentanol/water interface (buffer, pH 4.8) as a model system. This system is convenient as the entire mixture containing the product material can be filtered to collect the product.

2.5.2.1. The Effect of Aqueous Buffer Composition on β-Haematin Formation

Fig 2.6 shows the infrared spectra of β-haematin obtained in the presence of a pentanol/citrate buffer interface and a pentanol/MES buffer interface. The characteristic peaks at 1663 and 1209 cm^{-1} indicate that β-haematin is formed in both systems. The results indicate that the composition of the buffer does not have any effect on the production of β-haematin. The identity of the buffer therefore does not play any role in the process. The buffer is only used as an acidic medium to adjust the pH of the haematin solution to the correct pH (4.8) in order to allow the process of β-haematin formation to occur.

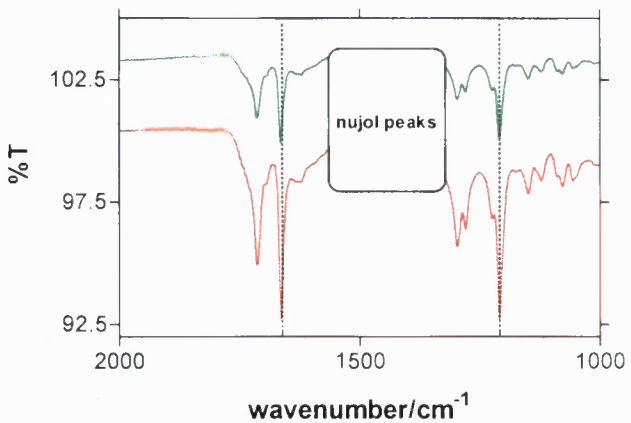

FIGURE 2.6. Infrared spectra of β-haematin prepared at the (—) pentanol/citrate buffer interface, pH 4.8 and (—) pentanol/MES buffer interface, pH 4.8. The reaction systems were incubated for 30 minutes at 37°C. Relative intensities of the spectra reflect different quantities of material in the IR beam and are not reflective of different yields of product.

2.5.2.2. The Effect of the Interface on β-Haematin Formation

The results obtained in Section 2.5.1 seem to suggest that β-haematin formation occurs at the interface. This suggestion was investigated by carrying out the reaction in both the aqueous medium alone and the pentanol alone (**Fig 2.7** (**a**)). No product was formed in either case as indicated by the absence of the key peaks at 1663 and 1209 cm^{-1}, respectively. The spectra are identical to haematin (**Fig 2.2** (**a**)) and different from the spectrum of β-haematin (**Fig 2.7** (**b**)) prepared at the pentanol/water interface. This demonstrates the critical importance of the interface in the formation of β-haematin.

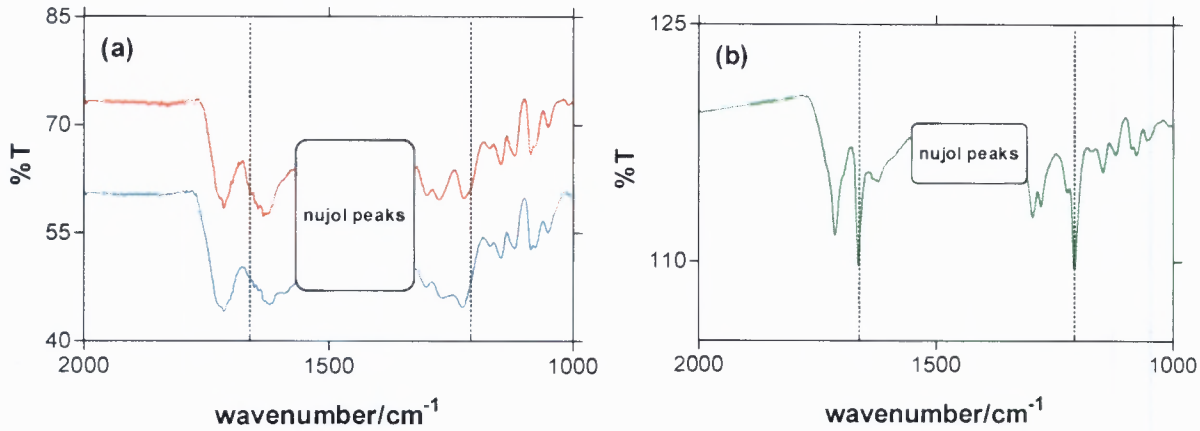

FIGURE 2.7. (**a**) Infrared spectra of (—) product prepared in pentanol alone and (—) product prepared in citrate buffer alone (pH 4.8) incubated for 5 minutes at 37°C. (**b**) Infrared spectrum of β-haematin prepared at the pentanol/water (pH 4.8) interface incubated for 5 minutes at 37°C.

2.5.2.3. The Effect of Organic Solvent on β-Haematin Formation

The effect of the identity of the organic layer on the efficiency of β-haematin formation was investigated. The experiments were conducted by replacing pentanol with either octanol or toluene. The product also forms in the presence of these solvents as observed from the IR spectra (**Fig 2.8**). The results, however indicate that a large fraction of haematin is left unreacted in the toluene/water system compared to the other systems as indicated by the relative size of the haematin peak at 1633 cm^{-1} (red box).

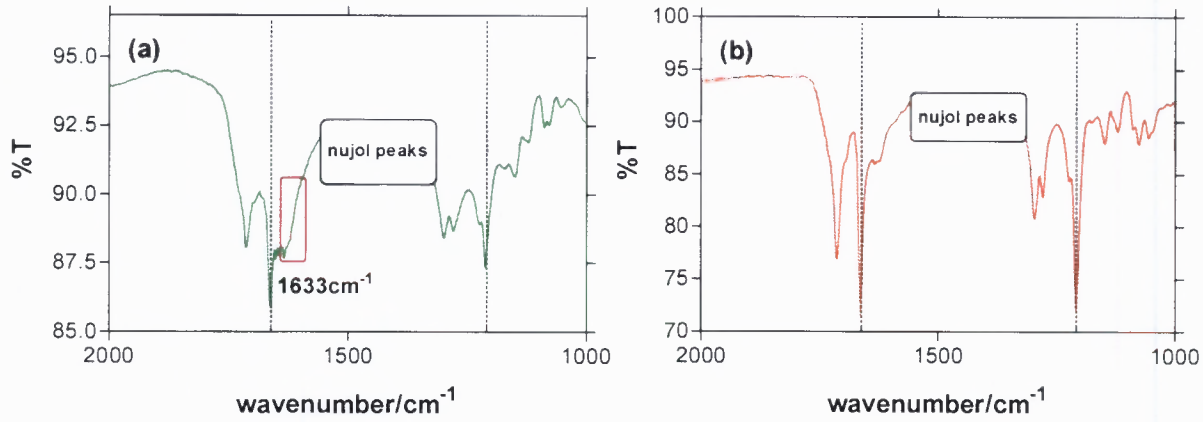

FIGURE 2.8. Infrared spectra of β-haematin prepared at the (**a**) toluene/water (pH 4.8) interface and (**b**) octanol/water (pH 4.8) interface. The reaction systems were incubated for 30 minutes at 37°C. The red box indicates a prominent haematin peak at 1633 cm^{-1}.

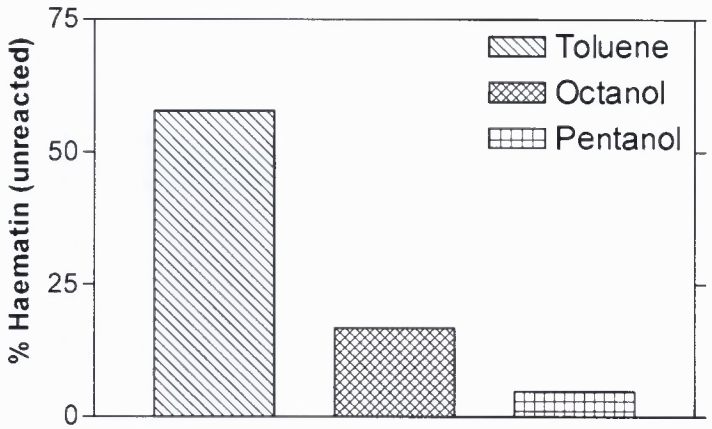

FIGURE 2.9. Haematin wash solutions obtained from the product obtained at the pentanol, octanol and toluene water interfaces. The reaction systems were incubated for 30 minutes at 37°C. The product was washed with 5% pyridine and the absorbance of the supernatant was measured at 405 nm to obtain the amount of unreacted material (haematin).

The efficiency of these solvents is further shown in **Fig 2.9**. The product obtained from each system was washed with 5% pyridine solution and the absorbance of the unreacted haematin-pyridine complex formed in the supernatant was measured at 405 nm. The results indicate that more than 60% of the haematin is still present after 30 minutes of incubation in the toluene/water system. The reaction is therefore highly efficient at the pentanol and octanol interface and much less efficient at the toluene

interface. The products obtained from the octanol/water interface and toluene/water interface were further characterised by XRD and SEM (**Fig 2.10**).

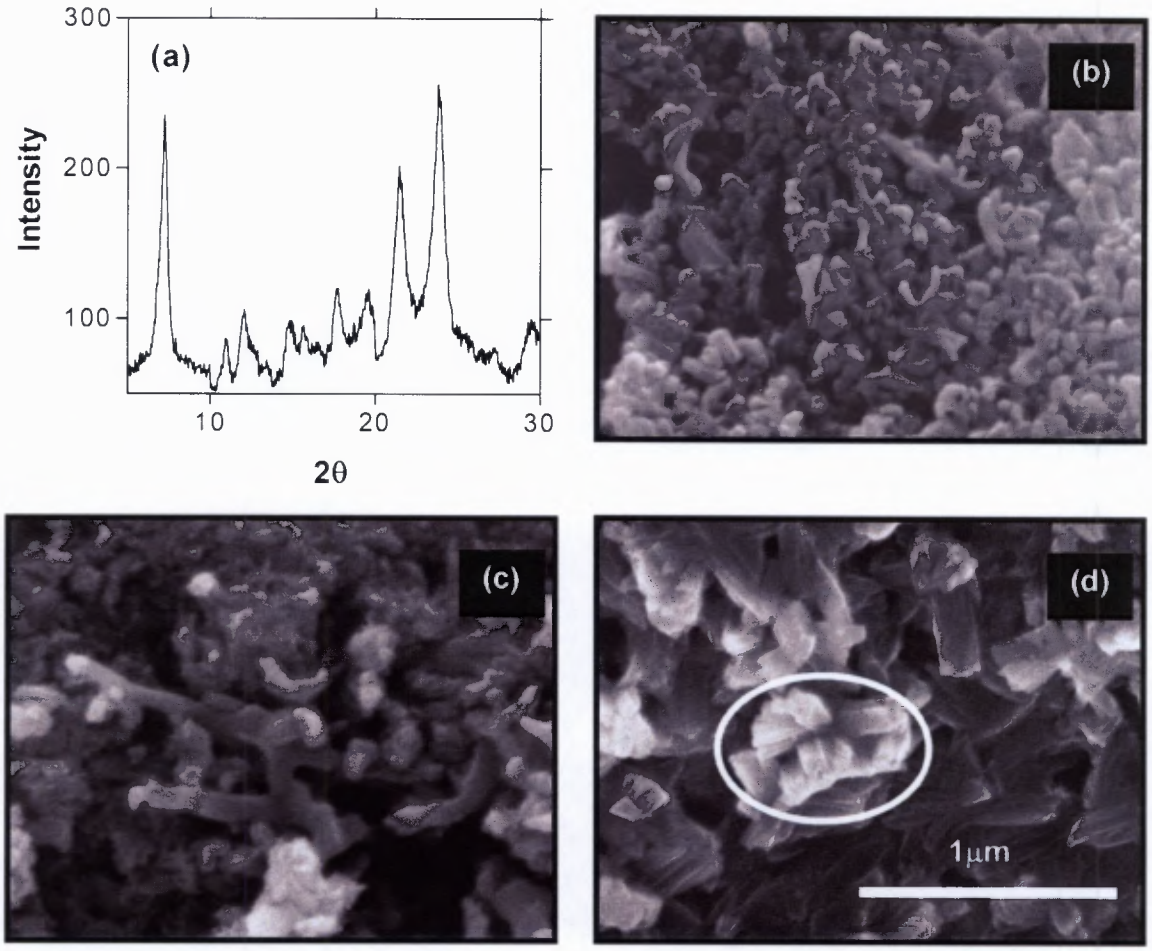

FIGURE 2.10. (**a**) X-ray diffraction pattern of β-haematin prepared at the octanol/water (pH 4.8) interface incubated for 30 minutes at 37°C. The data were collected with Cu Kα radiation, λ = 1.542 Å. Scanning electron micrographs of β-haematin prepared at the (**b**) toluene/water (pH 4.8) interface incubated for 30 minutes, (**c**) octanol/water interface (pH 4.8) incubated for 5 minutes and (**d**) 30 minutes. The white circle indicates crystals that appear to have grown from a common site of nucleation. The large white line shows the scale for all SEM panels.

The XRD pattern of the product obtained from the octanol/water interface confirms that β-haematin forms in this system (**Fig 2.10** (**a**)). The crystals obtained from the octanol system and the toluene system contain both small and big crystals (**Fig 2.10** (**b**) — (**d**)). The morphology of the crystals in both the toluene/water system and the octanol/water system is similar to that of haemozoin (**Fig 2.5** (**d**)) although crystals are clearly smaller in the former system. The SEM in **Fig 2.10** (**d**) (white circle) strongly suggests growth from a common nucleation site as observed also in **Fig 2.5** (**c**) (yellow circle).

2.5.2.4. The Effect of Medium in which Haematin is Dissolved on β-Haematin Formation

Haematin is deprotonated in NaOH, but becomes monoprotonated upon contact with the alcohol/water interface. In the case of haemin dissolved in methanol, the chloride is replaced by a hydroxyl group to form a monoprotonated species required for the formation of β-haematin. A study done by Orjih *et al.* has shown that erythrocyte membranes incubated with NaOH showed better activity towards β-haematin formation [77]. A control experiment was therefore performed using NaOH mixed with methyl red indicator to determine whether the base is neutralised at the interface. This experiment showed that NaOH is neutralised within 3 seconds of contact with the interface indicating that NaOH is not present during the reaction. This suggests that it plays no role in the β-haematin formation process, but needed to be confirmed.

Furthermore, a solution of haemin was prepared at the same concentration (3.33 x 10^{-3} g/ml) in methanol instead of NaOH to conclusively determine whether NaOH plays any role in β-haematin formation at the interface. A nujol mull IR spectrum of the unwashed product was obtained (**Fig 2.11**). β-haematin forms in the absence of NaOH thus indicating that NaOH does not play any role in the process. It is merely required to solubilise haematin.

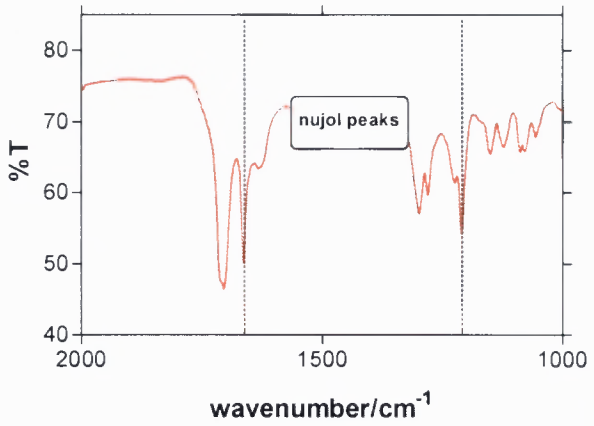

FIGURE 2.11. Infrared spectrum of β-haematin prepared at the pentanol/water (pH 4.8) interface for 30 minutes at 37°C. 0.005 g of haemin was dissolved in pure methanol. Haemin rather than haematin was used as the later is not sufficiently soluble in methanol.

2.5.2.5. The Effect of Ionic Strength on β-Haematin Formation

A 0.05 M citrate buffer containing 0.154 M $NaClO_4$, equivalent to the physiological ionic strength, was used as buffer to confirm that the product forms. $NaClO_4$ salt was used as it does not coordinate with haematin, and therefore will not interfere with the formation of β-haematin. The IR spectrum (**Fig 2.12**) clearly demonstrates that β-haematin is formed under these conditions.

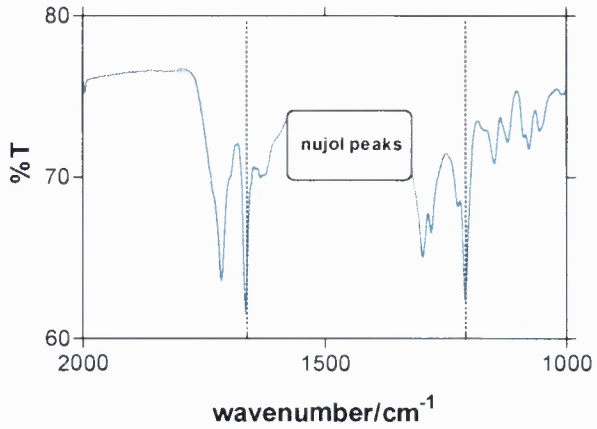

FIGURE 2.12. Infrared spectrum of β-haematin prepared at the pentanol/water (pH 4.8) interface after 30 minutes at 37°C. $NaClO_4$ salt was added into the citrate buffer to make up a final concentration of 0.154 M and the pH was adjusted to 4.8.

2.5.3. The Role of Lipids in the Formation of β-Haematin at the Interface

There is considerable evidence suggesting that the lipids are involved in haemozoin formation [60, 75, 78, 79, 81, 97, 203, 204]. These studies have shown that lipid extracts and commercially available lipids promote β-haematin formation *in vitro*. This study was therefore carried out to investigate the role of lipids in the formation of haemozoin at the lipid/water interface. The choice of lipids used in this study is based on the study done by Fitch (**Table 2.1** and **Fig. 2.1**) [78]. The experiments were carried out by replacing the organic solvent layer with a layer of lipid solution. The product was characterised and conversion of haematin to β-haematin was quantified with 5% pyridine (50% acetone, 0.02 M HEPES buffer, pH 7.5).

2.5.3.1. β-Haematin Formation at the MMG/water Interface: Characterisation

Rac-1-monomyristoylglycerol (MMG) was used as a model lipid (**Fig 2.1**) to investigate the formation of β-haematin at the lipid/water interface due to its structural similarity to pentanol. An incubation time of 30 was used in order to compare the results obtained using MMG to that obtained using pentanol/water, octanol/water and toluene/water interface. The IR spectrum in **Fig 2.13** (**a**) shows characteristic peaks of the iron-carboxylate bond at the 1663 and 1209 cm^{-1} positions. The diffraction lines occur at the same positions as that of β-haematin calculated from the structure of Pagola (**Fig 2.3** (**b**)). The crystals also have the same morphology compared to that of β-haematin formed in this study (**Fig 2.5** and **Fig 2.10**) and of haemozoin isolated from *Plasmodium falciparum* (**Fig 2.5** (**d**)). Furthermore, they are similar in shape and size compared to those of haemozoin (**Fig 2.5** (**d**)) as shown yellow in **Fig 2.13**. However, the crystals appear smaller in size. The results confirm that the product formed in the presence of MMG is indeed β-haematin and is identical to haemozoin.

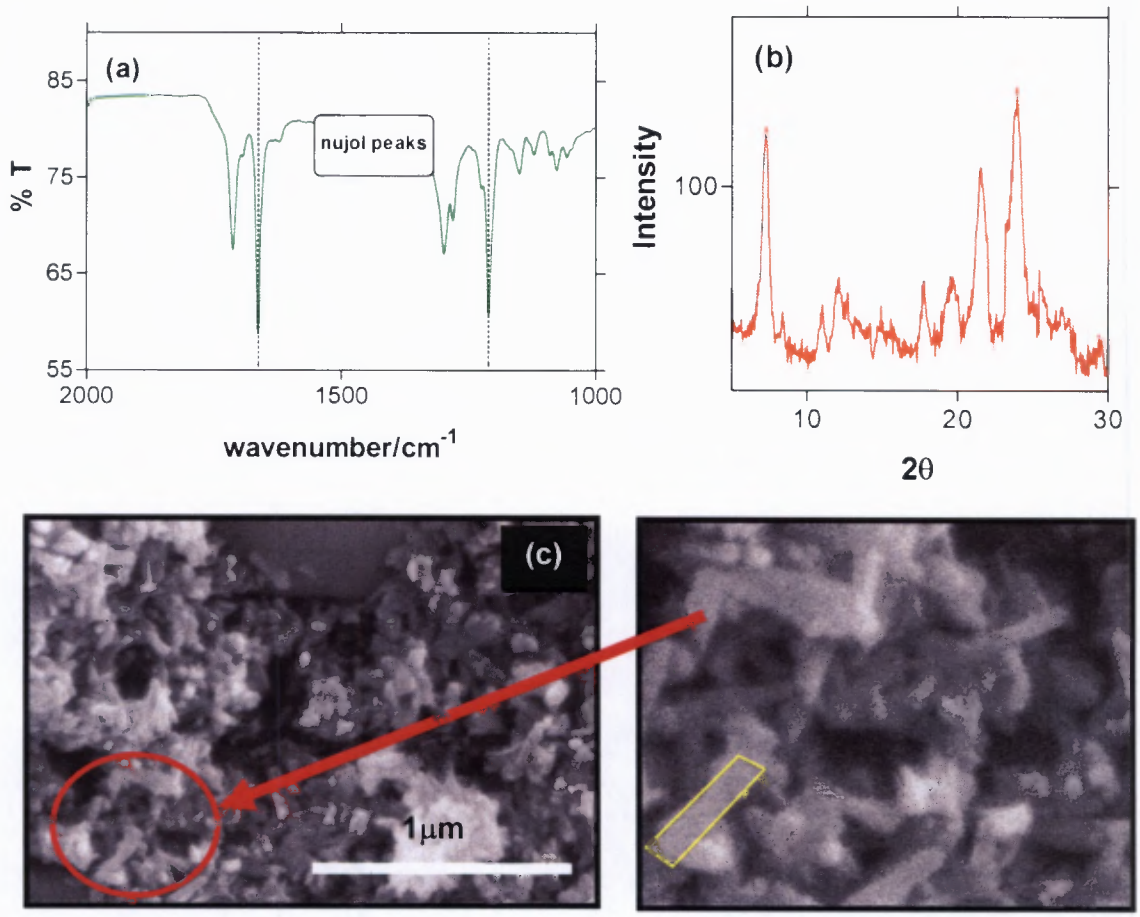

FIGURE 2.13. β-haematin prepared at the MMG/water (pH 4.8) interface incubated for 30 minutes at 37°C. (**a**) Infrared spectrum, (**b**) X-ray diffraction pattern of β-haematin prepared at the lipid/water interface, (**c**) SEM of β-haematin prepared at the lipid/water interface in 30 minutes. The panel on the right is an enlargement of the area in the red circle. The yellow line outlines the shape of the crystal. The large white line shows the scale for the SEM panel on the left.

2.5.3.2. Kinetic Study of β-Haematin Formation at the MMG/water Interface

A kinetic study of β-haematin formation was conducted to investigate the rate of β-haematin formation in the presence of lipids using the interfacial method. The kinetics at the MMG/water interface are shown in **Fig 2.14**. The results show nearly 50% conversion to β-haematin within 5 minutes. The reaction follows a first-order rate law with a rate constant, ***k***, of 0.199 ± 0.032 min^{-1}. Subsequent assays were conducted

using an incubation time of 15 minutes as the kinetic study shows that the reaction is almost complete at this time point. This time point would hopefully allow the reactions to proceed to such an extend that would make it possible to investigate the effects of these variables on β-haematin formation where they result in a decreased yield or drop in reaction rate.

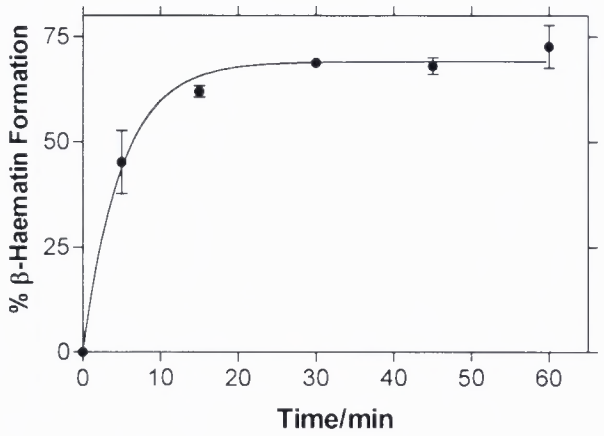

FIGURE 2.14. Kinetics of β-haematin formation at the MMG/water (pH 4.8) interface incubated at 37°C. The reaction follows a first-order rate law with a rate constant k = 0.199 ± 0.032 min^{-1}. Quantification was carried out by centrifugation of the product to obtain the solid material, followed by dissolution of the unreacted haematin with 5% aqueous pyridine at pH 7.5 containing 50% acetone. The absorbance of the solubilised haematin was measured at 405 nm to determine the amount of β-haematin formed. This solution dissolves haematin and not β-haematin. The extinction coefficient, ε = 160000 $M^{-1}cm^{-1}$ was obtained from the Beer's law plot at 405 nm. Error bars correspond to the standard deviations of triplicate runs.

2.5.3.3. The Effect of Lipid Mass on the Rate of β-Haematin Formation

The effect of lipid mass, which is calculated as the mass of lipid present at the interface on β-haematin is shown in **Fig 2.15**. The results show an increase in activity with an increase in lipid mass. This indicates that the formation of β-haematin is concentration-dependent, and therefore, the higher the amount of lipid, the higher the efficiency of β-haematin formation. The maximal activity was reached in the presence of 10 x 10^{-5} g of lipid. The conversion stayed constant thereafter as the reaction had already reached completation at 15 minutes and therefore it cannot proceed further.

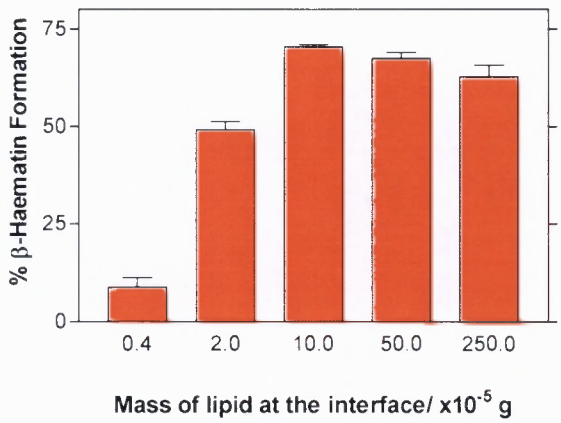

FIGURE 2.15. β-haematin formation at the MMG/water (pH 4.8) interface incubated at 37°C as a function of lipid mass. The reaction mixtures were incubated for 15 minutes. Error bars correspond to the standard deviations of triplicate runs.

2.5.3.4. The Effect of pH on β-Haematin Formation

Variation in the pH of the aqueous medium caused a change in the production of β-haematin in a given time (**Fig 2.16**). A decrease in the formation of β-haematin was observed with an increase in pH. The results show that β-haematin forms between pH 3 and 5.5 with maximum activity observed at pH 3 and 4.8. There is a substantial decrease in product formation at pH 5.5. β-haematin does not form at pH ≥ 6. Haematin stayed in solution at pH 6 and 6.5 and no solid β-haematin product formed. The formation of β-haematin is therefore dependrnt on pH.

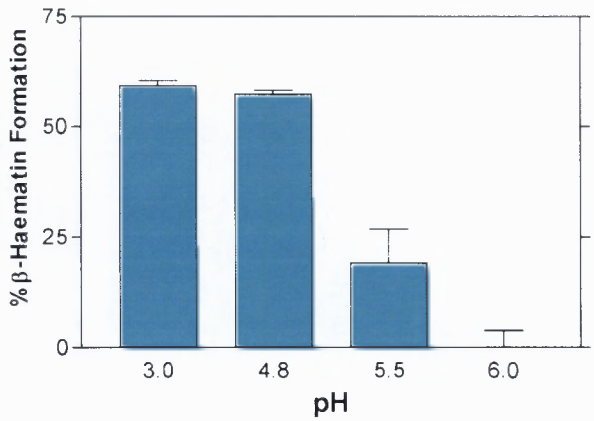

FIGURE 2.16. The effect of pH on β-haematin formation. The reactions were carried out at the MMG/water interface (pH 4.8), incubated for 15 minutes at 37°C. 0.2 ml of 5.0 x 10^{-4} g/ml of lipid was used. Error bars correspond to the standard deviations of triplicate runs.

2.5.3.5. The Effect of Temperature on β-Haematin Formation

The reactions were initially conducted at physiological temperature and later conducted at various temperatures to investigate its effect on the rate of β-haematin formation at the MMG/water interface. The amount of β-haematin formed at the interface in a fixed time increases with an increase in temperature (**Fig 2.17**). A sudden jump appears to occur between 30°C and 37°C. The reaction reached a maximum of 60% conversion in 15 minutes at 37°C. The yield however stayed constant thereafter (37°C — 40°C) as the reaction had already reached completation at 15 minutes and therefore it cannot proceed further.

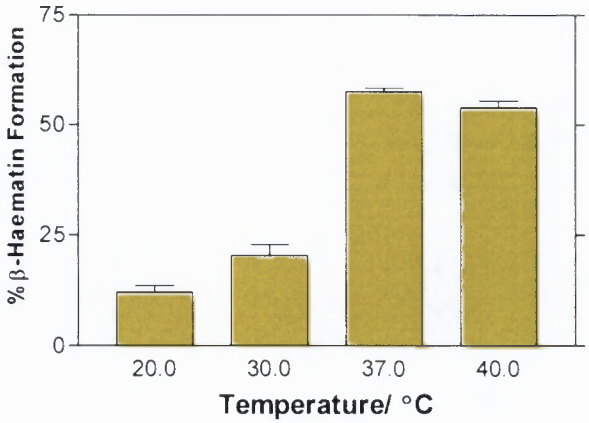

FIGURE 2.17. The effect of temperature on β-haematin formation. The reactions were carried out at the MMG/water interface (pH 4.8), incubated for 15 minutes at 20, 30, 37 and 40°C. 0.2 ml of 5.0 x 10^{-4} g/ml of lipid was used. Error bars correspond to the standard deviations of triplicate runs.

2.5.3.6. The Formation of β-Haematin in the Presence of other Lipids

The formation of β-haematin was investigated in the presence of monoglycerides, diglycerides, phosphoglycerides, glycolipid and cholesterol (**Fig 2.18**). An incubation time of 5 minutes was chosen as initial experiments of conducted using MMG that more than 50% β-haematin formation occurs within 5 minutes at 37°C at the MMG/water interface. This time point would therefore make it possible to determine the yields of β-haematin formed in the presents of other lipids in comparison to MMG. Fitch *et al.* have provided evidence that MOG, DOG, OGP and fatty acids such as

oleic and linoleic were active while cholesterol, TOG, DOPE and DOPC were either inactive or slightly active under their conditions [78]. The results obtained in this study show that most of the lipids are active with MMG, DOPE and DOPC being most active. TOG shows the lowest activity in comparison with less than 30% of the product formed at the TOG/water interface.

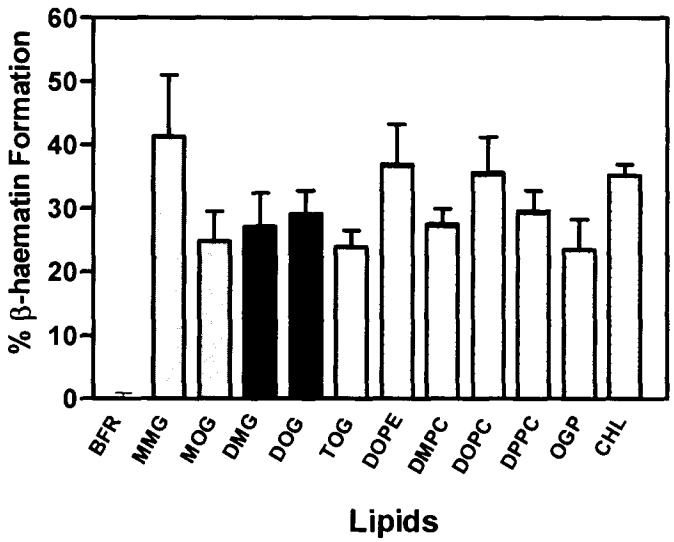

FIGURE 2.18. β-haematin formation in the presence of lipids: monoglycerides (MMG, MOG); diglycerides (DMG, DOG); triglycerides (TOG); phosphoglycerides (DOPE, DMPC, DOPC, DPPC); glycolipid (OGP) and cholesterol (CHL). The reaction systems were incubated for 5 minutes at pH 4.8 and 37°C. BFR: buffer. 0.0025 g of each lipid was dissolved in 5 ml of either 10% acetone/methanol or 10% chloroform/methanol. Error bars correspond to the standard deviations of triplicate runs.

2.5.3.7. The Efficiency of Mixed Lipids in Promoting the Formation of β-Haematin at the Interface

The efficiency of mixed lipids was investigated by carrying out a kinetic study using a mixture of lipids (**Fig 2.19**). The reaction also follows a first-order rate law with a rate constant, ***k***, of 0.049 ± 0.019 min^{-1}. The system is however 4 times slower than the MMG/water system. This system is probably less efficient due to the fact that the mixture contains lipids that are less active (**Fig 2.19**) thus resulting in a decrease in the activity.

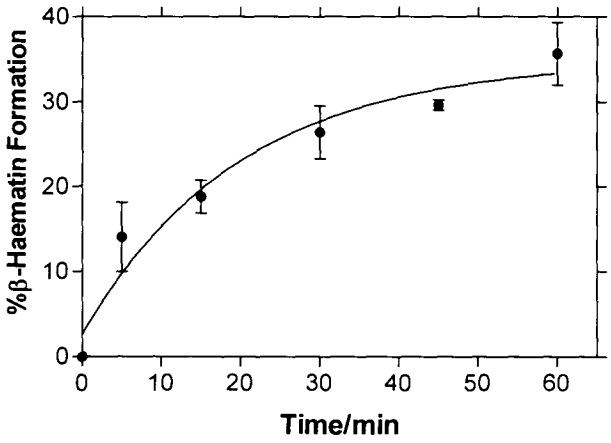

FIGURE 2.19. Kinetic study of β-haematin prepared in an equal mixture of neutral lipids (MMG, MOG, DMG, DOG, TOG and CHL). The reaction system follows a first-order rate law with rate constant k = 0.049 ± 0.019 min^{-1}. 0.2 ml of 8.33 x 10^{-5} g/ml of eacg lipid was used. Error bars correspond to the standard deviations of triplicate runs.

2.6. DISCUSSION

The pentanol/water interface model was initially developed to investigate the possible mechanism of haemozoin formation. Haematin in solution was introduced carefully to the interface using a syringe and the mixture was then incubated for 30 minutes at 37°C. The product was collected and analysed by IR, XRD, solubilisation and SEM. Comparison of the IR, XRD and solubilisation results of the product formed at the pentanol/water interface with that of haemozoin isolated from *Plasmodium falciparum* unequivocally demonstrates that the product is indeed β-haematin and is identical to haemozoin. Furthermore, the results show that a significant amount of β-haematin is formed within 5 minutes. Scanning electron micrographs (SEM) of the product showed that the crystals are very similar to natural haemozoin. The evidence of crystal growth from a common nucleation point supports the idea that the process follows a biomineralisation-like pathway which involves nucleation followed by crystal growth as proposed by Egan *et al.* [89] and Ziegler *et al.* [91]. A similar process is encountered in some microorganisms in which biomineralisation of metal salts often acts as a detoxification mechanism [205, 206]. The solubilisation profiles of the

product in DMSO and $NaHCO_3$ is almost identical to those reported by Slater *et al.* [63] for haemozoin, whereas the crystals formed in acetate solution (Egan *et al.*) are much more easily solubilised in comparison [89]. This has been attributed to the fact that the crystals formed in acetate buffer are smaller and less regular and therefore dissolve more rapidly in solvents. These differences have been attributed to the differences in the conditions in which the crystals are formed rather than atomic structures [60] as XRD and spectroscopic data confirm that the product formed in this study and in acetate buffer is indeed β-haematin, and is chemically identical to haemozoin.

Various conditions were investigated to determine their role, if any, in the formation of β-haematin using the interface model. The results show that the identity of the buffer used does not play any role in the process and that the buffer only acts as an acidic medium presumably to ensure that haematin is in the correct protonation state. In addition, the NaOH base used to dissolve haematin is neutralised very rapidly at the interface, indicating that it is not present during the reaction and, thus it does not play a role in the process. Adjustment of salt concentrations to physiological ionic strength also does not influence the formation of β-haematin. However, no product was formed when the reaction was conducted in pentanol alone or aqueous medium alone, indicating the critical importance of the interface. The reaction proceeded when pentanol was replaced with octanol and toluene. However, the results indicate that the process is highly efficient in pentanol and octanol systems, but not in the toluene system. Knowledge of the characteristics of the interface between two immiscible liquids is of utmost importance for understanding many phenomena in science and biology. The characteristics of the octanol/water interface have recently been studied in detail [200]. The study has shown that the interface formed between the two liquids has considerable resemblance to the surface of a lipid membrane in that the OH groups of the octanol preferentially orientate to form hydrogen bonds with the water molecules while the alkyl chains are aligned in a parallel arrangement resulting in a region that is less polar than that of both bulk liquids. This ordered layer is much bigger than that observed for alkane/water systems which is approximately 1

— 2 nm thick [200]. Pentanol can be expected to form an interface that is similar to that of octanol since they are both structurally similar. The thick water free environment of the aligned alkyl chains may facilitate β-haematin formation by allowing the haematin molecules to assemble without the competition of hydrogen bonds from water molecules. The toluene would on the other hand be expected to behave similarly to an alkane/water system, resulting in a narrow interface which would have a polarity similar to that of the bulk regions [200]. This region therefore might not be large enough to allow haematin molecules to orientate properly to form β-haematin, thus allowing only a fraction of the haematin to convert to β-haematin. Alternatively, the toluene molecules could also π-π stack together forcing the haematin molecules to intercalate in between toluene molecules and so preventing them from interacting with each other.

In order to model the biological system more closely, the organic solvent was replaced with a solution of the lipid *rac* 1-monomyristoylglycerol (MMG). The results confirm that the product formed in this system is indeed β-haematin. However, the crystals appear smaller in size compared to that of haemozoin. This is in agreement with the suggestion that the differences in size or shape of the crystal is not related to atomic structures but rather the conditions under which crystal formation occurs [60]. The results are consistent with that of haemozoin which also varies markedly in different organisms (See details in Chapter 1). Various conditions were investigated in order to provide direct insight into the mechanism haemozoin formation and to further investigate the role of lipids in the process. The effect of the amount of lipid available at the interface was investigated and the results show that the formation of β-haematin is dependent on the amount of lipid. The conversion of haematin to β-haematin levelled off in the presence of larger amounts of lipid at the interface. Fitch *et al* also showed that the formation of β-haematin is dependent on amount of lipid [78]. One explanation is that the lipid forms micelles thus proving a greater surface area at the interface. Therefore, the surface area is small in the presence of a small amount of lipid and becomes greater when the amount of lipid is increased. It would then be expected that increasing the amount of lipid beyond the minimum surface

area required for the quantity of haematin present does not increase the rate of β-haematin formation. A second explanation is that the lipid can dissolve more haematin when a higher mass of lipid is available in the system thus providing a larger soluble reservoir for conversion to β-haematin.

The formation of β-haematin at the interface is dependent on temperature as shown in the results section. The reaction reaches completion in 15 muntes above 37°C. Fitch *et al.* [78] showed that the formation of β-haematin increases continuously up to 70°C. The general increase in rate with temperature is probably due to the fact that there is a greater contact between haematin molecules due to thermal motion.

A change in β-haematin formation was observed when the pH of the buffer was varied. Maximal conversion of about 60% in 15 minutes was observed at pH 3 and 4.8 with a substantial decrease of more than 30% at pH 5.5. No solid β-haematin product was formed at pH ≥ 6. This study shows that the process occurs at an efficient rate at pH 4.8, which interestingly coincides with the most recent estimate of the initial pH of the food vacuole. Studies conducted by Egan *et al.* has also demonstrated the dependence of β-haematin formation under non-physiological conditions on pH [85, 89]. They observed a maximum conversion at pH 3.5 in both acetate medium and benzoic acid [85, 89]. Dorn *et al.* have indicated an optimum pH of between 4 and 5 [75]. The optimum pH therefore varies depending on the medium used to carry out the reaction. Egan *et al.* [85, 89] have interpreted the dependence of β-haematin formation on pH as a direct result of the species of haematin present in the reaction system that would react to form β-haematin. They suggested that the rate of β-haematin formation is maximal under acidic conditions where a monoprotonated species of haematin is most likely to predominate. However, at higher pH (more basic) both propionate groups are deprotonated, while both are protonated at lower pH (very acidic), and so the product cannot form at these pH values. The ionised propionic group is necessary to form the iron-carboxylate linkage

between the haematin subunits and the remaining protonated propionic acid group is required to form hydrogen bonds between the β-haematin dimers in the crystal.

The activity of a further ten lipids was measured. MMG, DOPE and DOPC showed the highest activity with TOG being least active. The interface formed between TOG and water may resemble that of toluene/water system thus forming a small amount of product at the interface. TOG lacks the OH groups needed to act as H-bond donors to form hydrogen bonds with the water molecules (although their ester groups can still act as H-bond acceptors). Kinetic studies of β-haematin was further investigated using MMG alone as well as a mixture of neutral lipids. The reaction system using MMG alone is about four times faster than the latter system. The mixed lipid system might result in a decrease in activity due to the presence of TOG in the mixture. However, the process in both systems occurs at a much faster rate than the methods previously reported in the literature. The most efficient method of β-haematin formation in the presence of lipids reported prior to this study was that of Fitch *et al.* [78]. They have shown a conversion of about 22% β-haematin using MOG. Their reactions were carried out for 2 hours at 37°C under physiological conditions. The MMG/water system is 54 times faster than that reported by Fitch *et al.* [78]. Furthermore, Jackson *et al.* [97] reported a maximum yield of about 50% obtained in a period of 24 hours using MOG. The reaction conducted using the lipid/water system is therefore fast enough to account for haemozoin biosynthesis in malaria parasite. Sullivan and co-workers [98] have also recently identified lipid nanospheres composed mainly of mono-acylglycerol (MAG) in close association with haemozoin inside the food vacuole and reported observing rapid β-haematin formation, although details were not provided. The lipids found in the nanospheres, predominantly MPG and MSG are very similar to MMG used in this study, differing only in having respectively two and four additional CH_2 groups in the alkyl chain.

2.7. SUMMARY OF KEY FINDINGS

The interfacial method involves the formation of β-haematin either at the alcohol/water interface or lipid/water interface. Several conditions were investigated to determine their role in β-haematin formation at the interface. It was found that β-haematin:

- Forms at the pentanol/water interface as shown by IR, XRD, solubility studies and SEM. Furthermore, it forms more efficiently at the pentanol/water interface and the octanol/water interface than at the toluene/water interface. This difference was attributed to the structural differences of the solvents. Pentanol and octanol form interfaces that resemble lipid membrane surfaces, providing an environment that promotes β-haematin formation much more strongly than the toluene/water interface which is probably more like that of the other organic/water systems.
- Forms at the interface under physiological conditions with citrate and MES buffer in the aqueous layer. The buffer only serves as an acidic medium. β-haematin however, does not form in aqueous medium alone or organic solvent alone without the interface. A suitable organic/water interface is therefore essential for β-haematin formation. Further evidence supporting this has been obtained by resonance Raman spectroscopy using a probe with a resolution of 1 μm. This confirms that the product is present within 2 μm of the interface (data collected by Bayden R. Wood and Shveta Pandiancherri, Centre for Biospectroscopy, Monash University, Australia as part of a collaborative project) [207].
- Forms at the lipid/water interface under physiological conditions at a rate that is sufficient to account for haemozoin formation *in vivo*.
- Forms under acidic conditions at the estimated pH of the food vacuole (pH 4.8) and does not form at higher pH (pH ≥ 6). **Fig 2.20** shows the haematin protonation states expected under acidic conditions comparable to the food vacuole pH (**Fig 2.20** (**a**)) and under more basic conditions (**Fig 2.20** (**b**)). For β-haematin to form, the deprotonated carboxylate group (**Fig 2.20** (**a**)) must

coordinate to the Fe(III) centre of the adjacent haematin molecule while the remaining protonated carboxylate group forms hydrogen bonds between the two dimers. Since the pKa of both propionic groups has not yet been established, it is not possible to deduce the pH at which these species are present. However, it is likely that the monoprotonated species can form readily at pH 3 as a result of competition of Fe(III) for propionate group, which would result in β-haematin formation as observed in this study. This species is also available and predominant at an optimum pH of 4.8. At low pH (very acidic) the diprotonated species dominates, thus the reaction is likely to be slower under these conditions. The concentration of H^+ is also probably sufficient to prevent binding to Fe(III). This has been shown in two previous studies on β-haematin formation in aqeous acetate and benzoate [85, 89]. At higher pH (pH ≥ 6) the reaction either does not proceed or is very slow as both carboxylate groups are deprotonated (**Fig 2.20** (**b**)) preventing hydrogen bonds from forming between the dimers.

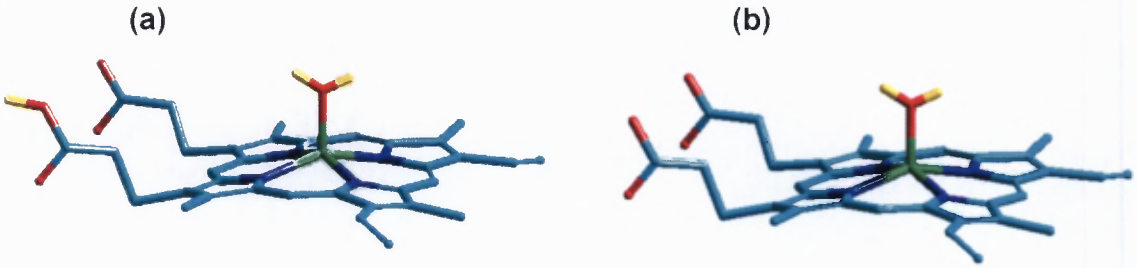

FIGURE 2.20. Protonation states of haematin propionic groups under different pH conditions. (**a**) monoprotonated under more acidic conditions and (**b**) deprotonated on the propionic acid groups under more basic conditions. The hydrogens atoms are represented in yellow. Above pH 7.5 the axial H_2O ligand will also deprotonate [34].

2.8. CONCLUSIONS

The mechanism of haemozoin biosynthesis in the malaria parasite, *Plasmodium falciparum* has remained unknown up to date. Several speculations and hypotheses have been made which include the involvement of lipids, among them. The studies were performed by monitoring the formation of β-haematin, a synthetic counterpart of haemozoin *in vitro* in model systems. However, the rates of formation under these earlier studies are too slow under physiological conditions. The reason for this is that haematin has always been introduced into the acidic aqueous medium before the reaction is initiated, which results in rapid precipitation of haematin. The solid material redissolves slowly and is then converted to β-haematin. Such a precipitate has not been observed in the food vacuole of the parasite. Therefore, it is unlikely that this process represents the formation of haemozoin *in vivo*. In the current study, the role of lipids was explored by developing a lipid/water interface method to mimic the biological system. The results obtained confirm that the product formed in this system is β-haematin and that an interface is required for rapid β-haematin formation under physiological conditions. The rate of formation is sufficient to account for haemozoin formation *in vivo*. These results demonstrate that lipids are likely to play an important role in haemozoin formation without the need of an enzyme or a catalytic promoter. On the basis of this evidence, a model can be proposed to account for the mechanism of haemozoin biosynthesis *in vivo*. Combined with the recent observations of the lipid nanospheres inside the food vacuole of malaria parasite by Pisciotta *et al.* [98], the findings make a compelling case for haemozoin formation being a self-assembly process at the surface of lipid nanospheres in the food vacuole (**Fig 2.21**).

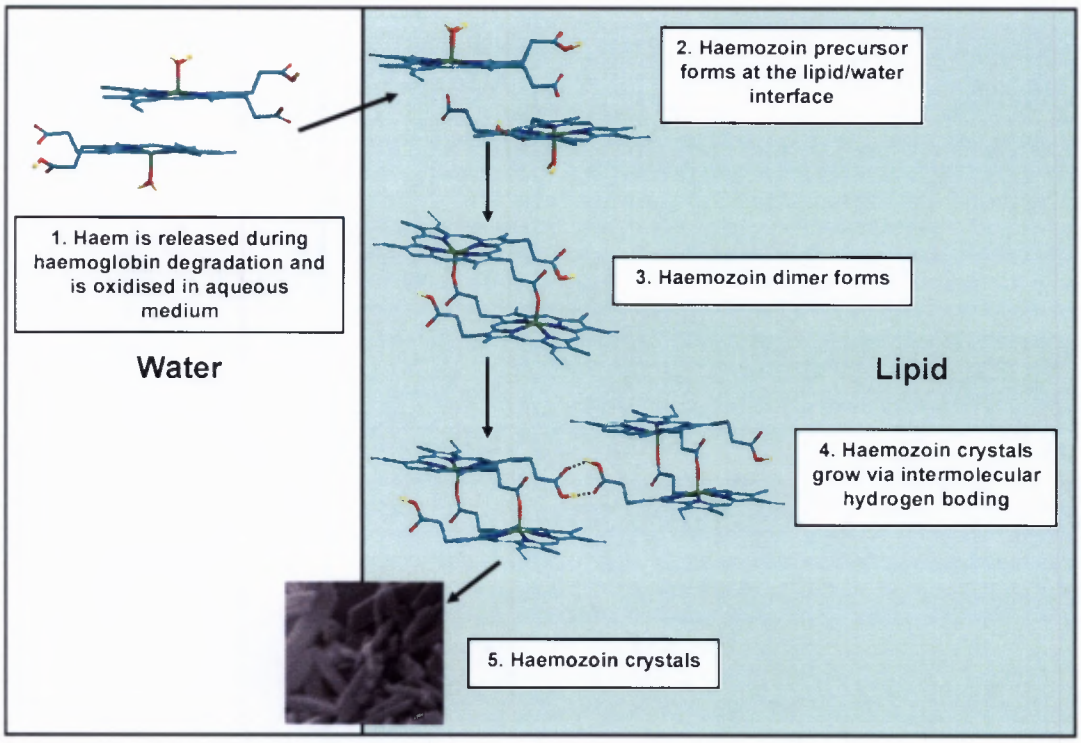

FIGURE 2.21. Proposed mechanism of haemozoin formation at the lipid/water interface *in vivo*. (**1**) Haematin dimerises in aqueous solution [34] and then (**2**) rapidly forms the β-haematin precursor at the lipid/water interface. (**3**) β-haematin precursor then assembles at the interface to form a haemozoin dimer. Hydrogen bonds between the protonated propionic groups then form (**4**) to finally build haemozoin crystals (**5**).

A molecular dynamics (MD) simulation was performed by Dr Jeff Chen to provide a direct insight into the mechanism of haemozoin formation. The simulation was performed in vacuum and in the presence of water molecules. In vacuum, the two haematin molecules interact and rapidly form an intermolecular precursor of the β-haematin dimer (**Fig 2.22** (**a**)). Conversion of the precursor dimer to the β-haematin dimer can then be envisaged to occur by bond formation of the propionate groups with the Fe(III) centre and release of coordinated water molecules from the opposite face of the porphyrin and also by hydrogen bond formation between the protonated propionic groups of the resulting dimer (**Fig 2.22** (**b**)). However, in the computational study, the β-haematin precursor disintegrates in the presence of water (**Fig 2.22** (**a**)), which would explain why β-haematin does not form in water as shown in this study.

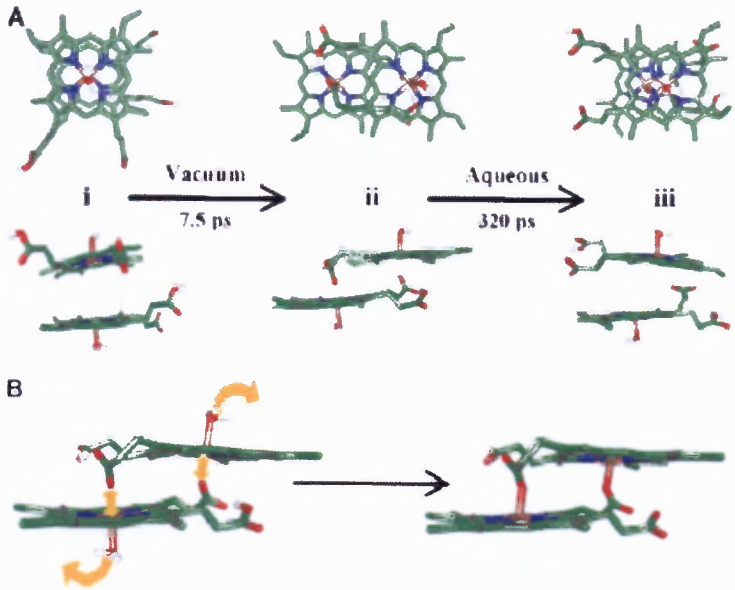

FIGURE 2.22. (**a**) Molecular dynamics simulation of the interaction of two monoprotonated haematin molecules (in the protonation state expected in the acidic food vacuole). The dynamics were started with the molecules placed in a back to back conformation with the propionate and propionic acid groups extended far apart (i). The two molecules rapidly form the β-haematin precursor in vacuum (ii). (**b**) Illustration of bond formation of the propionate groups with the Fe(III) centre followed by the release of water to form β-haematin from the precursor (ii). (iii) Dynamics were performed in a cube of water starting from the β-haematin precursor. The propionate groups move away from the Fe(III) centres to interact with water molecules to form the dimer in (iii). Water molecules are removed for clarity. Total simulation times were 5 ns in each case [207].

In vivo, the hydrophobic haematin dimer would enter the lipid layer producing the β-haematin precursor (**Fig 2.21**). This is followed by the release of water into the bulk water phase together with bond formation between the Fe(III) centre with the propionate groups. Whether the release precedes, is simultaneous with or follows bond formation depends on whether the reaction is dissociative, interchange or associative. Hydrogen bonds between the protonated propionic acid groups then form in the hydrophobic environment of the lipid to form haemozoin crystals. The formation of haemozoin therefore does not require an enzyme but requires a lipid/water interface environment for β-haematin to self-assemble.

CHAPTER 3.

THE DISTRIBUTION OF IRON IN CHLOROQUINE TREATED PLASMODIUM FALCIPARUM

THE DISTRIBUTION OF IRON IN CHLOROQUINE TREATED PLASMODIUM FALCIPARUM

3.1. INTRODUCTION

There is still dispute over the precise mechanism of action of quinoline antimalarials. However, it has been shown that 4-aminoquinolines such as chloroquine (CQ) interact with Fe(III)PPIX to prevent haemozoin formation *in vitro* and it is believed that in malaria parasites it thus causes a build-up of toxic Fe(III)PPIX or its complex with CQ (Chapter 1). The toxic Fe(III)PPIX can potentially bind to membranes, consequently compromising their integrity either by altering physical properties of the membranes or through redox processes. Their mode of action therefore relies on the digestion of endocytosed haemoglobin in the parasite food vacuole [208]. Their actions have been investigated extensively by visualisation of structural changes in the morphology of the parasite using mainly light microscopy and transmission electron microscopy (TEM). It has been shown that 4-aminoquinolines are stage specific in their activity and that they affect mainly the trophozoite stage of the parasite, but do not alter the ring and the schizont stage or merozoites [209, 210]. The TEM studies have shown that upon administration of 4-aminoquinolines, the changes in the morphology of the parasite observed included swelling of the food vacuole [211, 212], loss of pigment granules (haemozoin, Hz) [110], pigment clumping [213][112], and an increase in haemoglobin inside the treated parasite [214, 215]. Other changes include the presence of multimembrane structures (MMS) in close contact with the food vacuole and Maurers' clefts in large quantities compared to the control [111]. Olliaro *et al.* attributed this increase in MMS to a decrease in the demand for membrane lipids by the parasite [111]. Parasite growth is retarded in the presence of high concentrations of chloroquine, therefore the demand for membrane lipids would decrease. Furthermore, some damaged parasites lose their contact with the parasitophorous vacuole membrane (PVM), leaving a space filled with granular material separating the parasite and the red blood cell [111].

Other studies have reported a build-up of small vesicles containing electron-dense material within the parasite food vacuole and cytosol [112, 214, 216, 217]. The presence of vesicles has been ascribed to an inhibition of vacuolar hydrolase by the drug, thus preventing fusion of the transport vesicles with each other or the food vacuole [216]. This would thus result in a build-up of undigested haemoglobin [214], which would result in parasite starvation and ultimately death due to a reduction in the levels of digested haemoglobin. The vesicles contain no pigment, indicating that little or no digestion of haemoglobin takes place inside them [216]. These observations therefore suggest that chloroquine and other 4-aminoquinolines interfere with the feeding mechanism of the parasite. Olliaro *et al.* [218] and Hoppe *et al.* [215] have however shown that the presence of vesicles is not unique only to drug treated parasites, but that they are also present in drug free parasite. Hoppe *et al.* [215] have recently shown that the vesicles contain undigested haemoglobin using immunofluorescence. However, further evidence is required to gain a clearer picture of the distribution as well as the types of iron species present inside the transport vesicles. For example, is undigested haemoglobin the only form of Fe present in the chloroquine treated parasites, or can free Fe(III)PPIX also be detected? Is iron confined only to the small vesicles, or is it more widely distributed in the parasite?

A recent study has shown using electron spectroscopic imaging (ESI) with transmission electron microscopy (TEM) and chemical analysis the distribution of elemental iron in untreated malaria parasites [46]. The results show that the parasite contains ± 61% of the total iron in the infected red blood cell (RBC) of which ± 92% is located in the food vacuole and ± 89% of this is in the form of haemozoin [46] in late trophozoites. Mössbauer spectroscopy confirmed that at least 95% of the parasite iron is in the form of haemozoin, with no other detectable iron species present. Little work has been done, however, to investigate the distribution of iron in drug treated parasitised red blood cells. This study was therefore carried out to investigate: (i) the morphological changes induced by chloroquine, (ii) the redistribution of iron after chloroquine treatment if any and (iii) to confirm that that the transport vesicles observed in chloroquine treated malaria parasites contain iron, as would be expected

if they contain undigested haemoglobin, using electron spectroscopic imaging (ESI) and transmission electron microscopy (TEM) techniques to further understand the mechanism of action of 4-aminoquinolines.

3.2. MATERIALS

The materials used in the study are listed in **Table 3.1**. They were of AR or other high purity grade and were used without purification.

TABLE 3.1. A list of materials obtained from commercial suppliers

Materials	Commercial Supplier
RPMI 1640 culture medium powder	Biowhittaker
NaOH	Saarchem
N-2-[hydroxyethyl]piperizine-N'-2-[ethanesulfonic acid] (HEPES)	Sigma-Aldrich
Glucose	Sigma-Aldrich
Hypoxanthine	Sigma-Aldrich
Albumax II	Inuitrogen
Sodium bicarbonate	Sigma-Aldrich
D-sorbitol	Sigma-Aldrich
Chloroquine diphosphate	Sigma-Aldrich
Giemsa stain	Merck
PBS pellets	Oxoid
Percoll	Sigma-Aldrich
Microscopy Immersion Oil	Merck
Glutaraldehyde	Agar Scientific
Osmium tetroxide (OsO_4)	SPI CHEM
Agarose	Sigma-Aldrich
Ethanol	Merck

TABLE 3.1. A list of materials obtained from commercial suppliers (*continues*)

Materials	Commercial Supplier
Acetone	Saarchem
Spurr's epoxy resin	Agar Scientific
Uranyl acetate	BDH
Sodium citrate	Merck
Lead nitrate	Merck

3.3. SAMPLE PREPARATION

3.3.1. Preparation of the RPMI 1640 Culture Medium (Complete Medium)

The RPMI 1640 culture medium was prepared by dissolving RPMI 1640 culture medium powder (52 g), glucose (20 g), HEPES (30 g), hypoxanthine (0.44 g, dissolved in a minimum volume of 1 M NaOH), albumax II (25 g) and 6 ml of gentamycin (40 x 10^{-3} g/ml) in 5000 ml of distilled water. The solution was sterilised by filtration under pressure through a 0.22 μm filter into 500 ml autoclaved bottles. The medium was then stored in the fridge at 4°C until further use. The culture medium was supplemented with 5% sodium bicarbonate (8.4 ml of sodium bicarbonate to every 200 ml of RPMI 1640 culture medium) to obtain a complete medium which was used for culturing.

3.3.2. Preparation of the RPMI 1640 Wash Medium

The wash medium was prepared in the same way as the RPMI 1640 culture medium, but without the albumax. The solution was sterilised by filtration under pressure through a 0.22 μm filter into 100 ml autoclaved bottles. The medium was then stored at 4°C until further use. The solution was also supplemented with 5% sodium bicarbonate just before use.

3.3.3. Preparation of 5% Sodium Bicarbonate

5% sodium bicarbonate was prepared by dissolving 50 g of sodium bicarbonate in 1000 ml of distilled water. The solution was then sterilised by filtration through a 0.22 μm filter into 100 ml autoclaved bottles and was stored at 4°C.

3.3.4. Washing of the Human (O^+) Red Blood Cells (RBCs)

The blood used in the experiments was obtained from the Western Cape Province Blood Transfusion Service. The blood was washed with RPMI 1640 wash medium (supplemented with 5% sodium bicarbonate) to remove anticoagulant before it was used. A wash medium was mixed with RBCs (1:1 ratio) into a sterile centrifuge tube and centrifuged at 2000 rpm (revolutions per minute) for 5 minutes. The supernatant was removed by aspiration. The same amount of wash medium was added to the remaining RBCs pellet and centrifuged again and stored at 4°C until further use.

3.3.5. Preparation of 5% D-Sorbitol

5% D-sorbitol was prepared by dissolving 50 g of D-sorbitol in 1000 ml of distilled water. The solution was sterilised by filtration through a 0.22 μm filter into 100 ml autoclaved bottles. The solution was then stored at 4°C.

3.3.6. Preparation of the Giemsa Stain

The giemsa stain was prepared by diluting the concentrated stain 1:10 in PBS. PBS was prepared by dissolving 10 PBS pellets in 1000 ml of tap water.

3.3.7. Preparation of 5x RPMI/25% D-Sorbitol

1.05 g of RPMI 1640 powder and 5.0 g of D-sorbitol were dissolved in distilled water and the pH of the solution was adjusted to 7.4. The solution was made up to 20 ml with distilled water and then sterilised by filtration with a 0.22 μm filter and stored at 4°C.

3.3.8. Preparation of 60% and 80% Percoll

60% percoll solution was prepared by mixing 6 ml of percoll with 2 ml of 5x RPMI/ 25% D-sorbitol and 2 ml of wash medium. 80% percoll was prepared mixing 8 ml of percoll with 2 ml of 5x RPMI/ 25% D-sorbitol. The solutions were stored at 4°C until further use.

3.4. EXPERIMENTAL PROCEDURES

3.4.1. *Plasmodium falciparum* Culture *in vitro*

A chloroquine (CQ) sensitive strain (D10) of *Plasmodium falciparum* was used in this study. The strain is derived from FQC-27 obtained from Papua New Guinea [219]. The parasites were cultured using a modified version of the methods of Trager and Jensen [220] and Haynes *et al.* [221]. The parasites were maintained in complete medium to which O^+ RBC was added in the trophozoites stage to maintain a 2 — 10% parasitemia (pRBC/total RBC) and a 2 — 4% haematocrit (RBC/total volume of complete medium). The cultures were grown in 200 ml flat bottom flasks and incubated at 37°C with a gas environment of 1% O_2, 3% CO_2 and N_2. The medium was changed daily and a giemsa smear was made to monitor the progress. The smear was fixed on a glass slide with methanol and stained with giemsa stain for 2 — 5 minutes. The slide was then washed with water, air-dried and viewed under a light microscope, using 100 x oil-immersion objective.

3.4.2. Synchronisation of *Plasmodium falciparum* Culture *in vitro*

The parasite culture was synchronised using a 5% D-sorbitol solution while most of the culture was in the ring stage [222]. 20 ml of this solution was added to the parasite pellet and was left standing for 10 minutes. The synchronised pellet was centrifuged at 1200 rpm for 4 minutes. The supernatant was removed and the culture was returned to the culture medium and incubated at 37°C (Section 3.4.1).

3.4.3. Enrichment of *Plasmodium falciparum* Cultures

The procedure was used to separate trophozoite/schizont infected red blood cells from uninfected red blood cells. 0.2 ml of the 80% percoll solution was added to a 1.5 ml eppendorf tube. 0.2 ml of the 60% percoll was then layered carefully on top of the 80% percoll solution. This was followed by a layer of 0.1 ml of parasitised red blood cells. The mixture was centrifuged at 10 000 rpm for 20 minutes. The trophozoite- and schizont-infected RBCs were recovered from the 60% and 80% percoll interface and washed with 10 ml and 5 ml of RPMI complete medium, sequentially and centrifuged each time at 1200 rpm for 3 minutes. The resulting pellet had more than a 90% parasitemia.

3.4.4. Preparation of *Plasmodium falciparum* for Electron Microscopy

The culture was maintained as outlined in Section 3.4.1 and synchronised first to obtain a culture containing mainly the ring stage. As tight synchronisation was not achieved, some schizonts were present. This turned out to be advantageous as it allowed investigation of the effect of chloroquine on merozoite invasion as well as on ring stage parasites after considerable CQ exposure (16 hours). The remaining pellet was divided into four separate 50 ml flasks (1% haematocrit and 10 — 15% parasitemia). The first flask contained no drug (control), the second, third and fourth flasks contained final concentrations of 30, 60 and 120 nM of chloroquine, respectively. Samples (15 ml) were taken from each flask at 16, 24 and 32 hours after addition of chloroquine and centrifuged in 10 ml centrifuge tubes at 1200 rpm for 5 minutes and the supernatant was removed. The remaining pellet (0.1 ml) was enriched (Section 3.4.3) and then processed for electron microscopy as described below. The remaining cultures were gassed and put back into the incubator after sampling at 16 and 24 hours.

The samples for transmission electron microscopy (TEM) and electron spectroscopic imaging (ESI) were prepared by transferring the enriched pellet (0.1 ml) into a 1.5 ml eppendorf tube and suspending with an equal volume of 5% (v/v) glutaraldehyde in PBS (pH 7.4) for 10 minutes at room temperature. Glutaraldehyde was used to fix the

RBC membrane to prevent lysis during processing. 1 ml PBS was added to the samples and left for 5 minutes. The samples were then centrifuged for 45 seconds at 3000 rpm. The supernatant was aspirated and the pellet was resuspended in 1 ml of 2.5% (v/v) of glutaraldehyde in PBS solution and left at 4°C overnight for further fixation. The samples were post-fixed with 1% osmium tetroxide (OsO_4) in PBS for 1 hour. Samples were then washed twice with distilled water and immobilised in 1% agarose. The solidified samples were cut into 1 mm cubes and dehydrated with increasingly concentrated ethanol solutions in water (30% — 95% for 5 minutes, then twice with 100% ethanol for 10 minutes) and twice with acetone for 10 minutes. Acetone was gradually replaced with Spurr's epoxy resin (Wirsam) over two days and allowed to harden for 16 hours at 60°C. The resulting blocks were trimmed and cut into ultrathin sections with a Reichert Ultracut S ultratome using glass knives and mounted on 200 mesh square copper grids. The copper grids were stained with 1% uranyl acetate and 1% lead citrate (prepared according to the method of Reynolds) [223] for 10 — 20 minutes and washed thoroughly with distilled water.

Transmission electron microscopy (TEM) and electron spectroscopic imaging (ESI) were performed on the samples on a LEO 912 OMEGA transmission electron microscope to visualise the morphology of both chloroquine treated and untreated parasites and to determine the iron distribution in both samples. The ESI method is based on energy measurements of transmitted beam electrons for imaging. The transmitted electrons can interact with the specimen either elastically or inelastically. Inelastic scattering process occurs when a beam of electrons transmit energy to the sample thus releasing energy in the process (ΔE) which can be displayed by the energy loss spectrum. In some cases, a beam of electrons can transmit enough energy to excite the electrons to a higher energy level or to eject them completely from the atomic shell (ionisation). These energies are characteristic for each individual atom type. Therefore energy losses produced can provide information about the elemental composition of the sample under investigation. **Fig 3.1** shows an electron energy-loss spectrum of elemental iron. The figure shows a background energy loss obtained from non-specific scattering by electrons in the field of the

sample electron (black trace). Further energy is lost when the electron beam interacts with the Fe core electrons from either the second or the third energy level of the L-shell (Fe L_2 and Fe L_3) (green trace). The energy difference between the two traces therefore gives an energy-loss spectrum of Fe (blue trace).

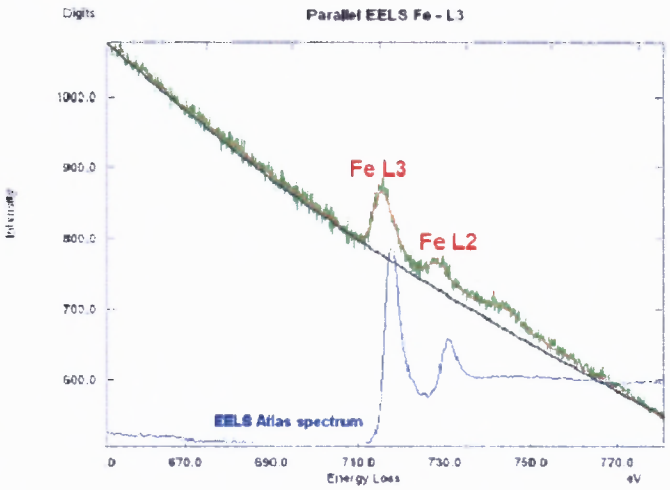

FIGURE 3.1. Energy electron-loss spectrum of the background (black trace) obtained from non-specific scattering by electrons in the field of the sample electron, core electrons of elemental iron from either the second or the third energy level of the L-shell (Fe L_2 and Fe L_3) (green trace) and the energy difference between the two traces (blue trace).

The iron distribution images in this study were obtained using a three-window power law method in which two images were recorded at energies before the Fe L_3 absorption edge, namely at 658 eV and 688 eV respectively and the third was recorded after the energy offset at 719 eV. The background image is then predicted by extrapolating the two images collected at 658 eV and 688 eV. The extrapolated background image is then subtracted from the image collected at an energy offset of 719 eV resulting in an elemental map with intensity values proportional to the amount of iron in a particular section. All images were collected using a slit width of 19 eV on a Tiedtz charge-coupled-devise camera (1024 x 1024 pixels) and processed with analySIS software from Soft Imaging System using a two window difference method to obtain the element-distribution image.

3.5. RESULTS

Electron microscopic (EM) techniques have proven to be reliable in many studies that require visualisation of biological materials. However, the technique has some limitations that should be noted. The first limitation is the possible presence of artefacts associated with sample preparation methods. The parasites being analysed are orientated randomly, therefore the plane of sectioning through the parasite is arbitrary, and a three-dimensional structure cannot be reached from analysis of a single image. In principle, levels can be cut through a sample to obtain several sections, but this is usually very difficult to achieve in practice. Furthermore, the copper grid obscures parts of the section which occasionally makes it difficult to visualise the entire section of any particular parasite. ESI intensity depends on the amount of iron present in the path of the electron beam, which depends on concentration as well as the thickness of the section which may not always be uniform. Therefore, ESI images provide evidence only of apparent concentration of elemental iron. Nonetheless, if variations in the thickness of the sections are kept at a minimum, the images do provide a qualitative picture of iron concentration. This is borne out by the rather uniform appearance of the red cell cytoplasm in images obtained of parasites at similar stages in the life-cycle.

A further potential pitfall is that sample processing could also result in redistribution of elemental iron. However, the distribution of iron in untreated parasites is confined to the red blood cell and haemozoin crystals in all of the images viewed. Therefore, the redistribution of iron only in treated parasites does not seem likely to arise from sample processing, but rather appears to be a genuine reflection of the changes in the parasite. Finally, ESI only shows where elemental iron is located and is not capable of identifying the chemical environment of the iron. This can be achieved using, for example, Mössbauer spectroscopy and it was in fact intended to submit a sample of treated parasites for such measurements. Unfortunately however, a new ^{57}Co source was required for the Mössbauer instrument and delivery delays precluded this experiment from being performed before submission of this thesis.

Despite these limitations, the selected images shown below are representative of the life cycle of *Plasmodium falciparum* and the distribution of elemental iron in both treated and untreated malaria parasites. In the associated discussion, the caveats mentioned above must however be kept in mind.

3.5.1. Study of the Life Cycle of *Plasmodium falciparum* using TEM and ESI

Electron spectroscopic imaging (ESI) together with transmission electron microscopy (TEM) was used to study the life cycle of *Plasmodium falciparum* inside the red blood cell (**Fig 3.2** — **Fig 3.4**). The life cycle starts when merozoites invade red blood cells by invaginating the red blood cell (RBC) membrane [224]. The merozoites are ovoid in shape with an apical prominence (**A**) [225]. **Fig 3.2** shows a merozoite after invasion. The merozoite transforms into thin discoidal or cup-like ring forms (**Fig 3.3**). The ring eventually changes shape and size to form a more spherical trophozoite.

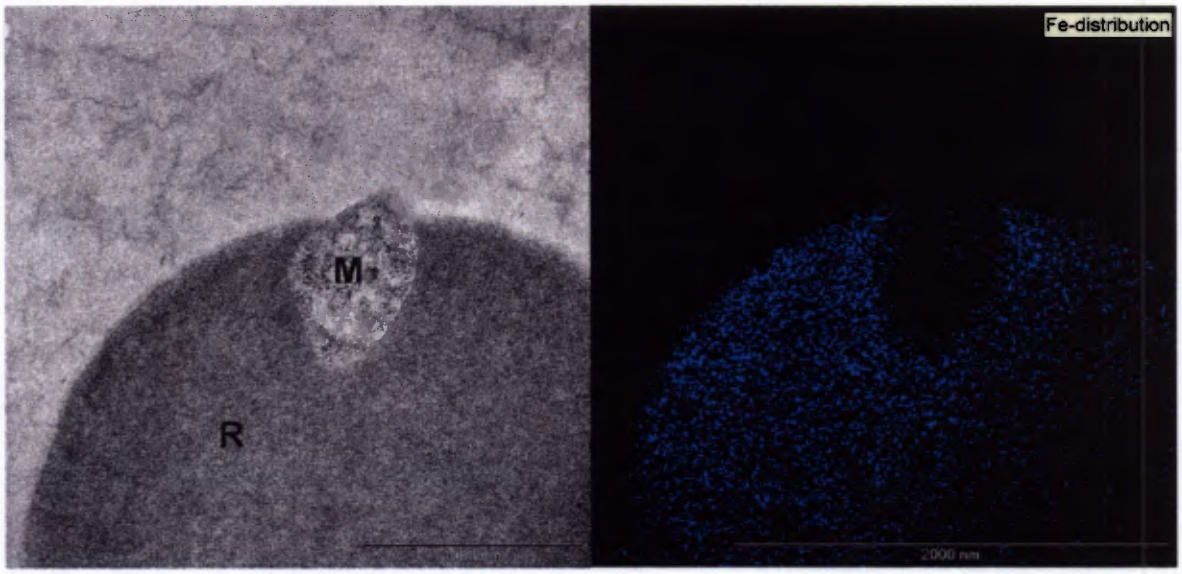

FIGURE 3.2. A transmission electron micrograph (left) and electron spectroscopic image (right) showing a merozoite after red blood cell invasion. The distribution of iron (blue) demonstrates that it is concentrated almost exclusively within the RBC cytoplasm. The merozoite is devoid of iron in comparison to the level in the RBC cytoplasm. The labelled structures are the RBC cytoplasm (**R**) and merozoite (**M**).

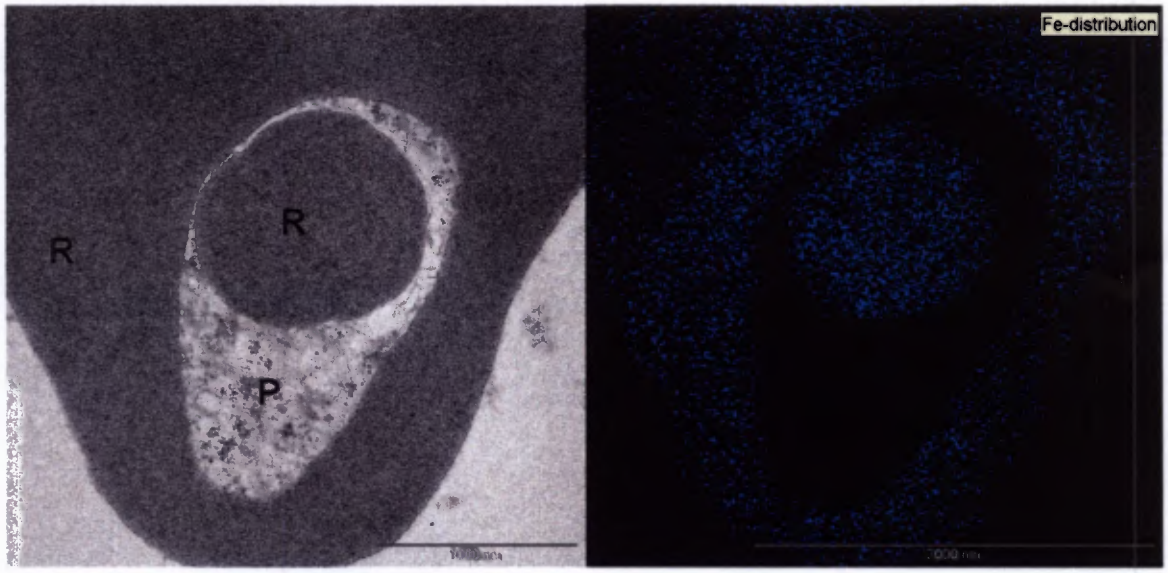

FIGURE 3.3. A transmission electron micrograph (left) and electron spectroscopic image (right) of an untreated ring-infected red blood cell. The distribution of iron (blue) demonstrates that it is concentrated almost exclusively within the RBC cytoplasm. The ring is devoid of iron in comparison to the level in the RBC cytoplasm. The labelled structures are the RBC cytoplasm (**R**) and the parasite cytosol (**P**).

The trophozoite contains many additional features including the food vacuole (**Fig 3.4** (**a**) and **Fig 3.4** (**b**)). While inside the red blood cell, the parasite ingests and digests haemoglobin releasing potentially toxic Fe(III)PPIX which is incorporated into haemozoin crystals (**H**) inside the food vacuole (**F**) (**Fig 3.4** (**a**) and **Fig 3.4** (**a**)). Cell division occurs during the late trophozoite stage to form schizonts and ultimately merozoites [225]. Finally, the merozoites are released and invade more red blood cells to start a new cycle. The iron distribution images (blue) show that the merozoites (**Fig 3.2**) are almost devoid of iron in comparison to the high concentration in red blood cell cytoplasm. **Fig 3.3** also shows that the ring is devoid of iron.

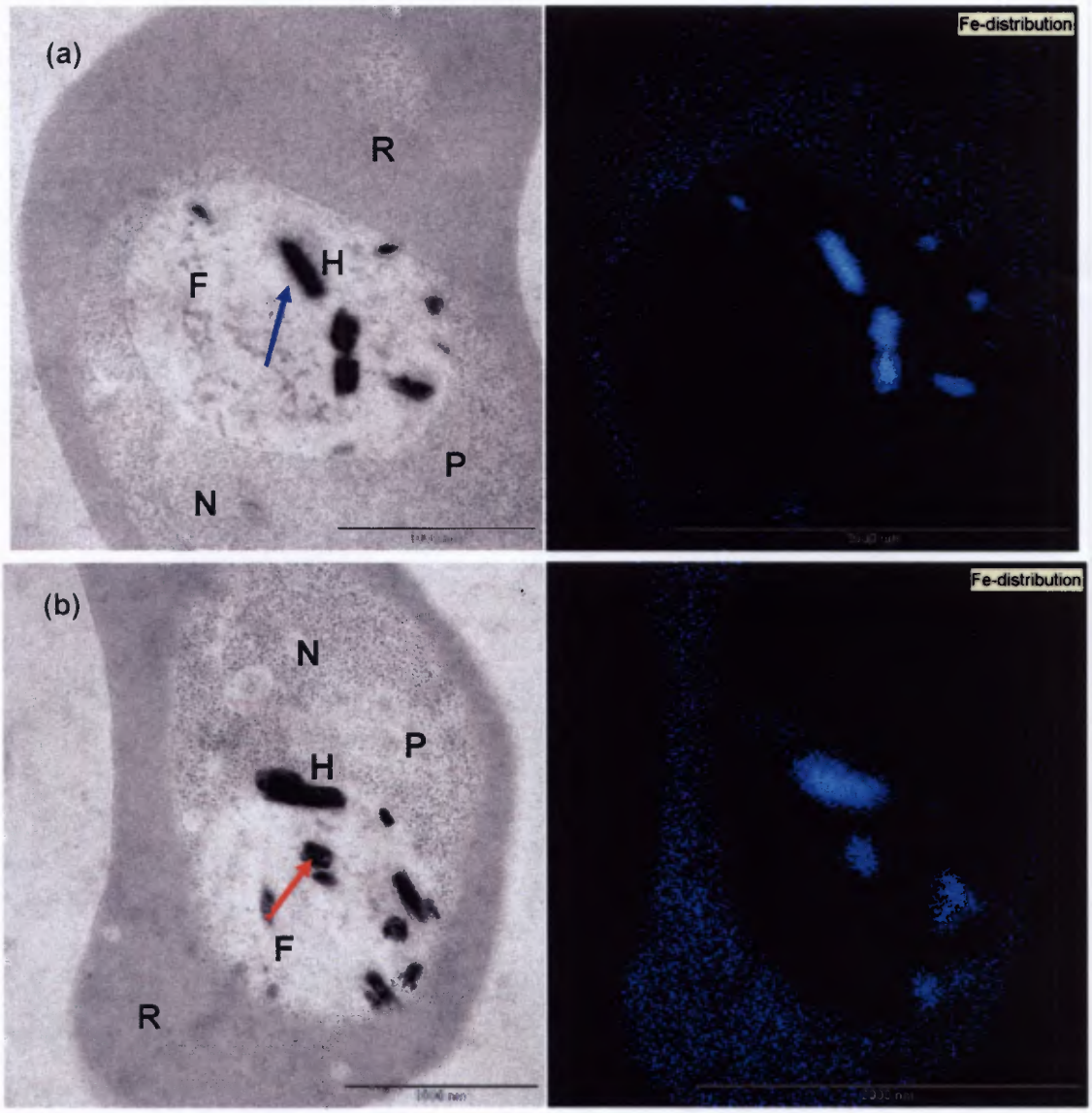

FIGURE 3.4. (**a**) and (**b**) Transmission electron micrographs (left) and electron spectroscopic images (right) of untreated trophozoite-infected red blood cells. The distribution of iron (blue) demonstrates that it is concentrated almost exclusively in haemozoin crystals within the parasite food vacuole. The rest of the parasite is devoid of iron in comparison to the level in the RBC cytoplasm. The labelled structures are the RBC cytoplasm (**R**), the parasite cytosol (**P**), the parasite food vacuole (**F**), haemozoin crystals (**H**) within the food vacuole and the parasite nucleus (**N**). The red and the blue arrows point to haemozoin crystals that are discussed in the main text.

The TEM of the trophozoite-infected red blood cells (**Fig 3.4** (**a**) and **Fig 3.4** (**b**)) show haemozoin crystals (**H**) of different shapes and sizes. The crystals are cuboidal (red arrow) and rhomboidal in shape (blue arrow). The differences in the shape of the crystals can be ascribed to the differences in the plane of cutting. The external morphology of the crystals however appears triclinic, which reflects the unit cell which is also triclinic [73]. The iron distribution images (blue) in **Fig 3.4** (**a**) and **Fig 3.4** (**b**) show that iron is concentrated almost exclusively in haemozoin crystals (**H**) in the food vacuole (**F**) inside the parasite. The rest of the parasite cytosol (**P**) including the nucleus (**N**) is almost devoid of iron in comparison to the red blood cell cytoplasm. Similar features and identical iron distribution were also observed in a study conducted by Egan *et al.* [46] on trophozoite-infected red blood cells (see Chapter 1).

3.5.2. The Effect of Chloroquine on the Morphology of *Plasmodium falciparum*

The study of the life cycle of *Plasmodium falciparum* using TEM and ESI described above in the absence of drug has shown features of morphology and iron distribution that are comparable with those reported in the literature. The technique was therefore considered suitable to be used to investigate the morphology and iron distribution in the parasite after treatment with chloroquine. Previous studies have suggested that chloroquine is stage specific and that it ultimately blocks haemoglobin degradation. These conclusions have been reached by visualisation using mainly transmission electron microscopy [110, 211, 216]. This inhibition results in the disruption of the feeding process of the parasite, which finally results in parasite death by mechanisms that remain poorly understood.

The current study has for the first time investigated the effect of chloroquine on the distribution of iron in drug treated *Plasmodium falciparum* at different stages of the parasite blood cycle using electron spectroscopic imaging (ESI) with transmission electron microscopy (TEM). The parasites containing mainly the ring stage and some schizonts were incubated with chloroquine (30, 60 and 120 nM) in order to investigate the effect of chloroquine on parasite development and on different stages of the parasites. The at of the D10 starin at 10% parasitemia was calculated to be

151 nM and was obtained as shown in the footnote[1]. The concentrations used in the study are lower than 151 nM, which allowed sufficient parasites to survive for examination and analysis. The samples were analysed after 16, 24 and 32 hours after incubation with the drug. The results of this study are discussed in detail below.

Fig 3.5 shows TEM and ESI images of parasites treated with 120 nM chloroquine acquired 16 hours after drug treatment. The merozoite is similar to that of untreated parasites. Furthermore, the iron distribution images (blue) also show that it is devoid of iron in comparison to the red blood cell cytoplasm as observed in untreated parasites (**Fig 3.2**).

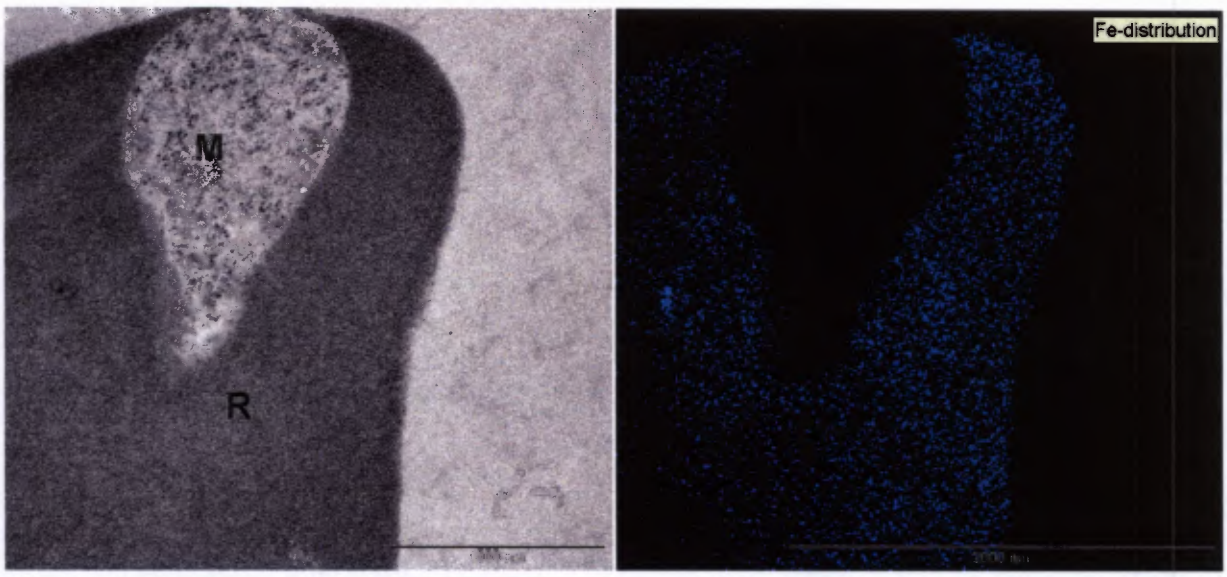

FIGURE 3.5. Transmission electron micrograph (left) and electron spectroscopic images (right) of a merozoite-infected red blood cell in parasite culture treated with 120 nM chloroquine. The image was acquired 16 hours after drug treatment. The distribution of iron (blue) demonstrates that it is concentrated almost exclusively in the RBC cytoplasm. The merozoite is devoid of iron in comparison to the level in the RBC cytoplasm. The labelled structures are the RBC cytoplasm (**R**) and the merozoite (**M**).

[1] IC_{50} (ng/ml) = m x V + IC_{50} (0), m = slope obtained from cellular accumulation graph (742 ng/ml), IC_{50} (0) = IC_{50} at infinite dilution (4 ng/ml), V = parasitemia of interest (10%). Data obtained from J Walden's thesis.

Fig 3.6 and **Fig 3.7** show ring-infected red blood cells treated with chloroquine. The red blood cell in **Fig 3.6** is infected with a young cup-like ring form that has been sectioned transversely. **Fig 3.7** (**a**) shows middle-stage ring containing the nucleus (**N**) and **Fig 3.7** (**b**) shows an early stage ring. **Fig 3.6** also shows an artefact caused during sample preparation. These parasites have the same features and morphology as reported in the literature for untreated parasites and as shown in **Fig 3.3** [111, 216, 218]. The ESI images (blue) show that the parasite cytosol is also devoid of iron in comparison to the red blood cell cytoplasm.

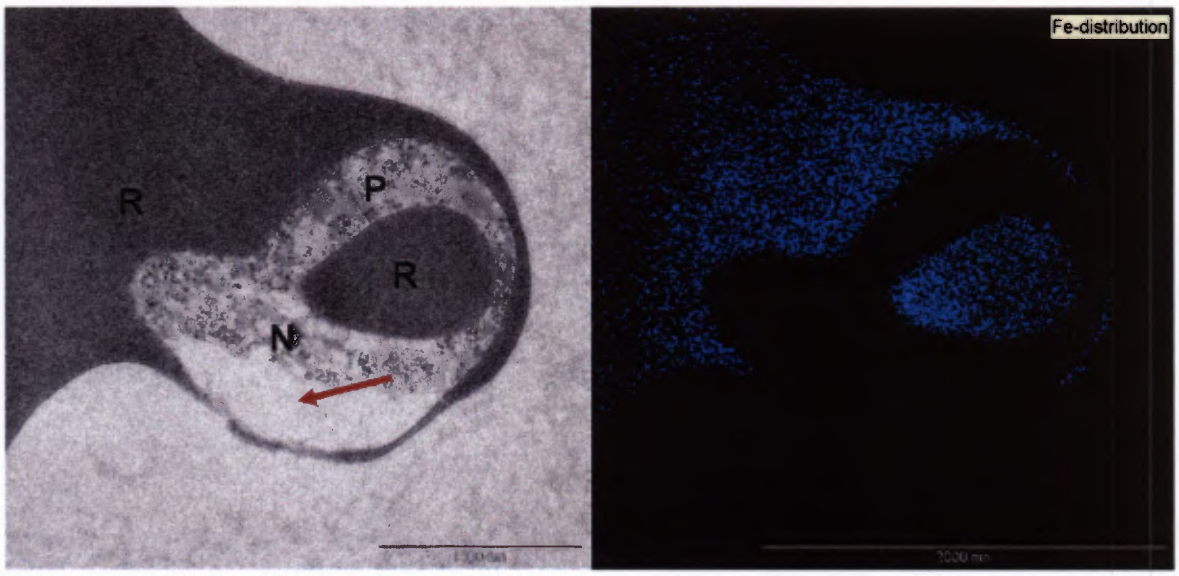

FIGURE 3.6. A transmission electron micrograph (left) and electron spectroscopic image (right) of a ring-infected red blood cell treated with 30 nM chloroquine. The images were acquired 16 hours after drug treatment. The distribution of iron (blue) demonstrates that it is concentrated only in the RBC cytoplasm. The parasite is devoid of iron in comparison to the RBC cytoplasm. The labelled structures are the RBC cytoplasm (**R**), the parasite cytosol (**P**) and the parasite nucleus (**N**). The red arrow shows an artefact caused during sample processing.

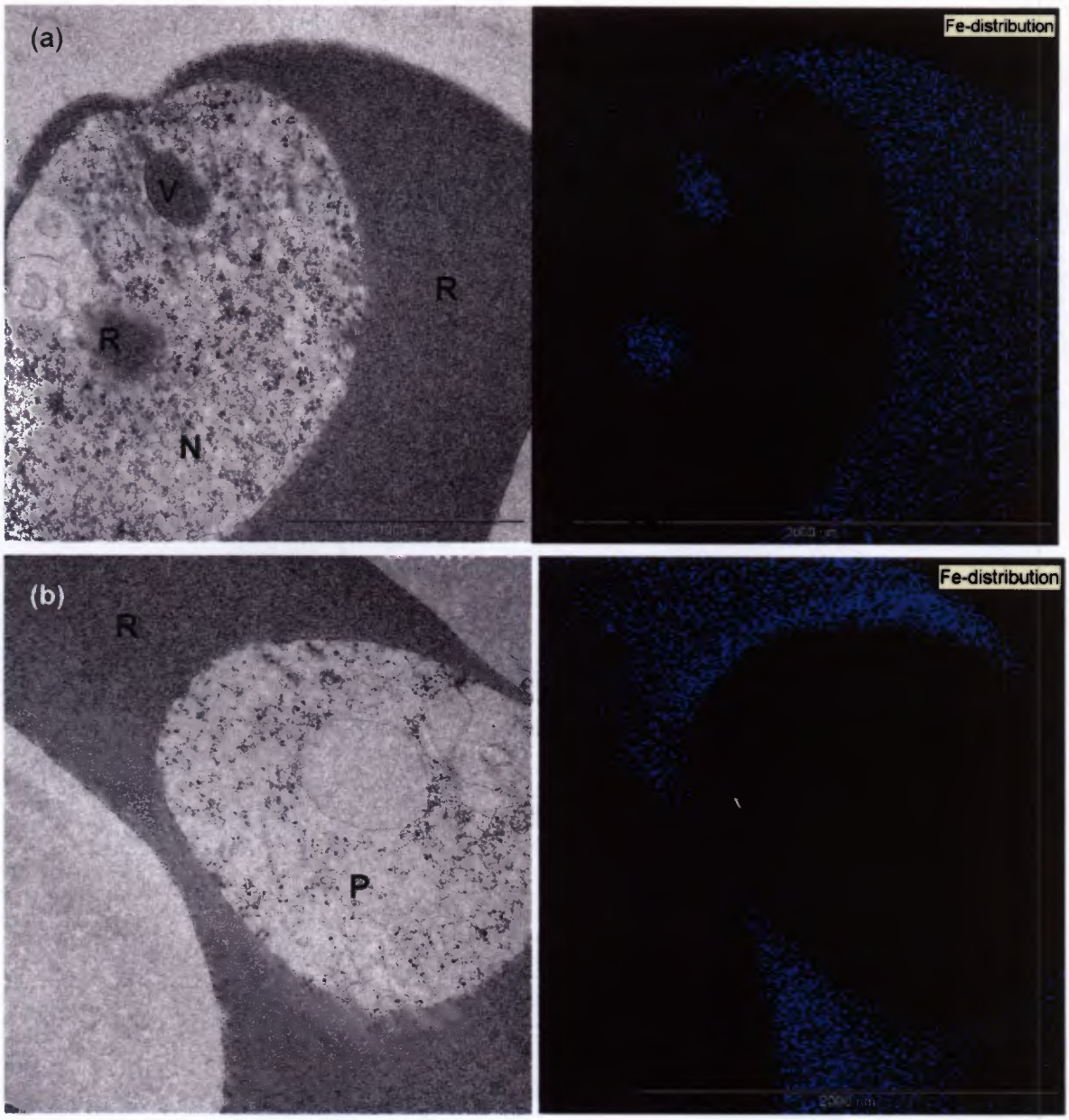

FIGURE 3.7. Transmission electron micrographs (left) and electron spectroscopic images (right) (**a**) of a middle-stage ring-infected red blood cells treated with 60 nM chloroquine and (**b**) of an early ring-infected red blood cells treated with 120 nM chloroquine. The images were acquired 16 hours after drug treatment. The distribution of iron (blue) demonstrates that it is concentrated only in the RBC cytoplasm. The parasite is devoid of iron in comparison to the RBC cytoplasm. The labelled structures are the RBC cytoplasm (**R**), a vesicle (**V**) containing iron, the parasite cytosol (**P**) and the parasite nucleus (**N**).

The effect of chloroquine on trophozoite-infected red blood cells was investigated in order to evaluate how iron distribution in this stage of the parasite life cycle is affected by chloroquine treatment. The parasites treated with 30 nM chloroquine show similar features to those of untreated parasites (**Fig 3.8** (**a**) and **Fig 3.8** (**b**)). The haemozoin crystals are similar in shape and morphology to those of the control (untreated). The number of haemozoin crystals inside the food vacuole in some of the parasites is also similar to the control (**Fig 3.4** (**a**) and **Fig 3.4** (**b**)). However, some of the parasites appear to contain fewer crystals on average (**Fig 3.8** (**b**)).

The iron distribution images indicate that iron is distributed mainly in the haemozoin crystals (blue) inside the food vacuole (**F**). However, the images also show the presence of iron in the parasite cytosol (yellow star), which is not present in the food vacuole (**F**). The amount is however less than that present in the red blood cell cytoplasm. **Fig 3.8** (**a**) shows the presence of what appears to be two food vacuoles (**F**) inside the parasite. Warhurst *et al.* [213] observed aggregation of the food vacuole containing haemozoin crystals after chloroquine treatment thus resulting in pigment clumping. This effect is not observed in **Fig 3.8** (**a**) due to lack of crystals in the adjacent food vacuole.

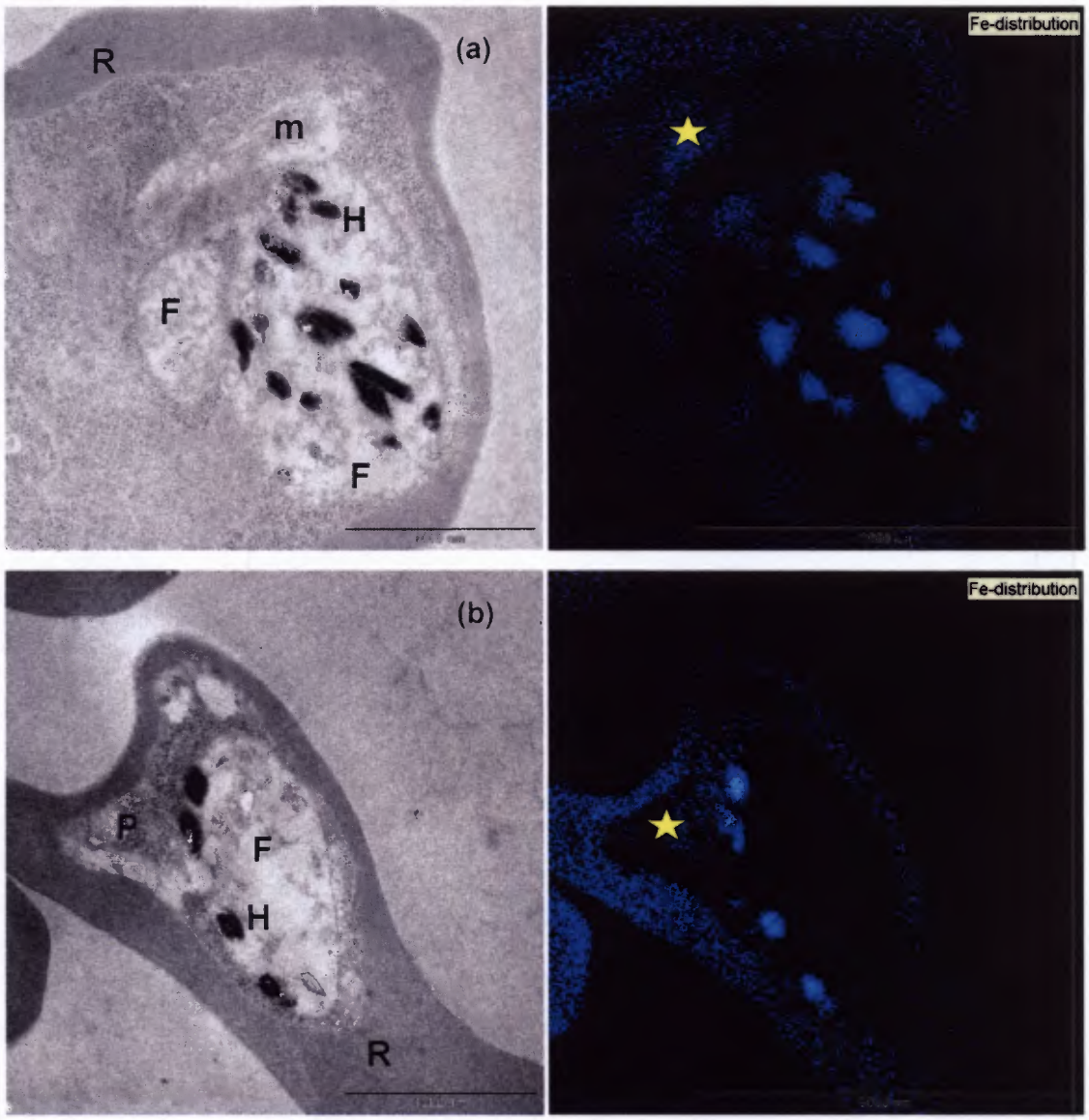

FIGURE 3.8. (**a**) and (**b**) Transmission electron micrographs (left) and electron spectroscopic images (right) of trophozoite-infected red blood cells treated with 30 nM chloroquine. The images were acquired 24 hours after drug treatment. The distribution of iron (blue) demonstrates that it is concentrated mainly in haemozoin crystals within the parasite food vacuole. There is also a small but significant quantity of iron present in the parasite cytosol (yellow star) comparable or lower than the level in the RBC cytoplasm. The labelled structures are the RBC cytoplasm (**R**), the parasite cytosol (**P**), the parasite food vacuole (**F**), haemozoin crystals (**H**) within the food vacuole and the mitochondria (**m**).

The parasites treated with higher concentrations of chloroquine (60 and 120 nM) show different morphological changes compared to untreated parasites or parasites treated with 30 nM chloroquine. The parasites treated with 60 nM chloroquine contain crystals that appear small, often with ill-defined outlines (**Fig 3.9**). The crystals in **Fig 3.10** seem to be very small and ill-formed, possibly as a result of chloroquine accumulation in the food vacuole, as observed previously [212][226]. The ESI images show that the parasites also contain iron (blue) in the parasite cytosol (yellow star). The concentration of iron in the parasite cytosol appears to be higher than in the parasites treated with 30 nM chloroquine. **Fig 3.10** also shows transport vesicle (red star) containing iron with the same apparent concentration as the red blood cell cytoplasm.

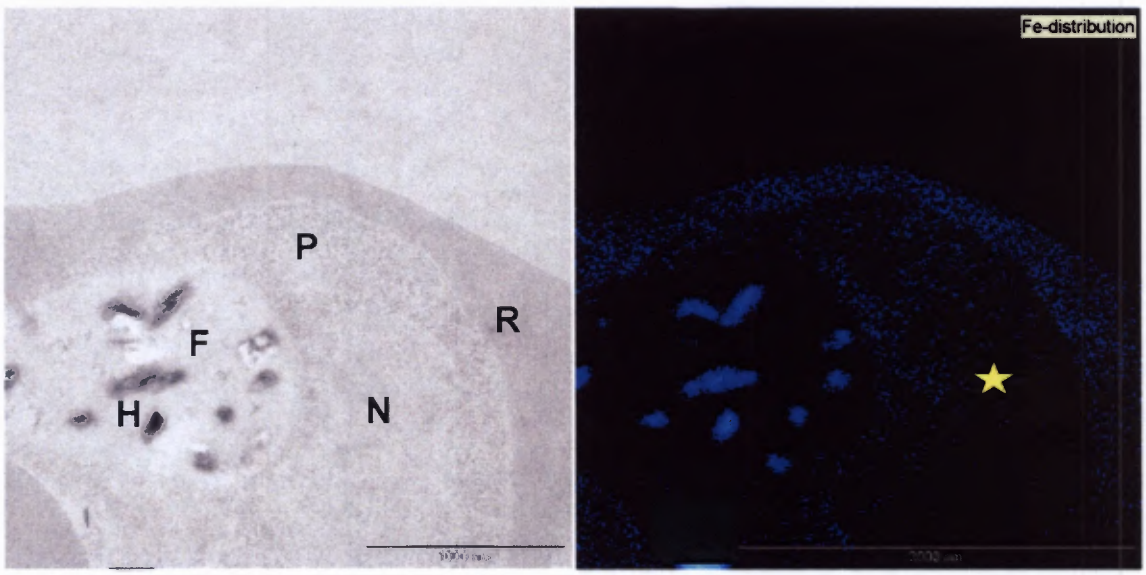

FIGURE 3.9. A transmission electron micrograph (left) and electron spectroscopic image (right) of a trophozoite-infected red blood cell treated with 60 nM chloroquine. The images were acquired 32 hours after drug treatment. The distribution of iron (blue) demonstrates that it is concentrated mainly in haemozoin crystals within the parasite food vacuole. There is a small quantity of iron present in the parasite cytosol (yellow star) apparently lower than that in the RBC. The labelled structures are the RBC cytoplasm (**R**), the parasite cytosol (**P**), the parasite food vacuole (**F**), the parasite nucleus (**N**) and haemozoin crystals (**H**) within the food vacuole.

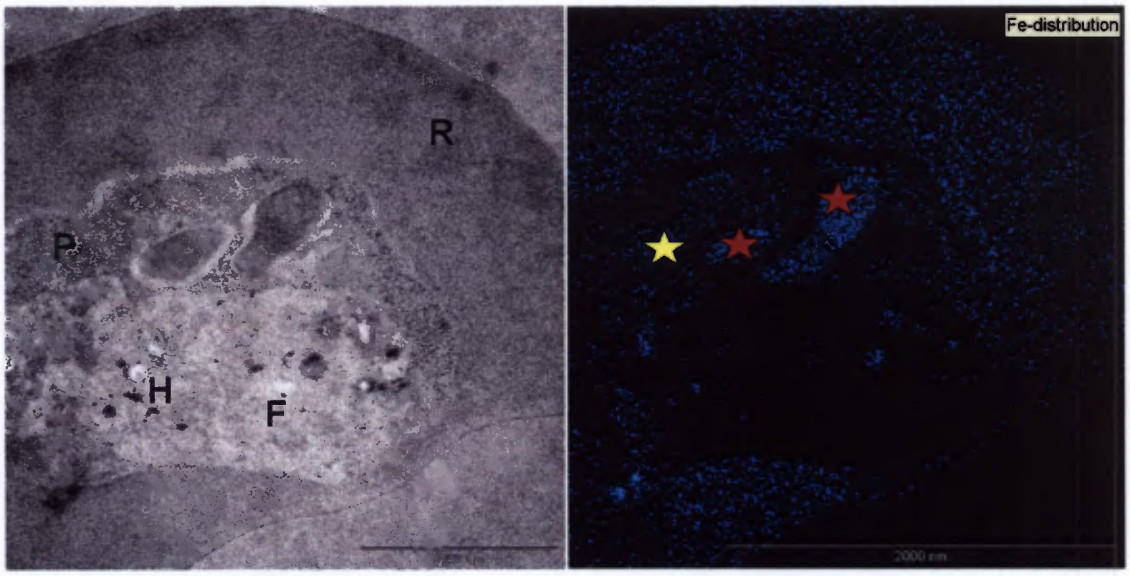

FIGURE 3.10. A transmission electron micrograph (left) and electron spectroscopic image (right) of a trophozoite-infected red blood cell treated with 60 nM chloroquine. The images were acquired 32 hours after drug treatment. The distribution of iron (blue) demonstrates that it is concentrated mainly in haemozoin crystals within the parasite food vacuole. There is a small quantity of iron present in the parasite cytosol (yellow star) apparently lower than that in the RBC. The vesicles (red star) contain the same apparent concentration of iron as the RBC cytoplasm. The labelled structures are the RBC cytoplasm (**R**), the parasite cytosol (**P**), the parasite food vacuole (**F**) and haemozoin crystals (**H**) within the food vacuole.

The parasites treated with 120 nM chloroquine exhibit much more dramatic changes. **Fig 3.11** shows haemozoin crystals (**H**) pushed to the side of the food vacuole. The crystals appear fuzzy or surrounded by halo (**Fig 3.11**). The parasites also contain iron in the parasite cytosol (yellow star) comparable or higher than the iron present in parasites treated with 60 nM chloroquine. The parasite in **Fig 3.12** contains a higher level of iron in the red blood cell compared to the other samples. This probably means that this section is thicker, resulting in higher signal intensity. Additionally, a large number of transport vesicles are present inside the parasite cytosol (red star) (**Fig 3.12**) containing iron (blue). The iron inside the vesicles is present at the same apparent concentration as the red blood cell cytoplasm. Transport vesicles are of course not unique to treated parasites, they are also present in untreated parasites

(see for example **Fig 3.13**). However, parasites exposed to higher concentrations of chloroquine (**Fig 3.13** (**c**) — (**f**)) contain large numbers of transport vesicles. The findings are consistent with a number of studies which have shown also evidence of large numbers of transport vesicles in chloroquine treated parasites compared to untreated parasites [112, 214-217].

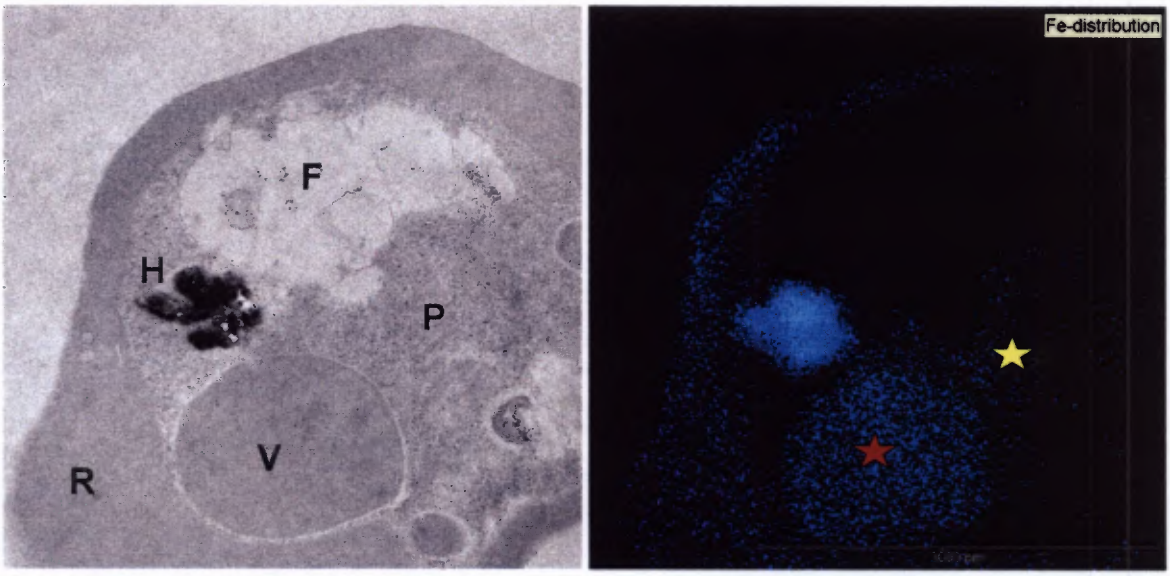

FIGURE 3.11. A transmission electron micrograph (left) and electron spectroscopic image (right) of a trophozoite-infected red blood cell treated with 120 nM chloroquine. The images were acquired 24 hours after drug treatment. The distribution of iron (blue) demonstrates that it is concentrated mainly in haemozoin crystals within the parasite food vacuole. There is a small quantity of iron present in the parasite cytosol (yellow star) apparently lower than that in the RBC. The large vesicle (red star) contains the same apparent concentration of iron as the RBC cytoplasm. The labelled structures are the RBC cytoplasm (**R**), the parasite cytosol (**P**), haemozoin crystals (**H**) pushed to the side of the food vacuole (**F**) and a vesicle (**V**) containing iron.

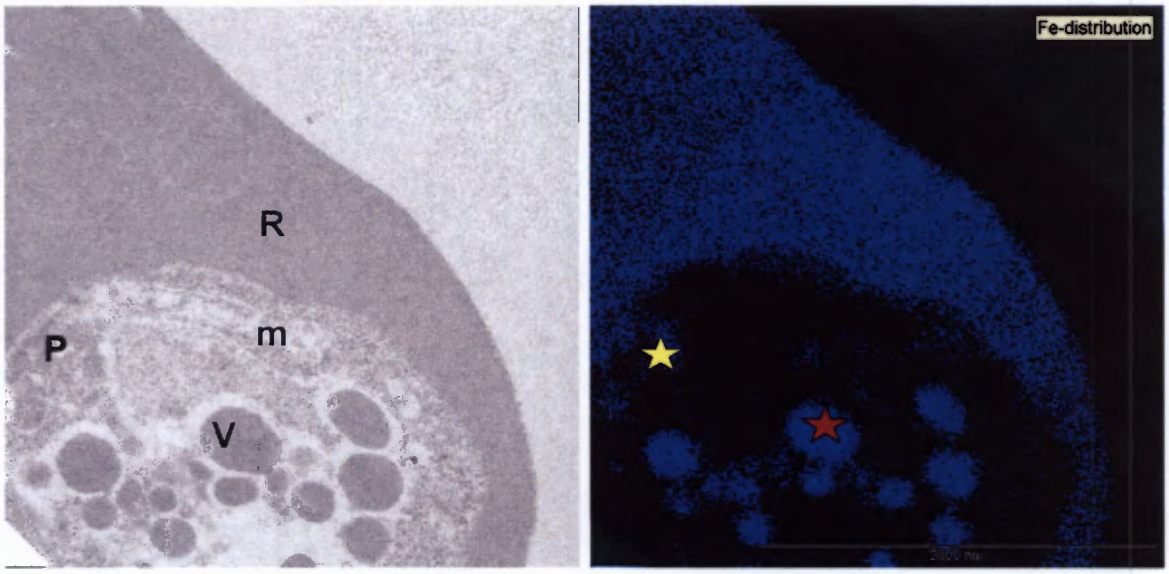

FIGURE 3.12. A transmission electron micrograph (left) and electron spectroscopic image (right) ofa trophozoite-infected red blood cell treated with 120 nM chloroquine. The images were acquired 32 hours after drug treatment. The distribution of iron (blue) demonstrates that it is concentrated mainly in RBC cytoplasm and vesicles. There is a small quantity of iron present in the parasite cytosol (yellow star) apparently lower than that in the RBC. The vesicles (red star) contain the same apparent concentration of as the RBC cytoplasm. The labelled structures are the RBC cytoplasm (**R**), parasite cytosol (**P**), mitochondria (**m**) and vesicles (**V**) containing iron.

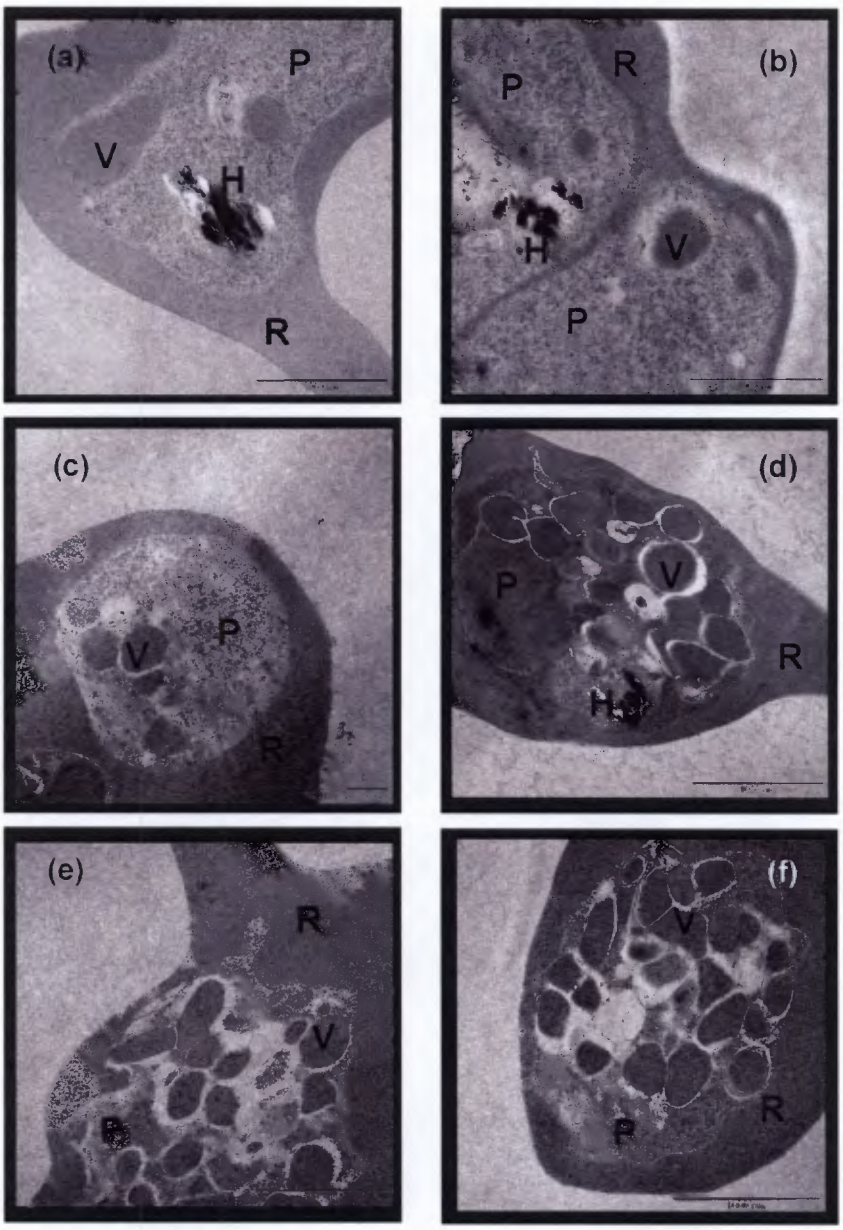

FIGURE 3.13. Transmission electron micrographs of trophozoite-infected red blood cells (**a**) untreated, (**b**) treated with 30 nM chloroquine, (**c**) and (**d**) treated with 60 nM chloroquine and (**e**) and (**f**) treated with 120 nM chloroquine. The images were acquired (**b**) 32 hours, (**c**) and (**d**) 24 hour and (**e**) and (**f**) 32 hours after drug treatment. The micrographs show different numbers of vesicles present in both chloroquine treated and untreated parasites. The labelled structures are the red blood cell cytoplasm (**R**), the parasite cytosol (**P**), haemozoin crystals (**H**) within the food vacuole and vesicles (**V**).

Fig 3.14 and **Fig 3.15** show segmenters with merozoites containing a high level of iron as shown by the electron spectroscopic images (red star) when compared with the red blood cell cytoplasm (green star) in parasites treated with 120 nM chloroquine. During cell division the merozoites budd off from the surface of the schizont, thus incorporating the content of the parasite cytosol. Therefore, the iron contained inside the merozoites might contain a high level of Fe(III)PPIX or Fe(III)PPIX-chloroquine complex that has leaked from the food vacuole into the parasite cytosol. The red blood cell cytosol contains a lower level of iron compared to the merozoites probably because the bulk of the red blood cell haemoglobin has been digested resulting in a depletion of haemoglobin in the red blood cell cytoplasm. **Fig 3.15** also shows multimembrane structures (red arrow). Olliaro *et al.* [111] have also observed the presence of multimembrane structures (MMS) in their studies. The electron density in **Fig 3.14** (left image) is higher than in the control (**Fig 3.2**, left image), which seems to confirm the finding that iron is redistributed in drug treated parasites.

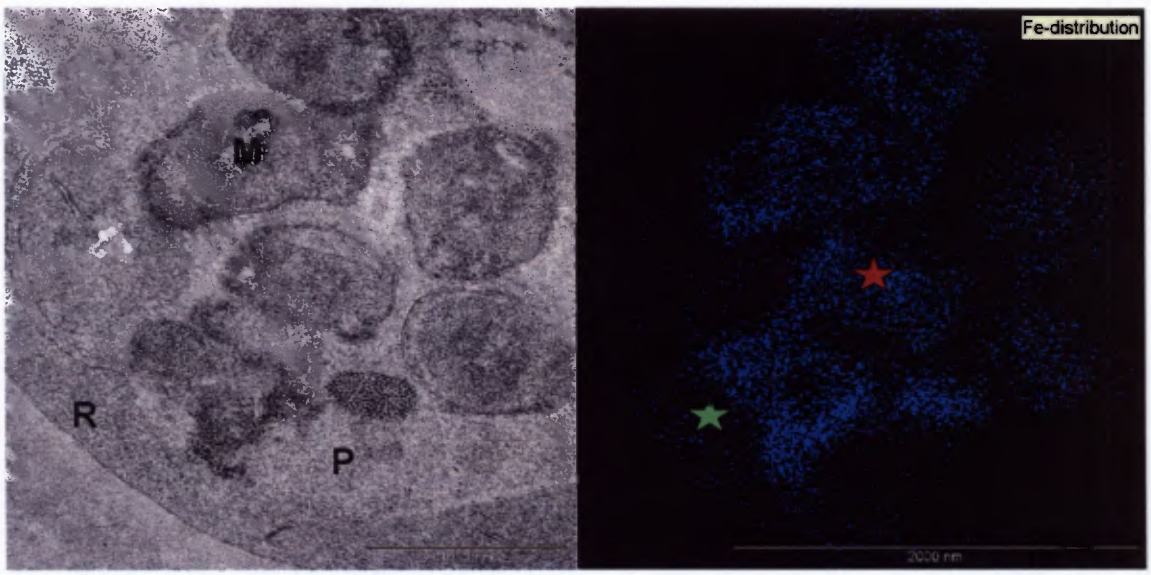

FIGURE 3.14. A transmission electron micrograph (left) and electron spectroscopic image (right) of a schizont-infected red blood cell treated with 120 nM chloroquine. The images were acquired 24 hours after drug treatment. The merozoites contain apparently higher concentrations of iron (red star) than that in the RBC cytoplasm (green star). The labelled structures are the RBC cytoplasm (**R**), merozoites (**M**) and the parasite cytosol (**P**).

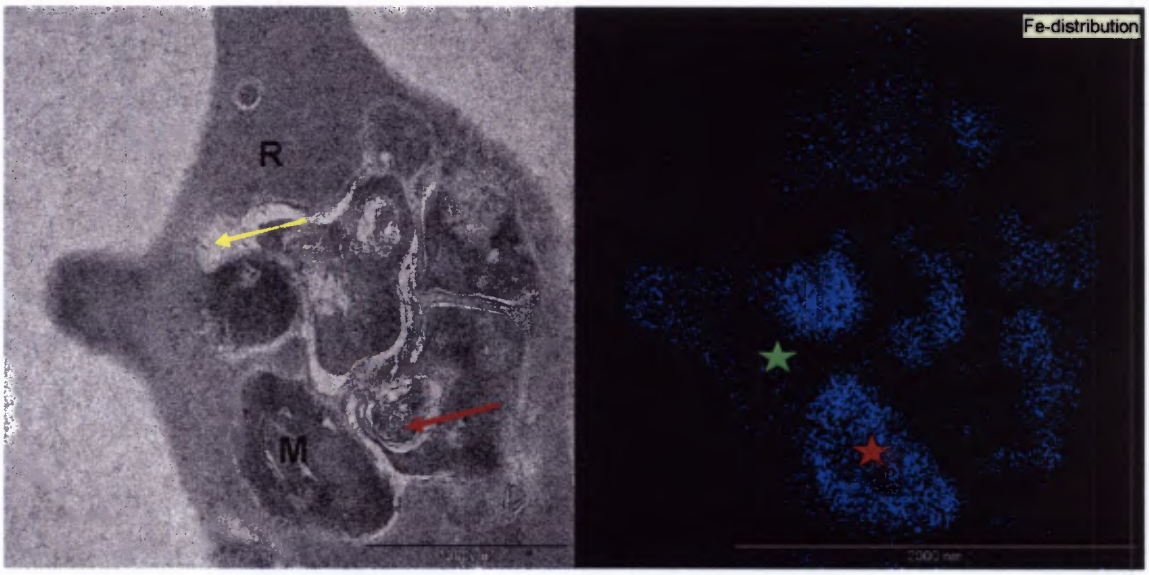

FIGURE 3.15. A transmission electron micrograph (left) and electron spectroscopic image (right) of a schizont-infected red blood cell treated with 120 nM chloroquine. The images were acquired 32 hours after drug treatment. The merozoites contain apparently higher concentrations of iron (red star) than that in the RBC cytoplasm (green star). The red arrow shows multimembrane structures (MMS) which are devoid of iron. The labelled structures are the RBC cytoplasm (**R**) and merozoites (**M**). The yellow arrow shows an artefact caused during sample processing similar to that described by Olliaro [111].

Previous studies have suggested that chloroquine induces vacuolar swelling [211]. **Fig 3.16** (**a**) and **Fig 3.16** (**b**) show TEMs of both untreated and treated parasites respectively to show the effect of chloroquine on the food vacuole. There were no apparent differences in the sizes of the food vacuoles in both treated and untreated parasites. In general, it was found that the apparent size of the food vacuole varied from parasite to parasite in both treated and untreated cultures owing to differences in the cross section cut through each parasite. It was therefore difficult to conclude whether there is any increase in size of the food vacuole in treated parasites due to the uncertainties associated with images. **Fig 3.16** (**b**) also shows a cytostome.

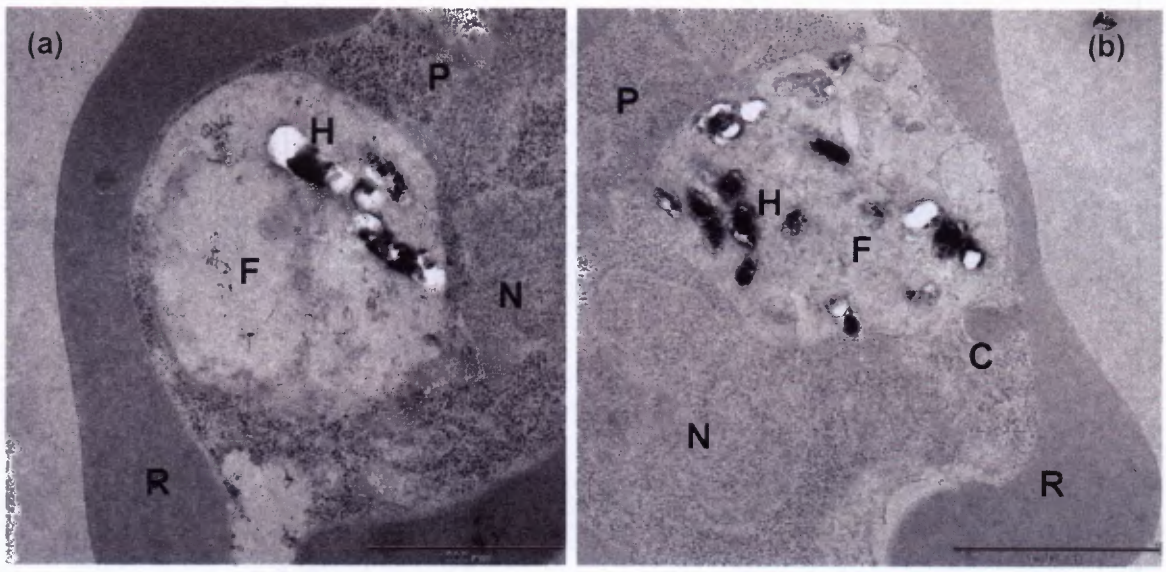

FIGURE 3.16. Transmission electron micrographs of trophozoite-infected red blood cells (**a**) untreated with chloroquine and (**b**) treated with 60 nM chloroquine. The images were acquired 24 hours after drug treatment. The micrographs illustrate the size of the food vacuole in both treated and untreated parasites which shows no obvious difference. The labelled structures are the red RBC cytoplasm (**R**), the parasite cytosol (**P**), the parasite nucleus (**N**), haemozoin crystals (**H**) within the food vacuole, the parasite food vacuole (**F**) and the cytostome (**C**).

Fig 3.17 below shows an early shizont-infected red blood cell with a structure that resembles a lipid body (**L**) in close association with haemozoin crystals (**H**). This structure is devoid of iron as indicated by the region in red circle in the ESI image when compared to other structures in the parasite cytosol (blue). Jackson *et al.* [97] observed in their studies lipid bodies in close association with the food vacuole. Thus, these bodies may be related to the lipids provided for haemozoin formation.

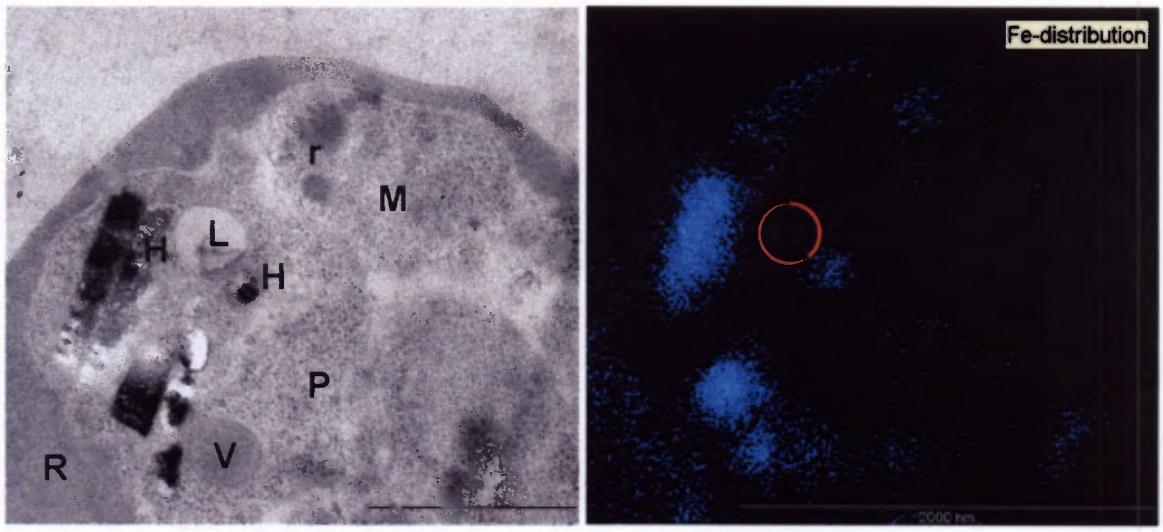

FIGURE 3.17. A transmission electron micrograph (left) and electron spectroscopic image (right) of an untreated trophozoite-infected red blood cell. The labelled structures are the RBC cytoplasm (**R**), the parasite cytosol (**P**), haemozoin crystals (**H**) within the food vacuole, vesicle (**V**) containing iron, merozoite (**M**), rhoptries (**r**) and a possible lipid body (**L**) associated with the food vacuole. The red circle represents the area occupied by the lipid body and illustrates that it is devoid of iron.

3.6. DISCUSSION

The TEM features of untreated *Plasmodium falciparum* observed in this study are in agreement with literature reports. A previous study carried out by Egan *et al.* [46] using ESI investigated the distribution of iron only for trophozoite-infected red blood cells. They showed that almost all the iron within the parasite is in the form of haemozoin, which is in agreement with the results obtained in this study. This technique was now further used to investigate the iron distribution in different stages of the parasite life-cycle. The ESI images showed that both the merozoite and the ring-infected red blood cells are almost devoid of iron in comparison to the high concentration in red blood cell cytoplasm. The lack of iron in the merozoites and the ring forms confirms that are they are not involved in haemoglobin degradation. The presence of crystals inside the food vacuole in the trophozoite-infected red blood

cells however is consistent with the evidence that haemoglobin is ingested and digested during the trophozoite stage and converted almost entirely to haemozoin.

Transmission electron microscopy (TEM) studies on parasites have previously been conducted to investigate the morphological changes induced after chloroquine treatment. These studies have shown that the drug targets mainly the trophozoite stage resulting in pigment clumping, a decrease in size and number of haemozoin crystals and an increase in transport vesicles, among others. The images in the current study suggest that chloroquine neither affects the invasion process nor the ring stage of the parasite in accordance with previous knowledge [224]. This observation is further consistent with the ring stage or merozoites not being involved in the feeding process and is in agreement with expectations that 4-aminoquinolines are stage-specific in their activity against *Plasmodium falciparum* [210]. However, treatment of the parasites with chloroquine results in a delay in parasite development as observed from parasite smears stained with giemsa stain viewed by light microscopy (not shown). The parasites in treated cultures remained in the ring stage for a longer period and the trophozoites appeared much smaller at higher chloroquine concentrations compared to either lower concentrations or untreated parasites.

Chloroquine treated trophozoite-infected red blood cells however show marked morphological changes. Parasites treated with 30 nM chloroquine are similar to untreated trophozoite-infected red blood cells. Thus, the morphology of the haemozoin crystals is similar to that of untreated parasites and the iron present inside the parasite is distributed mainly in the haemozoin crystals within the food vacuole. However, the electron spectroscopic images show the presence of some iron in the parasite cytosol, although not in the food vacuole lumen. This is the first direct evidence of a redistribution of iron into the parasite cytosol. The parasites treated with either 60 nM or 120 nM chloroquine have haemozoin crystals that are small, ill-formed and appear fuzzy, probably as a result of chloroquine accumulation in the food vacuole. This may result from Fe(III)PPIX that has precipitated in the food

vacuole or the interaction of chloroquine with Fe(III)PPIX forming a chloroquine-Fe(III)PPIX complex which may precipitate or interact with the haemozoin crystals and alter their formation and appearance. This could support the hypothesis that chloroquine accumulated inside the food vacuole interacts with Fe(III)PPIX [123-125], although the observation is marginal. What is clear is that parasites treated with 120 nM contain iron in the parasite cytosol which is higher in concentration than the iron present in parasites treated with lower concentrations of chloroquine. Furthermore, the parasites treated with high concentrations of chloroquine contain large numbers of transport vesicles containing iron.

The iron inside the parasite cytosol could be attributed to soluble Fe(III)PPIX or Fe(III)PPIX-chloroquine complex that has leaked out of the food vacuole into the parasite cytosol although haemoglobin that has escaped from the transport vesicles that build up in these parasites could also account for the observed iron. However, it would seem unlikely to be haemoglobin, as there were no observable ruptures around surface of the transport vesicles which could allow haemoglobin to escape. The iron is most likely to be toxic Fe(III)PPIX which is lipophilic and may thus leak into the parasite cytosol due to disruption of the normal impermeability of the food vacuole membrane. Perturbation of the food vacuole membrane by the Fe(III)PPIX-chloroquine complex could contribute to the accumulation of haemoglobin transport vesicles in chloroquine treated parasites by disrupting normal vesicle-vacuole docking and fusion. It could also be free iron which results from Fe(III) degradation by glutathione (GSH) as suggested by Ginsberg *et al.* [26]. The iron inside the vesicles is most likely to be undigested haemoglobin as shown by Hoppe *et al.* [215] using immunofluorescence. However, the technique used in this study (ESI) cannot be conclusive as to whether the vesicles contain undigested haemoglobin or Fe(III)PPIX released from haemoglobin. Some schizonts containing merozoites (segmenters) were observed in parasites treated with 120 nM chloroquine. Interestingly, the leakage of iron into the parasite cytosol is most prominent in the final segmenter stage of the parasite. Parasite cytosol is incorporated into the nearly formed merozoites, resulting in high iron content in the latter. The ESI iron signal in the

merozoites is even higher than in the red blood cell cytoplasm, probably because the bulk (up to 80%) of the haemoglobin content of the red blood cell has been taken up and digested by the parasite at this late stage of development. The presence of segmenters containing merozoites after 24 and 32 hours after chloroquine treatment suggest that merozoites formation is not inhibited by chloroquine. Some membranous structures were also observed in parasites treated with 120 nM chloroquine for 32 hours. During parasite development, the parasite accumulates large amounts of membranes in the form of vesicles, tubes and whorls within its lumen [227]. Parasite growth is retarded in the presence of high concentration of chloroquine, therefore the demand for membrane lipids would decrease as observed by Olliaro *et al.* [111].

3.7. SUMMARY OF KEY FINDINGS

Transmission electron microscopy (TEM) in conjunction with electron spectroscopic imaging (ESI) was used to investigate the effect of chloroquine on *Plasmodium falciparum*. The following was observed:

- Chloroquine does not affect the development of merozoites into the ring stage in accordance with the literature studies.
- Chloroquine does not have observable effects on the ring-stage of the parasite. This stage of the parasite is not expected to contain a large amount of elemental iron, with only a small amount likely to be present in iron proteins such as metalloenzymes which are expected to be insignificant in concentration compared to the background iron in the red blood cell. The parasite development to the trophozoite stage is however retarded.
- In contrast, the trophozoite stage showed major morphological changes when treated with chloroquine in comparison to untreated parasites.
- Parasites treated with 30 nM chloroquine showed small but significant changes compared to untreated parasites. The morphology of the haemozoin crystals was slightly different from the crystals in untreated parasites. The parasites also contained detectable iron in the parasite cytosol that was never seen in untreated parasites.

- Significant and pronounced changes were observed in trophozoite-infected red blood cells treated with 60 and 120 nM chloroquine. The amount and size of the haemozoin crystals was reduced. Some of the haemozoin crystals appeared to have a halo or were fuzzy, which might indicate the presence of a Fe(III)PPIX precipitate. The parasites also contained large numbers of transport vesicles inside the parasite cytosol which contain the same apparent concentration of iron as the red blood cell cytoplasm. A significant amount of iron was also observed inside the parasite cytosol. Based on reports in the literature, the transport vesicles probably contain a high concentration of undigested haemoglobin. Alternatively, they might contain a large quantity of precipitated Fe(III)PPIX which would also result in an enhanced iron signal
- Some schizonts containing merozoites were observed in parasites treated with 120 nM chloroquine contained a high level of iron incoporated during cell division compared to the red blood cell cytoplasm. The merozoites probably contain a large quantity of precipitated Fe(III)PPIX that has leaked into the parasite cytosol which would result in an enhanced iron signal extent. The presence of segmenters containing merozoites suggests that chloroquine does not have observable effect of merozoites formation.
- Some parasites treated with 120 nM chloroquine showed evidence of multimembrane structures inside the parasite cytosol which is attributed to a decrease in membrane utilisation resulting from retardation in parasite growth induced by chloroquine.

3.8. CONCLUSIONS

There is no definitive consensus as to the precise mechanism of action of chloroquine. However, it is clear from extensive evidence in the literature that its mechanism depends on haemoglobin digestion inside the food vacuole where toxic Fe(III)PPIX is released. The results obtained in this study have confirmed that chloroquine exclusively affects the appearance of the trophozoite stage of the parasite causing a radical redistribution of iron. A hypothesis can be suggested

therefore regarding the mechanism of action of chloroquine based on these observations. Chloroquine primarily accumulates inside the food vacuole where it interacts with Fe(III)PPIX released from haemoglobin degradation to inhibit haemozoin formation. Toxic Fe(III)PPIX or Fe(III)PPIX-chloroquine complex inside the food vacuole results in membrane damage. Fe(III)PPIX is then transported from the food vacuole into the parasite cytosol where it disrupts membranes, inhibiting vesicle fusion with the food vacuole resulting in an increase in transport vesicles inside the parasite cytosol. This could result in parasite starvation or enhanced oxidative stress leading to parasite death. However, further evaluation of the proposed mechanism is required. These would include the use of ESI to evaluate if the food vacuole or even the transport vesicles contain chloroquine for example by using an iodo-anologue to map out the distribution of iodine within the parasite. It is also essential to determine the chemical identity of the iron present in the parasite after treatment with chloroquine. Mössbauer spectroscopy would be useful for this purpose. The ability of Fe(III)porphyrins to inhibit vesicle infusion would also require extensive biological investigation. Nevertheless, the present study can be considered as a useful first step and has, within the limitations of the technique described above (at the beginning of Section 3.5), proven that chloroquine causes a radical redistribution of iron in the parasite, including redistribution to the cytosol which has not previously been reported.

CHAPTER 4.

INSIGHTS INTO ANTIMALARIAL DRUG-Fe(III)PPIX COMPLEX STRUCTURES IN SOLUTION USING NMR SPECTROSCOPY AND MOLECULAR MODELLING

INSIGHTS INTO ANTIMALARIAL DRUG-Fe(III)PPIX COMPLEX STRUCTURES IN SOLUTION USING NMR SPECTROSCOPY AND MOLECULAR MODELLING

4.1. INTRODUCTION

As discussed in Chapter 1, there is considerable evidence that CQ and related 4-aminoquinolines inhibit haemozoin formation by interacting with Fe(III)PPIX in solution. However, the details of how this occurs are still obscure. A number of studies have been performed using spectroscopic techniques such as UV-visible, NMR and Mössbauer spectroscopy to investigate the association of Fe(III)PPIX with quinoline antimalarial drugs [71, 84, 118, 128-135, 140, 228]. Computational studies of these complexes have also been performed using docking [142, 149] and molecular dynamics techniques [147, 148]. The docking studies show that there is a complementary interaction between the negative and positive potentials of the 4-aminoquinoline and the Fe(III)PPIX μ-oxo dimer upon complex formation. Leed *et al.* studied the structures of these complexes in aqueous solutions using NMR and molecular mechanics calculations with molecular dynamics [147, 148]. The distances between one of the iron centres of the putative Fe(III)PPIX μ-oxo dimer and the antimalarial drug were obtained from NMR inversion recovery methods, and these were used as distance constraints in molecular mechanics/dynamics calculations. Both studies supported previous work which indicates that Fe(III)PPIX interacts with 4-aminoquinoline antimalarial drugs through π-π interactions. According to the Leed model, the aliphatic side chains orient themselves into a conformation that maximises the van der Waals interactions with the porphyrin ring. Therefore, changing the side chain by lengthening or shortening it would be expected to alter the stability of the complexes. However, this is not in accord with experimental evidence which suggests that the side chain length is unimportant [125]. Thus the proposed structures require deeper investigation. In addition, no clear relationship between structure of the complex and the ability to inhibit β-haematin formation has so far been established. As a small set of short chain analogues of CQ with various

substituents at the 7-position had previously been prepared [141], an ideal opportunity existed to try to relate inhibition activity to structure of the complex with Fe(III)PPIX in this work.

4.1.1. Structure Determination of Fe(III)PPIX-Drug Complexes by NMR and Molecular Modelling

4.1.1.1. Longitudinal Relaxation Times

Paramagnetic effects have been used successfully in structure determinations. Such an effect occurs when the effective field at the nucleus is increased through induction by applied magnetic fields associated with unpaired electron(s) moving in their orbits [229]. This leads to deshielding of the nucleus and a shift of NMR peaks to lower magnetic field strengths and broadening of the spectrum. The most commonly used method for measuring T_1 is called the inversion recovery method as shown in **Fig 4.1**.

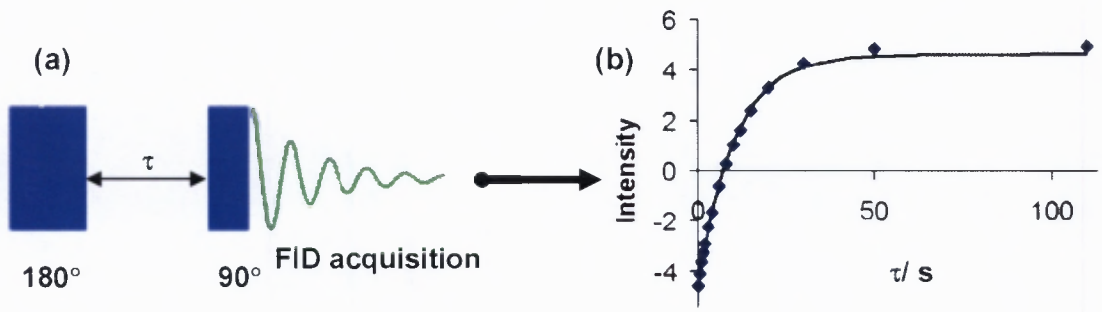

FIGURE 4.1. (**a**) A schematic representation of the general inversion recovery sequence (180°, τ, 90°) and (**b**) inversion recovery curve [230]. The dark blue bars represent the pulses of radiofrequency energy used to excite the protons.

The magnetisation vector M_0 arising from alignment of nuclear spins in the applied magnetic field of the NMR spectrometer is firstly inverted from the +z to the –z direction by a 180° pulse of electromagnetic radiation (in the radiofrequency range). The nuclei which are now in a higher energy state as they are aligned against the direction of the field are then allowed a period of τ to proceed back to the equilibrium +z orientation (longitudinal relaxation). The magnetisation is then rotated onto the xy

plane by a second pulse, 90°, where it emits radiofrequency energy as it returns to equilibrium. The emitted signal is known as a free induction decay (FID) signal and contains all of the frequency and intensity information for each of the protons in the molecule (**Fig 4.1** (**a**)). The process is repeated several times with different τ values to obtain a free induction decay (FID) plot of intensity as a function of τ where each point results from a separate 180°, τ, 90° sequence (**Fig 4.1** (**b**)). The relaxation time T_1 of each proton is then calculated using an exponential function using least-squares methods. The effect of an unpaired electron on the nucleus can be described according to Solomon and Bloembergen equation (Equation 1) [231, 232]:

$$r = \left\{ \frac{(\xi^2 [7j(\omega_e) + 3j(\omega_N)}{R_{complex}} \right\}^{\frac{1}{6}} \qquad (1)$$

$$\xi^2 = \frac{2}{15}[S(S+1)]\left(\frac{\mu_0}{4\pi}\right)^2\left(\frac{g_e\gamma_e\gamma_N h}{2\pi}\right)^2 ; \; [7j(\omega_e)+3j(\omega_N)] = \left[\frac{7\tau_c}{1+\omega_e{}^2\tau_c{}^2} + \frac{3\tau_c}{1+\omega_N{}^2\tau_c{}^2}\right]$$

where r is the Fe-H distance, S is the electronic spin ($\frac{5}{2}$) of the Fe(III)PPIX monomer (refer to Section 4.4.2.2) [34], τ_c is the electron relaxation time, ω_e and ω_N are the electron Larmor frequency (2.5179 x 10^9 s^{-1}) and the nuclear Larmor frequency (2.5133 x 10^9 s^{-1}) respectively obtained from a 400 MHz NMR machine, μ_0 is vacuum permeability (4π x 10^{-7} J s^2 C^{-2} m^{-1}), γ_e is the electron magnetogyric ratio (1.7608 x 10^{11} rad T^{-1} s^{-1}), γ_N is the nuclear magnetogyric ratio (2.6754 x 10^8 rad T^{-1} s^{-1}), g_e is the electron g value (2.00232), and h is the Planck constant (6.62608 x 10^{-34} J s) [231, 232].

The correlation time for the dipolar interactions, τ_c, can be expressed as:

$$\frac{1}{\tau_c} = \frac{1}{\tau_s} + \frac{1}{\tau_r} + \frac{1}{\tau_m} \qquad (2)$$

where τ_s is the electron spin correlation time, τ_r is the rotational relaxation time of the paramagnetic ion and τ_m is the lifetime of the nucleus in the bound state [233]. High

spin Fe^{3+} has relatively short electronic relaxation times ($\tau_s \approx 10^{-9}$ — 10^{-11} s) and therefore τ_c is dominated by τ_s [233, 234] when rotation of the complex is reduced, which is true in the case of the Fe(III)PPIX-drug complex [147]. In the method employed by Leed *at al.*, the calculated distances were then used as distance constraints in molecular dynamics calculations.

4.1.1.2. Molecular Modelling and Simulated Annealing

Molecular modelling is a collection of (computer based) techniques used to derive and manipulate molecular structures and their properties. The technique has been used in computational chemistry for a long time. The methods used in molecular modelling can be divided into two groups: quantum mechanics (QM) and molecular mechanics (MM). QM methods solve the Shrödinger equation to determine the electronic structure of the molecule. MM methods describe the potential energy of a molecule based on classically derived potential energy functions as shown in Equation 3 [235].

$$U_{total} = \sum_{molecule} (E_b + E_\theta + E_\phi + E_{nb}) \qquad (3)$$

where E_b is the deformation energy of a bond, E_θ is the angle deformation energy, E_ϕ is a torsional (dihedral) deformation energy and E_{nb} is a nonbonded (van der Waals) interaction energy.

The atoms are treated as spheres and the bonds as springs [236] to describe molecular structures, where the focus is on the positions of the nuclei only. According to the Born-Oppenheimer approximation one can separate nuclear motion from electronic motion in a system [237]. The energy of the system is then calculated as a function of the nuclear positions in the system and is determined by forces between them according to Hooke's law [236]. This energy can be calculated by fitting these parameters to a force field, which is an empirical fit to a Born-Oppenheimer potential energy surface (PES). Deformation of the structure results in change in the energy of the system that can be calculated if these equations and parameters (i.e. force constants) are known. It is important to remember that force field calculations are

done on a "molecular model" which is assigned properties that reproduce experimental data [236]. These data must therefore exist for a given class of compounds before the method can be applied. Initially, atomic coordinates are obtained from crystal structures or NMR data. Most of the force field methods developed are for organic molecules, however, they can be modified to suit any type of system such as those developed by Marques *et al.* [238] for metal porphyrins. The main advantage of MM is that it is computationally less demanding than QM. The dynamic behaviour of a molecular system can be studied using molecular dynamics simulation based on classical Newtonian equations of motion. Before simulation one needs to know the potential energy surface (PES) of the system as a function of atomic coordinates. These are obtained by MM calculations as described above. The atoms are then assigned velocities taken at random from a Maxwell distribution. Newtonian equations are then used to calculate future coordinates (positions) and velocities of atoms based on the current positions and velocities [235, 239]. A complete dynamic behaviour of a molecular system is called a trajectory. A number of algorithms can be used to solve these equations such as the leap-frog algorithm [235, 240].

Continued integration of the equations generates the position and velocities of the atoms as a function of time. The extent of the simulation can therefore be controlled by controlling the temperature and hence mean velocities of the atoms. The sum of these interactions gives rise to the conformation of the atoms in the system. A thorough conformational search can be performed by carrying out molecular dynamics with simulated annealing. Here the system is heated to a predetermined temperature, the dynamics are allowed to proceed for a period of time and then the system is allowed to cool down slowly to reach the local or global minimum energy. By repeating such a process many times, a picture of the lowest energy structures of the molecule can be built up. Molecular mechanics calculations coupled with molecular dynamics (MD) simulation provide extensive information on the interactions of the atoms in a system and its conformational changes. This information as well as experimental data is of great importance for investigating

structural properties of the system. This chapter will give an overview of how this technique can be used to study interactions of haematin with 4-aminoquinoline antimalarials and will highlight limitations of the method, especially relevant to the proposed structures of Leed *et al.*

The method developed by Leed *et al.* [147] was applied in this study to attempt to investigate the structures of the complexes of a series of substituted 4-aminoquinolines in order to gain further insight into how these compounds inhibit haemozoin (Hz) formation. Crystal structures of the complexes formed between haematin and antimalarial drugs are not available, the structures therefore have to be determined in solution. Fe(III) metal centres exert paramagnetic relaxation effects on the NMR spectra of nuclei close to the metal centre. The presence of the unpaired electrons in the magnetic field enhances the relaxation rate (T_1) of the nearby protons. Measurements of T_1 can provide information on the proximity of the paramagnetic centre (iron) to the resonating protons of the 4-aminoquinoline. We have thus used paramagnetic effects on T_1 exerted by the Fe(III) metal centre to try to determine distance constraints for complexes formed between the haematin monomer and 4-aminoquinolines for use in molecular mechanics modelling [147]. The study was carried out as follows:

- T_1 was determined for each of the protons in the 4-aminoquinolines studied as a function of haematin concentration.
- The T_1 data obtained were used to determine the putative distances between the Fe (III) metal centre and the protons of the 4-aminoquinolines.
- Molecular mechanics (MM) calculations were performed using these distances to obtain minimum energy conformations of the complexes formed between haematin and 4-aminoquinoline by means of molecular dynamics and simulated annealing (MD/SA).

4.2. MATERIALS

The materials used in the study are listed in **Table 4.1**. They were of AR or other high purity grade and were used without purification.

TABLE 4.1. A list of materials used in the study

Materials	Commercial Supplier
Chemicals	
Ferriprotoporphyrin IX hydroxide (Haematin)	Sigma-Aldrich
Ferriprotoporphyrin IX chloride (Haemin)	Sigma-Aldrich
D_2O	Aldrich
NaOH	Saarchem
HCl	BDH
Perchloric acid ($HClO_4$)	BDH
Dimethyl sulphoxide (DMSO)	BDH
Compounds[a]	
Chloroquine diphosphate (**CQ**)	Sigma-Aldrich
N^1,N^1-Diethyl-N^2-(7-chloro-4-quinolinyl)-1,2-ethanediamine (**1**)	—[b]
N^1,N^1-Diethyl-N^2-(7-iodo-4-quinolinyl)-1,2-ethanediamine (**2**)	—[b]
N^1,N^1-Diethyl-N^2-(7-fluoro-4-quinolinyl)-1,2-ethanediamine (**3**)	—[b]
N^1,N^1-Diethyl-N^2-(7-methoxy-4-quinolinyl)-1,2-ethanediamine (**4**)	—[b]
N^1,N^1-Diethyl-N^2-(4-quinolinyl)-1,2-ethanediamine (**5**)	—[b]

[a]Number or symbol in brackets represent the number or symbol given to the compound. [b]The compounds were synthesised by Dr C. H. Kaschula in an earlier study [141].

The chloroquine analogues (compounds **1**— **5**) were used without further purification. **CQ** and compounds **1**, **3** and **4** were used for complex structure determination while **CQ** and compounds **1**, **2**, **4** and **5** were used in the NMR and thermodynamic studies (**Fig 4.2**).

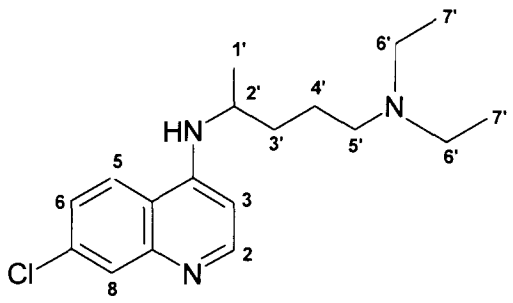

(**CQ**)

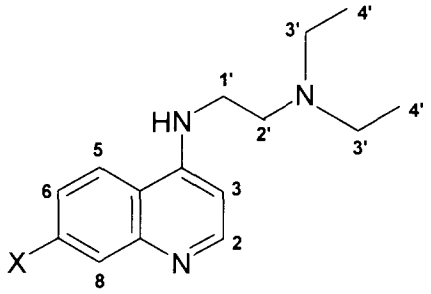

X= Cl (**1**), I (**2**), F (**3**), OCH_3 (**4**), H (**5**)

FIGURE 4.2. Structure of the compounds used in the study. **CQ** as well as compounds **1** and **2** bind to Fe(III)PPIX, inhibit β-haematin formation strongly and are strongly active against parasites. Compound **3** binds to Fe(III)PPIX, inhibits β-haematin formation weakly and is weakly active against parasites. Compounds **4** and **5** bind to Fe(III)PPIX, do not inhibit β-haematin formation (or do so extremely weakly) and are inactive against parasites. The numbering indicates the standard proton numbering scheme used in this class of compounds and refers to the protons attached to the carbon atoms numbered. Spectroscopically equivalent protons are all given the same numbers.

4.3. SAMPLE PREPARATION

4.3.1. Preparation of the Stock Solutions for Inversion Recovery Experiments

A 0.02 M stock solution of haematin was prepared by dissolving 0.0253 g in 2 ml of 0.1 M NaOH prepared in D_2O. Stock solutions of the 4-aminoquinoline compounds were dissolved in 10 ml of D_2O to give a final concentration of 0.02 M. The chloroquine analogues were not soluble in D_2O in their free base form, they were therefore acidified with 10.18 M HCl. Ten solutions were made up in 2 ml eppendorf tubes containing increasing haematin:4-aminoquinoline ratios for each compound. 0.5 ml of 0.02 M stock solution of each 4-aminoquinoline was added to each tube. This was followed by an addition of an increasing amount of haematin, with final concentrations ranging from 0 to 1.0 mM. The pH of the solutions was adjusted to 6.5 with 0.1 M NaOH or 0.1 M perchloric acid ($HClO_4$) determined using a Crison

microph 2000 pH meter. The volume of each solution was adjusted to 1 ml with D_2O. The final concentration of the 4-aminoquinoline in each tube was 0.01 M.

4.3.2. Sample Preparations for Thermodynamic Studies

4.3.2.1. Preparation of 0.2 M HEPES Buffer Stock Solution

The buffer solution was prepared by dissolving 4.776 g of HEPES in distilled water. A highly concentrated solution of NaOH was used to adjust the pH to 7.5. The solution was then made up to 100 ml with distilled water.

4.3.2.2. Preparation of 2 x 10^{-3} M 4-Aminoquinoline Solutions

Solutions of the 4-aminoquinolines (**CQ**, compounds **1**, **2**, **4**, and **5**) were prepared by dissolution in 40% (v/v) aqueous DMSO containing 0.02 M HEPES buffer (pH 7.5). The solutions were used in the 4-aminoquinoline association studies.

4.3.2.3. Preparation of the Haemin Stock Solution

A stock solution of haemin was prepared by dissolving 8 x 10^{-3} g of haemin chloride in 10 ml of pure DMSO. The solution was kept in the dark to avoid degradation.

4.4. EXPERIMENTAL PROCEDURES

4.4.1. Proton Longitudinal Relaxation Time Measurements (T_1)

The solutions prepared in Section 4.3.1 were transferred into NMR tubes and proton longitudinal relaxation measurements T_1 (^1H) of each solution were recorded on a 400 MHz Varian Unity NMR spectrometer at the University of Cape Town using the inversion-recovery sequence, 180°, τ, 90°, with presaturation of the water peak. The T_1 measurements were collected using τ of 0.025, 0.05, 0.1, 0.2, 0.4, 0.8, 1.6, 3.2, 6.4 and 12.8 seconds. The T_1 values were obtained by using the T_1 analysis menu on the NMR workstation. The programme calculates the values from Equation 4.

$$M_z = M_0\left(1 - 2e^{-t/T_1}\right) \quad (4)$$

where M_z is the magnetisation in the +z direction and M_0 is the magnetisation at time zero.

4.4.1.1. Distance Constraint Calculations

The T_1 values obtained for each proton of each 4-aminoquinoline were converted to effective relaxation rates ($R_{observed}$) according to Equation 5 [147].

$$R_{observed} = \frac{1}{T_{observed}} = \left[R_{complex} - R_{free}\right]\left[\frac{[Haematin]}{K_d + [4AQ]}\right] + R_{free} \quad (5)$$

where R_{free} is the relaxation rate of the drug, $R_{complex}$ is the relaxation rate of the complex formed between haematin monomer and the 4-aminoquinoline, K_d is the dissociation constant of the 4-aminoquinoline, **[haematin]** and **[4AQ]** are total concentrations of haematin and the 4-aminoquinoline, respectively.

The $R_{observed}$ values ($1/T_1$ (observed)) were then plotted against [haematin]/(K_d + [4AQ]) giving straight lines. The slope and the intercept obtained from these lines were used to determine $R_{complex}$. The values of the dissociation constants (K_d) for **CQ** and compounds **1** to **5** were calculated based on the log K_a (association constants) values reported. The values are 5.6 ± 0.2 (**CQ**) [123], 5.81 ± 0.01 (**1**), 5.02 ± 0.02 (**2**), 4.60 ± 0.02 (**3**), 4.83 ± 0.01 (**4**) and 4.75 ± 0.03 (**5**) [125, 141]. The values were obtained by calorimetric titration for **CQ** at 37°C at pH 6.5 in 0.25 M phosphate buffer and by spectrophotometric titration at 25°C at pH 7.5 in 0.02 M HEPES buffer and 40% DMSO (aq) for compounds **1**— **5**. The K_a values obtained in this study for the same compounds were not used to avoid discrepancies as the value for compound **3** was not determined due to lack of material. The values obtained in this study differ only by about 0.2 log units on average.

The $R_{complex}$ values calculated were used to obtain putative distances between each proton and the paramagnetic iron centre using a simplified Solomon-Bloembergen equation (Equation 1) [232, 241][231, 242]. The calculated Fe-H distances were then used as distance constraints in molecular dynamics calculations.

4.4.2. Computational Methods

4.4.2.1. Programs

All computational calculations and modelling were done using HyperChem Release 7.5 for Windows obtained from Hypercube Inc. (Gainesville, Florida).

4.4.2.2. Force Field Parameterisation and Refinement

In order to study the interaction between haematin and 4-aminoquinolines, it is important to determine which species of haematin is present under the conditions used. It has long been known that the study of haematin in aqueous solutions is problematic and it has been claimed that haematin exists in different forms, either as a monomer and/or μ-oxo dimer depending on the pH. However, recently de Villiers *et al.* [34] showed that the species present under the experimental conditions of this work exists as a dimer where the axial ligands are directed outwards as shown in **Fig 4.3**.

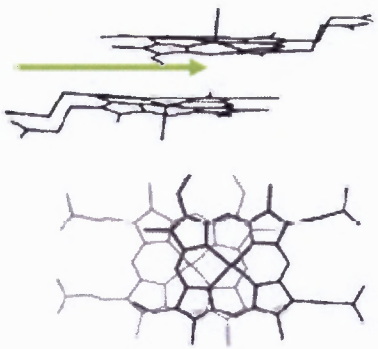

FIGURE 4.3. Structure of the proposed dimer in aqueous solution viewed from the side view (top) and top view (bottom). The green arrow indicates the side on which the drug is believed to interact with haematin (the so-called open face) [34].

In light of this, crystal structures of related Fe(III) porphyrin aqua-monomers were used as the starting point as neither the crystal structure of haematin nor the crystal structures of the complexes under study are available. The Cambridge Structural Database (CSD) was searched for porphyrins containing the Fe(III)-OH_2 backbone (**Table 4.2**). The parameterisation of the force field was based on the average of each of these structures.

TABLE 4.2. Compounds chosen for the Force Field Parameterisation

CSD Code	Compounds	Reference
HECZUK	Aqua-(octaethylporphyrinato)-iron(iii) perchlorate dehydrate	[243]
LOJKAW	Aqua-(5,10,15,20-tetraphenylporphyrinato)-iron(iii) 7,8,9,10, 11,12-hexachloro-1-carbadodecaborane monohydrate	[244]
QEZWUN	Hydroxy-(5,10,15-trimesityl-20-(2,7-di-t-butyl-4-carboxy-9,9-dimethylxanthen-5-yl)porphyrinato-N-N',N'',N''')-iron(iii) pentane solvate monohydrate	[245]

The force fields used in this study were those used to model the metal porphyrins and were developed by Marques *et al.* [229, 238, 246] as an extension of Allinger's MM2 force field available in the HYPERCHEM programme as MM+. The force fields were loaded into HyperChem as Tporph and were parameterised to model the present system in order to obtain meaningful results. The first step was to add missing atoms to the crystal structures and to number the porphyrin core in exactly the same way in HyperChem using a standard numbering scheme as shown in **Figure 4.4** using an Excel spreadsheet.

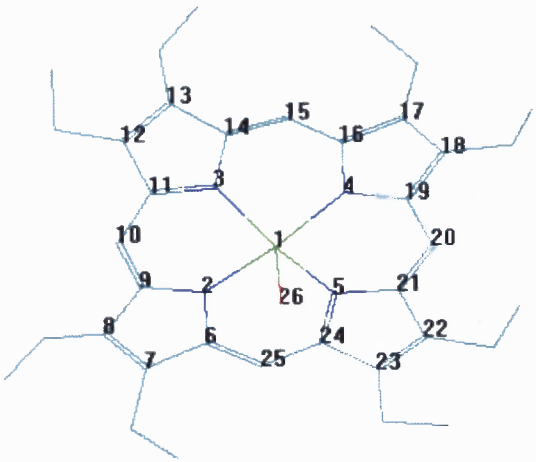

FIGURE 4.4. Schematic representation of the standard numbering scheme of porphyrins

In order for HyperChem to recognise the atoms in these structures, the atoms had to be assigned atom 'types' according to **Figure 4.5**. The definition of each atom type is shown in **Table 4.3** below.

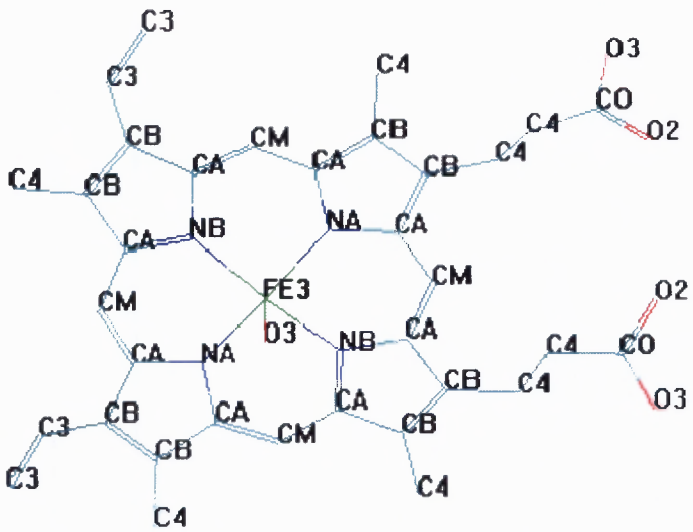

FIGURE 4.5. Schematic representation to show atom 'type' for the porphyrin ring

TABLE 4.3. Definition of the atom types used in the molecular modelling

Atom Type	Definition
FE3	Porphyrin Fe
NA and **NB**	*Trans* coordinating nitrogen atoms of the porphyrin ring
CA and **CB**	Pyrrole α and β carbon atoms
CM	Porphyrin *meso* carbon atoms
C4	All sp^3 carbon atoms
C3	All sp^2 carbon atoms other than those specified
CO	Carbonyl carbon atoms
O3	sp^3 oxygen atoms
O2	Carbonyl oxygen atoms
H	All hydrogen atoms

An Excel macro was used to communicate with HyperChem using a Dynamic Data Exchange (DDE) procedure to calculate bond angles, bond lengths and torsion angles of the porphyrin core of each crystal structure. The results were written into an Excel spreadsheet and were used in the parameterisation of the existing force field for iron porphyrins [238]. The force field contains parameters for bond stretching, angle bending, torsion angles, out-of-plane bending and van der Waals interactions and was set up in HyperChem as Tporph. The force field was modified by computing a single point calculation on all the structures to identify any missing parameters. The missing parameters were obtained from Alliger's original force field or from parameters obtained by Marques *et al.* [238], and were added into the existing force field. The MM2 force field, known as MM+ in Hyperchem does not handle atoms (**M**) with coordination number > 4 very well as the atoms are treated like any other atoms or as 'points-on-a-sphere'. This type of model proved to be unreliable from previous studies of iron porphyrins [238]. These parameters (**X-M-X** (angles) and **X-X-M-X** (torsions)) therefore need to be specified by adding restraints in to the force field.

The 'model' structures obtained from the crystal structures were geometry optimised with this force field using a Polak-Ribiére conjugate gradient algorithm method with a root mean squared energy gradient deviation (rmsd) of < 0.05 kcal mol^{-1} $Å^{-1}$. The bond angles, bond lengths and torsions of these energy minimised model structures were calculated using an Excel macro as with the crystal structures. A trial-and error method was used to adjust the model parameters to fit the data obtained from the crystal structures. This was done until the rmsd's between the crystal structures and the model structures were ≤ 0.01 Å for bond lengths, ≤ 2° for bond angles and ≤ 4° for torsion angles.

Since a crystal structure of the haematin monomer does not exist, a model of the porphyrin had to be built using one of the crystal structures as a starting point. This was done by adding hydrogens, vinyl, methyl and propionate groups in the appropriate positions. The added atoms were given atom 'type' labels (**Table 4.3**), and a single point calculation was performed to identify any missing parameters, which were added to the force field as described above to ensure that good model structures of haematin monomer were obtained. The model structures were then geometry optimised. The validity of the force field was determined by overlapping the porphyrin core (root mean square overlay) of the crystal structures of related porphyrins with that of the model structure. A good agreement means that the force field is appropriate for modelling molecules of this class. A crystal structure of chloroquine (CQ) was obtained from the Cambridge Structural Database [247]. Both the quinoline nitrogen and the terminal amino group were protonated, as this is the species present under acidic conditions as in the food vacuole and under experimental conditions used in this study (pH 6.5). The force field was parameterised further by performing a single point calculation on the model structure to obtain further missing parameters. These were added to the force field and the structure was geometry optimised as mentioned. Model structures of compounds **1**, **3** and **4** were built from **CQ** and were treated as mentioned above. The final parameter set of the force field was used for structure calculations.

4.4.2.3. Molecular Modelling and Simulated Annealing

4.4.2.3.1. Modelling the Haematin Monomer

The optimised force field was used to perform molecular dynamics and simulated annealing (MD/SA) calculations to obtain the lowest energy conformers, to be used to model the structures of the complexes. One of the haematin carboxylate groups was ionised and the other unionised as this is the species believed to be present in the parasite food vacuole. The conformers were generated by heating the monomer initially from 0 K to 300 K over 5 ps with a run time between 5 and 50 ps at this temperature (300 K). After the run was complete, the structures were cooled back to 0 K over a period of 10 ps. Each annealed structure was energy minimised using a Polak-Ribiére conjugate gradient algorithm and a minimum of 10 structures was obtained. The calculations were done in vacuum and the temperature of the system was controlled by coupling to a simulated heat bath, with a bath relaxation time of 0.1 ps.

4.4.2.3.2. Modelling the Complexes

The model complex structures were obtained by merging the energy minimised structure of each 4-aminoquinoline with the lowest energy conformation of the haematin molecule either on the open face or on the face occupied by the water ligand. The distance constraints obtained from NMR data were applied to the model complexes using a very weak constraint force constant, k, of 0.075 mdyne $Å^{-1}$ as reported by Clore *et al.* [248] and the complexes were energy minimised. During energy minimisation, in cases where the 4-aminoquinoline was placed on the side occupied by the water ligand it always moved to the open face. This is consistent with experimental studies where very much weaker associations have been observed between quinoline drugs and N-acetyl-microperoxidase-8 which is 6-coordinate with association having to occur on a face occupied by a water ligand [138]. This weak association was previously attributed to steric hindrance. Given this evidence, MD/SA simulation were all conducted using the starting geometries shown in **Fig 4.6** where the drug is located on the open face of the porphyrin. These simulations were used in order to attempt to search all possible conformational space.

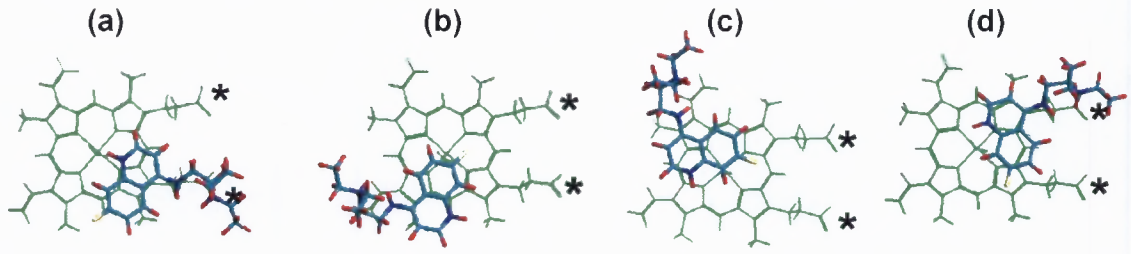

FIGURE 4.6. Representation of the starting geometries with distance constraints after energy minimisation was performed. The 4-aminoquinoline is positioned at four positions relative to the carboxylate groups (black asterisks). The haematin monomer is shown in green, yellow represent the group at the 7-position, nitrogen is represented in dark blue and the hydrogens are shown in red.

A molecular dynamic trajectory was obtained by performing calculations on all the starting structures shown in **Fig 4.6**. Each starting structure was heated in vacuum at 300 K for 50 ps in steps of 0.001 ps to obtain 1000 snapshots. The system was coupled to a heat bath with a bath time of 0.1 ps to ensure that a constant temperature was maintained throughout the calculation. Conformers were obtained in intervals of 1.25 ps along the trajectory and these were annealed with a cooling period of 20 ps to a final temperature of 0 K in steps of 0.001 ps. The final structures were energy minimised.

4.4.3. Association of 4-Aminoquinolines with Haematin

The association of **CQ**, compounds **1**, **2**, **4** and **5** with haematin were investigated by carrying out spectrophotometric titrations using a Varian Cary 100 UV-visible spectrophotometer fitted to a thermostated cell holder according to methods previously reported [125, 137, 141]. A 2 ml blank solution containing a mixture of 40% (v/v) aqueous DMSO with HEPES buffer (0.02 M, pH 7.5) was pipetted into a 1 cm cuvette and placed into the sample holder of the instrument. The solution was allowed to equilibrate to the appropriate working temperature (20, 25, 30, 35 or 40°C) before setting the absorbance to zero. A haematin solution (3.10×10^{-6} M) was prepared by pipetting 0.005 ml of the stock solution in DMSO to form a solution in

40% (v/v) aqueous DMSO and 0.02 M HEPES buffer (pH 7.5) making a total volume of 2 ml. The cuvette containing the 2 ml solution of haematin was placed into the sample holder and again the solution was stirred and allowed to equilibrate to the appropriate temperature. The absorbance of this solution was recorded at 402 nm. Predetermined aliquots of each 4-aminoquinoline were added to the 2 ml haematin solution and stirred and the absorbance was recorded after each addition for each temperature. The absorbances were corrected for dilution effects and the data was fitted to a 1:1 association model to obtain the association constants for each 4-aminoquinoline at each temperature as described previously [137, 139].

4.5. RESULTS AND DISCUSSIONS

4.5.1. Analysis of the Experimental NMR Data

4.5.1.1. NMR Spectra

The ^{1}H NMR spectra of **CQ** and compounds **1— 5** were recorded without haematin in order to assign each peak correctly. **Fig 4.7** (**a**) shows the spectrum of **CQ** with peak assignments based on chemical shift, peak integration and coupling constant [141].

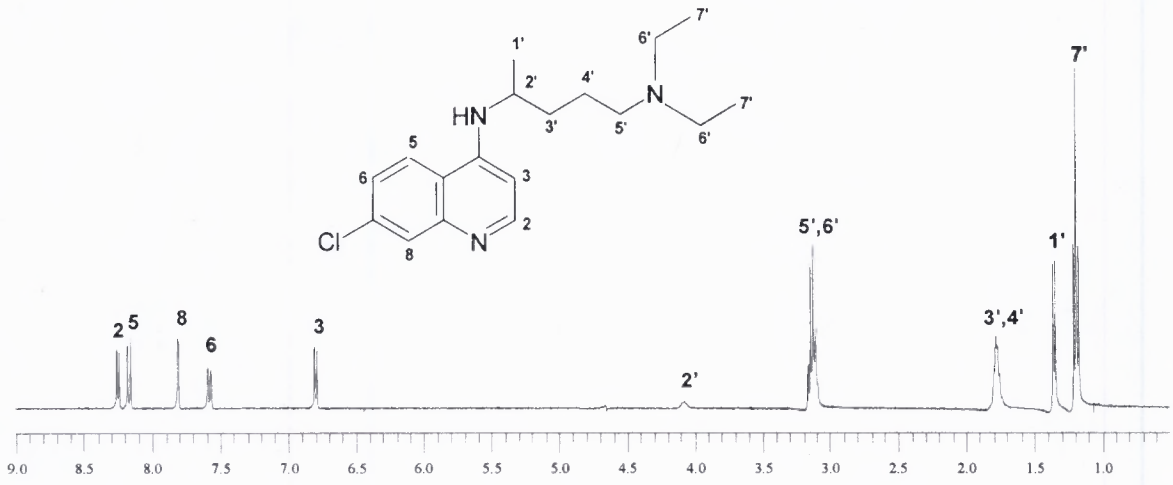

FIGURE 4.7(a). ^{1}H NMR spectrum of **CQ** with peak assignment.

Fig 4.7 (b) shows peak assignment of compound **1** as an example of the assignment for CQ-analogues (compounds **1**, **3** and **4**). The assignment of peak 1' and 2' were obtained by collecting the spectrum of compound **1** at different pH values and assigning the peaks depending on the change in chemical shift as a result in change in pH. The proton with the biggest change was assumed to be the most affected by protonation and hence closest to the tertiary amino nitrogen (N).

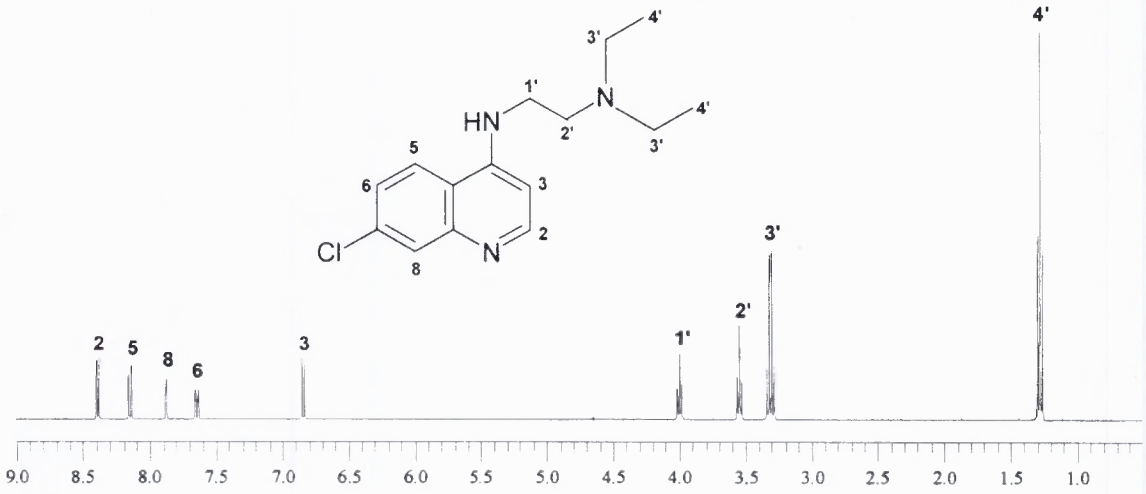

FIGURE 4.7(b). ^{1}H NMR spectrum of compound **1** with peak assignment.

4.5.1.2. The Effect of Unpaired Electrons on NMR Signals

The presence of a paramagnetic centre or metal ion is known to alter the NMR parameters of the nuclei interacting with it depending on their proximity to the paramagnetic centre or ion. One of the parameters affected is the NMR linewidth. An increase in line broadening and a decrease in signal intensity of the aromatic protons (**Fig 4.8** (**b**)) is observed for CQ in the presence of the paramagnetic iron centre of haematin compared to the normal spectrum in the absence of haematin (**Fig 4.8** (**a**)). The extent of the broadening depends on the electron relaxation rates caused by the iron centre, thus the bigger the broadening, the higher the relaxation rates. The nuclei with enhanced relaxation rates are closer to the paramagnetic centre, thus they interact strongly with the unpaired electron of the iron centre.

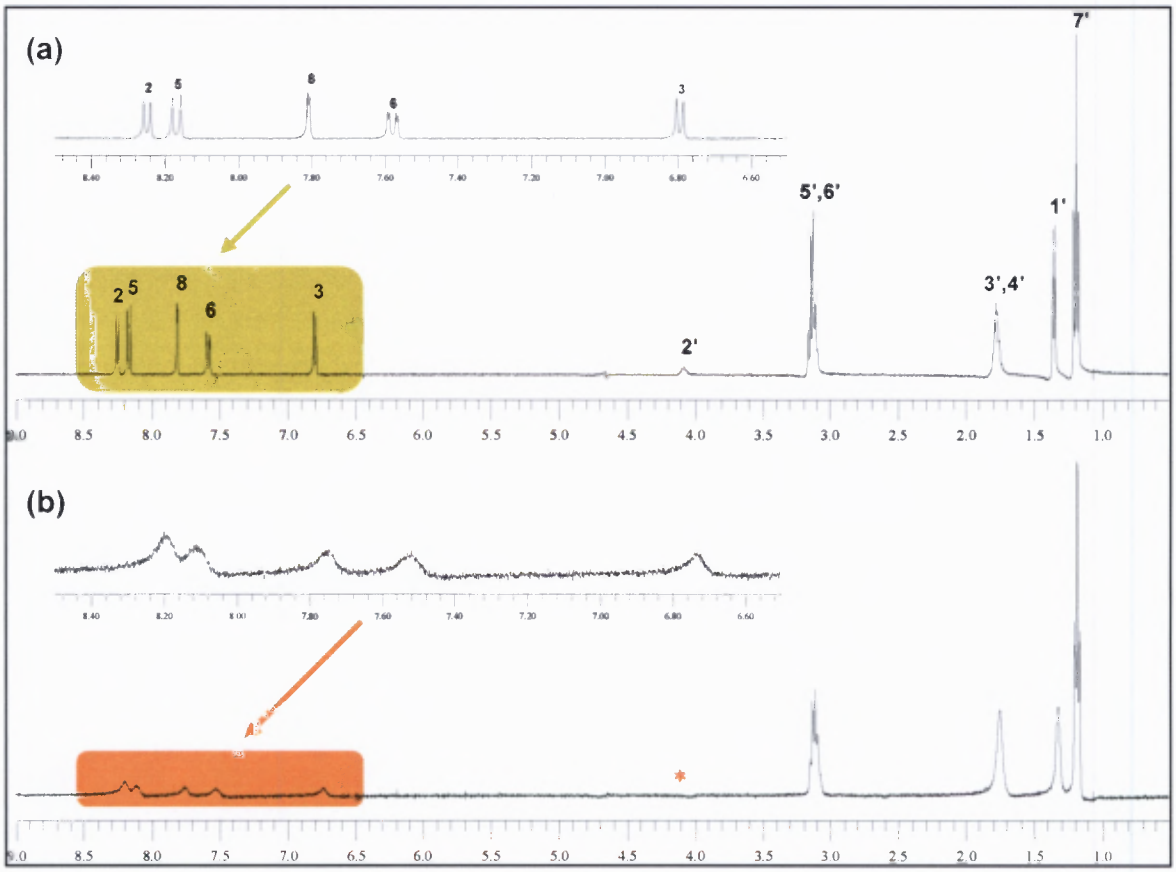

FIGURE 4.8. ^{1}H NMR spectra of **CQ** in (**a**) the absence of haematin and (**b**) the presence of 1 mM of haematin. The orange star (*) represents a peak that is undetected due to strong line broadening on account of its proximity to the paramagnetic centre.

The signal of proton 2'(orange star) has disappeared completely in **Fig 4.8** (**b**), which indicates that this nucleus is the closest one to the metal centre. The signals of the aromatic protons (**H2**, **H3**, **H5**, **H6** and **H8**) show significant changes as judged by their decrease in signal intensity and increase in line broadening, which is indicative of their close proximity to the Fe(III) centre. The signals of many of the other side chain protons, however do not show significant changes, suggesting that the protons are far away from the iron centre, and do not experience the effect of the unpaired electrons very strongly. This behaviour is an indication of complex formation between the two molecules. The results are in agreement with the previous proton [129, 147] and carbon [151] studies. The same trend was observed with the protons from compounds **1**— **5**.

4.5.1.3. Proton Longitudinal Relaxation Time (T_1)

Fig 4.9 shows a representative example of proton T_1 experimental data. The data was obtained from a mixture containing a 100:1 molar ratio of CQ:haematin and is shown as a typical example of a T_1 inversion recovery experiment. The aromatic protons recover more quickly than the side chain protons. This indicates that these protons have higher relaxation rates than the side chain protons. The results confirm that these protons are closer to the iron centre. This phenomenon was observed in all the 4-aminoquinolines studied and is in agreement with the observations made in Section 4.5.1.2 above. In general, the aromatic protons behave similarly to that observed by Leed *et al.* [147]. The proton longitudinal relaxation times of each proton obtained from T_1 experiments (**Fig 4.9**) were converted to effective relaxation rates, $R_{observed}$ ($1/T_1$ (observed)) and plotted against [haematin]/(K_d + [4AQ]) for increasing haematin:4AQ ratios (**Fig 4.10**).

An increase in the haematin:4-aminoquinoline ratio results in a decrease in relaxation times due to an apparent increase in the paramagnetic effect on the protons owing to more extensive complex formation, with the quinoline protons being more sensitive than the side chain protons. The linearity of the lines indicates a stoichiometry of one 4-aminoquinoline molecule to one haematin monomer in the complex at these concentrations. The steepness of the slopes is indicative of the proximity of the proton to the iron centre, thus, the steeper the slope the stronger the magnetic interaction between the proton and the paramagnetic iron centre. The lines conform to a 1:1 model and therefore demonstrate that the complexes conform to a 1:1 stoichiometric ratio. The results are in agreement with those reported previously [147] for CQ and with T_1 data observed in **Fig 4.9**.

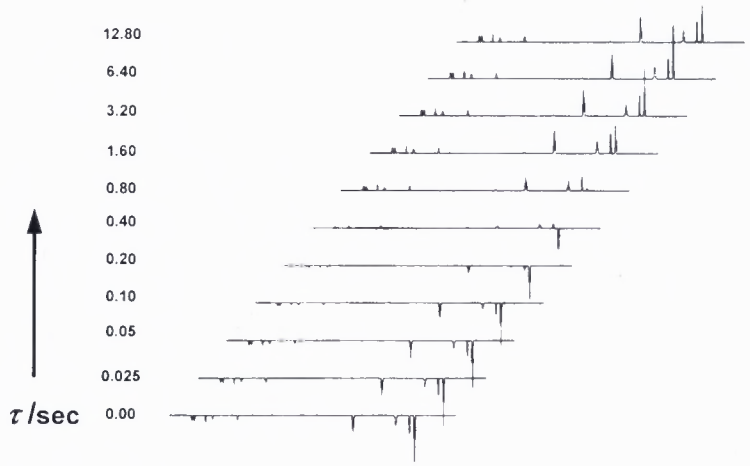

FIGURE 4.9. Inversion recovery data for a 100:1 mixture of **CQ**:haematin.

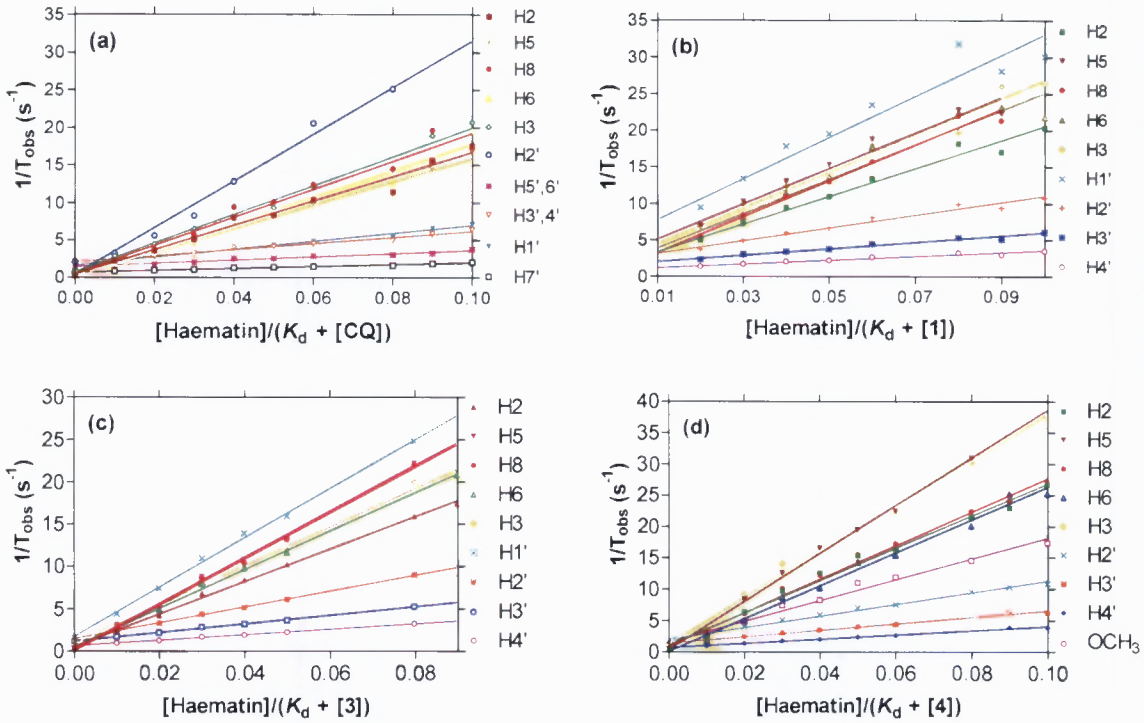

FIGURE 4.10. Plots of $1/T_{observed}$ against [haematin]/(K_d + [4AQ]) for (**a**) **CQ**, (**b**) compound **1**, (**c**) compound **3** and (**d**) compound **4**. **[haematin]** and **[4AQ]** represent the concentration of haematin monomer and the 4-aminoquinoline, respectively. K_d is the dissociation constant of the 4-aminoquinoline from the complex. The T_1 measurements of each proton were obtained from a single experiment for different haematin concentration.

The slopes and intercepts obtained from the plots in **Fig 4.10** were used to obtain $R_{complex}$ using Equation 5. These values were then converted to T_1 (complex) ($1/R_{complex}$). **Table 4.7** (**a**) shows the average experimental T_1 (complex) of all of the aromatic protons combined for each compound in the complex. These values provide information on the average distance of the quinoline aromatic nucleus from the Fe(III) centre in the complex, thus the smaller the value the closer the aromatic ring is on average to the Fe(III) centre. It is evident from these results that **CQ** is on average furthest from the Fe(III) centre, followed by compounds **2**, **1** and **3** respectively, while compounds **4** and **5** are closer. This might suggest that **CQ** as well as compound **1** to **3** bind weakly or have a lower affinity for haematin than compounds **4** and **5**, but in fact the opposite is true. Furthermore, **CQ** and compounds **1** and **2** are strong inhibitors of β-haematin formation and are strongly active compared to compound **3** which inhibits β-haematin formation weakly and is weakly active. Compounds **4** and **5** are reported not to inhibit β-haematin formation at all and are also inactive against *Plasmodium falciparum*. These observations seem to suggest that the proximity of the 4-aminoquinoline nucleus from the porphyrin is an important factor in predicting the activity of the 4-aminoquinolines. However, it should be noted that these complexes are dynamic and that the values of T_1 (complex) obtained from the NMR experiments are the averages of the conformations present in solution, and therefore larger average distances may simply reflect a more mobile complex.

TABLE 4.7(a). Average T_1 (complex) of all of the aromatic protons obtained from NMR

Compound	Average T_1 (complex)/ x10^{-3} s
CQ	5.71
2	4.72
1	4.26
3	4.19
4	3.25
5	3.06

Table 4.7 (**b**) shows the average experimental T_1 (complex) of all of the side chain protons combined for each compound in the complex. The signal of the **H1'** proton merged with that of the **OCH_3** for compound **4**, therefore, the T_1 (complex) for **H1'** was not computed. The average T_1 (complex) of the side chain protons for this compound was therefore omitted. The T_1 (complex) value for **CQ** is larger than that of the **CQ** analogues simply as a result of the longer side chain. On the other hand compounds **1**— **5** have side chains that are identical in length hence explaining the similarity in the T_1 (complex) values. The values are bigger on average than those obtained for the aromatic protons (**Table 4.7** (**a**)). This suggests that the side chain is further from the Fe(III) centre compared to the quinoline ring. The results however, do not exhibit to the same systematic trend observed in **Table 4.7** (**a**) for aromatic protons. This suggests that the side chain is flexible, and thus it can orientate itself in many conformations around the porphyrin ring. This shows that while the distance of the quinoline nucleus from the Fe(III) centre is correlated with the ability to inhibit β-haematin formation, the position of the side-chain apparently is not. A closer inspection of the T_1 (complex) values of the individual aromatic protons and, β-haematin inhibitory activity of the compounds indicates a strong correlation in some cases. It was therefore considered necessary to investigate this more closely to gain a deeper understanding of the inhibitory process and its relationship to the structure of these complexes.

TABLE 4.7(b). Average T_1 (complex) of all of the side-chain protons obtained from NMR

Compound	Average T_1 (complex)/ x10^{-3} s
CQ	11.22
2	7.41
1	8.89
3	8.47
4	—[a]
5	7.16

[a]Not available.

4.5.1.4. Comparison of the Experimental NMR Data with the β-Haematin Inhibitory Activity (Phiβ)

The results obtained from Section 4.5.1.3 seem to suggest the activity of the 4-aminoquinoline in inhibiting β-haematin formation is predicted by the conformations of the quinoline nucleus relative to the Fe(III) centre of Fe(III)PPIX. In order to better understand the relationship between β-haematin inhibition by the 4-aminoquinolines and the structure of the complexes formed between the 4-aminoquinoline and haematin, a correlation of the average of the T_1 (complex) (**Table 4.7** (**a**)) of all of the aromatic protons was plotted against the β-haematin inhibitory activity of the 4-aminoquinolines (**Table 4.8**).

TABLE 4.8. β-haematin inhibitory activities of the compounds used in the study

Compound	Phiβ (equivalents)[a]
CQ	1.91 ± 0.30[b]
2	3.0 ± 0.1[b]
1	3.6 ± 0.2[b]
3	8.9 ± 0.5[b]
4	107.8± 0.9[c]
5	390.5[d]

[a]Standard error of three determinations. [b]From Egan *et al.*, [202]. [c]This work. [d]Estimated from the normalised IC_{50} [141].

The correlation between the average T_1 (complex) of all of the aromatic protons in the complex and the β-haematin inhibitory activity (Phiβ) is shown in **Fig 4.11**. The log Phiβ values are significantly correlated with the T_1 (complex) values obtained from the NMR experiments. This suggests that the complexes formed between haematin with both the active and the non-active compounds are structurally different. A better correlation is observed when the Phiβ values are plotted against the T_1 (complex) of only **H2** and **H3** (**Fig 4.12**). A possible interpretation is that **H2** and **H3** lie closer on average to the Fe(III) centre for non-β-haematin inhibitors and lie further from Fe(III) for the 4-aminoquinolines that inhibit β-haematin formation.

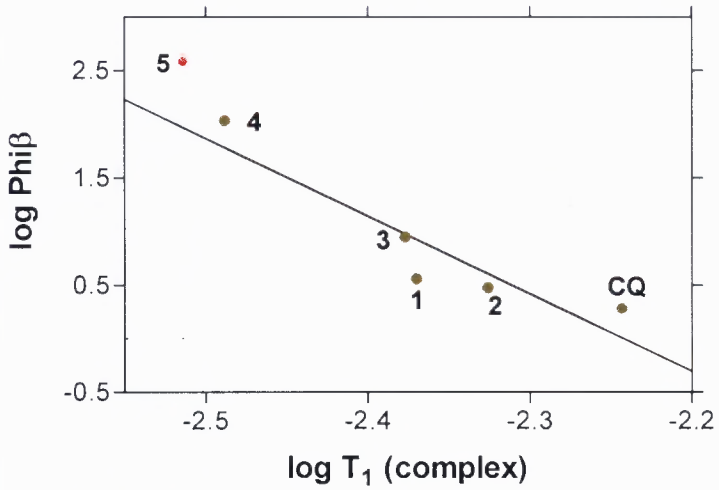

FIGURE 4.11. Correlation between the β-haematin inhibitory activity (Phiβ) and the average T_1 (complex) of all of the aromatic protons in the complex for **CQ** and compounds **1**, **2**, **3**, and **4**. The data for compound **5** (red, estimated from the normalised IC_{50}) was not included in the correlation as the value was not determined experimentally because the quantity required for inhibition exceeds its solubility limit under the assay conditions. The value of r^2 is 0.87 when the estimated value of compound **5** is included in the correlation and 0.84 when the data point is excluded from the correlation.

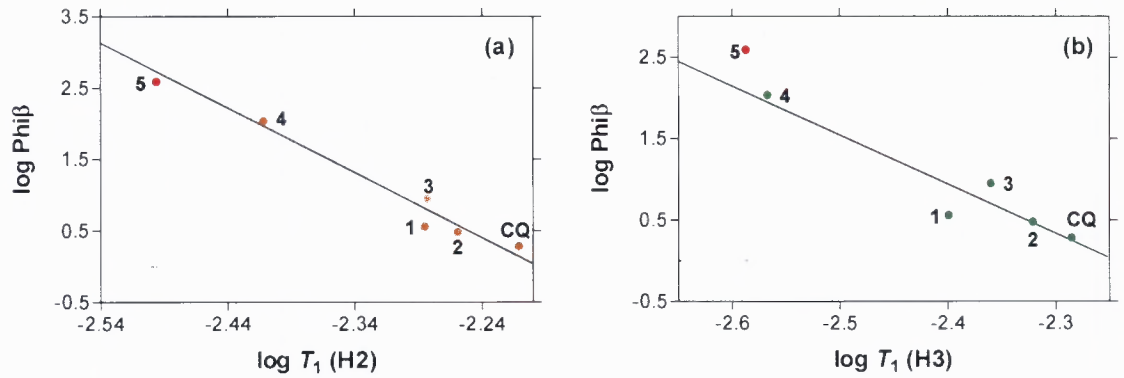

FIGURE 4.12. Correlation between the β-haematin inhibitory activity (Phiβ) and T_1 (complex) for **CQ** and compounds **1**, **2**, **3** and **4** for (**a**) **H2** and (**b**) **H3**. The data for compound **5** (red, estimated from the normalised IC_{50}) was not included in the correlation as the value was not determined experimentally because the quantity required for inhibition exceeds its solubility limit under the assay conditions. Values of r^2 of 0.97 and 0.92 were obtained when the estimated value of compound **5** was included in the correlation, and 0.94 and 0.89 when data point is excluded from the correlation for (**a**) and (**b**) respectively.

The dominant conformation adopted by the quinoline in the complex is apparently determined by the electronic properties of the atom at the 7-position (represented in yellow in **Fig 4.13**) which can be explained using the structure in **Fig 4.13**. Electron donating groups in compounds **4** and **5** result in an increase in electron density of the benzene ring. The electron rich benzo ring of the quinoline (blue rectangle) would therefore lie further away from the electron rich pyrrole ring of the porphyrin. This in turn positions the pyridinyl ring of the quinoline over the pyrrole ring and therefore moves **H2** and **H3** closer on average to the Fe(III) centre (**Fig 4.13**).

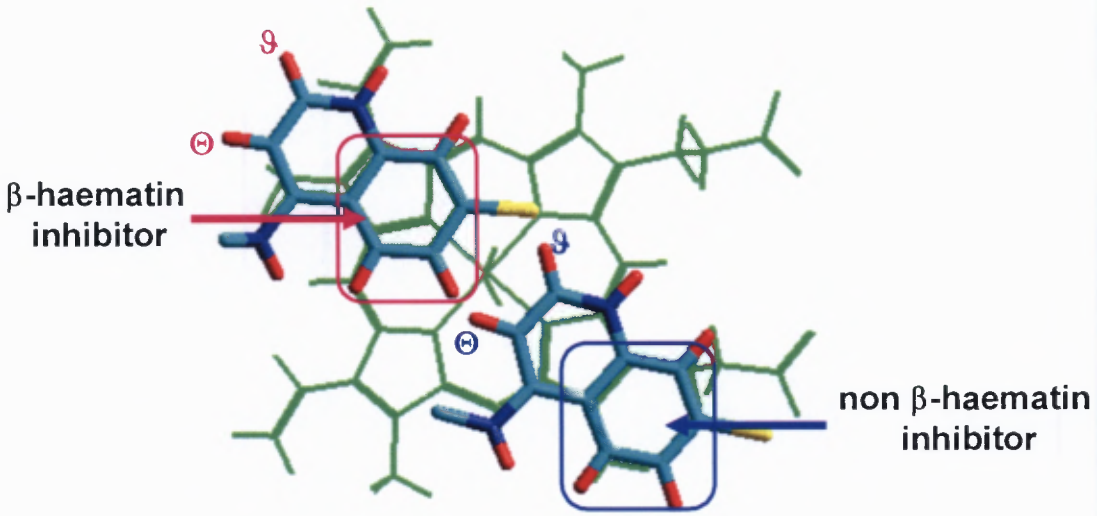

FIGURE 4.13. Representation of the postulated conformation of the complexes formed between 4-aminoquinolines studied with haematin monomer from the correlation of the T_1 of **H2** and **H3** with the log Phiβ. The atom at the 7-position is represented in yellow, the hydrogens are denoted in red, the carbon atoms in light blue and the nitrogens in blue. The haematin is shown in green. ϑ and Θ represent **H2** and **H3**, respectively. The rectangles show the benzene ring of the 4-aminoquinoline. The side-chain is omitted for clarity.

The opposite would be observed for the electron withdrawing groups in **CQ** and compounds **1**, **2**, and **3**. The pull of electron density away from the benzo ring would result in a decrease in electron density in this ring. The benzo ring which is now electron deficient (pink rectangle) would therefore lie over the electron rich pyrrole ring, thus moving the pyridinyl ring over the edge of the porphyrin and moving **H2** and **H3** further away from the Fe(III) centre. A study performed by Kaschula *et al.* [125,

141] has shown that an electron withdrawing group is required at 7-position for inhibition of β-haematin. These studies seem to suggest that the geometry of the complexes is largely determined by electrostatic interactions between haematin and 4-aminoquinolines. The electronic properties of the atom at the 7-position, which may affect the position of the benzene ring, therefore seems to play an important role in predicting the structure of the compounds which in turn determines whether they are active in preventing haemozoin formation.

4.5.1.5. Comparison of the Experimental NMR Data with Thermodynamic Data

The results obtained thus far (Section 4.5.1.3 and Section 4.5.1.4) seem to suggest the conformation of the complexes formed between haematin with the 4-aminoquinoline studied give rise to their differences in β-haematin inhibition activity. Thermodynamic studies were therefore conducted in order to gain further insight into the flexibility of the complexes formed between haematin and both β-haematin and non β-haematin inhibitors. The association of haematin with each of the 4-aminoquinolines studied was determined by spectrophotometric titration in 40% (v/v) aqueous DMSO at pH 7.5. The use of this method has been reported previously [137, 139, 141, 235] and provides a good indication of the trends in association constants that are likely to occur in the aqueous environment of the food vacuole by controlling the protonation state of the 4-aminoquiniline and maintaining Fe(III)PPIX in the monomeric state [249].

The absorbance of the haematin Soret band at 402 nm was monitored as a function of the concentration of the added drug at 20, 25, 30, 35 and 40°C. **Fig 4.14 (a)** shows a typical titration curve obtained from one of these titrations. The titrations all fitted to a 1:1 model which indicates that the complexes conform to a 1:1 stoichiometric ratio as seen in the aqueous system in **Fig 4.10**. These curves were then used to obtain the association constants at each temperature for each compound. The association constants were used to obtain the Van't Hoff plots shown in **Fig 4.14 (b)**. It is clear from these plots that the strengths of association between the 4-aminoquinolines and haematin are temperature dependent, with stronger complexes formed at lower

temperatures and weaker complexes formed at higher temperatures. It is also evident from these plots that **CQ** and compounds **1** and **2** on average, form stronger complexes compared to compounds **4** and **5**.

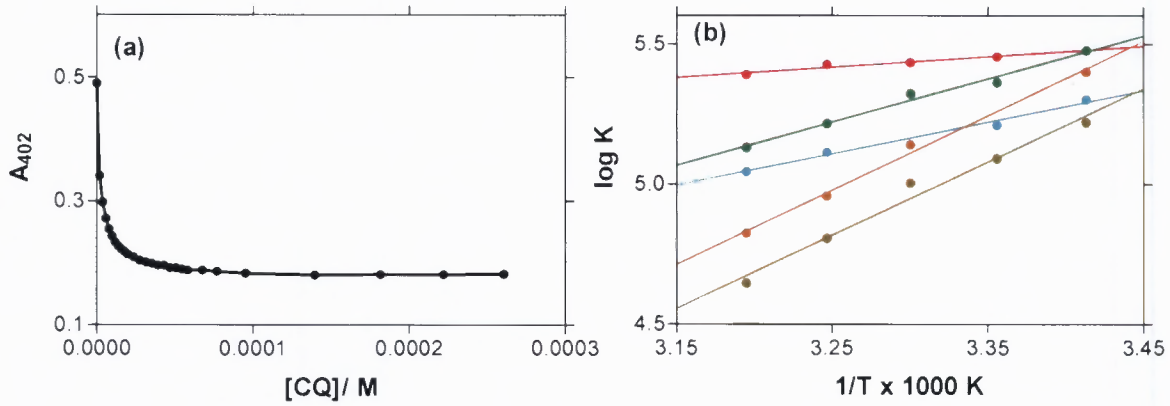

FIGURE 4.14. (**a**) Typical spectrophotometric titration curve for **CQ** in 40% (v/v) aqueous DMSO measured at 25°C, 0.020 M HEPES buffer (pH 7.5). The solid line is a best fit of the data to a 1:1 association model obtained by nonlinear least-squares analysis. (**b**) Variation of log *K* with the reciprocal of the absolute temperature (Van't Hoff plots) for (—) **CQ**, (—) compound **1**, (—) compound **2**, (—) compound **4** and (—) compound **5**. The data for compound **3** were not obtained due to lack of material.

Values of ΔH and ΔS (**Table 4.9**) were obtained from the slopes and the intercept of the Van't Hoff plot, respectively (**Fig 4.14** (**b**)). Previous studies have shown that there is a thermodynamic compensation effect between ΔH and ΔS in complexes formed between haematin and various quinoline drugs in 40% aqueous DMSO [137, 139] as well as in aqueous solution as described in Chapter 1 [123]. **Fig 4.15** shows that the same thermodynamic compensation phenomenon described by Equation 6 is observed with the compounds used in this study.

$$T\Delta S = \alpha\Delta H + T\Delta S_0 \qquad (6)$$

TABLE 4.9. Thermodynamic parameters obtained from the spectrophotometric titrations

Compound	[a]ΔH/ kJmol^{-1}	[a]ΔS/ JK^{-1}mol^{-1}
CQ	-7.16 ± 0.8	80.46 ± 2.60
1	-21.45 ± 1.7	28.15 ± 5.70
2	-29.49 ± 2.2	4.14 ± 7.10
4	-50.93 ± 2.8	-70.96 ± 14.10
5	-50.21± 4.3	-70.18 ± 9.30

[a]The values were obtained from the Van't Hoff plots. Standard errors were calculated from the values of the slope and intercept, respectively.

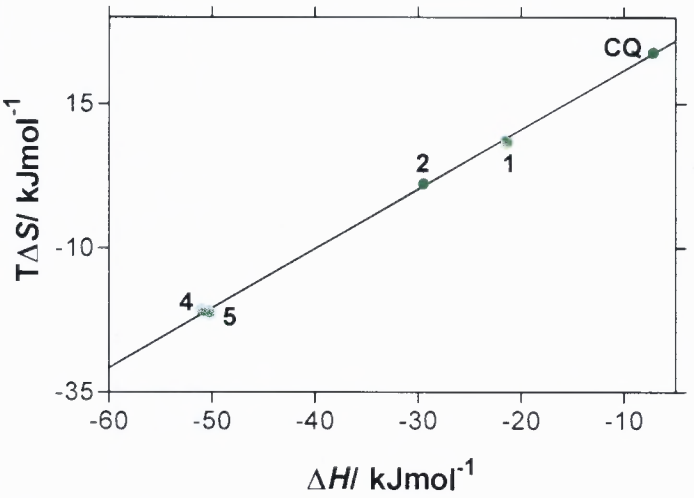

FIGURE 4.15. Thermodynamic compensation plot for the association of the 4-aminoquinoline used in the study with haematin in 40% (v/v) aqueous DMSO, pH 7.5 (0.02 M HEPES buffer) at 25°C. The slope (α) and intercept ($T\Delta S_0$) are 1.0 ± 0.02 and 31.2 ± 0.60 kJmol^{-1}, respectively. ΔS_0 is the value of ΔS when ΔH is zero. The data for compound **3** were not obtained due to lack of material.

The plot gives a linear relationship with a slope, α, of 1.0 ± 0.02 and intercept, $T\Delta S_0$, of 31.2 ± 0.60 kJmol^{-1} under these experimental conditions. Inoue and Wada have argued that α denotes the loss in flexibility of the host while $T\Delta S_0$ gives information about the degree of desolvation of the guest [143]. Large values of both α and $T\Delta S_0$ indicate a large loss of flexibility and a considerable degree of desolvation under

these conditions. Small values of α and $T\Delta S_0$ have been reported by Inoue and Wada for the association of porphyrins with quinones in organic solvents. These observations were ascribed to the fact that there is little desolvation in organic solvents and that the porphyrins are already rigid. This is expected as organic solvents in general solvate solutes weakly. The role of water in locking in the conformation of the complexes is apparently also crucial. The results obtained in this study are essentially identical to the values obtained by Egan *et al.* ($\alpha = 1.1 \pm 0.1$ and $T\Delta S_0 = 29 \pm 2$ kJmol^{-1}) using the same conditions [139] and Dorn *et al.* ($\alpha = 1.0 \pm 0.1$ and $T\Delta S_0 = 29 \pm 5$ kJmol^{-1}) for pure aqueous solution [123]. This indicates that the interactions of haematin with quinolines are similar under both sets of conditions with considerable loss of flexibility upon complexation. The degree of desolvation indicates that these interactions are hydrophobic in nature [139]. This means that some of the solvent molecules associated with the haematin crystal lattice are replaced by the 4-aminoquinoline upon complex formation. The results also show that formation of the complexes of **CQ** and compound **1** are mainly entropy driven while that of compound **2** is mainly enthalpy driven. Those of compounds **4** and **5** are entirely enthalpy driven as the entropy change is negative. These results would lead to the conclusion that the conformation of the complexes formed between haematin with **CQ** and compound **1** are more flexible that those formed with compounds **2**, **4** and **5** as predicted by the average distances observed between the aromatic protons and Fe(III) in the NMR experiments.

In order to confirm the results obtained above, the ΔH and ΔS values were correlated with the experimental NMR data T_1 (complex) of the average of all of the aromatic protons for each compound (**Table 4.7 (a)**) (**Fig 4.15**). Both the enthalpies and the entropies of formation show a good correlation with the average T_1 (complex) values as shown in **Fig 4.16**. Large positive ΔS values indicate that the complexes are flexible while large average T_1 (complex) indicates that the protons of the 4-aminoquinoline lie on average furthest from the Fe(III). The results therefore suggests that weak β-haematin inhibitors form rigidly fixed complexes, which results in protons being on average nearer to the Fe(III) centre. The strong β-haematin

inhibitors on the other hand form loose complexes. The protons of the 4-aminoquinoline in this complex therefore lie further on average from the Fe(III) centre.

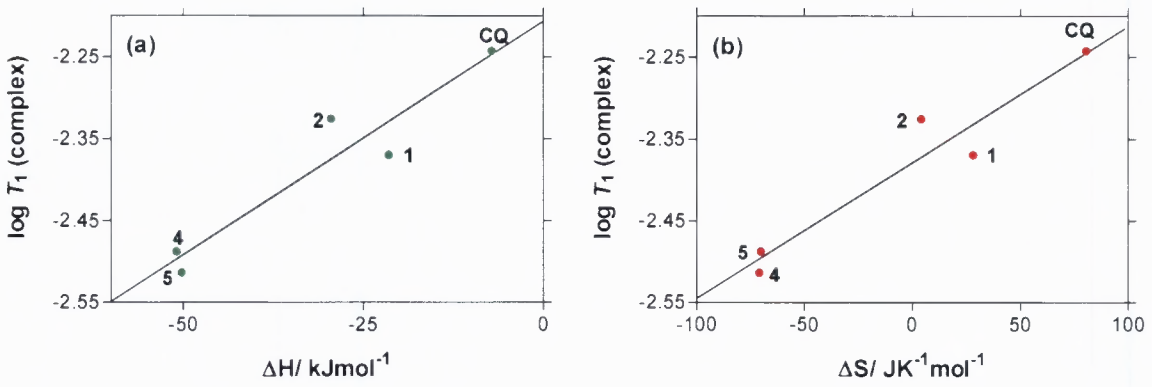

FIGURE 4.16. Correlation between the average T_1 (complex) of all of the aromatic protons in the complex with (**a**) enthalpy and (**b**) entropy of complex formation with Fe(III)PPIX for **CQ** and compounds **1**, **2**, **4** and **5**. The data for compound **3** were not obtained due to lack of material. The data were obtained from Van't Hoff's plots in 40% (v/v) aqueous DMSO, pH 7.5 (0.02 M HEPES buffer). The data show a good correlation, with r^2 = 0.91 and P = 0.0118 for (**a**) and r^2 = 0.92 and P = 0.0092 for (**b**).

A correlation between β-haematin inhibitory activity of the 4-aminoquinolines studied with the free energy of association (ΔG) and entropy (ΔS) was obtained in order to confirm further whether the apparent flexibility of the complexes formed between the 4-aminoquinoline and haematin affect the inhibitory activity of the 4-aminoquinoline. **Fig 4.17** (**a**) shows a plot of log Phiβ against ΔG. The ΔG values for each compound were obtained from Equation 7. The value of ΔG is a measure of the strength (free energy) of the complex.

$$\Delta G = -2.303RT \log K \qquad (7)$$

where R is the molar gas constant (8.3145 J K^{-1} mol^{-1}) and T is the temperature (K).

The poor correlation in **Fig 4.17** (**a**) (r^2 of 0.47) confirms that the activity of the 4-aminoquinoline is not related to the strength of the complex, however, it is related to the entropy of complex formation as shown in **Fig 4.17** (**b**) (r^2 of 0.84). The larger ΔS values of complex formation would suggest that the 4-aminoquinoline has the freedom to orientate itself in many conformations around the porphyrin ring thus preventing haematin molecules from interacting with each other to form β-haematin as compared to the tightly formed complexes observed with non β-haematin inhibitors. A lack of correlation between the β-haematin inhibition activity of the 4-aminoquinolines studied with the thermodynamics data observed by Dorn and co-workers [142] could be due to additional factors such a Fe(III)PPIX aggregation associated with aqueous conditions resulting in complexes with different stoichiometries.

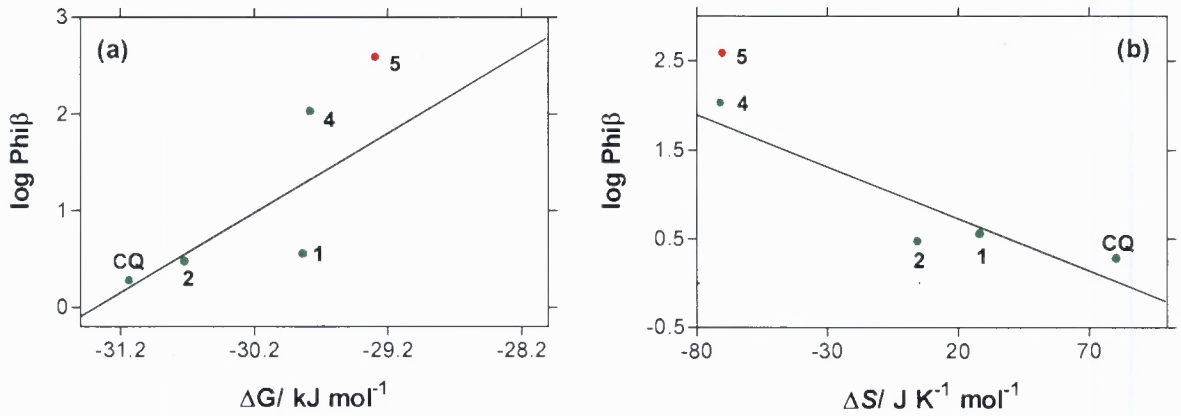

FIGURE 4.17. Correlation between the β-haematin inhibitory activity (Phiβ) and (**a**) ΔG (free energy of association) and (**b**) ΔS (entropy) of complex formation of **CQ** and compounds **1**, **2** and **4** with Fe(III)PPIX The Phiβ for compound **5** (red, estimated from the normalised IC_{50}) was not included in the correlation as the value was not determined experimentally because the quantity required for inhibition exceeds its solubility limit under the assay conditions. Values of r^2 of 0.69 and 0.85 were obtained when the estimated value of compound **5** was included in the correlation, and 0.47 and 0.84 when the data point is excluded from the correlation for (**a**) and (**b**) respectively. The thermodynamic data for compound **3** are not available due to lack of material.

4.5.2. Attempted Elucidation of the Geometry of the Haematin:4-Aminoquinoline Complex Structures

4.5.2.1. Distance Constraints

Proton longitudinal relaxation time (^{1}H T_1) was measured in order to obtain distance constraints as shown in **Table 4.10**. The values of $R_{complex}$ of each proton were firstly obtained from the slope and the intercept obtained from the plots shown in **Fig 4.10**.

TABLE 4.10. Distance constraints used in molecular dynamics calculations

			[a]Fe-H Distances (r)/ Å		
^{1}H	CQ	^{1}H	Compound 1	Compound 3	Compound 4
H2	6.41125	**H2**	6.22983	6.23642	5.93431
H5	6.46357	**H5**	5.98466	5.88372	5.55935
H8	6.26162	**H8**	5.98242	5.88685	5.89607
H6	6.31507	**H6**	6.01802	6.05986	5.91994
H3	6.23233	**H3**	5.96347	6.05338	5.89480
H1'	7.68696	**H1'**	5.60091	5.81309	—[b]
H2'	5.75196	**H2'**	7.07689	7.01226	7.01007
H3',4'	8.00894	**H3'**	7.92117	7.75141	7.72058
H5',6'	8.88388	**H4'**	8.63359	8.36122	8.30640
H7'	9.71391	**OCH_3**			6.37948

[a]Force constant, k = 0.075 mdyne Å^{-1} ($r \geq 4$Å) was used to obtain distance restraints [248]. [b]The peak could not be resolved from the OCH_3 signal.

The 'average' Fe-H distances were then calculated from the Solomon-Bloembergen equation using a τ_c value of 1.28 x10^{-11} s. This value was estimated based on the distances obtained by Leed *et al.* [147]. The results obtained for **CQ** suggest that the quinoline nucleus (**H2**, **H5**, **H8**, **H6**, and **H3**) lies close to the Fe(III) centre of the porphyrin ring with proton 2' being even closer. The side chain protons however are further away than either **H2'** or the aromatic protons. These results resemble those of Leed *et al.* [147]. The quinoline nucleus and the side chain of the rest of the 4-aminoquinolines also follow the same trend. However, compounds **1**, **3** and **4** on average seem to lie closer to haematin than **CQ**. The detailed structures of these

complexes can only be deduced using molecular modelling in order to model all possible conformations of the complexes.

4.5.2.2. Geometry of the Model CQ:Haematin Complex Structures.

The structures of the complexes obtained between the diprotonated form of CQ and haematin are shown in **Fig 4.18** (**a**) — (**d**) and were obtained from the starting structures shown in **Fig 4.6**. A total of 25 structures were obtained from each of the starting position and these were overlayed by aligning the porphyrin rings such that the 4 nitrogen atoms and the Fe centre coincide. These structures represent low energy conformations found by MD/SA using the experimentally derived Fe-H distance constraints. The ^{1}H-Fe(III) distances are assumed to agree with the experimental evidence as a result of the use of constraints (the validity of the assumption is discussed later in Section 4.5.2.4).

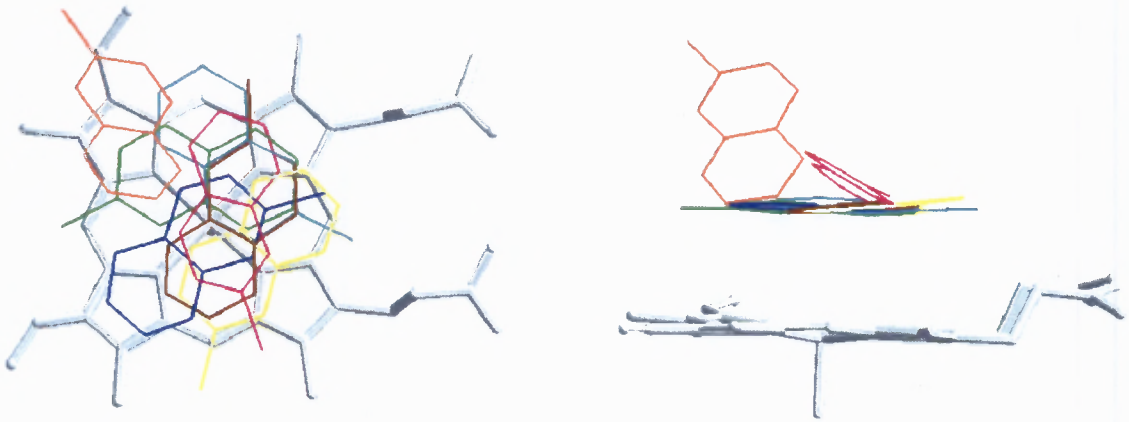

FIGURE 4.18(a). Overlay of complexes predicted between haematin monomer and the diprotonated form of **CQ** viewed from the axial view (left) and side view (right) obtained from starting position (**a**) in Fig 4.6. The structures were obtained by overlaying 25 complex structures. The preferred orientations are shown in different colours. Only the quinoline nucleus is displayed. In addition all the protons are omitted for clarity. Only 1 haematin molecule is represented for clarity and is represented in light blue.

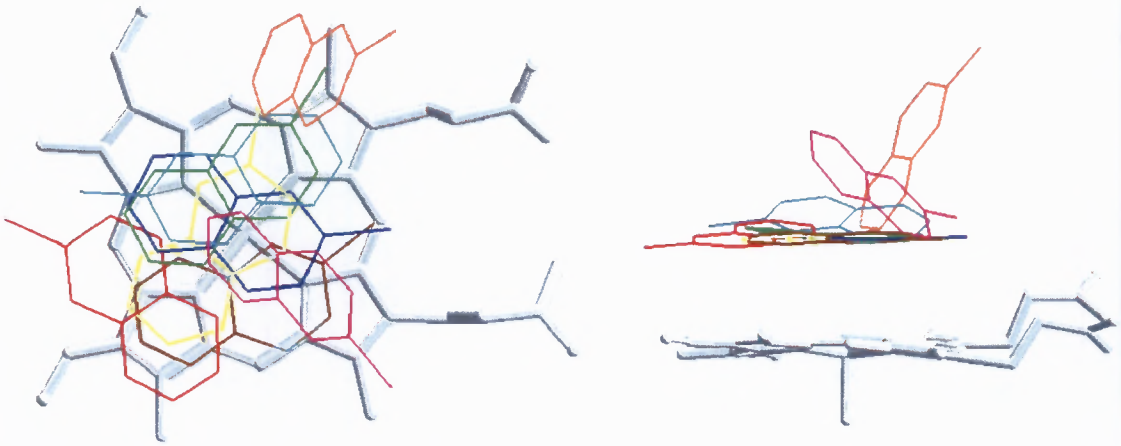

FIGURE 4.18(b). Overlay of complexes predicted between haematin monomer and the diprotonated form of **CQ** viewed from the axial view (left) and side view (right) obtained from starting position (**b**) in Fig 4.6. The structures were obtained by overlaying 25 complex structures. The preferred orientations are shown in different colours. Only the quinoline nucleus is displayed. In addition all the protons are omitted for clarity. Only 1 haematin molecule is represented for clarity and is represented in light blue.

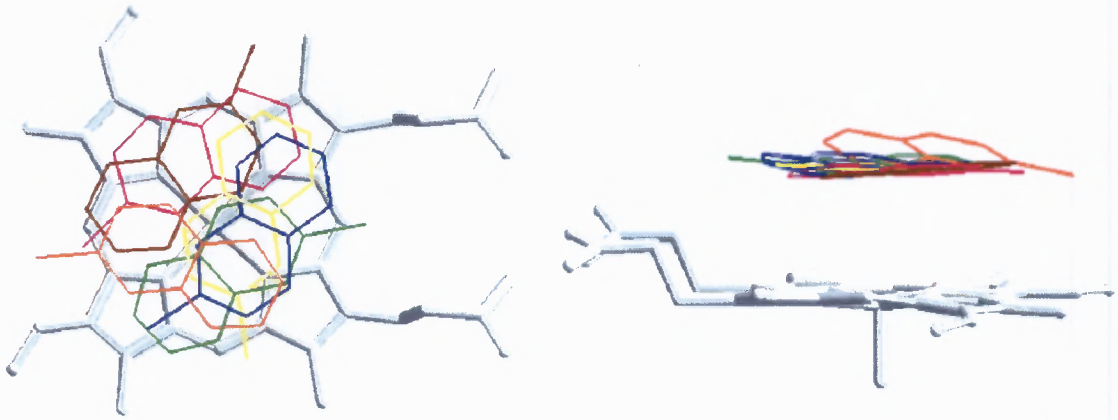

FIGURE 4.18(c). Overlay of complexes predicted between haematin monomer and the diprotonated form of **CQ** viewed from the axial view (left) and side view (right) obtained from starting position (**c**) in Fig 4.6. The structures were obtained by overlaying 25 complex structures. The preferred orientations are shown in different colours. Only the quinoline nucleus is displayed. In addition all the protons are omitted for clarity. Only 1 haematin molecule is represented for clarity and is represented in light blue.

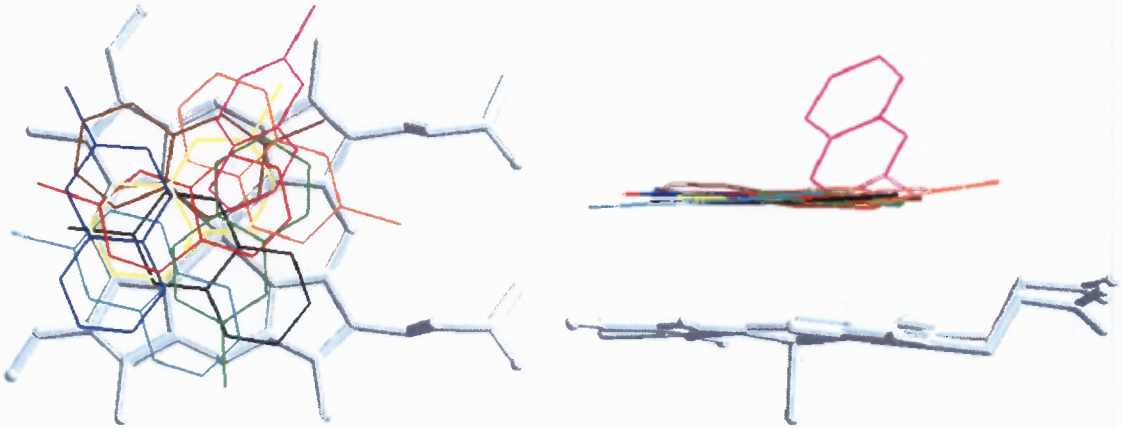

FIGURE 4.18(d). Overlay of complexes predicted between haematin monomer and the diprotonated form of **CQ** viewed from the axial view (left) and side view (right) obtained from starting position (**d**) in Fig 4.6. The structures were obtained by overlaying 25 complex structures. The preferred orientations are shown in different colours. Only the quinoline nucleus is displayed. In addition all the protons are omitted for clarity. Only 1 haematin molecule is represented for clarity and is represented in light blue.

In the majority of the structures the quinoline nucleus is not positioned directly above the Fe(III) centre but is located towards the edge of the porphyrin ring near the pyrrole rings. However, there is a minor contribution from structures in which the quinoline nucleus is orientated closer to the Fe(III) centre. The structures also show that the quinoline ring is not always co-planar with the porphyrin ring, but is tilted in some cases. This is in agreement with the hypothesis that the interactions between haematin and the 4-aminoquinolines are driven by π-π stacking between the aromatic group of the 4-aminoquinolines and the electron rich porphyrin ring [250]. The study also demonstrates that the complexes are dynamic in nature, meaning that the orientation of the complex changes with little change in energy of the system, resulting in different conformations. The structures obtained in this study are similar to those of Leed *et al.* [147] in that the quinoline nitrogen of CQ is always orientated towards the porphyrin rim, while the 4-amino group points towards the Fe(III) centre. The structures obtained by Leed *et al.* [147] and de Dios *et al.* [148] suggest that the aliphatic chain of the quinoline drugs (CQ, quinine, quinidine and amodiaquine) used in their studies is wrapped around the edge of the tetrapyrrole ring of the porphyrin.

Fig 4.19 shows the orientation of the side chain. It is clear that in the current model the side chain is flexible and can orientate randomly. There is no evidence of the side chain winds around the porphyrin rim in comparison to the structures obtained by Leed *et al.* [147]. In fact, there is no evidence of interaction of the side chain with the porphyrin.

FIGURE 4.19. Preferred orientations of the aliphatic side chain of **CQ** viewed from the axial view (left) and side view (right). The structures were obtained by overlaying 10 complex structures obtained from the modelling. The structures were overlayed by aligning the quinoline nucleus such that the group at 7-position and the quinoline nitrogen coincide. The haematin monomer is shown in brown. All the protons are omitted for clarity.

4.5.2.3. Comparison of the Geometry of CQ Complexes with Haematin with those of Short-chain 4-Aminoquinoline Analoques

The geometries of the complexes obtained from each of the starting structures (**Fig 4.6**) for **CQ** and compounds **1**, **3** and **4** were obtained by MS/SA to obtain low energy conformations. A total of 100 complex structures were overlayed by aligning the porphyrin rings such that the 4 nitrogens and the Fe centre coincide. The predicted structures for each complex, including that of CQ are shown in **Fig 4.20** (**a**) — (**b**) and **Fig 4.21** (**a**) — (**b**). It is evident from the pictures that the atom at the 7-position (4-aminoquinoline molecule) is pointed towards the periphery of the porphyrin ring and in most cases lies parallel to the plane of the porphyrin ring, with a minor contribution from structures in which the atom at the 7-position is orientated upwards. These atoms are probably orientated in this way in order to minimise steric interactions with the porphyrin and its side chain as these atoms or groups are relatively bulky. The quinolines are also clustered around the porphyrin nucleus. These figures therefore give a sense of the dynamic nature of the model complexes.

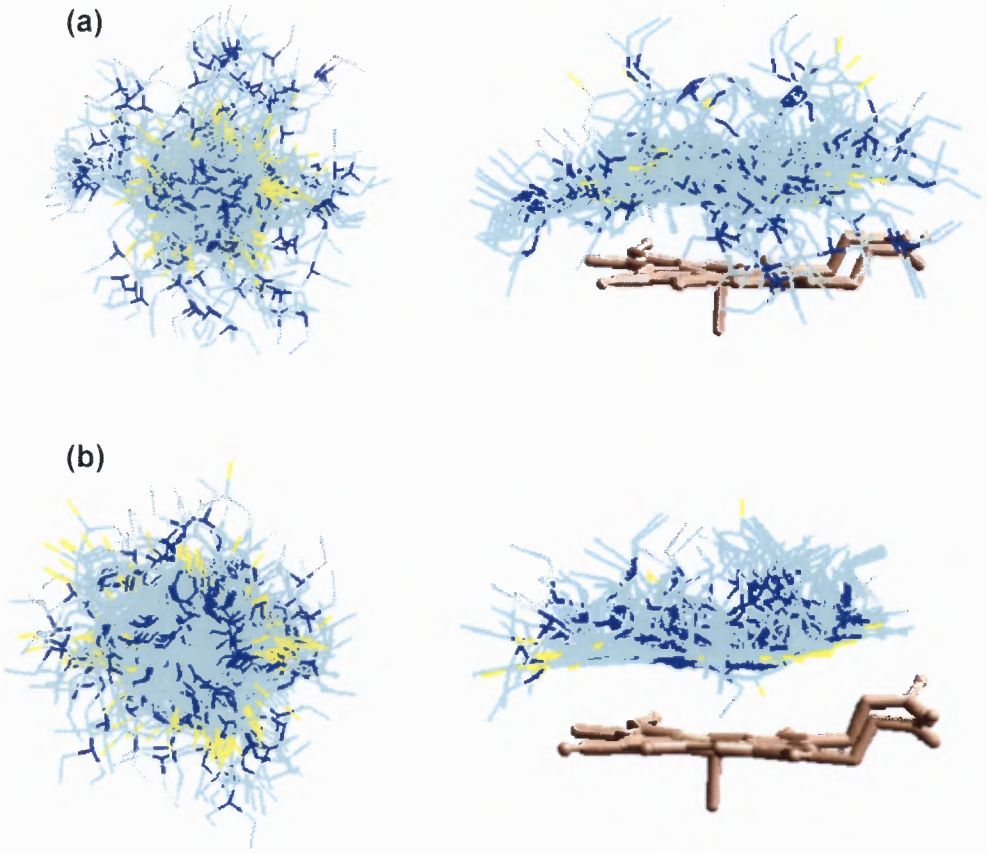

FIGURE 4.20. Overlay of complexes predicted between haematin monomer with the diprotonated form of (**a**) **CQ** and (**b**) compound **1** viewed from the axial view (left) and side view (right). Yellow represents the chlorine atom at the 7-position on the quinoline, dark blue represents the nitrogen atoms on the quinoline, light blue represents the carbon atoms on the quinoline and brown represents the haematin monomer. The haematin on the left and all the protons are omitted for clarity. The structures were obtained by overlaying 100 complex structures. Only 1 haematin molecule is represented for clarity on the right.

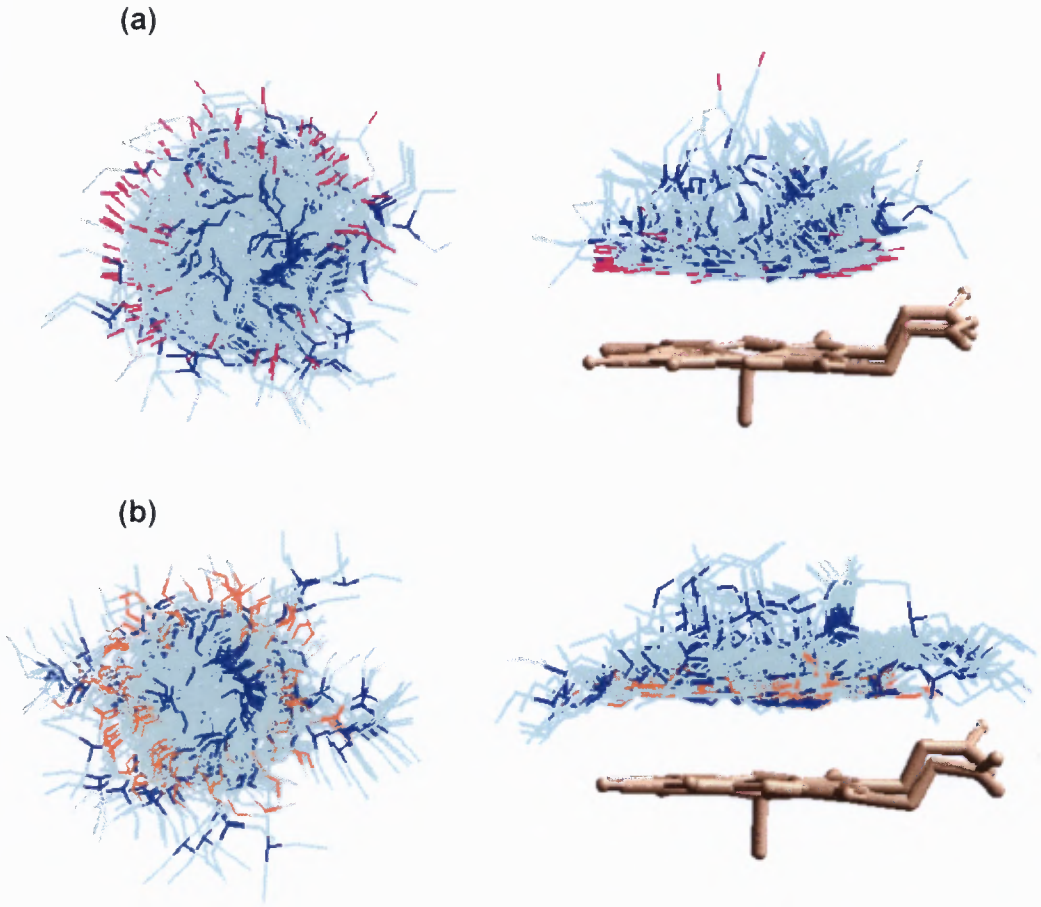

FIGURE 4.21. Overlay of complexes predicted between haematin monomer with the diprotonated form of (**a**) compound **3** and (**b**) compound **4** viewed from the axial view (left) and side view (right). Violet (**a**) and orange (**b**) represent the fluorine and methoxy group at the 7-position on the quinoline respectively, dark blue represents the nitrogen atoms on the quinoline, light blue represents the carbon atoms on the quinoline and brown represents the haematin monomer. The haematin on the left and all the protons are omitted for clarity. The structures were obtained by overlaying 100 complex structures. Only 1 haematin molecule is represented for clarity on the right.

The side chains of compounds **1**, **3** and **4** behave differently from that of **CQ** (**Fig 4.22** (**a**) — (**c**)). The chain is extended upwards away from the periphery of the porphyrin ring and appears to wrap around the rim when viewed from above (although little contact appears to occur). This may be due to the differences in chain

length and probably in part reflects the more limited number of possible conformations. No major structural differences in conformations were observed between the 4-aminoquinolines that are active against β-haematin formation (**CQ** and compounds **1** and **3**) and the 4-aminoquinolines that are not active (compound **4**). This suggests that these models are inadequate in predicting the nature of the complexes between the 4-aminoquinolines and haematin.

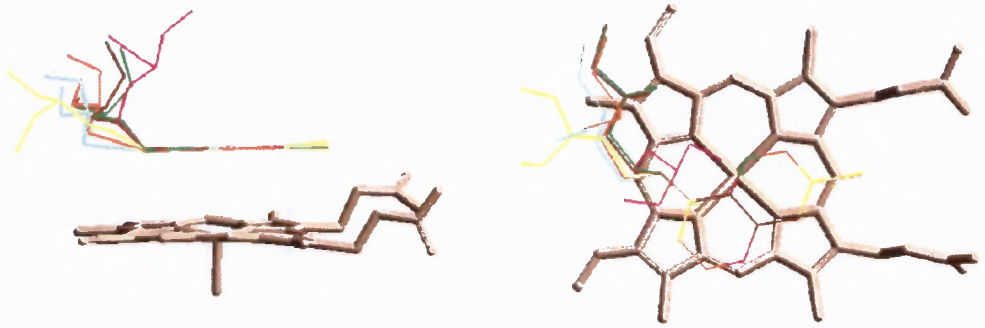

FIGURE 4.22(a). Preferred orientations of the aliphatic side chain of compound **1** viewed from the axial view (left) and side view (right). The structures were obtained by overlaying 10 complex structures obtained from the modelling. The structures were overlayed by aligning the quinoline nucleus such that the group at 7-position and the quinoline nitrogen coincide. The haematin monomer is shown in brown. All the protons are omitted for clarity.

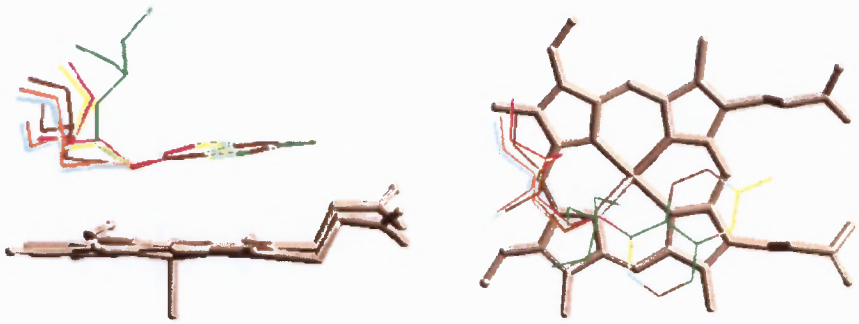

FIGURE 4.22(b). Preferred orientations of the aliphatic side chain of compound **3** viewed from the axial view (left) and side view (right). The structures were obtained by overlaying 10 complex structures obtained from the modelling. The structures were overlayed by aligning the quinoline nucleus such that the group at 7-position and the quinoline nitrogen coincide. The haematin monomer is shown in brown. All the protons are omitted for clarity.

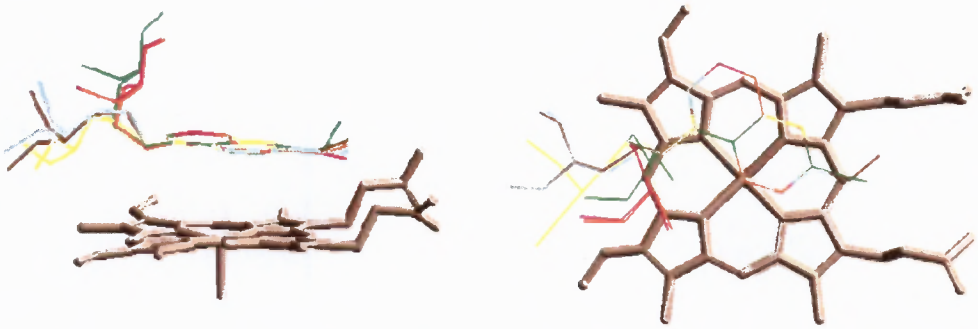

FIGURE 4.22(c). Preferred orientations of the aliphatic side chain of compound **4** viewed from the axial view (left) and side view (right). The structures were obtained by overlaying 10 complex structures obtained from the modelling. The structures were overlayed by aligning the quinoline nucleus such that the group at 7-position and the quinoline nitrogen coincide. The haematin monomer is shown in brown. All the protons are omitted for clarity.

4.5.2.4. Comparison of the Experimental NMR Data with the Computed MM Data

The results obtained from molecular modelling (**Fig 4.20** (**a**) — (**b**) and **Fig 4.21** (**a**) — (**b**)) seem to suggest that the structures of the complexes formed between haematin and the different 4-aminoquinolines (**CQ** and compounds **1**, **3** and **4**) studied all exhibit a very similar range of conformations. This clearly does not agree with the NMR evidence described above (Section 4.5.1) which clearly shows different T_1 (complex) values for **H2** and **H3** in the different complexes. It is therefore important to compare these model structures in greater detail with the results obtained from the NMR experiments. Correlation plots of the NMR data (T_1 (complex)) against the computed average T_1 (complex) value obtained for each proton from the 100 model structures obtained for each compound from MD/SA simulations are shown in **Fig 4.23** — **Fig 4.26**. A good correlation is observed when all the protons of the 4-aminoqunolines are plotted. This is however a statistical artefact. The points fit a straight line due to the fact that the side chain proton T_1 values are much larger than the aromatic ring T_1 values, so that the data points at two extremes giving a seemingly good correlation. However, as seen when experimental T_1 values were correlated with β-haematin inhibitory strength, the importance of the conformation of the aromatic ring in the complexes is of primary

importance (Section 4.5.1), Therefore, correlation plots of only the aromatic protons were also obtained. When only the aromatic protons are compared, there is a poor correlation for all the compounds between the NMR T_1 (complex) data and the computed T_1 (complex) data (**Fig 4.23 — Fig 4.26**), with r^2 of 0.09, 0.15, 0.11 and 0.37 for **CQ** and compounds **1**, **3** and **4**, respectively. The correlation for compound **4** only is somewhat better (**Fig 4.26** (**b**)). In all of the compounds the average T_1 (complex) of **H3** and **H5** is always smaller in the model than in the experiment, with **H6** being small also for compounds **3** and **4**. This indicates that these protons are on average closer to the Fe(III) centre in the model than in the real complex. The average T_1 (complex) of **H6** and **H8** is on the other hand always larger in the model for **CQ** and compound **1** (**Table 4.11**). These protons are further away from the Fe(III) centre in the model. These results show that the conformations from the molecular dynamics calculations are probably not similar to those occuring experimentally. This indicates that the modelling method reported by Leed *et al.* [147] is in fact inadequate to simulate these types of complexes.

Careful reflection shows that there is in fact a fundamental theoretical flaw in using the Solomon-Bloembergen expression for modelling the structures of flexible complexes such as those formed between haematin and the 4-aminoquinolines. This arises from a statistical problem associated with it (see conclusion).

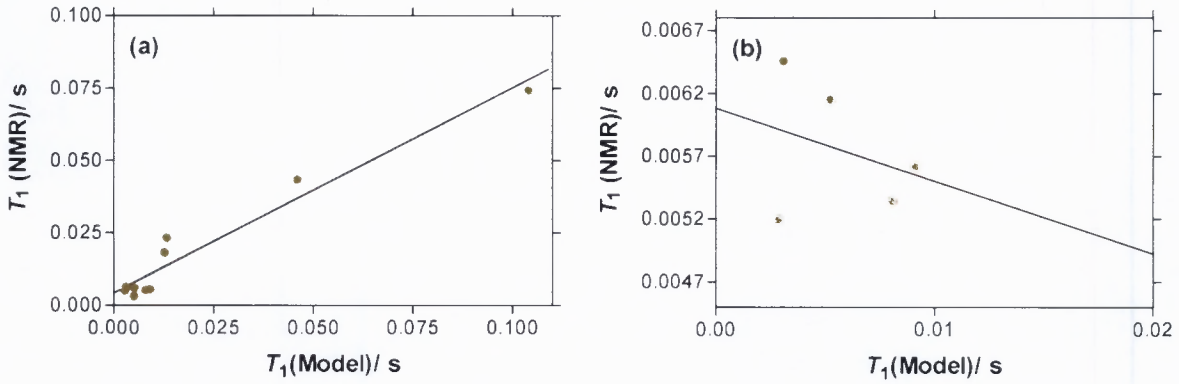

FIGURE 4.23. Correlation between the average NMR T_1 (complex) and the average computed T_1 (complex) values for **CQ** for (**a**) all of the protons and (**b**) the aromatic protons only, with r^2 of 0.95 and 0.09 respectively. The computed values were obtained by converting the average distances obtained from the complexes to T_1 (complex) for each proton using the Solomon-Bloembergen equation (Equation 1).

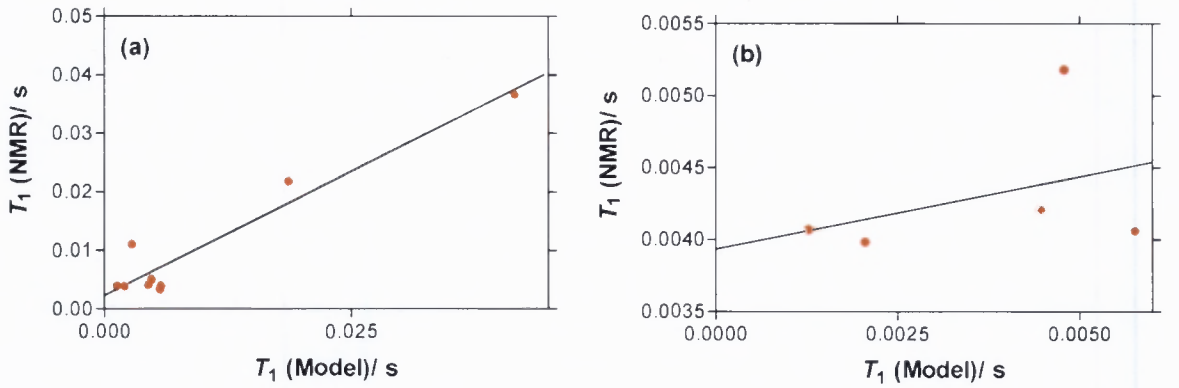

FIGURE 4.24. Correlation between the average NMR T_1 (complex) and the average computed T_1 (complex) values for compound **1** for (**a**) all of the protons and (**b**) the aromatic protons only, with r^2 of 0.92 and 0.15 respectively. The computed values were obtained by converting the average distances obtained from the complexes to T_1 (complex) for each proton using the Solomon-Bloembergen equation (Equation 1).

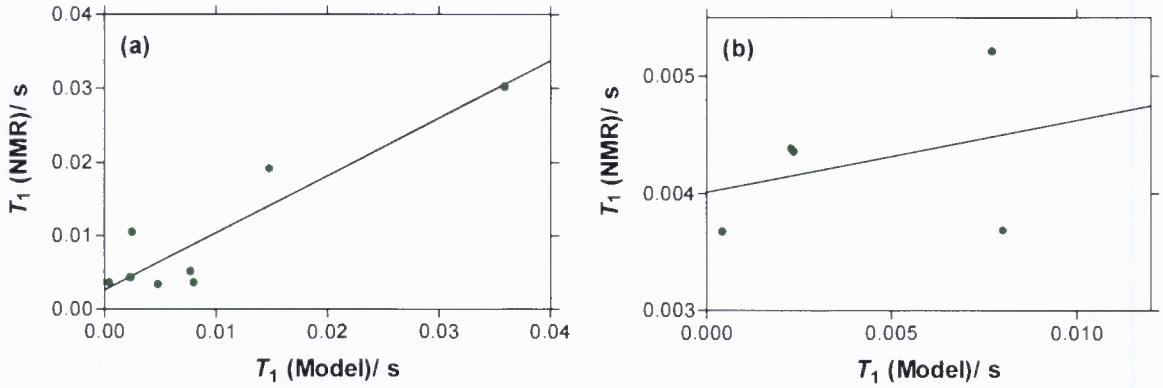

FIGURE 4.25. Correlation between the average NMR T_1 (complex) and the average computed T_1 (complex) values for compound **3** for (**a**) all of the protons and (**b**) the aromatic protons only, with r^2 of 0.84 and 0.11 respectively. The computed values were obtained by converting the average distances obtained from the complexes to T_1 (complex) for each proton using the Solomon-Bloembergen equation (Equation 1).

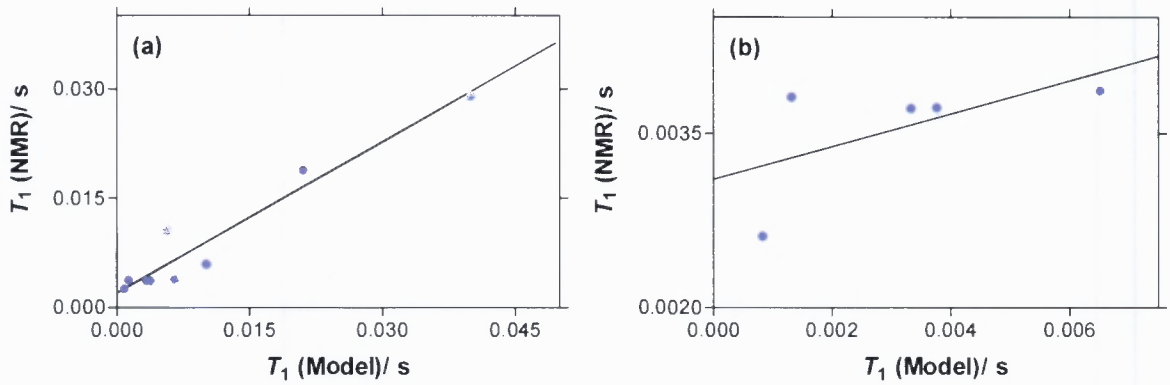

FIGURE 4.26. Correlation between the average NMR T_1 (complex) and the average computed T_1 (complex) values for compound **4** for (**a**) all of the protons and (**b**) the aromatic protons only, with r^2 of 0.93 and 0.37. The computed values were obtained by converting the average distances obtained from the complexes to T_1 (complex) for each proton using the Solomon-Bloembergen equation (Equation 1).

TABLE 4.11. Comparison between the experimental NMR data and the computed data for the aromatic protons

^{1}H	T_1 (Model)/ s	T_1 (NMR)/ s	T_1 (Model)/ s	T_1 (NMR)/ s
	CQ		**Compound 1**	
H2	0.0052	0.0062	0.0048	0.0052
H5	0.0031	0.0065	0.0013	0.0041
H8	0.0081	0.0053	0.0058	0.0041
H6	0.0091	0.0056	0.0045	0.0042
H3	0.0029	0.0052	0.0021	0.0040
	Compound 3		**Compound 4**	
H2	0.0077	0.0052	0.0065	0.0039
H5	0.0004	0.0037	0.0008	0.0026
H8	0.0080	0.0037	0.0038	0.0037
H6	0.0023	0.0044	0.0013	0.0038
H3	0.0024	0.0044	0.0033	0.0037

4.6. SUMMARY OF KEY FINDINGS

The interactions between 4-aminoquinolines (**CQ** and compounds **1** — **5**) with haematin monomer were studied and the following observations were made:

- The presence of the unpaired electrons on the Fe(III) core causes NMR line broadening and a decrease in signal intensity of the 4-aminoquinoline protons especially those of the aromatic protons. This is attributed to the enhancement of the relaxation rates of these protons due to their interactions with the unpaired electrons of the Fe(III) centre. The closer the proton is to the metal centre, the broader the NMR signal of that particular proton and the smaller the signal intensity.
- The ^{1}H T_1 relaxation experiments further indicated that the aromatic protons of these 4-aminoquinolines lie much closer to the Fe(III) centre than the side chain protons other than **H2'** based on their enhanced relaxation rates. The relaxation times further decrease with an increase in haematin concentration due to increased complex formation with rapid exchange. It was also observed that the

4-aminoquinoline:haematin complexes form with a stoichiometry of 1:1. The aromatic protons of **CQ** and compounds **1**, **2** and **3** are on average further from the Fe(III) centre, while those of compounds **4** and **5** lie closer.

- A strong thermodynamic compensation effect between enthalpies and entropies of interaction between these compounds and haematin were observed. These results indicate that there is a large loss of flexibility and high degree of desolvation upon complex formation. This probably means that hydrophobicity plays a major role as release of solvating water molecules is a feature of such interactions. It supports the hypothesis that the complexes form through π-π stacking. The complexes formed between haematin and **CQ** and compound **1** are more strongly driven by entropy and compound **2** is mainly enthalpy driven, while those formed with compounds **4** and **5** are entirely enthalpy driven.
- A significant correlation between the experimental NMR data T_1 (complex) and ΔH and ΔS were observed. Weak β-haematin inhibitors (compound **4**) and non β-haematin inhibitors (compounds **5** and **6**) seem to form tighter, less mobile complexes while strong β-haematin inhibitors (**CQ** and compounds **1** and **2**) form loosely bound complexes. Thus β-haematin inhibitors appear to form more flexible complexes than non β-haematin inhibitors.
- A significant correlation between the NMR data (T_1 (complex)) and the IC_{50} of the 4-aminoquinolines for β-haematin inhibition was also observed, with the strongest correlations observed between β-haematin inhibition strength and T_1 (complex) of **H2** and **H3**. The geometry of the complex structures formed between haematin with β-haematin inhibitors and non β-haematin inhibitors are probably different due to their differences in the electronic properties of the group at the 7-position. Activity of the 4-aminoquinolines is thus related to the geometry and flexibility of the complexes and not their association constants.
- The conformations of the models of the complexes obtained from MD/SA for **CQ** are similar to the structures obtained by Leed *et al.* The 4-amino group points towards the Fe(III) centre while the quinoline nitrogen of CQ orients towards the porphyrin rim. The quinoline nucleus does not lie directly above the

Fe(III), furthermore, it does not lie co-planar relative to the porphyrin ring in all cases. This behaviour would allow π-π interactions between the aromatic region of the 4-aminoquinoline and the electron dense porphyrin ring. The side chain extends over the porphyrin rim compared to the structures obtained by Leed *et al.* which turn to wrap around the rim in their structures [147] (See Chapter 1). The conformations of the models of the complexes obtained for **CQ** are similar to those of compounds **1**, **3** and **4**, with the atom or group at 7-position extended towards the periphery of the porphyrin rim. The side chains of compounds **1**, **3** and **4** tend to extend upwards.

- A poor correlation if any, was observed between the experimental NMR T_1 (complex) data and those predicted by models obtained from the computer simulations. Furthermore, unlike the NMR T_1 data itself, the models show no obvious correlation with β-haematin inhibitory activity.

This calls into question the validity of the models with the problem probably arising from mathematical inconsistencies related to the method used to extract distance data from average T_1 measurements in a non-rigid system. This problem has not been acknowledged in the structures reported by Roepe and co-workers to date [147, 148] and seriously calls the validity of their proposed haem-chloroquine, quinine, quinidine and amodiaquine, structures into question.

4.7. CONCLUSIONS

The interactions between haematin and 4-aminoquinoline antimalarials are important if we are to understand the mechanism by which these antimalarials inhibit haemozoin formation in *Plasmodium falciparum*. Since the crystal structures of these complexes are not yet available, it was attempted to obtain structural information and to compute the structures of these complexes in solution from NMR and molecular modelling. The structures obtained in this study using a combination of NMR and molecular dynamics do not correlate well with the experimental data, but are similar to the structures obtained by Leed *et al.* [147] for CQ using different force fields and

parameters. All the 100 structures collected for each 4-aminoquinoline are similar in energy (within 2 kcal mol^{-1}) which indicate that all 100 conformations are accessible at room temperature and should therefore resemble the structures obtained experimentally. The lack of correlation between the computed data and the NMR data therefore leads to the conclusion that the models are inadequate in reproducing the complex structures that might exist in the parasite.

The model complexes obtained in this study were based on a method used by Roepe and co-workers [147]. The method employed has several limiting factors that could affect the structures obtained from this method and their interpretation. One uncertainty is that calculation of the average distances obtained from the Solomon-Bloembergen equation (Equation 1) relies on τ_c which is hard to obtain experimentally [231, 232]. Most calculations therefore use an estimated value and this is the case of Leed *et al.* Nonetheless, relative values can be used so that this problem can in principle be overcome. Secondly, assumptions about the net spin state of Fe(III) used in the calculations may also give different distance constraints as these values appear in the Solomon-Bloembergen equation. The calculated constraints would either be bigger or smaller than the expected experimental distances and could result in distortions of the structures.

Thirdly, the study does not take the solvent into account in the molecular dynamics calculations. However, the complexes exist in aqueous solution inside the parasite food vacuole. Furthermore, a study by Egan *et al.* has indicated that the interactions between 4-aminoquinolines and haematin are hydrophobic in nature [139] with solvent playing a major role. To compensate for this deficiency the model therefore makes use of experimentally derived constraints to attempt to confine the structure to physically realistic conformations. The calculations therefore rely on the relatively weak force constants associated with these constraints to allow the complex the freedom to move so that the structures are not restricted to a single confined conformer. In theory this should alleviate the problem of omitting solvation from the model. Fourthly, the most serious problem is a statistical error associated with the

method which renders the distance constraints invalid. In the Solomon-Bloembergen equation T_1 is proportional to r^6. The observed T_1 values are an average, but the average distance cannot be obtained from the average T_1 on account of the inequality shown in Equation 8.

$$\langle r \rangle \neq \left(\langle r^6 \rangle \right)^{\frac{1}{6}}$$

or (8)

$$\frac{\sum_{i=1}^{n} r_i}{n} \neq \left(\frac{\sum_{i=1}^{n} r_i^6}{n} \right)^{\frac{1}{6}}$$

If it were possible to obtain T_1 for each conformation independently, r could be calculated using the Solomon-Bloembergen equation for each and the average r obtained would correspond to the left hand side of Equation 8, the true average distance. However, this is not possible. Computing the "r" value from the Solomon-Bloembergen equation using an average T_1 value obtained from experiment corresponds to the situation in the right hand side of Equation 8. The two values are not equal.[1] There is no mathematical solution to this averaging problem. It is nonetheless possible in principle to use molecular dynamics simulation to obtain the structures of the complexes directly, provided one mimics the experimental conditions fully by using sufficiently sophisticated models of the interacting molecules (probably taking orbital factors into account through quantum mechanics (QM) calculations) and explicitly including solvent molecules. However these calculations would require a great amount of computing power and were beyond the scope of this study.

Despite the weakness of the modelling method described above, the raw T_1 data from the NMR nonetheless contain valuable structural information. The T_1 data values themselves are statistically unbiased and an attempt was made to correlate these data with β-haematin inhibitory activity as well as thermodynamic

[1] For example: the average of 1, 2 and 3 = 2, but the average of 1^6, 2^6 and 3^6 is 264.7 and $264.7^{1/6} = 2.53$

measurements. The experimental T_1 data clearly correlate with β-haematin inhibitory activity and confirm that haematin interacts with 4-aminoquinolines primarily through π-π interactions with the aromatic quinoline ring. Thermodynamic measurements indicate that β-haematin inhibitory activity is related to the flexibility of the complex, with more flexible complexes showing stronger β-haematin inhibition. The orientation of the aromatic ring may also differ in the strongly inhibitory complexes. Such NMR measurements may prove useful in guiding the design of more potent inhibitors.

CHAPTER 5.

OVERALL CONCLUSIONS AND FURTHER STUDIES

OVERALL CONCLUSIONS AND FURTHER STUDIES

5.1. OVERALL CONCLUSIONS

At least 90% of toxic Fe(III)PPIX released after haemoglobin degradation is disposed by conversion to haemozoin (Hz) or malaria pigment in *Plasmodium falciparum* [46]. The mechanism of its formation is however not well understood. A number of proposals have been suggested over the past decade, however, a number of recent studies strongly support the proposal that lipids take part in this process [97, 98]. The most recent study has shown that haemozoin forms within lipid nanospheres. While these studies have demonstrated that haemozoin occurs at the lipid interfaces inside malaria parasites and other haemozoin forming organisms, it is however, very challenging to observe this process directly *in vivo* inside the organisms. Furthermore, the rates of formation reported to date in these biological model systems are too slow to account for its formation *in vivo* [78, 97, 98]. In addition, these studies have not been able to provide a mechanistic rationale for haemozoin formation. In the current study, the role of lipids was explored by developing a simple lipid/water interface method to mimic the biological system. The results obtained confirm that the product formed in this system is β-haematin and that an interface is an absolute requirement for rapid β-haematin formation at physiological pH and temperature. The process proceeds at a rate sufficient to account for haemozoin formation *in vivo*. The formation of haemozoin therefore does not appear to require a protein, but rather requires a lipid environment for β-haematin to self assemble. It is proposed that haemozoin forms spontaneously by self-assembly at the lipid/water interface in the parasite.

Quinoline antimalarials are believed to act by interfering with this process, thus inhibiting haemozoin formation causing a build-up of toxic Fe(III)PPIX [112, 121, 122, 126, 127]. Several morphological changes including vacuolar swelling, pigment clumping, loss of haemozoin granules, increase in haemoglobin and a build-up of vesicles containing electron-dense material have been observed by transmission

electron microscopy (TEM) [110, 112, 211-217]. Several studies have suggested that these vesicles contain undigested haemoglobin, however, no study has previously reported the effect of chloroquine on the overall distribution of iron in the malaria parasite. This study investigated this distribution of iron in *Plasmodium falciparum* using ESI and TEM. Major changes were observed mainly in the trophozoite-stage. These parasites contained significant amounts of iron in the parasite cytosol and a large number of transport vesicles containing iron. It is clear that significant quantities of iron accumulate not only in the transport vesicles, but also in the parasite cytosol, which is almost free of iron in untreated parasites. The chemical form of the iron cannot be identified by ESI and so may be haemoglobin. Fe(III)PPIX or "free" iron. Although these studies do not provide definitive mechanistic evidence about the action of quinoline antimalarial, they do suggest the following hypothesis: (i) the drug accumulates primarily inside the food vacuole where it interacts with Fe(III)PPIX released from haemoglobin, (ii) this results in accumulation of potentially toxic Fe(III)PPIX or Fe(III)PPIX-chloroquine complex inside the food vacuole causing membrane damage. (iii) The toxic Fe(III)PPIX is transported from the food vacuole into the parasite cytosol where it disrupts membranes altering their properties and inhibiting vesicle fusion with the food vacuole resulting in an increase in transport vesicles inside the parasite cytosol. Clearly, extensive further studies are required to demonstrate this hypothesis. Irrespective of this hypothesis, the results do show that chloroquine exclusively targets the trophozoite-stage of the parasite causing a radical redistribution of iron in the parasite.

A considerable number of studies have previously been conducted using spectroscopic techniques and computational studies to investigate further the interaction of the 4-aminoquinolines with Fe(III)PPIX understand further how they might inhibit haemozoin formation *in vivo* [123, 128, 129, 134, 135, 137, 138, 142, 147-149]. These studies have provided evidence that these drugs interact with Fe(III)PPIX by forming π-π complexes and that they inhibit β-haematin formation. However, no clear relationship between the strength or structure of these complexes and ability to inhibit β-haematin formation has been established. Association studies

in the current work conducted in 40% (v/v) aqueous DMSO (pH 7.5) indicate that complex formation between Fe(III)PPIX and the 4-aminoquinolines result in a loss of flexibility and a high degree of desolvation, suggesting that the interactions are mainly hydrophobic in nature and supporting the hypothesis that the complexes occur through π-π stacking. The results also suggest that the activity of the 4-aminoquinolines is not related to strength of complex formation, but to geometric properties of the complexes, especially the flexibility as β-haematin inhibitory strength increases with increasing entropy of interaction. Based on previous findings [141], electronic properties of the group at the 7-position appear to govern the inhibitory strength and thus apparently also the flexibility of the structures formed between Fe(III)PPIX and 4-aminoquinolines. β-haematin inhibitors (**CQ** and compounds **1** and **2**) form more flexible complexes than weak β-haematin inhibitors (compound **3**) or non β-haematin inhibitors (compounds **4** and **5**). The the results suggest that β-haematin inhibitors have the freedom to move around the porphyrin nucleus preventing Fe(III)PPIX monomers from interacting with each other to form haemozoin crystals. Non-inhibitors on the other hand seem to adopt very few conformations and these are ineffective in preventing interaction of Fe(III)PPIX monomers.

Structural information from ^{1}H T_1 NMR data further suggest that on average in the inhibitory compounds the 4-amino group points towards the Fe(III) centre while the quinoline nitrogen is directed towards the porphyrin rim. The group at 7-position is always extended towards the periphery of the porphyrin rim in this mode of interaction. Overall, the quinoline aromatic ring is situated towards the edge of the porphyrin nucleus and does not lie directly above the Fe(III).

Attempts to model the comformations of such complexes by molecular dynamics and simulated annealing (MD/SA) calculations using distance constraints obtained from the Solomon-Bloembergen equation using the method of Leed *et al.* [147] for **CQ** and CQ-analogues (compounds **1**, **3** and **4**) exhibited little if any difference in the structures of β-haematin inhibitors and non-inhibitors. It was therefore not possible to show from these structures any relationship between the structure of the complexes

and the ability of the 4-aminoquinoline studied to inhibit β-haematin formation and their differences in antimalarial activity. Furthermore, a lack of significant correlation between the experimental T_1 NMR data and the computed T_1 values obtained from the set of model structures for each compound lead to the conclusion that the model structures obtained in this study are inadequate in reproducing the structures that might exist in solution. This was traced back to a fundamental statistical problem in the method described by Leed *et al.* which has not been acknowledged in previous studies.

The overall conclusion which can be drawn from this study is that the 4-aminoquinolines interact with Fe(III)PPIX a compound known to be released during haemoglobin degradation. Imaging studies suggest that this Fe(III)PPIX iron is redistributed in the parasite, possibly as a result of accumulation of Fe(III)PPIX or Fe(III)PPIX-drug complex inside the parasite arising from inhibition of haemozoin formation at the lipid/water interface of the lipid nanospheres within the food vacuole. The toxic Fe(III)PPIX that builds up can potentially bind to membranes, thus compromising their integrity either by altering their physical properties or through oxidative processes, which may be responsible for the resulting drastic redistribution of iron in the parasite.

5.2. FURTHER STUDIES

This study has indicated in Chapter 2 that the formation of haemozoin inside the malaria parasite can occur by self-assembly at the lipid/water interface without a protein promoter or an enzyme. Further investigations are required in order to understand this process in detail. The following studies are suggested:

- To study the lipids isolated from *Plasmodium falciparum* by Sullivan and co-workers (mono-palmiticglycerol and mono-stearicglycerol) [98] using the lipid/water interface system described in this work.
- To study in detail the kinetics of haemozoin formation with these lipids and the lipid used in this study (MMG) to obtain kinetic parameters such as rate order,

rate constants and activation energy, furthermore, to compare the results obtained for MMG with that of the lipids isolated from the parasite.

- To understand the structure of the lipid at the interface using various techniques such as light scattering and fluorescent spectroscopy to show whether they form micelles or lipid layers.
- To investigate the effect of drug inhibition in this system in order to understand further their mechanism of this inhibition.

Treatment of *Plasmodium falciparum* with 4-aminoquinolines results in accumulation of transport vesicles containing iron and the presence of iron in the parasite cytosol as shown in Chapter 3. The mechanism of action of these drugs proposed in this study needs further evaluation. This would include the use of ESI to evaluate the site of drug accumulation inside the parasite, for example by using an iodo-analogue of chloroquine to map out the distribution of iodine within the parasite. This study would further show whether the drug accumulates in the transport vesicles as well. The chemical species of iron present in the parasite after treatment with chloroquine can also be investigated using Mössbauer spectroscopy in order to show whether the iron present in the parasite cytosol and transport vesicles is Fe(III)PPIX, undigested haemoglobin or "free" iron or some mixture of these.

Additional evidence for the role of Fe(III)PPIX in chloroquine activity could be obtained by lysing red blood cells in a hypotonic medium to release some of the haemoglobin and resealing them in isotonic medium, followed by invasion by malaria parasites. The antimalarial activity of chloroquine and other antimalarial drugs as a function of the haemoglobin remaining in the cell could then be evaluated. The parasites would be expected to be relatively insensitive to these drugs if Fe(III)PPIX is the target.

Further understanding of the interactions between Fe(III)PPIX and 4-aminoquinoline antimalarials are important in order to understand the mechanism by which these antimalarials inhibit haemozoin formation in *Plasmodium falciparum*. The study of

these interactions and the structures of these complexes formed between the two species in solution is problematic as shown in Chapter 4. The complexes are hydrophobic in nature and form by non-covalent π-π stackings. Furthermore, the 4-aminoquinoline drugs are diprotonated inside the food vacuole. A more detailed understanding of these interactions and the geometry of the complexes would require a force field that can sufficiently represent the structure of complex in the presence of solvent, which would require an extensive computational power and computer time. Quantum mechanics together with molecular mechanics (QM/MM) studies would be required to include the charge in order to obtain a more representative model complex if the π-π stacking interaction is to be properly modelled. A sufficiently accurate model would allow experimental distance restraints to be dispenced with.

Sullivan *et al.* [126] have shown using autoradiographic electron micrographs that show that chloroquine is associated with haemozoin in the food vacuole and have since suggested that the drug binds to Fe(III)PPIX and the complex formed attaches itself to the growing haemozoin crystal thus terminating (capping) crystal extension. Drug inhibition studies recommended using the method developed in Chapter 2 are necessary in order to investigate whether chloroquine penetrates the lipid nanosphere as a free base or forms a complex with Fe(III)PPIX in the aqueous environment to prevent β-haematin formation. Structural evidence for this type of interaction has been proposed by Leiserrowitz [156], but use of both inhibitory and non-inhibitory coumpounds could test the validity of this hypothesis. Docking studies of the free quinolines or Fe(III)PPIX-quinoline complexes with the haemozoin surface are required in order to show if this proposal is plausible.

Finally, it would be recommended that every effort be made to obtain the crystal structures of these complexes be obtained in an attempt to provide accurate structures that might provide the structural insight necessary for the design of novel drugs of this class.

CHAPTER 6.

REFERENCES

REFERENCES

1. L. J. Bruce-Chwatt, *Chemotherapy of Malaria*, WHO, 1981.
2. I. W. Sherman, *Malaria: Parasite Biology, Pathogenesis and Protection.*, ASM Press, 1998.
3. N. Rasti, Wahlgren, M., Chen, Q., *FEMS. Immunol. Med. Microbiol.*, 2004, **41**, 9.
4. *National Centre for Infectious Diseases, Division of Parasitic Diseases, http://www.cdc.gov/Malaria_/distribution_epi/distribution.htm, accessed on 13/06/2006.*
5. N. J. White, *J. Clin. Invest.*, 2004, **113**, 1084.
6. S. C. Oaks, V. S. Mitchell, G. Pearson and C. Carpenter, *Malaria: Obstacles and Opportunities.*, National Academic Press, 1991.
7. L. Malaguarnera, Musumeci, S., *Lancet. Infect. Dis.*, 2002, **2**, 472.
8. W. H. Wernsdorfer and I. McGregor, in *Malaria: Principles and Practice of Malariology*, Edinburgh, 1988.
9. A. F. G. Slater, *Pharmac. Ther.*, 1993, **57**, 203.
10. T. J. Egan, *Targets*, 2003, **2**, 115.
11. M. Krugliak, F. Zhang and H. Ginsburg, *Mol. Biochem. Parasitol.*, 2002, **119**, 249.
12. V. L. Lew, T. Tiffert and H. Ginsburg, *Blood*, 2003, **101**, 4189.
13. H. Ginsburg, *Blood Cells*, 1990, **16**, 225.
14. R. Hayward, Saliba, K. J., Kirk, K., *J. Cell. Sci.*, 2006, **119**, 1016.
15. T. G. Geary, J. B. Jensen and H. Ginsburg, *Biochem. Pharmacol.*, 1986, **35**, 3805.
16. D. J. Krogstad, P. H. Schlesinger and I. Y. Gluzman, *J. Cell Biol.*, 1985, **101**, 2302.
17. T. G. Geary, A. D. Divo, J. B. Jensen, M. Zangwill and H. Ginsburg, *Biochem. Pharmacol.*, 1990, **40**, 685.
18. A. Yayon, Z. I. Cabantchik and H. Ginsburg, *Proc. Natl. Acad. Sci. USA*, 1985, **82**, 2784.

19. H. Ginsburg, E. Nissani and M. Krugliak, *Biochem. Pharmacol.*, 1989, **38**, 2645.

20. N. T. Bennett, D. A. Kosar, L. M. B. Ursos, S. M. Dzekunov, A. b. S. Sidhu, A. D. Fidock and P. D. Roepe, *Mol. Biochem. Parasitol.*, 2004, **133**, 99.

21. S. M. Dzekunov, L. M. B. Ursos and P. D. Roepe, *Mol. Biochem. Parasitol.*, 2000, **110**, 107.

22. L. M. B. Ursos, S. M. Dzekunov and P. D. Roepe, *Mol. Biochem. Parasitol.*, 2000, **110**, 125.

23. P. G. Bray, K. J. Saliba, J. D. Davies, D. G. Spiller, M. R. White, K. Kirk and S. A. Ward, *Mol. Biochem. Parasitol.*, 2002, **119**, 301.

24. F. Wissing, C. P. Sanchez, P. Rohrbach, S. Ricken and M. Lanzer, *J. Biol. Chem.*, 2002, **277**, 37747.

24A. Y. Kuhn, P. Rohrbach and M. Lanzer, *Cell. Microbiol.*, 2007, **9**, 1004.

25. P. Loria, S. Miller, M. Foley and L. Tilley, *Biochem. J.*, 1999, **339**, 363.

26. H. Ginsburg, O. Famin, F. Zhang and M. Krugliak, *Biochem. Pharmacol.*, 1998, **56**, 1305.

27. P. J. Rosenthal, J. H. McKerrow, M. Aikawa, H. Nagasawa and J. Leech, *J. Clin. Invest.*, 1988, **82**, 1560.

28. R. Banerjee, J. Liu, W. Beatty, L. Pelosof, M. Klemba and D. E. Goldberg, *Proc. Natl. Acad. Sci. USA*, 2002, **99**, 990.

29. K. K. Eggleson, K. L. Duffin and D. E. Goldberg, *J. Biol. Chem.*, 1999, **274**, 32411.

30. I. Y. Gluzman, S. E. Francis, A. Oksman, C. E. Smith, K. L. Duffin and D. E. Goldberg, *J. Clin. Invest.*, 1994, **93**, 1602.

31. D. E. Goldberg, A. F. G. Slater, R. Beavis, B. Chait, A. Cerami and G. B. Henderson, *J. Exp. Med.*, 1991, **173**, 961.

31A. C. S. Gavigan, J. P. Dalton and A. Bell, *Mol. Biochem. Parasitol.*, 2001, **117**, 37.

32. D. E. Goldberg, A. F. G. Slater, A. Cerami and G. B. Henderson, *Proc. Natl. Acad. Sci. USA*, 1990, **87**, 2931.

33. S. B. Brown, T. C. Dean and P. Jones, *Biochem. J.*, 1970, **117**, 733.

34. K. A. de Villiers, Kaschula, C. H., Egan, T. J., Marques, H. M., *J. Biol. Inorg. Chem.*, 2007, **12**, 101.
35. H. Ladan, Y. Nitzan and Z. Malik, *FEMS Microbiol. Lett.*, 1993, **112**, 173.
36. F. Omodeo-Sale, Motti, A., Dondorp, A., White, N. J., Taramelli, D., *Eur. J. Haematol.*, 2005, **74**, 324.
37. A. C. Chou and C. D. Fitch, *J.Clin.Invest*, 1980, **66**, 856.
38. A. C. Chou and C. D. Fitch, *J. Clin. Invest.*, 1981, **68**, 672.
39. A. U. Orjih, H. S. Banyal, R. Chevli and C. D. Fitch, *Science*, 1981, **214**, 667.
40. J. O. Ashong, I. P. Blench and D. C. Warhurst, *Trans R. Soc. Trop. Med. Hyg.*, 1989, **83**, 167.
41. P. Goldie, E. F. Roth, J. Oppenheim and J. P. Vanderberg, *Am. J. Trop. Med. Hyg.*, 1990, **43**, 584.
42. D. E. Goldberg and A. F. G. Slater, *Parasitol. Today*, 1992, **8**, 280.
43. A. V. Pandey, Tekwani, B. L.,Pandey, V. C., *Biomed. Res-Tokyo*, 1995, **16**, 115.
44. A. D. Sullivan, Ittarat, I., Meshnick, S. R., *Parasitology*, 1996, **112**, 285.
45. G. S. Noland, N. Briones and D. J. Sullivan, *Mol. Biochem. Parasitol.*, 2003, **130**, 91
46. T. J. Egan, J. M. Combrinck, J. Egan, G. R. Hearne, H. M. Marques, S. Ntenteni, B. T. Sewell, P. J. Smith, D. Taylor, D. A. van Schalkwyk and J. C. Walden, *Biochem. J.*, 2002, **365**, 343.
47. T. J. Egan, *Drug Design Revs Online*, 2004, **1**, 93.
48. M. F. Oliveira, J. R. Silva, M. Dansa-Petretski, W. de Souza, U. Lins, C. M. S. Braga, H. Masuda and P. L. Oliveira, *Nature*, 1999, **400**, 517.
49. M. F. Oliveira, J. R. Silva, M. Dansa-Petretski, W. de Souza, C. M. S. Braga, H. Masuda and P. L. Oliveira, *FEBS Lett.*, 2000, **477**, 95.
50. M. Oliveira, J. C. P. d'Avila, C. R. Torres, P. L. Oliveira, A. J. Tempone, F. D. Rumjanek, C. M. S. Braga, J. R. Silva, M. Dansa-Petretski, M. A. Oliveira, W. de Souza and S. T. Ferreira, *Mol. Biochem. Parasitol.*, 2000, **111**, 217.
51. M. M. Chen, L. Shi and D. J. Sullivan, *Mol. Biochem. Parasitol.*, 2001, **113**, 1.

52. M. F. Oliveira, d'Avila, J. C. P., Tempone, A. J., Soares, J. B. R. C., Ramjanek, F. D., Ferreira-Pereira, A., Ferreira, S. T., Oliveira, P. L., *J. Infect. Dis.*, 2004, **190**, 843.

53. J. D. Lawrence, *J. Parasitol.*, 1973, **59**, 60.

54. P. J. Brindley, Kalinna, B. H., Dalton, J. P., Day, S. R., Wong, J. Y., Smythe, M. L., McManus, D. P., *Mol. Biochem. Parasitol.*, 1997, **89**, 1.

55. *Rhodnius prolixus, www.icb.usp.br/~marcelcp/rhodius.htm, accessed on 22/10/2006.*

56. *Wikipedia Encyclopedia, http://en.wikipedia.org/wiki/Schistosoma_mansoni, accessed on 23/10/2006.*

57. *InvetebrateBiodiversity, ww.eeob.iastate.edu/faculty/DrewesC/htdocs/invert-thumbs.htm, accessed on 25/10/2006.*

58. J. M. Pisciotta, Ponder, E. L., Fried, B., Sullivan, D., *Int. J. Parasitol.*, 2005, **35**, 1037.

59. T. K. Graczyk, Fried, B., *Am. J. Trop. Med. Hyg.*, 1998, **58**, 501.

60. M. F. Oliveira, Kycia, S. W., Gomez, A., Kosar, A. J., Bohle, D. S., Hempelmann, E., Menezes, D., Vannier-Santos, M. A., Oliveira, P. L., Ferreira, S. T., *FEBS Lett.*, 2005, **579**, 6010.

61. D. J. Sullivan, *Int. J. Parasitol.*, 2002, **32**, 1645.

62. G. R. C. Braz, Coelho, H. S. L., Masuda, H., Oliveira, P. L.. *curr. Biol.*, 1999, **9**, 703.

63. A. F. G. Slater, Swiggard, W. J., Orton, B. R., Flitter, W. D., Goldberg, D. E., Cerami, A., Henderson, G. B., *Proc. Natl. Acad. Sci. USA.*, 1991, **88**, 325.

64. W. Brown, *J. Exp. Med.*, 1911, **13**, 290.

65 B. N. Ghosh and J. A. Sinton, *Rec. Mal. Survey India*, 1934, **4**, 43.

66. B. N. Ghosh, Nath, M. C., *Rec. Mal. Survey India*, 1934, **4**, 321.

67. A. Hamsik, *Z. Physiol. Chem.*, 1936, **241**, 156.

68. I. W. Sherman, Mudd, J. B., Trager, W., *Nature*, 1965, **208**, 691.

69. I. W. Sherman, Ting, I. P., Ruble, J. A., *J. Protozool.*, 1968, **15**, 158.

70. C. D. Fitch and P. Kanjananggulpan, *J. Biol. Chem.*, 1987, **262**, 15552.

71. P. A. Adams, P. A. M. Berman, T. J. Egan, P. J. Marsh and J. Silver, *J. Inorg. Biochem.*, 1996, **63**, 69.

72. D. S. Bohle, Helms, J. B., Dinnebier, R. E., Madsen, S. K., Stephens, P. W., *J. Biol. Chem.*, 1997, **272**, 713.

73. S. Pagola, Stephens, P. W., Bohle, D. S., Kosar, A. D., Madsen, S. K., *Nature*, 2000, **404**, 307.

74. A. F. G. Slater and A. Cerami, *Nature*, 1992, **355**, 167.

75. A. Dorn, S. R. Vippagunta, H. Matile, A. Bubendorf, J. L. Vennerstrom and R. G. Ridley, *Biochem. Pharmacol.*, 1998, **55**, 737.

76. D. S. Bohle, Helms, J. B., *Biochem. Biophys. Res. Commun.*, 1993, **193**, 504.

77. A. U. Orjih, *Exp. Biol. Med.*, 2001, **226**, 746.

78. C. D. Fitch, G.-z. Cai, Y.-F. Chen and J. D. Shoemaker, *Biochim. Biophys. Acta*, 1999, **1454**, 31.

79. K. Bendrat, B. J. Berger and A. Cerami, *Nature*, 1995, **378**, 138.

80. R. G. Ridley, A. Dorn, H. Matile and M. Kansy, *Nature*, 1995, **378**, 138.

81. A. K. Tripathi, Garg, S. K., Tekwani, B. L., *Biochem. Biophys. Res. Commun.*, 2002, **290**, 595.

82. D. J. Sullivan, I. Y. Gluzman and D. E. Goldberg, *Science*, 1996, **271**, 219.

83. V. Papalexis, M.-A. Siomos, N. Campanale, X.-g. Guo, G. Kocak, M. Foley and L. Tilley, *Mol. Biochem. Parasitol.*, 2001, **115**, 77.

84. T. J. Egan, D. C. Ross and P. A. Adams, *FEBS Lett.*, 1994, **352**, 54.

85. T. J. Egan, Tshivhase, M. G., *Dalton. Trans.*, 2006, **42**, 5024.

86. A. V. Pandey and B. L. Tekwani, *FEBS Lett.*, 1996, **393**, 189.

87. T. J. Egan, E. Hempelmann and W. W. Mavuso, *J. Inorg. Biochem.*, 1999, **73**, 101.

88. P. A. Adams, T. J. Egan, D. C. Ross, J. Silver and P. J. Marsh, *Biochem. J.*, 1996, **318**, 25.

89. T. J. Egan, W. W. Mavuso and K. K. Ncokazi, *Biochemistry*, 2001, **40**, 204.

90. R. Mashima, L. Tilley, M.-A. Siomos, V. Papalexis, M. J. Raftery and R. Stoker, *J. Biol. Chem.*, 2002, **277**, 14514.

91. J. Ziegler, R. T. Chang and D. W. Wright, *J. Am. Chem. Soc.*, 1999, **121**, 2395.

92. C. Y. H. Choi, J. F. Cerda, H.-A. Chu, G. T. Babcock and M. A. Marletta, *Biochemistry*, 1999, **38**, 16916.

93. A. Lynn, S. Chandra, P. Malhotra and V. S. Chauhan, *FEBS Lett.*, 1999, **459**, 267.

94. A. V. Pandey, H. Bisht, V. K. Babbarwal, J. Srivastava, K. C. Pandey and V. S. Chauhan, *Biochem. J.*, 2001, **355**, 333.

95. A. V. Pandey, V. K. Babbarwal, J. N. Okoyeh, R. M. Joshi, S. K. Puri, R. L. Singh and V. S. Chauhan, *Biochem. Biophys. Res. Commun.*, 2003, **308**, 736.

96. C. D. Fitch, G.-z. Cai and J. D. Shoemaker, *Biochemica et Biophysica Acta*, 2000, **1535**, 45.

97. K. E. Jackson, Klonis, N., Ferguson, D. J. P., Adisa, A., Dogovski, C., Tilley, L., *Mol. Microbiol.*, 2004, **54**, 109.

98. J. M. Pisciotta, Coppens, I., Tripathi, A. K., Scholl, P. F., Shuman, J., Bajad, S., Shulaev, V., Sullivan, D. J., *Biochem. J.*, 2007, **402**, 197.

99. L. J. Bruce-Chwatt, *Essential Malariology*, William Heinemann Medical Books, 1985.

100. R. L. Kenyon, Wiesner, J. A., Kwartler, C. E., *J. Ind. Eng. Chem.*, 1949, **41**, 654.

101. F. S. Parker and J. L. Irvin, *J. Biol. Chem.*, 1952, **199**, 897.

102. N. Surolia and G. Padmanaban, *Proc. Natl. Acad. Sci. USA*, 1991, **88**, 4786.

103. C. A. Homewood, D. C. Warhurst and V. C. Baggaley, *Trans R. Soc. Trop. Med. Hyg.*, 1971, **65**, 10.

104. I. W. Sherman, *Comp. Biochem. Physiol.*, 1976, **53B**, 447.

105. G. C. Kirby, M. J. O' Neill, D. Phillipson and D. C. Warhurst, *Biochem. Pharmacol.*, 1989, **38**, 4367.

106. E. Königk, S. Mirtsch, B. Putfarken and S. Abdel-Rasoul, *Trop. Parasit.*, 1981, **32**, 73.

107. C. A. Homewood, D. C. Warhurst, W. Peters and V. C. Baggaley, *Nature*, 1972, **235**, 50.

108. P. G. Bray, M. Mungthin, R. G. Ridley and S. A. Ward, *Mol. Pharmacol.*, 1998, **54**, 170.

109. P. M. O' Neill, D. J. Willock, S. R. Hawley, P. G. Bray, R. C. Storr, S. A. Ward and B. K. Park, *J. Med. Chem.*, 1997, **40**, 437.

110. G. H. Jacobs, M. Aikawa, W. K. Milhous and J. R. Rabbege, *Am. J. Trop. Med. Hyg.*, 1987, **36**, 9.

111. P. Olliaro, F. Castelli, S. Caligaris, P. Druihe and G. Carosi, *Microbiologica*, 1989, **12**, 15.

112. P. B. Macomber, H. Sprinz and A. J. Tousimis, *Nature*, 1967, **214**, 937.

113. D. C. Warhurst and D. J. Hockley, *Nature*, 1967, **214**, 935.

114. K. J. Saliba, P. I. Folb and P. J. Smith, *Biochem. Pharmacol.*, 1998, **56**, 313.

115. H. Ginsburg and T. G. Geary, *Boichem. Pharmacol.*, 1987, **36**, 1567.

116. H. Ginsburg and M. Krugliak, *Biochem. Pharmacol.*, 1992, **43**, 63.

117. F. N. Gyang, B. Poole and W. Trager, *Mol. Biochem. Parasitol.*, 1982, **5**, 263.

118. D. C. Warhurst, *Biochem. Pharmacol.*, 1981, **30**, 3323.

118A. R. Zidovetzki, I. W. Sherman, J. Prudhomme and J. Crawford, *Parasitology*, 1994, **108**, 249.

119. S. N. Cohen, K. O. Phifer and K. L. Yielding, *Nature*, 1964, **202**, 805.

120. A. C. Chou, R. Chevli and C. D. Fitch, *Biochemistry*, 1980, **19**, 1543.

121. C. D. Fitch, *Parasitol. Today*, 1986, **2**, 330.

122. S. Moreau, Prensier, G., Maalla, J., Fortier, B., *Eur. J. Cell. Biol.*, 1986, **42**, 207.

123. A. Dorn, S. R. Vippagunta, H. Matile, C. Jaquet, J. L. Vennerstrom and R. G. Ridley, *Biochem. Pharmacol.*, 1998, **55**, 727.

124. B. Panijpan, Rao, C. M., Balasubramanian, D., *Bioscience. Rep.*, 1983, **3**, 1113.

125. T. J. Egan, R. Hunter, C. H. Kaschula, H. M. Marques, A. Misplon and J. C. Walden, *J. Med. Chem.*, 2000, **43**, 283.

126. D. J. Sullivan, I. Y. Gluzman, D. G. Russell and D. E. Goldberg, *Proc. Natl. Acad. Sci. USA*, 1996, **93**, 11865.

127. D. J. Sullivan, H. Matile, R. G. Ridley and D. E. Goldberg, *J. Biol. Chem.*, 1998, **273**, 31103.

128. S. Moreau, B. Perly and J. Biguet, *Biochimie*, 1982, **64**, 1015.

129. S. Moreau, B. Perly, C. Chachaty and C. Deleuze, *Biochim. Biophys. Acta.*, 1985, **840**, 107.

130. G. Blauer, *Arch. Biochem. Biophys.*, 1986, **251**, 306.

131. G. Blauer, *Arch. Biochem. Biophys.*, 1986, **251**, 315.

132. G. Blauer, *Biochem. Int.*, 1988, **17**, 729.

133. G. Blauer and H. Ginsburg, *Biochem. Int.*, 1982, **5**, 519.

134. I. Constantinidis and J. D. Satterlee, *J. Am. Chem. Soc.*, 1988, **110**, 4391.

135. I. Constantinidis and J. D. Satterlee, *J. Am. Chem. Soc.*, 1988, **110**, 927.

136. G. Blauer, M. Akkawi and E. R. Bauminger, *Biochem. Pharmacol.*, 1993, **46**, 1573.

137. T. J. Egan, W. W. Mavuso, D. C. Ross and H. M. Marques, *J. Inorg. Biochem.*, 1997, **68**, 137.

138. H. M. Marques, K. Voster and T. J. Egan, *J. Inorg. Biochem.*, 1996, **64**, 7.

139. T. J. Egan and K. K. Ncokazi, *J. Inorg. Biochem.*, 2004, **98**, 144.

140. S. R. Vippagunta, A. Dorn, R. G. Ridley and J. L. Vennerstrom, *Biochim. Biophys. Acta.*, 2000, **1475**, 133.

141. C. H. Kaschula, T. J. Egan, R. Hunter, N. Basilico, S. Parapini, D. Taramelli, E. Pasini and D. Monti, *J. Med. Chem.*, 2002, **45**, 3531.

142. S. R. Vippagunta, A. Dorn, H. Matile, A. K. Bhattacharjee, J. M. Karle, W. Y. Ellis, R. G. Ridley and J. L. Vennerstrom, *J. Med. Chem.*, 1999, **42**, 4630.

143. Y. Inoue and T. Wada, *Adv. Supramolec. Chem.*, 1997, **4**, 55.

144. R. J. Abraham, Bedford, G. R., McNeillie, D., Wright, B., *Org. Magn. Reson.*, 1980, **14**, 418.

145. M. M. Warshaw, Tinoco, I., *J. Mol. Biol.*, 1966, **20**, 29.

146. S. Moreau, Proceedings of the 2nd International Conference on Malaria and Babesiosis, Annecy, France, 1983.

147. A. Leed, K. DuBay, L. M. B. Ursos, D. Sears, A. C. de Dios and P. D. Roepe, *Biochemistry*, 2002, **41**, 10245.

148. A. C. De Dios, Casabianca, L. B., Kosar, A., Roepe, P. D., *Inorg. Chem.*, 2004, **43**, 8078.

149. C. Portela, C. M. M. Afonso, M. M. M. Pinto and M. J. Ramos, *FEBS Lett.*, 2003, **547**, 217.

150. D. De, F. M. Krogstad, F. B. Cogswell and D. J. Krogstad, *Am. J. Trop. Med. Hyg.*, 1996, **55**, 579.

151. A. C. De Dios, Tycko, R., Ursos, L. M. B., Roepe, P. D., *J. Phys. Chem. A*, 2003, **107**, 5821.

152. M. J. Dascombe, Drew, M. G. B., Morris, H., Wilairat, P., Auparakkitanon, S., Moule, W. A., Alizadeh-Shekalgourabi, S., Evans, P. G., Lloyd, M,, Dyas, A. M., Carr, P., Ismail, F. M. D., *J. Med. Chem.*, 2005, **48**, 5423.

153. C. Portela, Afonso, C. M. M., Pinto, M. M. M., Joao Ramos, M., *Bioorg. Med. Chem.*, 2004, **12**, 3313.

154. D. De, F. M. Krogstad, L. D. Byers and D. J. Krogstad, *J. Med. Chem.*, 1998, **41**, 4918.

155. S. R. Hawley, P. G. Bray, M. Mungthin, J. D. Atkinson, P. M. O' Neill and S. A. Ward, *Antimicr. Agents Chemother.*, 1998, **42**, 682.

156. R. Buller, M. L. Peterson, Ö. Almarsson and L. Leiserowitz, *Cryst. Growth Des.*, 2002, **2**, 553.

157. D. A. Van Schalkwyk, Egan, T. J., *Drug Resist. Updates*, 2006, **9**, 211.

158. K. Kirk and K. J. Saliba, *Drug Resist. Updates*, 2001, **4**, 335.

159. P. G. Bray, Martin, R. E., Tilley, L., Ward, S. A., Kirk, K., Fidock, D. A., *Mol. Microbiol.*, 2005, **56**, 323.

160. S. G. Valderramos, Fidock, D. A., *Trends Pharmacol. Sci.*, 2006, **27**, 594.

161. D. J. Krogstad, I. Y. Gluzman, D. E. Kyle, A. M. J. Oduola, S. K. Martin, W. K. Milhous and P. H. Schlesinger, *Science*, 1987, **238**, 1283.

162. C. D. Fitch, *Proc. Natl. Acad. Sci. USA*, 1969, **64**, 1181.

163 F. Verdier, Le Bras, J., Clavier, F., Hatin, I., Blayo, M. C., *Antimicrob. Agents. Chemother.*, 1985, **27**, 561.

164. P. G. Bray, Howells, R. E., Ritchie, G. Y., Ward, S. A., *Biochem. Pharmacol.*, 1992, **44**, 1317.

165. J. A. Martiney, A. Cerami and A. F. G. Slater, *J. Biol. Chem.*, 1995, **270**, 22393.

166. C. P. Sanchez, S. Wünsch and M. Lanzer, *J. Biol. Chem.*, 1997, **272**, 2652.

167. H. Ginsburg and W. Stein, *Biochem. Pharmacol*, 1991, **41**, 1463.

168. P. G. Bray, R. E. Howells and S. A. Ward, *Biochem. Pharmacol.*, 1992, **43**, 1219.

169. L. M. B. Ursos, Roepe, P. D., *Med. Res. Rev.*, 2002, **22**, 465.

170. C. P. Sanchez, W. Stein and M. Lanzer, *Biochemistry*, 2003, **42**, 9383.

171. S. Wünsch, C. P. Sanchez, M. Gekle, L. Grosse-Wortmann, J. Wiesner and M. Lanzer, *J. Cell Biol.*, 1998, **140**, 335.

172. P. G. Bray, O. Janneh, K. Raynes, M. Mungthin, H. Ginsburg and S. A. Ward, *J. Cell Biol.*, 1999, **145**, 363.

173. S. K. Martin, A. M. J. Oduola and W. K. Milhous, *Science*, 1987, **235**, 899.

174. A. F. Cowman, S. Karcz, D. Galatis and J. G. Culvenor, *J. Cell Biol.*, 1991, **113**, 1033.

175. S. J. Foote, J. K. Thompson, A. F. Cowman and D. J. Kemp, *Cell*, 1989, **57**, 921.

176. S. J. Foote, D. E. Kyle, R. K. Martin, A. M. J. Oduola, K. Forsyth, D. J. Kemp and A. F. Cowman, *Nature*, 1990, **345**, 255.

177. M. B. Reed, Saliba, K. J., Caruana, S, R., Kirk, K., Cowman, A. F., *Nature*, 2000, **403**, 906.

178. T. E. Wellems, L. J. Panton, I. Y. Gluzman, V. E. do Rosario, R. W. Gwadz, A. Walker-Jonah and D. J. Krogstad, *Nature*, 1990, **345**, 253.

179. A. b. S. Sidhu, D. Verdier-Pinard and D. A. Fidock, *Science*, 2002, **298**, 210.

180. X. Su, Kirkman, L. A., Fujioka, H., Wellems, T. E., *Cell*, 1997, **91**, 593.

181. D. A. Fidock, T. Nomura, A. K. Talley, R. A. Cooper, S. M. Dzekunov, M. T. Ferdig, L. M. B. Ursos, A. b. S. Sidhu, B. Naudé, K. W. Deitsch, X.-z. Su, J. C. Wootton, P. D. Roepe and T. E. Wellems, *Molec. Cell*, 2000, **6**, 861.

182. A. Djimde, Doumbo, O. K., Cortese, J. F., Kayentao, K., Doumbo, S., Diourte, Y., Dicko, A. Su, X., Nomura, T., Fidock, D. A., Wellems, T. E., Plowe, C. V., *N. Engl. J. Med.*, 2001, **344**, 257.

183. R. A. Cooper, M. T. Ferdig, X. Z. Su, L. M. B. Ursos, J. Mu, T. Nomura, H. Fujioka, D. A. Fidock, P. D. Roepe and T. E. Wellems, *Mol. Pharmacol.*, 2002, **61**, 35.

184. T. E. Wellems, Plowe, C. V., *J. Infect. Dis.*, 2001, **184**, 770.

185. D. C. Reeves, Liebelt, D. A., Lakshmanan, V., Roepe, P.D., Fidock, D. A., Akabas, M. H., *Mol. Biochem. Parasitol.*, 2006, **150**, 288.

186. C. P. Sanchez, McLean, J. E., Rohrbach, P., Fidock, D. A., Stein, W. D., Lanzer, M., *Biochemistry*, 2005, **44**, 9862.

187. P. G. Bray, Mungthin, M., Hastings, I. M., Biagini, G. A., Saidu, D. K., Lakshmanan, V., Johnson, D. J., Hughes, R. H., Stocks, P. A., O'Neill, P. M., Fidock, D. A., Warhurst, D. C., Ward, S. A., *Mol. Microbiol.*, 2006, **62**, 238.

188. D. C. Warhurst, Craig, J. C., Adagu, I. S., *Lancet*, 2002, **360**, 1527.

189 D. J. Johnson, Fidock, D. A., Mungthin, M., Lakshmanan, V., Sidhu, A., Bray, P. G., Ward, S. A., *Mol. Cell.*, 2004, **15**, 867.

190. V. Lakshmanan, Bray, P. G., Verdier-Pinard, D., Johnson, D. J., Horrocks, P., Muhle, R. A., Alakpa, G. E., Hughes, R. H., Ward, S. A., Krogstad, D. J.; Sidhu, A., Fidock, D. A., *EMBO J.*, 2005, **24**, 2294.

191. D. A. Van Schalkwyk, Walden, J. C., Smith, P. J., *Antimicrob. Agents. Chemother.*, 2001, **45**, 3171.

192. J. Guan, Kyle, D. E., Gerena, L., Zhang, Q., Milhous, W. K., Lin, A. J., *J. Med. Chem.*, 2002, **45**, 2741.

193. P. G. Bray, S. R. Hawley, M. Mungthin and S. A. Ward, *Mol. Pharmacol.*, 1996, **50**, 1559.

194. P. G. Bray, S. R. Hawley and S. A. Ward, *Mol. Pharmacol.*, 1996, **50**, 1551.

195. P. A. Stocks, K. J. Raynes, P. G. Bray, B. K. Park, P. M. O'Neill and S. A. Ward, *J. Med. Chem.*, 2002, **45**, 4975.

196. R. G. Ridley, W. Hofheinz, H. Matile, C. Jaquet, A. Dorn, R. Masciadri, S. Jolidon, W. F. Richter, A. Guenzi, M. A. Girometta, H. Urwyler, W. Huber, S. Thaithong and W. Peters, *Antimicr. Agents Chemother.*, 1996, **40**, 1846.

197. D. C. Warhurst, *Malaria J.*, 2003, **2**, 31.

198. C. Biot, G. Glorian, L. A. Maciejewski and J. S. Brocard, *J. Med. Chem.*, 1997, **40**, 3715.

199. K. Chibale, J. R. Moss, M. Blackie, D. van Schalkwyk and P. J. Smith, *Tetrahedron Lett.*, 2000, **41**, 6231.

200. I. Benjamin, *Chem. Phys. Lett.*, 2004, **393**, 453.

201. K. A. Yamada, Sherman, I. W., *Exp. Parasitol.*, 1979, **48**, 61.

202. K. K. Ncokazi, Egan, T. J., *Anal. Biochem.*, 2005, **338**, 306.

203. A. K. Tripathi, S. I. Khan, L. A. Walker and B. L. Tekwani, *Anal. Biochem.*, 2004, **325**, 85.

204. E. Hempelmann, C. Motta, R. Hughes, S. A. Ward and P. G. Bray, *Trends Parasitol.*, 2003, **19**, 23.

205. W. Yu, Farrell, R. A., Stillman, D. J., Winge, D. R . *Mol. Cell Biol.*, 1996, **16**, 2464.

206. D. A. Bazylinski, *Int. Microbiol.*, 1999, **2**, 71.

207. T. J. Egan, J. Y., de Villiers, K. A., Mabotha, T. E., Naidoo, K. J., Ncokazi, K. K., Langford, S. J., McNaughton, D., Pandiancherri, S., Wood, B. R., *FEBS. Lett.*, 2006, **580**, 5105.

208. M. Mungthin, P. G. Bray, R. G. Ridley and S. A. Ward, *Antimicrob. Agents Chemother.*, 1998, **42**, 2973.

209. D. J. Krogstad and D. De, in 'Chloroquine: modes of action and resistance and the activity of chloroquine analogs', ed. I. W. Sherman, Washington DC, 1998.

210. A. Yayon, J. A. Vande Waa, M. Yayon and T. G. Geary, *J. Protozool.*, 1983, **30**, 642.

211. G. H. Jacobs, A. M. J. Oduola, D. E. Kyle, W. K. Milhous, S. K. Martin and M. Aikawa, *Am. J. Trop. Med. Hyg.*, 1988, **39**, 15.

212. M. Aikawa, Beaudoin, R. L., *Am. J. Trop. Med. Hyg.*, 1969, **18**, 166.

213. D. C. Warhurst and G. Gould, *Ann. Trop. Med. Parasitol.*, 1982, **76**, 257.

214. Y. Zhang, *Exp. Parasitol.*, 1987, **64**, 322.

215. H. C. Hoppe, van Schalkwyk, D. A., Wiehart, U. I. M., Meredith, S. A., Egan, T. J., Weber, B. W., *Antimicrob. Agents. Chemother.*, 2004, **48**, 2370.

216. A. Yayon, R. Timberg, S. Friedman and H. Ginsburg, *J. Protozool.*, 1984, **31**, 367.

217. P. Olliaro, F. Castelli, S. Caligaris, A. Matteelli and G. Carosi, *Microbiologica*, 1990, **13**, 137.

218. P. Olliaro, F. Castelli, F. Milano, G. Filice and G. Carosi, *Microbiologica*, 1989, **12**, 7.

219. R. M. Ekong, Robson, K. J. H., Baker, D. A., Warhurst, D. C., *Parasitology*, 1993, **106**, 107.

220. W. Trager and J. B. Jensen, *Science*, 1976, **193**, 673.

221. J. D. Haynes, Diggs, C. L., Hines, F. A., Desjardins, R. E., *Nature*, 1976, **263**, 767.

222. C. Lambros, Vanderberg, J. P., *J. Parasitol.*, 1979, **65**, 418.

223. E. S. Reynolds, *J. Cell. Biol.*, 1963, **17**, 208.

224. S. G. Langreth, P. Nguyen-Dinh and W. Trager, *Exp. Parasitol.*, 1978, **46**, 235.

225. L. H. Bannister, J. M. Hopkins, R. E. Fowler, S. Krishna and G. H. Mitchell, *Parasitol. Today*, 2000, **16**, 427.

226. M. Aikawa, *Am. J. Pathol.*, 1972, **67**, 277.

227. L. H. Bannister, Hopkins, J. M., Margos, G., Dluzewski, A. R., Mitchell, G. H., *Microsc. Microanal.*, 2004, **10**, 551.

228. K. Bachhawat, Thomas, C. J., Surolia, N., Surolia, A., *Biochem. Biophys. Res. Commun.*, 2000, **276**, 1075.

229. O. Q. Munro, Bradley, J. C., Hancock, R. D., Marques, H. M., Marsicano, F., Wade, P. W., *J. Am. Chem. Soc.*, 1992, **114**, 7218.

230. R. Hoffman, in *NMR Relaxation: T1, T2, etc, http://drx.ch.huji.ac.il/nmr/team/hoffman/hoffman.htm, accessed on 14/02/2007.*

231. I. Bertini, Kuretz, D. M., Eidsness, M. K., Liu, G., Luchinat, C., Rosato, A., Scott, R. A., *J. Biol. Inorg. Chem.*, 1998, **3**, 401.

232. D. F. Hansen, Hass, M. A. S., Christensen, H. M., Ulstrup, J., Led, J. J., *J. Am. Chem. Soc.*, 2003, **125**, 6858.

233. L. Banci, Piccioli, M., Scozzafava, A., *Coord. Chem. Rev.*, 1992, **120**, 1.

234. I. Bertini, Luchinat, C., Rosato, A., *Prog. Biophys. Mol. Biol.*, 1996, **66**, 43.

235. H. M. Marques, Brown, K. L., *Coord. Chem. Rev.*, 2002, **225**, 123.

236. L. Banci, *Curr. Opin. Chem. Biol.*, 2003, **7**, 143.

237. V. Gold, Bethell, D., *Advances in Physical Organic Chemistry.*, Academic Press, 1976.

238. H. M. Marques, Munro, O. Q., Grimmer, N. E., Levendis, D. C., Marsicano, F., Pattrick, G., Markoulides, T., *J. Chem. Soc. Faraday Trans.*, 1995, **91**, 1741.

239. M. Karplus, Petsko, G. A., *Nature*, 1990, **347**, 631.

240. E. Saiz, Tarazona, M. P., *J. Chem. Edu.*, 1997, **74**, 1350.

241. J. Jacob, Baker, B., Bryant, R. G., Cafiso, D. S., *Biophys. J.*, 1999, **77**, 1086.

242. F. Arnesano, Banci, L., Bertini, I., Felli, I. C., Luchinat, C., Thompsett, A. R., *J. Am. Chem. Soc.*, 2003, **125**, 7200.

243. B. Cheng, Safo, M. K., Orosz, R. D., Reed, C. A., Debrunner, P. G., Scheidt, W. R., *Inorg. Chem.*, 1994, **33**, 1319.

244. D. R. Evans, Reed, C. A., *J. Am. Chem. Soc.*, 2000, **122**, 4660.

245. C. Yeh, Chang, C. J., Nocera, D. G., *J. Am. Chem. Soc.*, 2001, **123**, 1513.

246. O. Q. Munro, Marques, H. M., Debrunner, P. G., Mohanrao, K., Scheidt, W. R., *J. Am. Chem. Soc.*, 1995, **117**, 935.

247. J. M. Karle and I. L. Karle, *Acta Crystallogr., Sect. C: Cryst. Struct. Commun.*, 1988, **44**, 1605.

248. G. M. Clore, Bruenger, A. T., Karplus, M., Gronenborn, A. M., *J. Mol. Biol.*, 1986, **191**, 523.

249. G. S. Collier, J. M. Pratt, C. R. De Wet and C. F. Tshabalala, *Biochem. J.*, 1979, **179**, 281.

250. C. A. Hunter and J. K. M. Sanders, *J. Am. Chem. Soc.*, 1990, **112**, 5525.